Machines and Methods for Trapping Antihydrogen

A thesis presented
by

Philippe Larochelle

to
The Department of Physics
in partial fulfillment of the requirements
for the degree of
Doctor of Philosophy
in the subject of

Physics

Harvard University
Cambridge, Massachusetts
September 2009

Thesis advisor

Gerald Gabrielse

Author

Philippe Larochelle

Machines and Methods for Trapping Antihydrogen

Abstract

A new generation of antihydrogen experiments was designed built and commissioned for use by the ATRAP at the European Center for Nuclear Research (CERN) to further progress towards the long term goal of antihydrogen laser spectroscopy. A comparison of the 1S-2S transition in hydrogen and antihydrogen would be the best test of CPT invariance in a combined lepton-baryon system. Cold antihydrogen was first produced in 2002 but a new set of experiments incorporating a magnetic field minimum Ioffe trap had to be undertaken in order to confine antihydrogen long enough to conduct the measurement. Two new experimental zones and two new Penning-Ioffe trap apparatuses were constructed to conduct these experiments. New particle loading methods for antiprotons, electrons and positrons were implemented yielding far higher loading rates. Experiments were conducted at a lower field compatible with a Ioffe trap than previous experiments. The stability of charged particles and the formation of antihydrogen atoms in a combined 375 mK deep quadrupole Penning-Ioffe trap configuration was demonstrated resolving a several year long debate over whether this would be possible, but no trapped antihydrogen atoms were detected.The first resonant detection of single antiprotons in an apparatus capable of producing antihydrogen was achieved, paving the way for antihydrogen ion experiments and sensitive detection calibrations. The temperature of the electrodes surrounding the particles

was brought down to 1.2°K greatly improving the prospects for trapping antihydrogen. Preliminary work towards a next generation apparatus to be commissioned in late 2009 or 2010 was undertaken.

Contents

List of Figures

List of Tables

Papers and Publications

1. *Antihydrogen Production within a Penning-Ioffe Trap*
   G. Gabrielse, P. Larochelle, D. Le Sage, B. Levitt, W.S. Kolthammer, R. McConnell, P. Richerme, J. Wrubel, A. Speck, M.C. George, D. Grzonka, W. Oelert, T. Sefzick, Z. Zhang, A. Carew, D. Comeau, E.A. Hessels, C.H. Storry, M. Weel, and J. Walz, Phys. Rev. Lett. 100, 113001 (2008).

2. *Single-Component Plasma of Photoelectrons*
   B. Levitt, G. Gabrielse, P. Larochelle, D. Le Sage, W.S. Kolthammer, R. McConnell, J. Wrubel, A. Speck, D. Grzonka, W. Oelert, T. Sefzick, Z. Zhang, D. Comeau, M.C. George, E.A. Hessels, C.H. Storry, M. Weel, and J. Walz, Phys. Lett. B 656, 25-29 (2007).

3. *Density and Geometry of Single Component Plasmas*
   A. Speck, G. Gabrielse, P. Larochelle, D. Le Sage, B. Levitt, W.S. Kolthammer, R. McConnell, J. Wrubel, D. Grzonka, W. Oelert, T. Sefzick, Z. Zhang, D. Comeau, M.C. George, E.A. Hessels, C.H. Storry, M. Weel, and J. Walz, Phys. Lett. B 650, 119-123 (2007).

4. *Antiproton Confinement in a Penning-Ioffe Trap for Antihydrogen*
   G. Gabrielse, P. Larochelle, D. Le Sage, B. Levitt, W.S. Kolthammer, I. Kuljanishvili, R. McConnell, J. Wrubel, F.M. Esser, H. Glueckler, D. Grzonka, G. Hansen, S. Martin, W. Oelert, J. Schillings, M. Schmitt, T. Sefzick, H. Soltner, Z. Zhang, D. Comeau, M.C. George, E.A. Hessels, C.H. Storry, M. Weel, A. Speck, F. Nillius, J. Walz and T.W. Haensch, Phys. Rev. Lett. 98, 113002 (2007).

Acknowledgments

On three different occasions, the three most senior members of the ATRAP collaboration Gerald Gabrielse, Walter Oelert and Theodor Hänsch each told me that building a great physics experiment was like building a cathedral. I would like to thank my adviser Jerry Gabrielse for the opportunity to contribute a few bricks to the ATRAP edifice over the years and for providing the guidance and support to help me navigate my graduate career. Working with antimatter, at the world's largest physics laboratory was an incredibly interesting and challenging project, and I believe I have become a better person for taking on that task.

I was privileged to work with an incredible group of people both at Harvard and at CERN. I worked very closely with four graduate students from Harvard who were also working on the ATRAP project: David Le Sage, Steve Kolthammer, Robert McConnell and Phil Richerme. David was a year ahead of me and was often an inspiration in terms of his sheer perseverance to get things done. He has also been a good friend through three years at Harvard and another two living together in Europe. He has given me a piece of advice that I shall take with me to the grave: "don't *****[1], fix it!" Steve Kolthammer and I worked closely together on the preliminary design of the second generation Ioffe trap for the antihydrogen experiment and I was grateful to to him for taking over the project when I went off to CERN. Robert and I lived and worked together through the very difficult experimental year of 2008 at CERN, celebrated when things went well, and commiserated when things did not. Phil Richerme was very helpful during his brief visits to CERN and has done a spectacular job in the construction of the new apparatus. The Harvard end of the

[1] expletive synonym for "complain" replaced for good taste.

ATRAP experiment is being left in very good hands with Steve, Rob, and Phil at the controls. Andrew Speck, a graduate student on ATRAP who worked at CERN prior to my involvement has been a tremendous help over the years on nearly all aspects of the experiment. I am very thankful for his assistance.

Four postdoctoral researchers had a very big impact on my work and education. Benjamin Levitt and Jonathan Wrubel from Harvard were the leaders at CERN when Jerry was not around and they were always there to help and guide my progress. I am grateful for their instruction, support and camaraderie. Matthew Weel and Matthew George from York University not only did a spectacular job of getting a new positron system up and running in a very short amount of time, they also frequently helped with other ATRAP projects when the rest of us were a little overwhelmed. I am especially grateful to Matt George for giving me substantial help getting the tuned circuit amplifiers running in 2008. I got to know two other postdocs only very briefly, Irma Kuljanishvili at Harvard in 2006 and Joe Borbely at CERN in 2009 but I am grateful for the contributions they have made to the project as well.

It was a pleasure working with the rest of our collaborators from York University, Forshungzentrum Jü and Mainz University. Professors Cody Storry and Eric Hessels from York taught me a lot on a number of topics, were willing to talk over both theory and experiment, and helped me become a better experimentalist. Professor Walter Oelert and Dieter Grzonka from Jülich labored diligently to make sure the detectors were running properly were extremely helpful on a number of projects elsewhere in ATRAP. They were also very kind to me and I valued their input and advice. I am also very grateful for the hard work they did and strings they pulled to get the

quadrupole Ioffe trap built in a timely manner in 2006. I am also grateful to Helmut Soltner, also from Jülich for the work he did on the Ioffe trap. The graduate students from the other institutions, Daniel Comeau and Adam Carew from York, Zhongdong Zhang and Marcin Zielinski from Jülich and Andreas Müllers from Mainz were all valued colleagues and friends.

The other graduate students in the Gabrielse group proved to be very valuable resources as well. I am very grateful to Nick Guise and Jack Disciacca for their help on the tuned circuit resonance amplifiers. The progress we made at CERN would have been impossible without their efforts. David Hanneke, Dan Farkas, Josh Goldman, Shannon Fogwell, Yulia Gurevitch and Josh Doerr were all very handy to bounce ideas off of. I am especially thankful to Josh Goldman for reading over drafts of this thesis and making comments.

I am grateful to a new number of staff members at Harvard, but most notably to Jan Ragusa, the administrative coordinator for the Gabrielse group. She was always incredibly kind and helpful to me on both continents and she Isaac were, and remain, a delight to talk to. I am also grateful to Stan Cotreau of the Harvard physics student machine shop for teaching me a great deal about machining while ensuring that I didn't gravely injure myself.

We have had a number of undergraduates who have helped out at CERN and Harvard during my graduate career and I am grateful to all of them. I am especially grateful for the contributions of three Harvard students who worked with us for extended periods of time and on several occasions: Max Chalfin, Max Swiatlowski and John Noss. Each of them helped me out on crucial projects that may not have gone

forward without their efforts.

I would like to thank my parents for their support throughout my more than two decades of education, without their sacrifice and guidance none of my achievements would have been possible. I would also like to thank Manuela Oprea for her extraordinary kindness, patience and encouragement while I have been writing this thesis. Lastly I would like to thank the people and taxpayers of the world, and Europe in particular, for supporting the efforts of scientists like myself at institutions like CERN.

Chapter 1

Introduction

Antihydrogen ($\overline{\mathrm{H}}$) is the simplest antimatter atom, consisting of a bound state of an antiproton ($\overline{\mathrm{p}}$) and a positron (e^+). The existence of each of the constituent parts was suggested by Dirac, the positron was discovered in 1932 and the antiproton in 1955. The demonstration of the existence of antihydrogen occurred in 1996 when 9 antihydrogen atoms were observed at close to the speed of light [2]. The first production of cold antihydrogen occurred in 2002 [3, 4]. The study of antihydrogen is motivated by two tests of fundamental physics. First, a comparison of the energy levels of hydrogen and antihydrogen is a test of charge parity time (CPT) invariance which requires that they be the same. Second, a gravity measurement between the two would be a test of the weak equivalence principle. Three collaborations at the European Center for Nuclear Research (CERN), ATRAP, ALPHA and ASACUSA, are currently working on experiments to probe the internal energy states of antihydrogen, while a fourth one also at CERN, AEGIS, has received approval to begin working on an antihydrogen gravity measurement.

This thesis describes work done with the ATRAP collaboration from 2004 through 2009 working towards the eventual laser spectroscopy of antihydrogen. Prior to this work, antihydrogen had been successfully formed using two different methods in a Penning trap. After its creation, however, the antihydrogen would leave the trap in less than a ms and annihilate as its net neutral charge was no longer confined by the electric and magnetic fields of the Penning trap. The next logical step towards spectroscopy is to superimpose a magnetic trap capable of confining the antihydrogen for a sufficient period of time to conduct the measurement. Five major advances towards achieving trapped antihydrogen were accomplished during this work through the construction of two new apparatuses in a new experimental zone at CERN:

1. **Significantly larger numbers of antiprotons, positrons, and electrons were loaded than previous experiments**.Larger numbers of electrons and positrons were achieved by using loading methods that differ significantly from previous experiments. The method for loading electrons is described in chapter 4 and the method for loading positrons in 6. Larger numbers of antiprotons, see 5, were loaded by using larger electrodes and a larger bore more homogeneous magnet. Larger numbers of trapped particles facilitate the formation of more antihydrogen and thus increase the chances to successfully trap some.

2. **Antihydrogen was formed, and particles were loaded at 1 tesla compared with previous experiments above 5 tesla**. When superimposing a magnetic field minimum Ioffe trap (see chapter 9) on the background field of a Penning trap, the total trap depth will be given by the difference between the total field at the edge of the trap and that at the center. For a given radial field

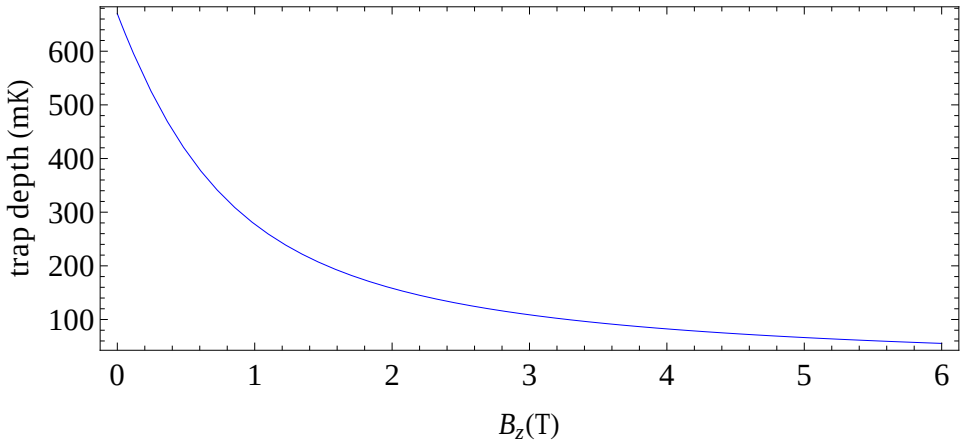

Figure 1.1: The trap depth in a Ioffe trap for a 1 T radial field as a function of axial field.

at the edge of the trap B_r and uniform axial background field B_z the total trap depth will be given by:

$$\Delta B = \sqrt{B_r^2 + B_z^2} - B_z \tag{1.1}$$

To maximize the trap depth of the Ioffe trap when the antihydrogen is produced, it is important to use the smallest B_z field possible. Fig. 1.1 illustrates this for a radial field of $B_r = 1$ tesla for different axial background fields. The trap depth in a 1 T background field is about 275 mK whereas at 5 tesla the trap depth it is down to under 70 mK. This illustrates the importance of establishing procedures for operation at lower field.

3. **Sufficient charged particle lifetimes and antihydrogen formation was demonstrated in a 375 mK deep combined quadrupole Penning-Ioffe trap**. It had been a matter of some debate (see chapter 10) as to whether charged particles could survive long enough in the presence of a quadrupole magnetic field to form antihydrogen. Experiments were conducted in 2006 es-

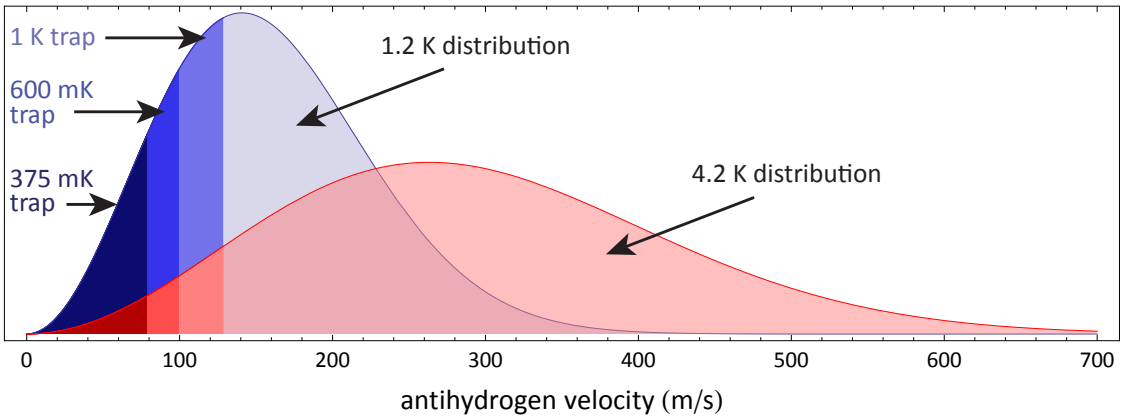

Figure 1.2: The Maxwell-Boltzmann distribution of antihydrogen velocities at 4.2 K and 1.2 K and the fractions trapped by different strength Ioffe traps.

tablishing a sufficient lifetime for such particles [5] and further experiments were conducted in 2007 demonstrating the formation of antihydrogen in a quadrupole Penning-Ioffe trap [6].

4. **The base temperature of the apparatus was lowered from 4.2°K down to 1.2°K**. The maximum magnetic trap depth which it is practically feasible to achieve with a Ioffe trap in a 1 tesla background field is 1°K or below. Therefore forming the antihydrogen at the lowest possible temperature is of significant importance. Fig. 1.2 shows the Maxwell-Boltzmann distribution for antihydrogen formed at 1.2°K and 4.2°K. Up to now antihydrogen has been formed at a significantly higher temperatures than this (see chapter **??**), but this represents the best case scenario if we are able to form antihydrogen in thermal equilibrium with the trap. As we can see from Fig. 1.2 and Table 1.1, there is a very significant advantage to lowering the temperature of the antihydrogen when looking at the fraction that will be trapped for a given magnetic field minimum trap: even our first generation Ioffe trap (375 mK) is likely to trap

Configuration	**Trap depth**	$\bar{H}$ **trapped at** 1.2 °K	$\bar{H}$ **trapped at** 4.2 °K
1st generation ATRAP Ioffe trap	375 °mK	10.9 %	1.9 %
2nd generation ATRAP Ioffe trap	600 °mK	19.9 %	2.9 %
Best realistic Penning-Ioffe trap	1000 °mK	35.6 %	7.6 %

Table 1.1: Fraction of antihydrogen atoms trapped for different magnetic trap depths and $\bar{H}$ Maxwell-Boltzmann temperature distributions.

more antihydrogen at 1.2 °K than the best realistic Ioffe trap could do operating at 4.2 °K.

5. **Single antiprotons were detected within an apparatus capable of making antihydrogen, paving the way for antihydrogen ion experiments and sensitive detector calibrations**. Single antiprotons had been regularly detected in previous apparatus using non-destructive tuned circuit resonance techniques, but only with smaller electrodes and at a higher field both of which significantly improve the detection sensitivity. The first demonstration of single antiproton detection, see chapter 7, in an apparatus that has made an antihydrogen enables the detection sensitivity necessary for future antihydrogen ions experiments where very small numbers of ions are expected to be formed, see chapter 8. This sensitivity also allows for a very sensitive calibration of the antiproton annihilation detectors by leaking out one antiproton at a time.

This thesis will describe the theory and operation of the platform for these ex-

periments, the combined Penning-Ioffe trap, and present a series of results. A review of Penning trap theory along with the behavior of charged particles within such a trap is given in chapter 2. The details of the construction of the new Penning-trap apparatus is given in chapter 3 with emphasis on the commissioning of a new 247 henry 20 inch bore 3 tesla superconducting magnet, and the implementation of a 1.2 °K pumped helium system. The advances in particle loading and diagnostics for electrons, antiprotons, and positrons are given in chapters 4, 5 and 6 respectively, with a discussion of electron plasma mode diagnostics given in chapter 4.

Chapter 7 describes the resonant detection of antiprotons using tuned circuit amplifiers and chapter 8 discusses the prospects and challenges for antihydrogen ion formation and the suitability of using tuned circuit amplifier detection techniques to complement such experiments. Chapter **??** describes the design, construction, and operation of a 375 mK deep first generation quadrupole Ioffe trap and preliminary work done towards the commissioning of a second generation combined quadrupole and octupole Penning-Ioffe trap. Chapter **??** gives a brief review of the theory of charged particle behavior in both quadrupole and octupole Penning-Ioffe traps and presents experimental results demonstrating the sufficiently long lifetimes of both electrons (and thus positrons) and antiprotons in a quadrupole Penning-Ioffe trap for antihydrogen experiments. Chapter **??** discusses experiments showing the first antihydrogen formation in a combined quadrupole Penning-Ioffe trap demonstrating that it is possible to create antihydrogen in such a configuration and achieving a crucial milestone towards the magnetic trapping of antihydrogen.

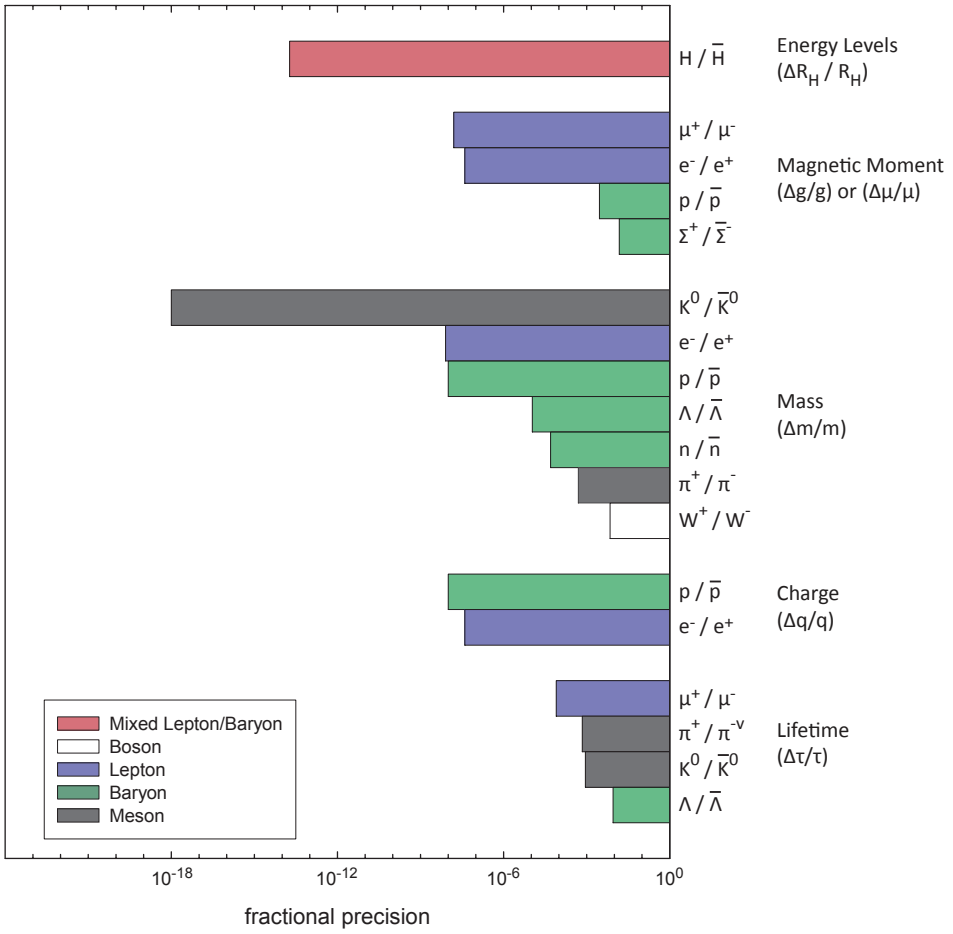

Figure 1.3: Fractional precision of potential H-$\overline{\text{H}}$ experiments compared to existing CPT tests. H-$\overline{\text{H}}$ precision is taken from the best 1S-2S spectroscopy to date [7], other values are from the particle data group [8].

1.1 CPT Invariance

The main motivation behind our antihydrogen experiments is to test the combined charge parity and time (CPT) invariance of nature. The CPT theorem states that any quantum field theory that obeys both Lorentz invariance and locality requires that all physical systems be invariant under a combined charge parity and time transformation [9]. Antihydrogen is the system that you get if you perform a charge, parity and time

transformation on hydrogen and therefore any discrepancy between the two would be a violation of the CPT theorem. Comparing the frequencies of the $1S \rightarrow 2S$ transition in hydrogen and antihydrogen down to their 1.3 Hz natural linewidth would allow in principle a comparison of better than one part in 10^{15} making it the best test of CPT for a combined lepton-baryon system.

shows the experimental precision that has been reached in various tests of the CPT theorem. As it is unknown by what mechanism CPT invariance could be violated it is logical to pursue tests in many different systems. The measurement of the 1S-2S transition in hydrogen has thus far been accomplished down to 1.8 parts in 10^{14} [7]. The measurement of the transition in both hydrogen and antihydrogen would essentially be a comparison of the values of the Rydberg constant for the two atoms, which is sensitive to many different parameters:

$$\frac{R_{\overline{\mathrm{H}}}}{R_H} = \frac{\left(1+\frac{m_{\mathrm{e}^-}}{m_{\mathrm{p}}}\right)}{\left(1+\frac{m_{\mathrm{e}^+}}{m_{\overline{\mathrm{p}}}}\right)} \left(\frac{m_{\mathrm{e}^+}}{m_{\mathrm{e}^-}}\right) \left(\frac{q_{\overline{\mathrm{p}}}}{q_{\mathrm{p}}}\right)^2 \left(\frac{q_{\mathrm{e}^+}}{q_{\mathrm{e}^-}}\right)^2 \tag{1.2}$$

Both parity (P) and charge parity (charge parity) were once thought to be valid symmetries of nature, but instances where both were broken were discovered in the 1957 and 1964 respectively [10, 11]. The CPT symmetry is on firmer theoretical footing than either of those due to the CPT theorem but models suggesting possible violations have been proposed [12, 13].

1.2 Antihydrogen formation and trapping method

Antihydrogen has thus far been created using two methods. In the first method demonstrated in 2002, antihydrogen is formed through a three body recombination

process where a second positron takes away excess energy allowing the formation:

$$\overline{\mathrm{p}} + \mathrm{e}^+ + \mathrm{e}^+ \rightarrow \overline{\mathrm{H}}^* + \mathrm{e}^+ \tag{1.3}$$

In 2004 a second method was developed using a charge exchange process with positronium where the extra electron in the positronium takes away excess energy allowing for the formation:

$$\mathrm{Ps} + \overline{\mathrm{p}} \rightarrow \overline{\mathrm{H}} + \mathrm{e}^- \tag{1.4}$$

The three body recombination method yields a much higher formation rate than the charge exchange method, but is also likely to make much more energetic antihydrogen atoms that are more difficult to capture in a magnetic field minimum trap, as described in chapter 11. During the course of this work, only the three body recombination method of antihydrogen formation was accomplished, but preliminary work to allow for the charge exchange formation method was also pursued.

The method chosen to trap antihydrogen is through the use of a magnetic field minimum Ioffe trap configuration [14]. A research group at the Massachusetts Institute of Technology has used this trap configuration to confine and perform 1S-2S laser spectroscopy on hydrogen atoms [15, 16].

1.3 ATRAP, BTRAP, Zone 2 and Zone 3

The first antihydrogen produced by the ATRAP collaboration took place in two similar apparatuses known as hbar 1 and hbar 2. To make further progress two completely new apparatuses were constructed, eventually known as ATRAP and BTRAP. If the hbars were the equivalent of the glider that the Wright brothers flew at kitty

hawk, ATRAP and BTRAP are more like Boeing 747s. They were meant to do everything that the hbars did but on a much larger scale and with the capability to incorporate many new instruments critical to furthering progress. The largest change is that the new apparatuses were built to incorporate a magnetic field minimum Ioffe trap which significantly increased the radial space needed in the bore of the magnet providing the background field for the Penning trap. Learning to deal with such a large magnet, located in the experimental area known as "zone 2" whereas prior experiments had a occurred in "zone 1", was a challenge in and of itself as described in chapterchp:PenningApp.

The first apparatus built for use the new experimental zone was referred to as ATRAP. It was installed in 2006 with the Ioffe trap surrounding the upper electrode stack of the Penning trap. In 2007 a nearly identical copy of the ATRAP apparatus, named BTRAP, was built and the Ioffe trap was removed from ATRAP and placed on BTRAP. ATRAP had a titanium cylindrical can in the section where the Ioffe trap was usually situated. Throughout 2007 and 2008 ATRAP and BTRAP were interchanged into the beamline to perform different experiments.

Another significant change was the use of a different positron accumulation method, described in chapter 6. Prior experiments had used a Rydberg positronium method of loading positrons whereas this experiment now uses a positron buffer gas accumulation method leading to a several hundred fold increase in the rate of positron accumulation. The positron accumulator takes up a significantly larger amount of space than the previous method did and required the construction of a new experimental zone, named "zone 3".

Chapter 2

Charged Particle Confinement in a Penning Trap

The first step towards creating antihydrogen atoms for further study is the confinement of the two charged particle species, positrons and antiprotons, required for its creation. While there exist a variety of charged particle confinement methods, the ATRAP collaboration relies on a penning trap configuration in order to both confine and recombine the two species into antihydrogen. One group pursuing similar research goals is also using a penning trap configuration [3], while another group trying to study ground state antihydrogen in a beam is planning on using a completely different radio frequency "cusp" trap configuration [17].

The penning trap was first pioneered by Hans Dehmelt in 1959 and named after the Dutch physicist Frans Michel Penning based on his work on discharge tubes for use in vacuum gauges [18]. Radial confinement for charged particles in a penning trap is accomplished by applying a uniform magnetic field which the particles will

execute cyclotron motions around and trapping in the third dimension is achieved by placing an electrostatic potential minimum for the given charge species along the magnetic field axis. The use of a quadrupole electrostatic potential leads to easily analyzable particle trajectories and is therefore often used, but other configurations with significant contributions from non quadratic terms in the potential are also common. ATRAP often uses electrostatic potentials which differ significantly from quadratic during both particle transfer, manipulation and antihydrogen recombination experiments. We also vary the uniformity of the magnetic field for reasons that will be discussed in later chapters. However, studying the ideal case of an electrostatic quadrupole potential in a uniform magnetic field is instructive for understanding the behavior of particles in our apparatus.

2.1 Electromagnetic Fields in a Penning Trap

In the ideal penning trap configuration, the magnetic field is uniform in what we label the axial direction $\hat{z}$.

$$\vec{B} = B_0\hat{z} \tag{2.1}$$

With only such a field present, a charged particle will undergo circular motion around the field, and is thus confined in 2 dimensions, but it is free to move in the direction parallel to the field. The addition of an electrostatic quadrupole potential adds a confining potential in the direction parallel to the field $\hat{z}$ which is proportional to z^2. However, since the electric potential with the absence of sources must satisfy the Laplace equation $\nabla^2\Phi = 0$, the center of the trap cannot be an electric potential minimum in three dimensions. Instead the center of the field is a saddle point,

meaning that it is confining in z direction and anti-confining in the radial ρ direction.

In spherical coordinates, the general form of an electrostatic potential with azimuthal symmetry about the axis z can be expressed as a product of radial functions and Legendre Polynomials of the polar angle θ [19].

$$\Phi(r,\theta) = \sum_{l=0}^{\infty} [A_l r^l + B_l r^{-(l+1)}] P_l(\cos\theta) \tag{2.2}$$

Since the potential is finite at $r = 0$, we can set all of the B_l terms to zero. The quadratic contribution to the potential corresponds to the $l = 2$ terms. The second Legendre polynomial has the form $P_2(x) = \frac{1}{2}(3x^2 - 1)$. Using the conversions from spherical to cylindrical coordinates $z = r\cos\theta$ and $\rho = r\sin\theta$ we arrive at the general form of the quadratic potential:

$$\Phi(\rho, z) \propto \left(z^2 - \frac{\rho^2}{2}\right) \tag{2.3}$$

This describes a potential which would have equipotentials along hyperboloids in three dimensions. Since the solution to Laplace's equation is unique, the simplest way to create such a potential would be to simply place conductors along the surfaces that satisfy the equation $\Phi_0 = z^2 - \rho^2/2$ and put each of them at a uniform voltage: this guarantees that the potential at all other points within the conductors would also be a quadrupole potential.

2.1.1 Hyperbolic Electrode Penning Trap

To ensure that all boundaries are held at fixed voltages, it is necessary to completely surround the trap space so that the particles see conductors at a fixed potential

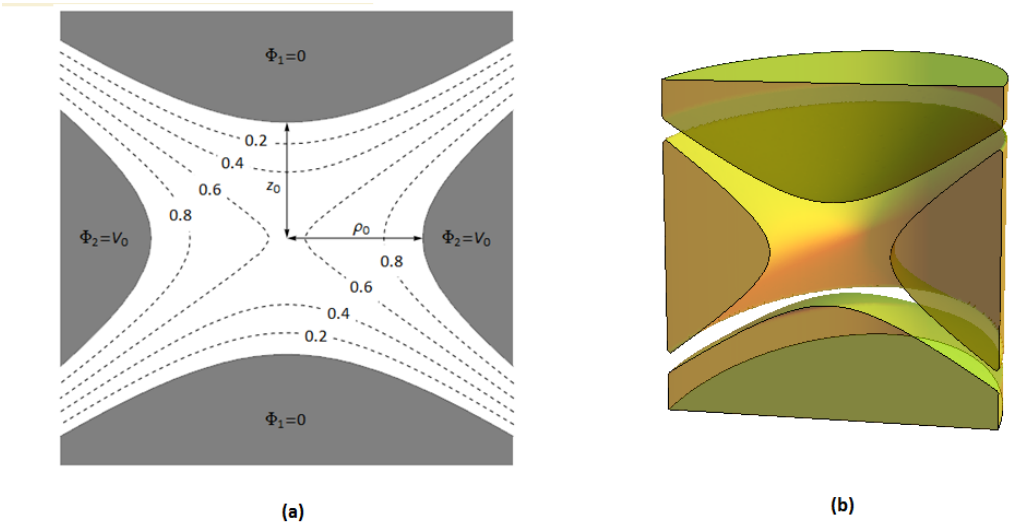

Figure 2.1: (a) Potential contours in a hyperbolic electrode geometry. The numbers indicate the fraction of V_0 at each of the contours. (b) A 3 dimensional cutaway representation.

in all directions. One way to do this is to have one conductor that intersects the position $z = 0$ and radius $\rho = \rho_0$ and have two other conductors which intersect the points $z = z_0$ and $z = -z_0$ at $\rho = 0$. If we place the first conductor at a potential Φ_2 it must satisfy the equation $\Phi_2 = -A\rho_0$ at $z = 0$, where A is an arbitrary constant that we have placed in front of the potential. Similarly, the other conductors must satisfy the equation $\Phi_1 = Az_0^2$ at $\rho = 0$. Therefore we have the condition:

$$\Phi_2 - \Phi_1 = -A\left(z_0^2 + \frac{\rho^2}{2}\right) \tag{2.4}$$

If you are to build an electrode configuration like this it is convenient to rewrite the potential with the constant in the form

$$A = \frac{\Phi_2 - \Phi_1}{z_0^2 + \frac{\rho^2}{2}} \tag{2.5}$$

If we define the geometric constant $d^2 = \frac{1}{2}\left(z_0^2 + \frac{\rho_0^2}{2}\right)$ and assume that we will be

holding the electrodes that intersect $z = z_0$ at $\rho = 0$ at ground ($\Phi_1 = 0$), and placing the electrode that intersects $\rho = \rho_0$ at $z = 0$ at a voltage V_0 ($\Phi_2 = V_0$) then we can rewrite the general form of our quadrupole potential as:

$$\Phi(\rho, z) = \frac{C_2 V_0}{2d^2}\left(z^2 - \frac{\rho^2}{2}\right) \tag{2.6}$$

The constant C_2 is introduced to represent how closely the potential produced represents an ideal quadrupole potential, in which case $C_2 = 1$ and $C_{n\neq 2} = 0$. If it is not an ideal quadrupole C_2 can vary from 1 and we can get non-zero contributions from the other terms. This hyperbolic electrode method was how the first penning traps for high precision experiments for single leptons were constructed [20]. The hyperbolic electrode configuration presents several difficulties for antihydrogen experiments, however, as it is both difficult to load large numbers of particles into such a trap, and it is not possible to make potential structures that can trap two species of opposite charge.

2.1.2 Cylindrical Electrode Penning Trap

To overcome these difficulties an electrode configuration using conductors in the form of many hollow cylindrical tubes is employed. This both allows a for a wide range of potential structures to accommodate different charge species and allows for many particles to be loaded from the top and bottom of the electrode stack.

Clearly, placing the surface of such a conductor at a fixed potential will not lead to a quadrupole potential throughout the region enclosed by the electrode, as their surface does intersect the equipotential lines of a quadrupole. However, by properly designing the geometry of the cylindrical electrodes and the potential applied to each

of them, a very good quadrupole potential can be created near the center of the trap.

To analyze the field created by different cylindrical electrode configurations, we can analyze the solution to Laplace's equation in cylindrical coordinates. The general, separable, form of the potential can be written as:

$$\Phi(\rho, z, \phi) = R(\rho)Z(z)H(\phi) \tag{2.7}$$

Where ϕ is the azimuthal angle. Upon plugging this into the Laplace equation in cylindrical coordinates we find solutions for the z and ϕ dependence of the form:

$$Z(z) \propto \begin{cases} e^{\pm ikz} \text{ if } c_z = -k^2 \leq 0 \\ e^{\pm \alpha z} \text{ if } c_z = \alpha^2 > 0 \end{cases} \qquad H(\theta) \propto \begin{cases} e^{\pm i\nu\phi} \text{ if } c_\phi = -\nu^2 \leq 0 \\ e^{\pm \beta\phi} \text{ if } c_\phi = \beta^2 > 0 \end{cases} \tag{2.8}$$

Arriving at these forms involves setting first the z dependent terms in the differential equation equal to a constant c_z, and then setting the remaining ϕ dependent terms equal to another constant c_ϕ that will vary depending on the boundary conditions [21]. These two constants will then become part of the solution for the remaining ρ dependence. If the boundary conditions require oscillatory solutions, ie $c_z = -k^2$ and $c_\phi = -\nu^2$ then the solution for the ρ dependence is given by the solution to the differential equation:

$$\frac{\partial^2 R(\rho)}{\partial \rho^2} + \frac{1}{\rho}\frac{\partial R(\rho)}{\partial \rho} - k^2 R(\rho) - \frac{\nu^2}{\rho^2} R(\rho) = 0 \tag{2.9}$$

One set of solutions to this equation are called Bessel functions of the first kind, and take the form:

$$R(\rho) \propto J_\nu(ik\rho) = \sum_{m=0}^{\infty} \frac{(-1)^m}{m!(m+\nu)!} \left(\frac{ik\rho}{2}\right)^{2m+\nu} \tag{2.10}$$

There is another set of solutions called Bessel functions of the second kind, denoted $Y_\nu(ik\rho)$. However, these go to $-\infty$ at $\rho = 0$ and are thus not applicable for the problems we are interested in. It is more convenient to put (2.10) into a form which is completely real, these are called modified bessel functions of the first kind:

$$I_\nu(k\rho) = i^{-\nu} J_\nu(ik\rho) \tag{2.11}$$

Solving for a potential which includes contributions from all of the terms in the Bessel function expansion would be complicated, luckily the azimuthal symmetry of the cylindrical electrode geometry substantially simplifies the problem. As there can be no ϕ dependence in the $H(\phi)$ part of the potential, the only contribution from the ν terms comes from $\nu = 0$. This also means the only contribution from the Bessel functions must come from the $I_0(k\rho)$ term.

Solving for the coefficients of the problem requires imposing boundary conditions in all directions, and therefore imposing a set potential at a sufficient axial distance away from the center of the trap. This is accomplished by modeling our open endcap electrode geometry as a closed endcap configuration, assuming that a sufficiently long set of electrodes held at a given potential above the model would approximate the closed endcap condition.

In this configuration, shown for different cylindrical electrode geometries in figure Fig. 2.2, the boundary condition on the axial dependence imposes the following constraint on k:

$$k_n = \frac{(n + \frac{1}{2})\pi}{L} \tag{2.12}$$

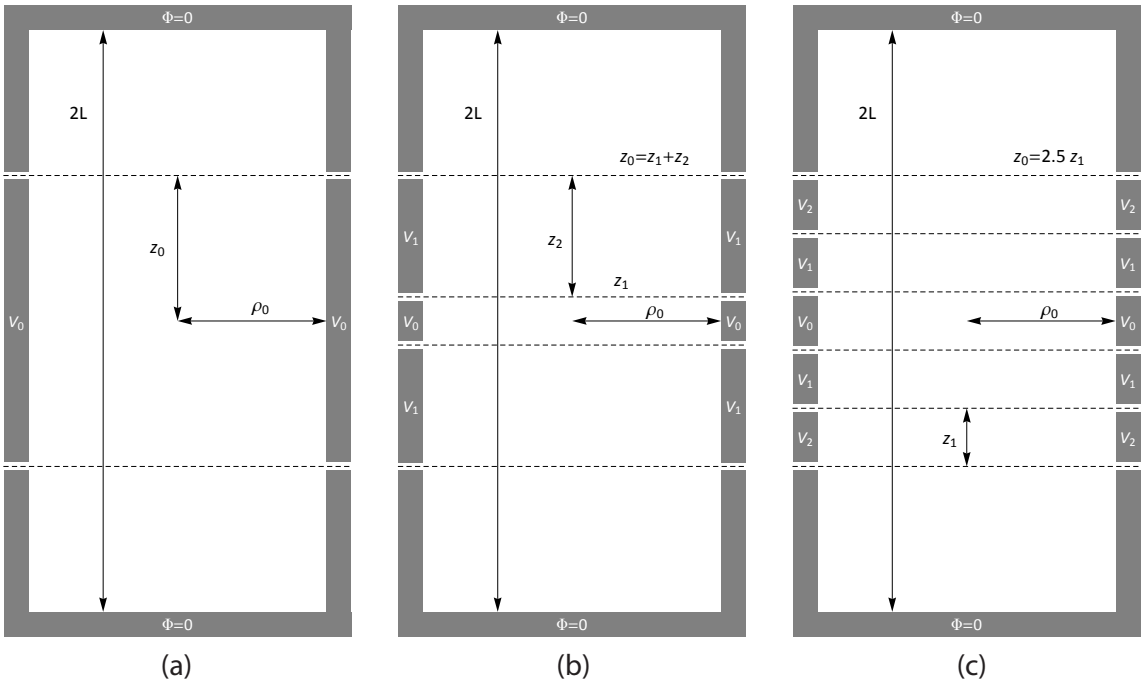

Figure 2.2: Boundary Conditions for Analytic Calculation of Potentials

The overall form for the potential is now written:

$$\Phi(z,\rho) = \sum_{n=0}^{\infty} S_n I_0(k_n \rho)\cos(k_n z) \tag{2.13}$$

Multiplying both sides of equation (2.13) by $\sum_m^{\infty}\cos(k_m z)$ and integrating we can now use the following orthogonality relation for the cosine functions:

$$\int_0^L \cos(k_n z)\cos(k_m z)dz = \frac{L}{2}\delta_{mn} \tag{2.14}$$

To arrive at the following solution for the expansion coefficients:

$$S_n = \frac{2}{LI_0(k_n\rho)}\int_0^L \Phi(\rho,z)\cos(k_n z)dz \tag{2.15}$$

Equation (2.6) is a special case of the more general Legendre expansion for a cylindrically symmetric potential with a reflection symmetry about the axial center

($\Phi(\rho, z) = \Phi(\rho, -z)$):

$$\Phi(r, \theta) = \frac{V_0}{2} \sum_{\substack{j=0 \\ even}}^{\infty} C_j \left(\frac{r}{d}\right)^j P_j(\cos\theta) \tag{2.16}$$

These coefficients, C_j, can be related to the Bessel function coefficients S_n by taking a Taylor series expansion of $\cos(k_n z)$ and equating the coefficients of z^j on both sides for $\rho = 0$. Noting that $I(0) = 1$ and $P_j(1) = 1$ we get:

$$C_j = \frac{2}{V_0} \frac{(-1)^{\frac{j}{2}}}{j!} \sum_{n}^{\infty} S_n (k_n d)^j \tag{2.17}$$

The goal of this analysis is to pick the relevant parameters of different electrode geometry and voltage values in order to tune out the non-quadratic terms in the potential on axis. The value of S_n can be determined by integrating equation (2.15) at the boundary of the electrodes $\rho = \rho_0$ where the potentials are known. The analysis follows most simply if we consider the total potential as being the superposition of the potentials created by each set of electrodes held at a given voltage with all of the others held at ground. If there are a total of p sets of electrodes (a set being one above and one below the origin, save for the central one) then the total potential will be given by:

$$\Phi(\rho, z) = \sum_{m=0}^{p-1} \sum_{n}^{\infty} S_n^m I_0(k_n \rho) \cos(k_n) \tag{2.18}$$

For the simple case in figure Fig. 2.2a where we only have potential on one electrode, if we approximate the gap between electrodes to be ≈ 0 the value of the coefficients are:

$$S_n^0 = \frac{2V_0}{k_n L} \frac{\sin(k_n z_0)}{I_0(k_n \rho_0)} \tag{2.19}$$

For the case in figure Fig. 2.2b where we have potentials on three electrodes the

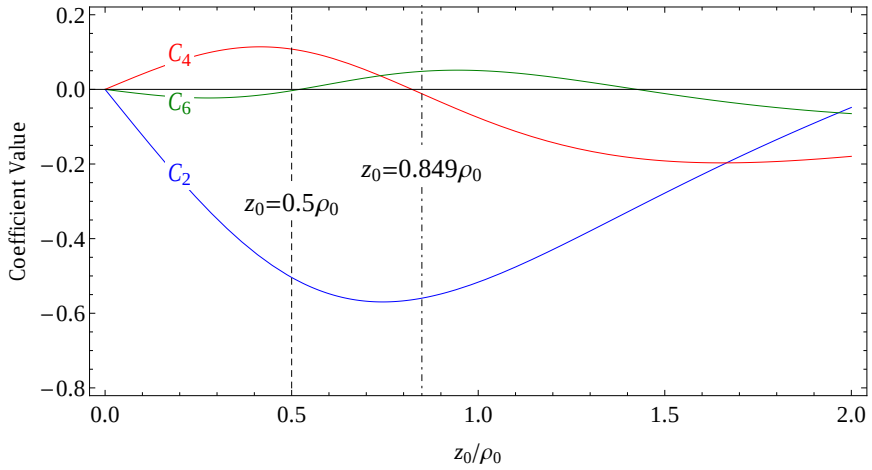

Figure 2.3: Polynomial coefficients vs. axial length for 3 electrode trap

coefficients are:

$$S_n^0 = \frac{2V_0}{k_n L}\frac{\sin(k_n z_1)}{I_0(k_n\rho_0)} \tag{2.20}$$

$$S_n^1 = \frac{2V_1}{k_n L}\frac{\sin(k_n z_0) - \sin(k_n z_1)}{I_0(k_n\rho_0)} \tag{2.21}$$

For the case in figure Fig. 2.2c for potentials on 5 electrodes we have:

$$S_n^0 = \frac{2V_0}{k_n L}\frac{\sin(\frac{1}{2}k_n z_0)}{I_0(k_n\rho_0)} \tag{2.22}$$

$$S_n^1 = \frac{2V_1}{k_n L}\frac{\sin(\frac{3}{2}k_n z_0) - \sin(\frac{1}{2}k_n z_0)}{I_0(k_n\rho_0)} \tag{2.23}$$

$$S_n^2 = \frac{2V_2}{k_n L}\frac{\sin(\frac{5}{2}k_n z_0) - \sin(\frac{3}{2}k_n z_0)}{I_0(k_n\rho_0)} \tag{2.24}$$

Using these values we can see what the impact of different electrode geometries and voltages will be on the multipole expansion coefficients in (2.17). For the case in figure Fig. 2.2a we get a straightforward curve relating the value of C_2, C_4 and C_6 for different ratios of z_0/ρ_0, as show in figure Fig. 2.3. To tune out the C_4 contribution, we see that we would be best off picking $z_0 = 0.822\rho_0$. In the ATRAP and BTRAP

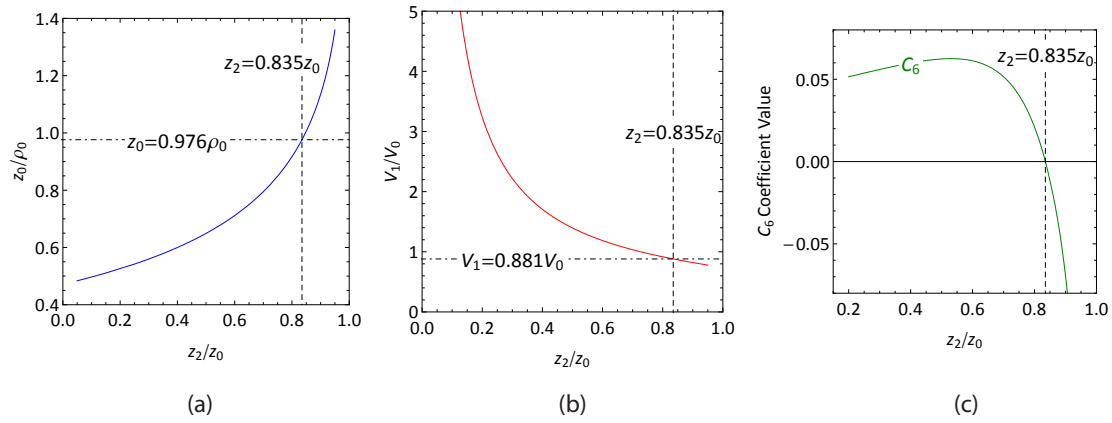

Figure 2.4: Constrained dimensions and voltages for tuning out C_4 and C_6 for a 5 electrode trap. (a) Length of compensation electrode to orthogonalize trap. (b) Voltage ratio to eliminate C_4 and (c) C_6 as a function of compensation electrode length.

apparatuses that are the subject of the thesis the majority of electrodes where chosen with either $z_0 = 0.5\rho_0$ (these are called "radius length electrodes") or with $z_0 = 0.849\rho_0$ (called "endcap" electrodes) in order to achieve a desired balance between potential penetration on axis and the ability to adjust several voltages within a confined axial space.

Because there was only one parameter to tune in the 3 electrode configuration we could only tune out one of the anharmonic components. If we move to either a 5 electrode configuration (Fig. 2.2b) or a 7 electrode configuration (Fig. 2.2c) we now have enough parameters to tune in order to eliminate both C_4 and C_6. In the 5 electrode case we have two electrode size ratios (z_1/ρ_0 and z_2/z_1) and one voltage ratio (V_1/V_0). In the 7 electrode case we have one electrode size ratio (z_1/ρ_0) and two voltage ratios (V_2/V_0 and V_1/V_0).

In the 5 electrode case each coefficient will result from the addition of the contri-

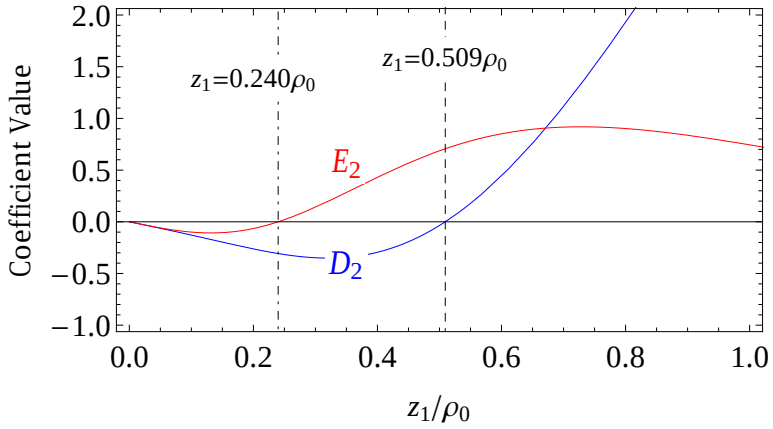

Figure 2.5: D_2 and E_2 coefficients for a 7 electrode trap as a function of axial electrode length.

butions from each set of electrodes. Following equation (2.16) where we have defined the coefficients in terms of the voltage V_0 on the central electrode, we can define the total coefficient as the superposition of the contribution to that coefficient from each set of electrodes with the other sets held at ground:

$$C_k = C_k^{(0)} + \frac{V_1}{V_0} D_k \tag{2.25}$$

Where $C_k^{(0)}$ is the contribution from the electrode with V_0 applied and D_k the contribution from the V_1 electrode. Following the work done in [22] it is convenient to pick a geometry such that changing the voltage V_1 does not change the quadratic part of the potential, and instead only affects the tuning out of the C_4 and C_6 components. For this reason, the electrode with V_1 is called a compensation electrode. This configuration is called an **orthogonalized** trap and can be achieved by picking a geometry where $D_2 = 0$.

For a given ratio of z_0/ρ_0 there will be a unique value of z_2/z_1 that makes $D_2 = 0$ (Fig. 2.4a). To tune out C_4 we can see that $\frac{V_1}{V_0} = -\frac{C_4^{(0)}}{D_4}$, thus we can plot z_2/z_1 against

	3 Electrodes			5 Electrodes	7 Electrodes
ρ_0	1				
z_0	0.5	0.822	0.849	0.976	1.273
z_1	-	-	-	0.162	0.509
z_2	-	-	-	0.815	-
d	0.612	0.767	0.781	0.852	1.030
V_1/V_0	-	-	-	0.881	0.931
V_2/V_0	-	-	-	-	0.706
C_2	-0.509	-0.577	-0.574	-0.545	-0.638
C_4	0.108	0	-0.012	0	0
C_6	-0.004	0.046	0.048	0	0
C_8	-0.006	-0.006	-0.004	0.037	0.049

Table 2.1: Polynomial coefficients for 3, 5 and 7 electrode penning trap configurations. These coefficients are given for a default electrode radius of $\rho_0 = 1$. For the ATRAP and BTRAP apparatuses all dimensions are multiplied by 18 mm, and in an apparatus currently under construction, all dimensions are multiplied by 36 mm.

$\frac{V_1}{V_0}$ (Fig. 2.4b) taking into account the value of ρ_0 from the previous constraint. Lastly we can plot the behavior of C_6 as a function of z_2/z_1 using the previous constraints to pick a value of where $C_6 = 0$ (Fig. 2.4c) . This last value turns out to be $z_2/z_0 = 0.835$ and plugging that back in to the other constraints gives the optimum geometry for the 5 electrode trap listed in table Table 2.1.

For the 7 electrode configuration, the contributions for the polynomial coefficients on axis will be given by:

$$C_k = C_k^{(0)} + \frac{V_1}{V_0} D_k + \frac{V_2}{V_0} E_k \tag{2.26}$$

As before, D_k is the contribution from the electrodes with V_1 and now E_k is the contribution from the electrodes with V_2. Because we have constrained all the

electrodes to have the same length, we can only eliminate either D_2 or E_2 but not both. These values are shown in Figure as a function of axial electrode length. In a new apparatus, under construction during the writing of this thesis, the choice was made to eliminate D_2. Given this electrode ratio we can solve for the proper values of V_0, V_1 and V_2 that are listed in table Table 2.1.

2.1.3 Numerical Potential Calculations

This analytic method of calculating the potentials in a cylindrical geometry is useful for choosing the optimal lengths and voltages to apply to obtain a harmonic potential. However, in the regions where the field changes very rapidly a very large number of terms in the series is necessary to get a high level of accuracy. Also, there are some parts of our apparatus that are not just cylindrical electrodes of the same radius. Due to this, another relaxation method is used to calculate the potentials throughout our experiment.

The basic principle behind this relaxation method is easiest to understand working in cartesian coordinates. We write the field values on a grid in the x-y plane as shown in Fig. 2.6.

In a geometry that is independent of z (for example, a conductor that extends infinitely in the z direction) Laplace's equation can be written as:

$$\nabla^2\Phi = \frac{\partial^2}{\partial x^2}\Phi + \frac{\partial^2}{\partial y^2}\Phi \tag{2.27}$$

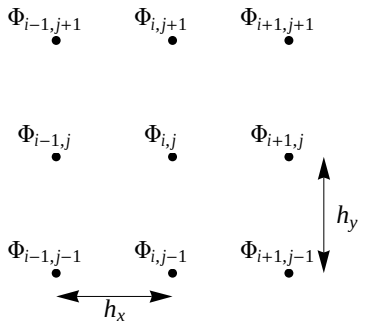

Figure 2.6: Labeling of grid points for relaxation calculation

Then the first derivatives on either side of $\Phi_{i,j}$ will be:

$$\frac{\partial \Phi_{i,j}}{\partial x} = \begin{cases} \frac{\Phi_{i,j}-\Phi_{i-1,j}}{h_x} \\ \frac{\Phi_{i+1,j}-\Phi_{i,j}}{h_x} \end{cases} \qquad \frac{\partial \Phi_{i,j}}{\partial y} = \begin{cases} \frac{\Phi_{i,j}-\Phi_{i,j-1}}{h_y} \\ \frac{\Phi_{i,j+1}-\Phi_{i,j}}{h_y} \end{cases} \tag{2.28}$$

The second derivatives will be the difference between the derivatives on either side, again divided by the length factors h_x or h_y.

$$\frac{\partial^2 \Phi_{i,j}}{\partial x^2} = \frac{1}{h_x}\left[\left(\frac{\Phi_{i+1,j}-\Phi_{i,j}}{h_x}\right) - \left(\frac{\Phi_{i,j}-\Phi_{i-1,j}}{h_x}\right)\right] \tag{2.29}$$

$$\frac{\partial^2 \Phi_{i,j}}{\partial y^2} = \frac{1}{h_y}\left[\left(\frac{\Phi_{i,j+1}-\Phi_{i,j}}{h_y}\right) - \left(\frac{\Phi_{i,j}-\Phi_{i,j-1}}{h_y}\right)\right] \tag{2.30}$$

If we choose the grid spacing to be the same in the x and y directions ($h_x = h_y$) Laplace's equation reduces to:

$$\Phi_{i,j} = \frac{\Phi_{i-1,j} + \Phi_{i-1,j} + \Phi_{i,j-1} + \Phi_{i,j+1}}{4} \tag{2.31}$$

Which is the remarkably simple condition that each point on the grid needs to be the average of the four surrounding points. Writing a code to satisfy this condition involves specifying the boundary conditions and allowing the code to iteratively "relax" by taking the average of the four surrounding points from the previous iteration.

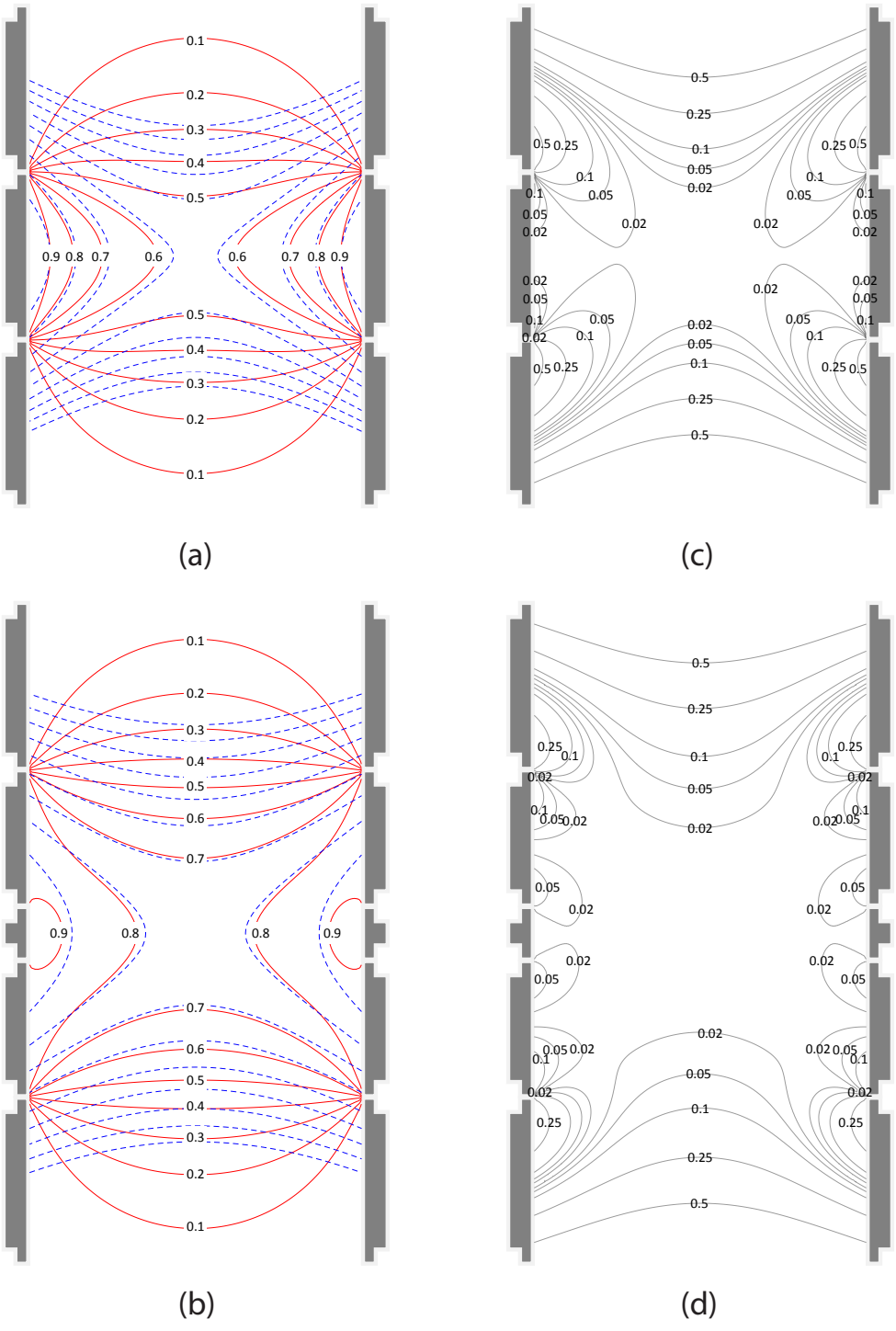

Figure 2.7: Comparison at $V_0 = 1$ of actual (solid) vs. ideal quadrupole (dashed) equipotentials for (a) 3 and (b) 5 electrode traps. Difference between ideal and actual potentials as a fraction of V_0 for (c) 3 and (d) 5 electrode traps. Dimensions given in Table 2.1

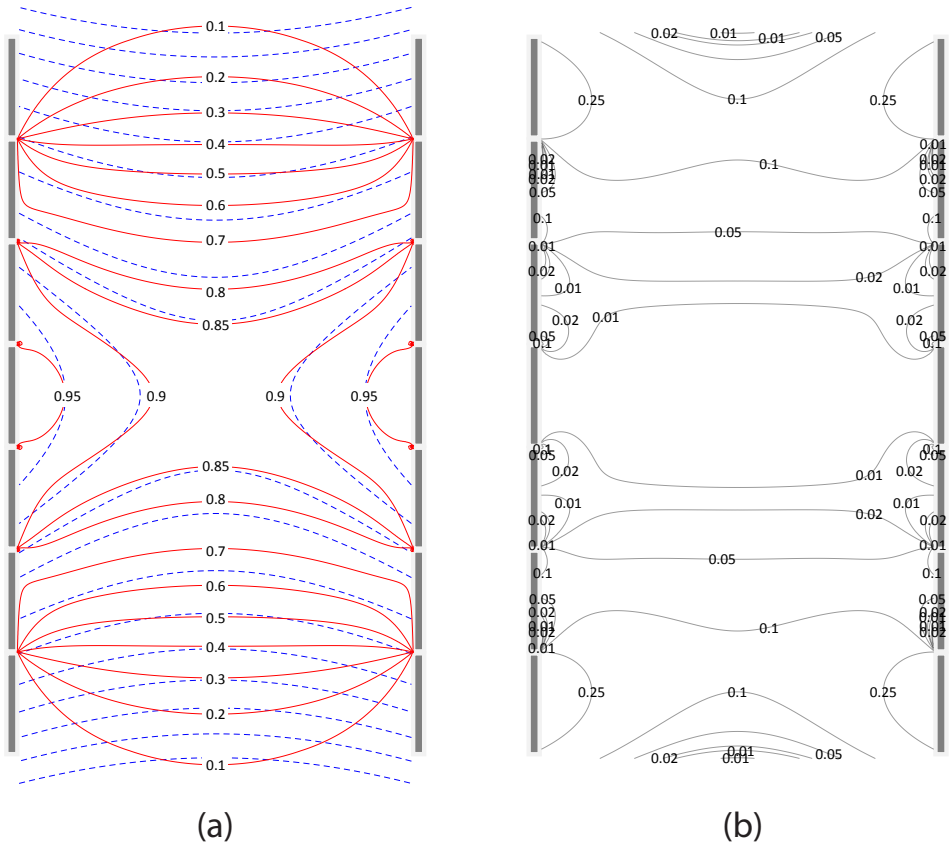

Figure 2.8: (a) Comparison at $V_0 = 1$ of actual (solid) vs. ideal quadrupole (dashed) equipotentials for 7 Electrode Trap. (b) Difference between ideal and actual potentials as a fraction of V_0. Dimensions given in Table 2.1

This procedure is slightly more complicated in the case of a cylindrically symmetric potential in cylindrical coordinates. Although each plane for any angle ϕ is the same, and thus it resembles the case of a potential independent of z in the cartesian coordinate system, the ρ dependence of the grid spacing must be taken into account. The modification of the above procedure for these conditions is discussed in a previous thesis [23].

Using this relaxation method we can calculate the potential profile of our actual electrode configurations to see exactly what the values are off axis. These are

compared to the ideal quadrupole potentials for the case of 3 electrode trap with $z_0 = 0.5\rho_0$ and 5 electrode harmonic trap in Fig. 2.7 and the optimized 7 electrode trap in Fig. 2.8. A detailed description of the penning trap configurations used in the ATRAP and BTRAP apparatuses will be given in section 3.3.

2.2 Single Particle Trajectories in a Penning Trap

The motions of charged particles in an ideal Penning trap consisting of a uniform axial magnetic field and electrostatic quadrupole are easily analyzable and separate out into three distinct motions. The analysis proceeds most easily in cartesian coordinates where we can write the magnetic field and electric potential in equation (2.6) as:

$$\vec{B} = B_0\hat{z} \qquad \Phi(x,y,z) = \frac{C_2V_0}{2d^2}\left(z^2 - \frac{x^2+y^2}{2}\right) \tag{2.32}$$

The motion of a particle of mass m and charge q, defining $\vec{r} = x\hat{x} + y\hat{y} + z\hat{z}$ will be governed by the Lorentz force equation:

$$m\ddot{\vec{r}} = q\vec{E} + 1\left(\dot{\vec{r}} \times \vec{B}\right) \tag{2.33}$$

In the presence of the magnetic field alone ($\vec{E} = 0$), the particles would undergone cyclotron motion around the magnetic field with a cyclotron frequency of

$$\omega_c = \frac{qB_0}{m} \tag{2.34}$$

With a nonzero quadrupole field the motion is the solution to the following equa-

	e^-/e^+					
Magnetic Field (T)	1			3		
Voltage (V_0)	50	100	150	50	100	150
ω_c' (GHz)	27.993	27.993	27.993	83.978	83.978	83.978
ω_z (MHz)	22.718	32.128	39.348	22.718	32.128	39.348
ω_m (kHz)	9.6	18.5	27.8	3.1	6.2	9.3

Table 2.2: Modified cyclotron, axial and magnetron frequencies for electrons and positrons in ATRAP and BTRAP penning trap configurations.

tions:

$$m\ddot{x} = \frac{qC_2V_0}{2d^2}x - q\dot{y}B_0 \tag{2.35a}$$

$$m\ddot{y} = \frac{qC_2V_0}{2d^2}y + q\dot{x}B_0 \tag{2.35b}$$

$$m\ddot{z} = -\frac{qC_2V_0}{d^2}z \tag{2.35c}$$

The equation in the z direction is simple harmonic motion with an axial frequency of:

$$\omega_z = \sqrt{\frac{qC_2V_0}{md^2}} \tag{2.36}$$

The motion in the x-y plane is more complicated, with a term which is confining due to the magnetic field, and anti-confining due to the electric field. The effect of this is twofold: first, the two forces fighting each other leads to a decrease in the frequency of the rapid cyclotron motion ω_c to what is called the modified cyclotron frequency ω_c' and second, there is a much slower mass independent $\vec{E}\times\vec{B}$ drift motion which leads to a procession around the center of the quadrupole potential at what is called the magnetron frequency ω_m [20]. This can be seen analytically by defining two new variables $u = x + iy$ and $v = x - iy$. Combining equations (2.35)a and b we

	$p/\bar{p}$					
Magnetic Field (T)	1			3		
Voltage (V_0)	50	100	150	50	100	150
ω_c' (MHz)	15.236	15.227	15.217	45.732	45.729	45.726
ω_z (kHz)	531.4	751.5	920.426	531.4	751.5	920.426
ω_m (kHz)	9.6	18.5	27.8	3.1	6.2	9.3

Table 2.3: Modified cyclotron, axial and magnetron frequencies for protons and antiprotons in ATRAP and BTRAP penning trap configurations.

get:

$$\ddot{u} + i\omega_c\dot{u} - \frac{1}{2}\omega_z^2 u = 0 \tag{2.37a}$$

$$\ddot{v} + i\omega_c\dot{v} - \frac{1}{2}\omega_z^2 v = 0 \tag{2.37b}$$

Using the two ansatz of $u = Ae^{-i\omega t}$ and $v = Be^{-i\omega t}$ we arrive at two possible solutions, the aforementioned modified cyclotron and magnetron frequencies:

$$\omega_c' = \frac{1}{2}\left(\omega_c + \sqrt{\omega_c^2 - 2\omega_z^2}\right) \tag{2.38a}$$

$$\omega_m = \frac{1}{2}\left(\omega_c - \sqrt{\omega_c^2 - 2\omega_z^2}\right) \tag{2.38b}$$

There exist two convenient relations between the four frequencies listed above $(\omega_c, \omega_c', \omega_z, \omega_m)$:

$$\omega_m = \frac{\omega_z^2}{2\omega_c'} = \omega_c - \omega_c' \tag{2.39}$$

Table 2.2 and Table 2.3 shows the typical frequencies that we get in our penning traps with $\rho_0 = 18mm$ for 1 and 3 Tesla for particles species in a 5 electrode Harmonic well.

If the frequencies in (2.38) were to become complex our ansatz would cease to be oscillatory and instead would be an increasing exponential function indicating an

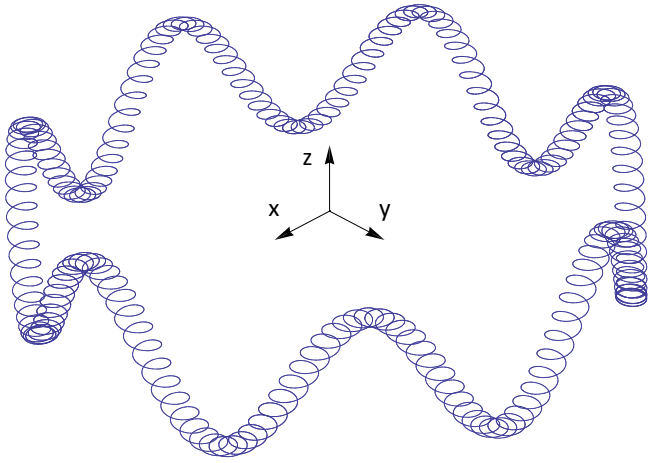

Figure 2.9: Motion of a charged particle in a penning trap. This is an exaggerated representation with $\omega_z = 7\omega_m$, $\omega_c' = 200\omega_m$. The frequencies in our actual traps are spaced much further apart as can be seen in Table 2.2 and Table 2.3.

unstable orbit. Therefore this gives the confinement condition within a penning trap of $\omega_c > \sqrt{2}\omega_z$ which is equivalent to:

$$B_0 > \sqrt{\frac{2mC_2}{qd^2}V_0} \tag{2.40}$$

Intuitively, this just says that the magnetic field must be strong enough to counteract the radial potential hill created by the quadrupole electric field.

Since $x = (u+v)/2$ and $y = (u-v)/2i$ they will also consist of just linear superpositions of the two frequency components. For a particle starting on the x axis with a velocity going in the y direction $x(t=0) = x_0$, $\dot{x}(t=0) = 0$ and $y(t=0) = 0$, $\dot{y}(t=0) = v_0$. the initial conditions and equations (2.35)a and (2.35)b are satisfied by:

$$x(t) = \left(\frac{v_0 - \omega_m x_0}{\omega_c' - \omega_m}\right)\cos(\omega_c' t) + \left(\frac{v_0 - \omega_c' x_0}{\omega_m - \omega_c'}\right)\cos(\omega_m t) \tag{2.41a}$$

$$y(t) = \left(\frac{v_0 - \omega_m x_0}{\omega_c' - \omega_m}\right)\sin(\omega_c' t) + \left(\frac{v_0 - \omega_c' x_0}{\omega_m - \omega_c'}\right)\sin(\omega_m t) \tag{2.41b}$$

The combination of these three motions is shown with a set of frequencies that make each of the different motions apparent, but that are far from the ones we find in our trap in Fig. 2.9. As we can see, the motion in both the axial and radial directions is always centered around the center of the electric quadrupole potential.

2.2.1 Energy in Penning Trap Trajectories

The overall energy for the motion will be a combination of the kinetic energy and the electric potential energy:

$$E(\vec{r}) = \frac{1}{2}m\dot{\vec{r}}^2 + q\Phi(\vec{r}) \tag{2.42}$$

The axial energy will always be equal to the electric potential energy of the motion at its furthest excursion from the axial center of the trap:

$$E_{axial} = \frac{1}{2}m\omega_z^2 z_{max}^2 \tag{2.43}$$

The radial energy will be:

$$E_{radial} = \frac{1}{2}m\dot{\rho}^2 - \frac{1}{4}\omega_z^2\rho^2 \tag{2.44}$$

We can break this up into an energy associated with the modified cyclotron orbit and the magnetron orbit by rewriting $\rho = \rho_c + \rho_m$ and observing:

$$E_{radial} = \frac{1}{2}m(\rho_c'^2\omega_c'^2 + \rho_m^2\omega_m^2 + \rho_c'\rho_m\omega_c'\omega_m) - \frac{1}{4}m\omega_z^2(\rho_c'^2 + \rho_m^2 + 2\rho_m\rho_c') \tag{2.45}$$

The two cross terms will cancel due to the relation in (2.39) and we are left with contributions that we can neatly divide out into a magnetron motion contribution

	$e-/e+$		$p/\bar{p}$	
Magnetic Field (T)	1	3	1	3
Velocity ($\frac{m}{s}$)	2.985×10^8	2.996×10^8	1.722×10^6	5.171×10^6
Kinetic Energy	4.91 MeV	15.69 MeV	15.48 keV	139.61 keV
γ	10.61	31.7	1.00002	1.00015
$\nu_c'(m_0) - \nu_c'(\gamma m_0)$	25.35 GHz	81.33 GHz	252 Hz	6.81 kHz

Table 2.4: Maximum Radial Velocity and Energy for Particles in ATRAP and BTRAP configurations in an ideal harmonic well with $V_0 = 100$.

and a modified cyclotron energy contribution.

$$E_c' = \frac{1}{2} m \rho_c'^2 \left(\omega_c'^2 - \frac{\omega_z^2}{2} \right) \tag{2.46a}$$

$$E_m = \frac{1}{2} m \rho_m^2 \left(\omega_m^2 - \frac{\omega_z^2}{2} \right) \tag{2.46b}$$

Because $\omega_c' >> \omega_z >> \omega_m$ the modified cyclotron energy is positive and the magnetron energy is negative. Furthermore, a larger magnetron orbit ρ_m corresponds to a decreased energy, the opposite of the cyclotron motion. This is, once again, a consequence of the radial hill created by the electric quadrupole potential and can be understood due to the fact that it would require energy to push the charged particle back up the hill.

Since the magnetron energy is negative, the most radially energetic particle that will remain within a certain radius is one that has $\rho_m = 0$ and has all of its energy in the cyclotron motion. We can solve for what kinetic energy this particle will have as a function of radius R by looking at the condition for circular motion within our fields:

$$\frac{v^2}{R} = \ddot{\vec{r}}_{center} = \omega_c v - \frac{1}{2}\omega_z^2 R \tag{2.47}$$

Solving the quadratic equation for v we obtain two possible solutions $v = \omega_c' R$ and $v = \omega_m R$. We can confirm these values by observing that setting $x_0 = \omega_c' v_0$ in equations (2.41a)a and b sets the amplitude of the magnetron oscillation to zero and gives an amplitude of x_0 on the modified cyclotron oscillation. Similarly, setting $x_0 = \omega_m v_0$ sets of the amplitude of the cyclotron oscillation to zero and gives an amplitude of x_0 to the magnetron oscillation.

We can see very quickly that for protons or antiprotons the highest velocity particle that will remain in our trap, which has a radius of $18mm$ is $v = 1.72 \times 10^6\, m/s = 0.0057c$ which has a $\gamma = 1.00002$. Although this is a tiny relativistic effect, it is possible to see it in the frequency shifts of the particles. For electrons the maximum velocity using this classical calculation is $3.17 \times 10^9\, m/s = 10.56c$ which indicates that a relativistic calculation is needed. The calculation proceeds the same as before, except now we must take into account the relativistic mass shift that accompanies the velocity and put that into the frequencies and subsequent calculation. The maximum radial energy for the different particle species, taking into account the relativistic mass shift, in our ATRAP and BTRAP ($\rho_0 = 18mm$) are shown in Table 2.4.

Given these frequencies, it is also possible to drive the different motions within a penning trap by applying time varying electric fields. If we apply a uniform electric field E_0 in the x direction modulated by a drive frequency ω_D then our motion will be given by the solution to the equations:

$$m\ddot{x} = \frac{qC_2V_0}{2d^2}x - q\dot{y}B_0 + qE_0\cos(\omega_D t) \tag{2.48a}$$

$$m\ddot{y} = \frac{qC_2V_0}{2d^2}y + q\dot{x}B_0 \tag{2.48b}$$

This can be solved numerically, and a couple of examples driving near the modified

cyclotron resonance for protons/ antiprotons are shown in Fig. 2.10. As we can see, depending on how far off of the resonance we are driving we get a different beat frequency which gives the result that the amount of amplification to the motion you give is dependent on how long you drive for in this idealized approximation. The sensitivity of the different particle motions to frequencies around $\omega_z, \omega_c', \omega_m$ shows the potential for heating the motions of the particles unless a large effort is made reduce the electrical noise which gets down to the trap.

2.3 Radiative Cooling of Particles

When particles enter into the penning trap they have a mechanism to come into thermal equilibrium with their surroundings (the electrodes in the trap) through the emission of electromagnetic radiation. Eventually the photons radiated from the particle and those absorbed by the particle from the blackbody radiation of the electrodes should balance at the ambient temperature of the trap. The non-relativistic amount of energy radiated from an accelerating charge is given by the Larmor formula [19]:

$$P = \frac{e^2}{6\pi\epsilon_0 c^3}\left|\ddot{\vec{r}}\right|^2 = -\frac{dE}{dt} \tag{2.49}$$

If we were to deal with only the cyclotron motion, neglecting the effect of the electric potential, then the acceleration of the charged particle would be

$$|\ddot{\vec{r}}| = \left|\frac{qB}{m}\dot{\vec{r}} \times \hat{z}\right| = \omega_c\dot{\rho} \tag{2.50}$$

Since the Energy would be $E = \frac{1}{2}m\dot{\rho}^2$ we arrive at the relation:

$$\frac{dE}{dt} = -\gamma_c E \qquad\qquad \gamma_c = \frac{e^2\omega_c^2}{3\pi\epsilon_0 mc^3} \tag{2.51}$$

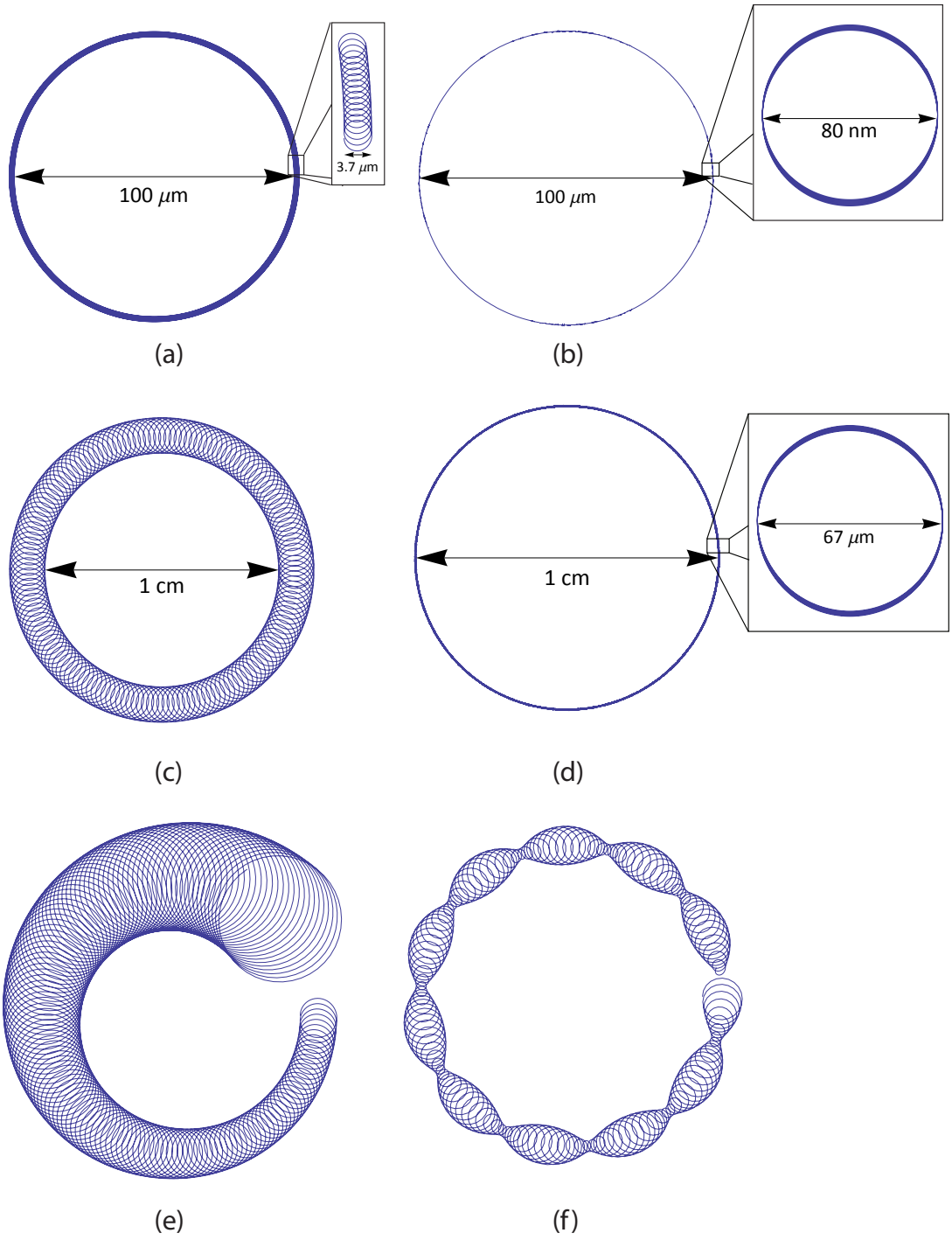

Figure 2.10: Sample radial motions of particles in our penning traps in a 1 T field. 1.1 K (a) $p/\bar{p}$ (b) e^-/e^+ in a $V_0 = 100V$ well. 100 eV (c) $p/\bar{p}$ (d) e^-/e^+ in a $V_0 = 500V$ well. $p/\bar{p}$ driven at (e)ν_c' + 1 kHz (f)ν_c' + 1 MHz

	$e-/e+$		$p/\bar{p}$	
Magnetic Field (T)	1	3	1	3
$1/\gamma_c'$ (s)	2.58	0.287	1.59×10^{10}	1.77×10^{9}
$1/\gamma_z$ (s)	3.92×10^{6}	3.92×10^{6}	1.32×10^{13}	1.32×10^{13}
$1/\gamma_m$ (s)	9.03×10^{18}	7.31×10^{20}	8.97×10^{18}	7.31×10^{20}

Table 2.5: Radiation damping rates for the different particle motions in the ATRAP and BTRAP configurations in a 100 V harmonic well.

A full calculation [20] taking into account the effect of the electric field yields damping rates for the three motions as:

$$\gamma_c' = \frac{e^2\omega_c'^2}{3\pi\epsilon_0 mc^3}\frac{\omega_c'}{\omega_c' - \omega_m} \qquad \gamma_m = \frac{e^2\omega_m^2}{3\pi\epsilon_0 mc^3}\frac{\omega_m}{\omega_c' - \omega_m} \qquad \gamma_z = \frac{e^2\omega_z^2}{6\pi\epsilon_0 mc^3} \tag{2.52}$$

Damping times for the different particles and motions are listed in Table 2.5 at both 1 and 3 T. As the solution to (2.51) is $E = E_0 e^{-\gamma t}$, $\frac{1}{\gamma}$ is the $\frac{1}{e}$ decay time of the energy. From the table, we can see that the only useful cooling time relevant for the timescales during which we do experiments is the modified cyclotron cooling rate of the electrons and the positrons, all others being far too long to meaningfully affect the energy of the particles. The cooling times of the axial motion of protons can also be somewhat decreased through the use of an external circuit, but this takes place on the order of days [24].

2.4 Non-Neutral Plasmas in a Penning Trap

After exploring the behavior of individual particles in a penning trap, a natural question is when do the fields generated by the particles themselves begin to make an important contribution to their collective behavior. The presence of a single other

charged particle or ion can be observed to affect the motion of a second particle, as demonstrated by the observed effect of an $H-$ ion on the decay rate of a single antiproton in a penning trap [25]. However, in terms of investigating a sharp change in behavior for a large number of particles, we can say that the other particles in the trap become important when they effectively screen out the external potential created by the charge on the electrodes. The most common model for this effect is the specification of a Debye length for a collection of charged particles.

Following standard introductions to plasma physics [26, 27] if we have a conductor in a plane held at a potential Φ_0, the Maxwell-Boltzmann distribution of charged particles q will be given by:

$$n(\vec{r},\dot{\vec{r}}) = A\exp[-(\frac{1}{2}m(\dot{\vec{r}})^2 + q\Phi(\vec{r}))/KT_e] \tag{2.53}$$

We can integrate out over the velocities, adding that result to the constant out front. To avoid an infinite charge buildup over our entire model we say that out at infinity there is a common ion and electron density $n_i(\Phi \to 0) = n_e(\Phi \to 0) = n_\infty$. We also model the ions as being heavy and unable to move on the timescales of our experiment so their density n_i is uniform throughout the region of interest. The electron density is therefore given by:

$$n_e = n_\infty \exp(e\Phi/KT_e) \tag{2.54}$$

If the conductor is an infinite plane in the y-z plane held at the potential Φ_0, then Poisson's equation over the region of charge will be:

$$\nabla^2\Phi = \frac{d^2\Phi}{dx^2} = -\frac{e}{\epsilon_0}(n_i - n_e) = \frac{en_\infty}{\epsilon_0}\left[\exp\left(\frac{e\Phi}{KT_e}\right) - 1\right] \tag{2.55}$$

For the region such that $|e\Phi/KT_e| << 1$ we can take a Taylor expansion yielding the result:

$$\frac{d^2\Phi}{dx^2} = \frac{en_\infty}{\epsilon_0}\left[\left(\frac{e\Phi}{KT_e}\right) + \mathcal{O}\left(\frac{e\Phi}{KT_e}\right)^2 + ...\right] \tag{2.56}$$

This gives the result that the potential will fall off like:

$$\Phi(x) = \Phi_0 e^{-\frac{|x|}{\lambda_D}} \qquad \lambda_D = \sqrt{\frac{\epsilon_0 KT_e}{ne^2}} \tag{2.57}$$

Where λ_D is called the Debye length. Therefore, if the spatial extent of your collection of particles is significantly larger than the Debye length given the number density and temperature, then the external electric field is largely screened out, and your setup is considered to be a plasma. While experiments and calculations have been done to establish the number density of electrons in the ATRAP and BTRAP apparatus at 1 Tesla, no studies have been done to establish what the antiproton number density in the newer apparatuses are. For a typical cloud of 40 million electrons in a 100 volt well, we would see a number density of around $5 \times 10^{13}/m^3$ in a plasma with a diameter of 10 mm giving a Debye length of 10 μm at 1.1 Kelvin. Previous experiments and calculations in an older apparatus operating at 5.4 Tesla and 4.2 K established a Debye length of $70\mu m$ for $150,000$ antiprotons in a 6 V well and cloud size of 440 μm [28]. These results indicate that our electron and positron clouds, which are typically in excess of 50 million, and often as high as 400 million in the case of electrons, are well into the plasma regime. Antiproton clouds typically in the hundreds of thousands and which do not exceed 1 million in total are more borderline in terms of such a treatment.

To understand the behavior of large numbers of charges in a penning trap, often referred to as non-neutral plasmas, we must first look at the thermodynamic

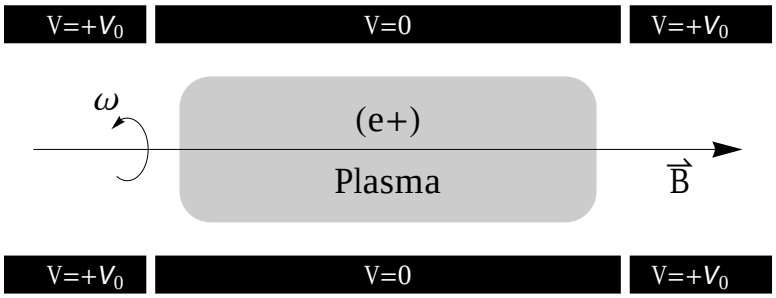

Figure 2.11: Plasma Model for Thermal Equilibrium Calculations.

equilibrium of such systems and then look at their dynamics.

2.4.1 Thermodynamic Equilibrium of Non-Neutral Plasmas

A comprehensive mean field description of the thermal equilibrium states of non-neutral plasmas in a penning trap is given in a review by Dubin and O'Neill [29]. This section will highlight some of the key results from that review pertinent to our work.

We model a general plasma distribution in a setup shown in Fig. 2.11, where there is a positively charged plasma (with charge = +e) radially confined by a uniform axial magnetic field $\vec{B} = B\hat{z}$ and axially confined by electrodes with a positive potential on either side, and ground in the middle. This general setup is called a Malmberg Penning trap. We shall treat the special case of the quadrupole penning trap soon, but for now we analyze the general case. Due to the cylindrical symmetry of the setup, the Hamiltonian will be invariant under translations in the azimuthal angle ϕ and therefore the total canonical angular momentum will be conserved and equal to a constant we call L. With N particles of charge $+e$ and mass m we have:

$$P_\phi = L = \sum_{j=1}^{N} p_{\phi j} = \sum_{j=1}^{N} m v_{\phi j} \rho_j + \frac{eB\rho_j^2}{2} \tag{2.58}$$

In large magnetic fields the second term dominates and we are left with a conservation requirement on $\sum_{j=1}^{N} \rho_j^2 =$ constant, which turns out to be a very powerful condition for radially confining the vast majority of the particles. For example if we have 100 particles at $\rho = \rho_0$ and a single particle were to move out to $\rho = 10\rho_0$ then the remaining 99 particles would essentially have to move to $\rho \to 0$ to conserve this quantity.

In order to analyze the arrangement of the charges within the plasma, we write the total potential as the sum of the trap potential Φ_T and the contributions from the charges on each other, which we choose to express using a Green's function:

$$\Phi(\vec{r}) = \Phi_T(\vec{r}) + \sum_j eG(\vec{r}_i|\vec{r}_j) \tag{2.59}$$

If we define a frame that rotates with a frequency $-\omega$ then the Hamiltonian can be written as [30]:

$$H_R = H + \omega P_\phi \tag{2.60}$$

With some algebra we can write:

$$H_R = \sum_{j=1}^{N} \frac{m}{2}(\vec{v}_j + \omega\rho_j\hat{\phi}_j)^2 + \sum_{j=1}^{N} e\Phi_R(\rho_j, z_j) + \sum_{\substack{i,j=1 \\ i\neq j}}^{N} e^2 G(\vec{r}_i|\vec{r}_j) \tag{2.61}$$

Where we have defined the new potential Φ_R as:

$$e\Phi_R(\rho, z) = e\Phi_T(\rho, z) + m\omega(\omega_c - \omega)\frac{\rho^2}{2} \tag{2.62}$$

Given the electrode configuration in Fig. 2.11 the trap potential $\Phi_T(\rho, z)$ will be anticonfining in the ρ direction, but we can see that the term $m\omega(\omega_c - \omega)\frac{\rho^2}{2}$ gives a potential which is confining in the ρ direction. If it is the dominant contribution, being also bigger than the contribution from the self charge of the plasma, the $eG(\vec{r}|\vec{r}_j)$ term,

then we would expect the overall combined potential to look like equipotential lines for a given ρ within the plasma. As we shall later see in the numerical calculations in Fig. 2.14, this does turn out the be the case.

In order to proceed further with the approach outlined in [29] we must note that their approach is valid when the correlations between plasmas are small:

$$\Gamma = \frac{e^2}{akT} \ll 1 \tag{2.63}$$

Where a is the interparticle spacing, defined as $\frac{4\pi a^3 n_0}{3} = 1$. For our electron plasmas, with a density of $10^{13}/m^3$ at 4.2 K we have $\Gamma = 0.16$ and at 1.1 K we have a $\Gamma = 0.60$. We are therefore straddling the regime where this approach is valid. Nevertheless, we outline the approach, keeping in mind that some experimental deviations from their results may be due to a breakdown in this regime.

Several approaches [31, 32, 33, 34] can be used to demonstrate that the Boltzman distribution of particles in this configuration can be written as:

$$f(\vec{r},\vec{v}) = \frac{N \exp\left[-\frac{1}{kT}(h+\omega p_\phi)\right]}{\int d^3\vec{r} d^3\vec{v} \exp\left[-\frac{1}{kT}(h+\omega p_\phi)\right]} \tag{2.64}$$

Where h and p_ϕ are the single particle Hamiltonian and angular momentum:

$$h = \frac{mv^2}{2} + e\Phi(\vec{r}) \qquad\qquad p_\phi = mv_\phi\rho + \frac{eB}{2}\rho^2 \tag{2.65}$$

The distribution can be rewritten:

$$f(\vec{r},\vec{v}) = n(\rho,z)\left(\frac{m}{2\pi kT}\right)^{\frac{3}{2}} \exp\left[\frac{-m}{kT}(\vec{v}+\omega\rho\hat{\phi})^2\right] \tag{2.66}$$

Where the density is given by:

$$n(\rho,z) = N\frac{\exp\left\{-\frac{1}{kT}[e\Phi_R(\rho,z)+e\Phi_P(\rho,z)]\right\}}{\int d^3\vec{r}\exp\left[-\frac{1}{kT}(e\Phi_R+e\Phi_P)\right]} \tag{2.67}$$

Where Φ_R is the potential described in equation (2.62) and Φ_P is the mean field version of the effect of the plasma charge on itself:

$$\Phi_P(\vec{r}) = \int d^3\vec{r}' d^3\vec{v}' f(\vec{r}', \vec{v}') G(\vec{r}|\vec{r}') \tag{2.68}$$

The local fluid velocity can be obtained by taking the integral:

$$\vec{v}(\rho) = \frac{\int d^3\vec{v} f \vec{v}}{\int d^3\vec{v} f} = \omega\rho\hat{\phi} \tag{2.69}$$

Since the velocity all points in the plasma is just $\omega\rho\hat{\phi}$ this indicates a shear free rotation - that is all points in the plasma rotate about the z-axis at the same frequency.

To investigate what the total potential in the plasma will be we can solve Poisson's equation for Φ_P in the trap region using the boundary condition that $\Phi_p \to 0$ at the electrode boundary.

$$\nabla^2\Phi_P = -\frac{e}{\epsilon_0} n(\rho, z) \tag{2.70}$$

We can solve this using the fact that in the rest frame of the plasma, the charges within the plasma will rearrange themselves so that an external electric field is Debye shield out [33], that is the total field will be a constant within the plasma:

$$\Phi_P(\rho, z) + \Phi_R(\rho, z) \simeq \text{Constant} \tag{2.71}$$

The left hand side of Poisson's equation in (2.70) becomes:

$$\begin{aligned} \nabla^2\Phi_P(\rho, z) &= \nabla^2(-\Phi_R(\rho, z) + \text{Constant}) && (2.72)\\ &= \nabla^2(\Phi_T(\rho, z) + \frac{m\omega(\omega_c - \omega)\rho^2}{2e}) && (2.73)\\ &= \frac{2m}{e}\omega(\omega_c - \omega) && (2.74) \end{aligned}$$

In the last line we have used the fact that the trap potential must satisfy Laplace's equation $\nabla^2\Phi_T = 0$ inside the electrodes. Combining with the right hand side of (2.70) we get:

$$\omega_p^2 = 2\omega(\omega_c - \omega) \tag{2.75}$$

Where $\omega_p = \sqrt{\frac{ne^2}{\epsilon_0 m}}$ is called the plasma frequency. This result tells us that the density is uniform within the plasma. This is corroborated by the more general result that for self consistent solutions the plasma density is nearly constant out to the a surface and then drops to zero on the scale of a Debye length [32]. Solving for ω in equation (2.75) we get:

$$\omega_\pm = \frac{\omega_c \pm \sqrt{\omega_c^2 - 2\omega_p^2}}{2} \tag{2.76}$$

Which gives the plasma rotation frequency ω as a function of the density and magnetic field. This shows that the allowable plasma frequency is a double valued function - that is, for a given density and magnetic field there are two allowable plasma rotation frequencies ω.

For the case of an ideal quadrupole potential, when we plug the appropriate Φ_T into equation (2.62) we get:

$$\Phi_R(\rho, z) = \frac{m\omega_z^2}{2e}\left(z^2 + \left(\frac{\omega(\omega_c - \omega)}{\omega_z^2} - \frac{1}{2}\right)\rho^2\right) + \text{Constant} \tag{2.77}$$

Which we can see describes the equipotential surfaces of a spheroid (an ellipse in three dimensions). As before, due to the Debye shielding, we have $\Phi_P + \Phi_R = \text{Constant}$. For this to be true Φ_P must also be quadratic within the plasma. A spheroid of uniform charge produces this potential inside of the plasma and the potential falls to zero at infinity [35]. If the electrodes in our setup are far enough away this condition

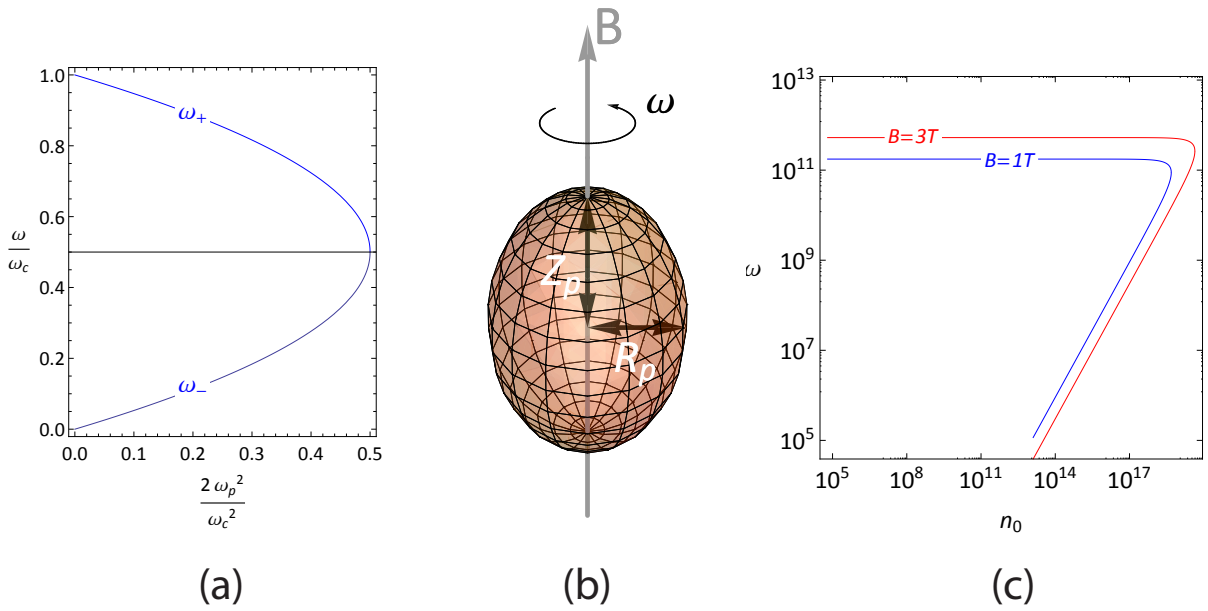

Figure 2.12: (a) The general constraint on the plasma rotation frequency for a given magnetic field and particle density. (b) A spheroidal plasma shape, rotating about the magnetic field. (c) The plasma rotation frequency in a penning trap taking into account the density and frequency constraints in a 100 V harmonic well.

is mimicked as $\Phi_p \to 0$ there. By matching such a model to Φ_R above we get:

$$\frac{\omega_z^2}{\omega_p^2} = \frac{Q_1^0\left(\frac{\alpha}{\sqrt{\alpha^2-1}}\right)}{\alpha^2-1} \tag{2.78}$$

Where α is the aspect ratio of the spheroid $\left(\alpha = \frac{Z_p}{R_p}\right)$, Z_p is the half length of the axial extent of the plasma and R_p is half of the radial diameter of the plasma, as indicated in Fig. 2.12. Q_1^0 is the associated Legendre polynomial of the second kind and has the form:

$$Q_1^0(x) = \frac{x}{2}\ln\left(\frac{x+1}{x-1}\right) - 1 \tag{2.79}$$

In the case of a quadrupole potential there are more restrictions on the plasma frequency than is implied by equation (2.76). Because there is a minimum density

requirement for the charges to be considered a plasma, this sets the requirement that $\omega_p > \omega_z$, and because the radial confining force must be negative ($-e\partial\Phi_R/\partial\rho$) we have the additional requirement that $\omega_m < \omega < \omega_c$ [29]. The allowable plasma rotation frequencies ω in our setup, in a 100 V harmonic well, taking into account these constraints is shown in Fig. 2.12 c.

Given this spheroidal shape, and the fact that the density is uniform throughout the plasma, the total number of particles N will be related to the number density n_0 by:

$$N = \frac{4}{3}\pi n_0 Z_p R_p^2 \tag{2.80}$$

With these equations, we are able to determine all of the parameters N, n_0, R_p, Z_p, ω or α of a spheroidal plasma as long we just have any two of them. The easiest number to obtain is N as we have robust destructive counting methods to determine the numbers of large numbers of positrons or electrons, as will be described in chapter 4. It is possible to obtain the aspect ratio of a plasma by measuring the collective axial oscillation modes of the plasma, as will be discussed in the next section.

2.4.2 Non-Neutral Plasma Dynamics

In the single particle case, the axial oscillation in an ideal quadrupole potential is simple harmonic motion at the axial frequency ω_z. Once we move into the many particle plasma regime the axial motion becomes more complicated, with particles being out of phase with each other, at different radii, through interactions with the self field of the plasma as well as other effects. The result is that there can be collective "sloshing" modes where different parts of the plasma are moving axially with respect

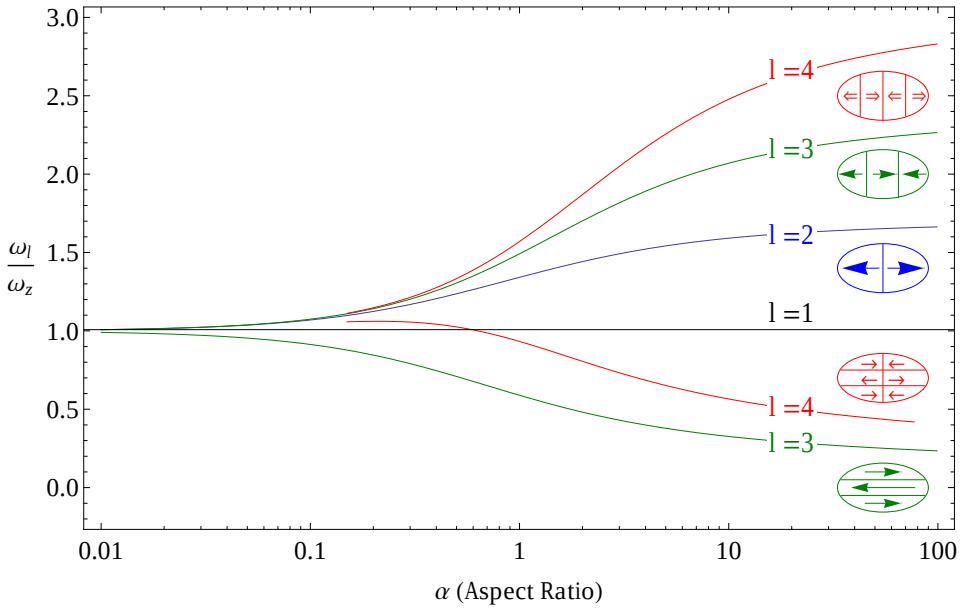

Figure 2.13: Plasma axial oscillation modes as a function of aspect ratio.

to each other. An analysis done in the zero temperature limit by Dan Dubin [36] for strongly magnetized plasmas $\omega_c >> \omega_p$ (as is the case for our plasmas) has shown that these different sloshing modes, that can be characterized by two numbers (l, m), exhibit characteristic frequencies that are a function of the aspect ratio. The $m = 0$ modes are the ones that do not break the azimuthal symmetry about the magnetic field, and are the ones that are most interest given for an axial detection scheme. His analysis can be put into the following form [37]:

$$1 - \frac{\omega_p^2}{\omega_l^2} = \frac{k_2}{k1} \frac{P_l(k_1) Q_l'(k_2)}{P_l'(k_1) Q_l(k_2)} \tag{2.81}$$

Where ω_l is the frequency of the mode with $l = l, m = 0$, P_l and Q_l are the Legendre polynomials of the first and second kind, as before α is the aspect ratio and

ω_p is the plasma frequency and:

$$k_1 = \frac{\alpha}{\sqrt{\alpha^2 - 1 + \frac{\omega_p^2}{\omega_l^2}}} \qquad k_2 = \frac{\alpha}{\sqrt{\alpha^2 - 1}} \tag{2.82}$$

Equations (2.81) and (2.78) make it possible to create a graph of the axial plasma mode frequencies ω_l with respect to the aspect ratios for different l numbers as is demonstrated in Fig. 2.13. The lowest order $l = 1$ mode is just the center of mass mode corresponding to the axial frequency ω_z. Fig. 2.13 also demonstrates what the different sloshing modes represent in terms of particle movements within the plasma itself [37].

Further work by Dubin has produced an analytic calculation of what the temperature dependence of these quadrupole mode should be [37, 38]:

$$(\omega_2)^2 = (\omega_2^0)^2 + 5\left\{3 - \frac{\alpha^2}{2}\frac{\omega_p^2}{(\omega_2^0)^2}\frac{\partial^2}{\partial\alpha^2}\left[\frac{2Q_1(k_2)}{\alpha^2 - 1}\right]\right\}\frac{kT}{mZ_p^2} \tag{2.83}$$

Where ω_2^0 is the quadrupole ($\omega_{l=2}$) mode zero temperature limit result from (2.81). Experiments have been corroborating these predictions in the region from $\simeq 290 - 1500\,K$ [37]. Section 4.4.2 shows results trying to apply this analysis to plasmas in the much lower temperature regime from $1.1 - 4.2\,K$.

2.4.3 Numerical Plasma Code Calculations

The theoretical work outlined above makes assumptions about both the exactness of the quadrupole potential as well as an assumption that the plasmas remain far from the electrode walls, meaning that the effect of image charges can be neglected. As we can see in Fig. 2.7 the potentials in our cylindrical electrode differ from an ideal quadrupole potential, and for some of our applications we deal with electron plasmas

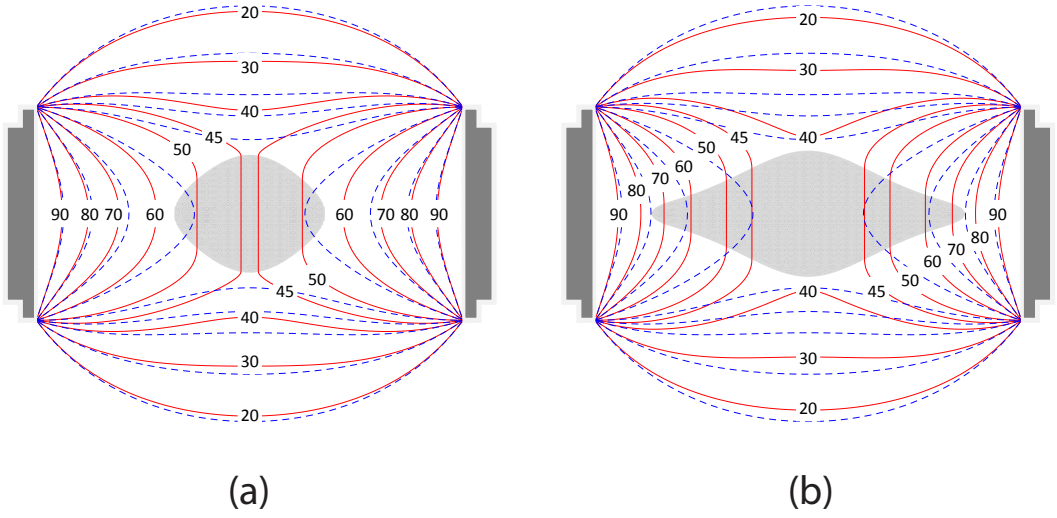

Figure 2.14: Two example plasma shapes and effect of space charge potential. (a) A 40 million electron cloud with $\alpha = 0.7$ and (b) A 100 million electron cloud with $\alpha = 0.3$ in a 100 V radius length electrodes. The blue dashed lines are the unmodified electrode potentials. The red lines are the potential taking into account the effect of the space charge.

on order of 5×10^8 particles which take up a substantial portion of the trap and do approach the electrode walls. To compensate for this, numerical calculation codes are used both to establish the thermodynamic equilibrium condition for the plasmas, as well as calculating the modifications to the plasma axial oscillation modes for these non ideal conditions.

The thermodynamic equilibrium is calculated using a code called equilsor2 developed by R.L. Spencer and others [39] and modified for the special conditions of our trap by A.Speck and R.Parrott [23]. A couple of examples of plasma equilibria using the equilsor code for electrons/positrons is show in Fig. 2.14.

The dynamics of the axial motions will also be modified and these can be calculated with another code called rattle also developed by Spencer et al [40] meant to work in conjunction with equilsor. Numerical calculations using rattle have been done in a

previous thesis [41] relating to the conditions in our experiment and compared with the ideal result.

Chapter 3

Penning Trap Apparatus

The theories of charged particle behavior in 2 allow for a wide variety of cylindrical penning traps to be constructed. As long as the important ratios between the electrode dimensions are maintained, the traps can be made bigger or smaller within the constraints of machining precision and space available. Previous electron, antiproton and antihydrogen experiments used cylindrical electrodes with a diameter of about 12 mm, current studies involving protons are using electrodes that are 6 mm in diameter, and a new apparatus for antihydrogen experiments is being constructed that will use electrodes that are over 36 mm in diameter.

The ATRAP and BTRAP apparatuses described in this thesis use electrodes that are approximately 18 mm in diameter. In addition to using a larger electrode size than previous experiments, extra radial space was needed in order to accommodate the presence of a magnetic field minimum Ioffe trap, a different antiproton annihilation detection setup, laser access for eventual antihydrogen cooling and spectroscopy as well as other apparatus. This chapter describes the superconducting magnet, cryo-

genic, vacuum and electrode stack configuration used to form the penning trap for our experiments.

3.1 3 Tesla Large Bore Superconducting Magnet

The previous generation of antihydrogen experiments conducted by the ATRAP collaboration [28] used a 10 cm diameter bore 6 T superconducting magnets produced by the NALORAC cryogenics corporation. Because of the new generation of experiments need for larger radial experiment space and lower operating field to accommodate a magnetic field minimum trap, we had a 3 Tesla 50.8 cm diameter bore magnet constructed for us in 2003 by American Magnetics Incorporated (AMI) which had previously bought out the NALORAC cryogenics corporation. Because of the size, large inductance (247 henries), and large amounts of cryogens needed to operate the magnet, the support equipment and operation of the magnet were not trivial tasks. The magnet experienced a larger number of unintended quenches in 2004 and 2006 before steps were taken to properly handle the helium gas flow and charging of the magnet. This section will outline the salient aspects of the magnet, the support equipment and its operation.

3.1.1 Magnet Specifications

This magnet is intended to remain in operation during the next several phases of ATRAP experiments, beginning with antihydrogen production studies at low field, trapping of antihydrogen atoms and eventually precision spectroscopy. Particularly due to this last step, it is critical that we have a uniformity of the magnetic field over

Maximum Rated Field (@ 4.2 K)	3 Tesla
Maximum Rated Current (@ 4.2 K)	122.1 Amps
Field to Current Ratio	0.024569 T/Amp
Homogeneity in Center	+/- 0.015 %
Inductance	247 Henries
Recommended Charging Rate (0-2.75 T)	2 V (0.0085 A/s)
Recommended Charging Rate (2.75-3 T)	1 V (0.0045 A/s)
Axial Bore Diameter	20"
Magnet Weight	1750 lbs
Magnet and Cryostat Weight	4400 lbs
Recommended Persistent Switch Heater Current	50 mA
Persistent Switch Heater's 300 K Resistance	85 Ohms

Table 3.1: 3 T magnet specifications and operating characteristics.

a large region in order to reduce uncertainties in eventual measurements. The salient specifications of the magnet are list in Table 3.1.

The requested specification for the uniformity of the magnet was 1 part in 10^4 over a 50 cm long 5 cm diameter cylinder. Upon its completion the makers of the magnet measured the field of the magnet with a Metrolab NMR teslameter, and the performance reached approximately 1.5×10^{-4} uniformity over that region. The results of the NMR measurement at 2 T, along with the calculated field profile at 1 T of the magnet are shown in Fig. 3.1.

The coil windings consist of one primary coil wound in a cylindrical form approximately 150 cm long at a diameter of about 60 cm. There are also 5 additional shim coils, 3 on the outside and 2 on the inside of the primary winding, which are used to tailor the uniformity of the field. They all run at the same current. As can be seen

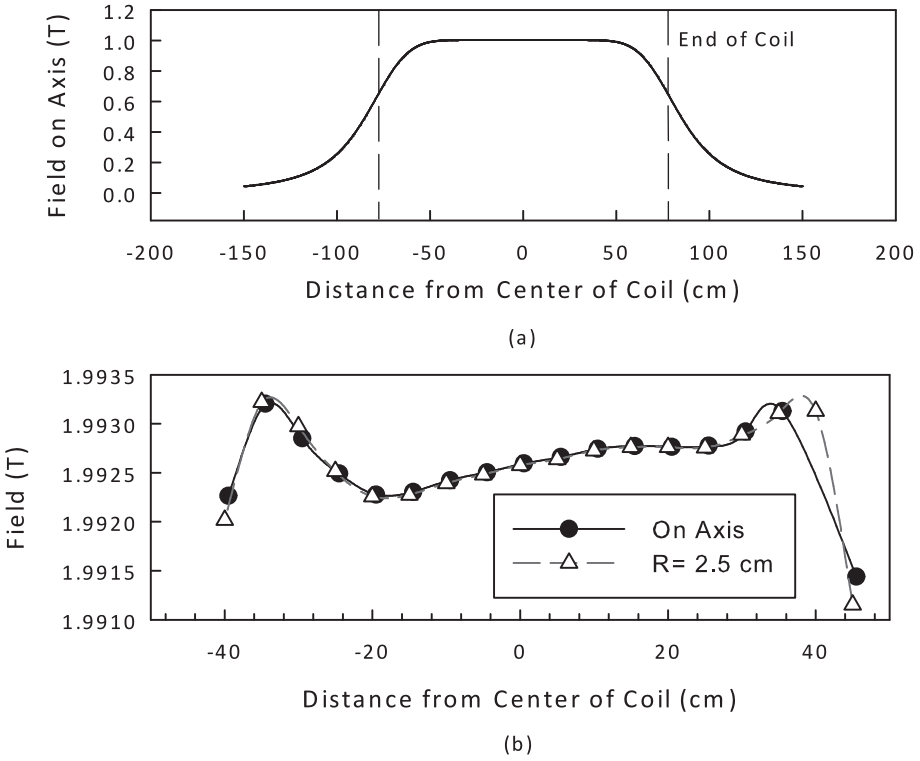

Figure 3.1: 3T magnet magnetic field profile. (a) The field calculated for the coil configuration using Vector Fields Opera software at 1 T. (b) Measured 2 T field with an Metrolab NMR teslameter after construction in 2002.

in Fig. 3.3b, the current in four of the shim coils runs in the same direction as the primary coil, but a small shim coil on the outside in the axial center has the current running in the opposite direction.

3.1.2 Cryogenic and Gas Flow Control Systems

In order to cool such a big magnet, a very large amount of cryogens is needed. When both the liquid nitrogen and liquid helium dewars are full they take approximately 180 Liters and 550 Liters respectively. The coil windings fill up nearly the entire height of the liquid helium dewar as can be seen in Fig. 3.2. Both the nitrogen

and helium spaces are surrounded by a common vacuum space which is pumped out to 10^{-5} Torr at room temperature, descending into the 10^{-7} Torr region when the magnet is cold. A first level of cold protection for the helium space is provided by a shield which is connected to the liquid nitrogen dewar. An additional layer of thermal insulation is provided by a vapor cooled shield (VCS) which sits inside the nitrogen cooled shield, where helium gas that has boiled off from the 4.2 K liquid is passed through two long tubes which are well heat sunk to the shield, run along the length of the shield several times and exhaust out at the top of the magnet. These shields are also shown in Fig. 3.2.

The liquid nitrogen is filled through one port and the gas boiloff is exhausted through another as is shown in Fig. 3.3. In addition to the two vapor cooled shield (VCS) exhausts mentioned above, there are 5 more escape paths for the helium boiloff exhaust. There are two 150 amp vapor cooled current leads (VCCL). These are leads that can pass a large amount of current through them given their size due to the fact that the resistive heating of the current being transmitted is actively cooled with the boiloff of liquid helium gas that passes from the helium dewar through tiny tubes in the conductors. The effect of not passing sufficient helium gas to cool the leads can be catastrophic. In 2003 a lead on the magnet was burned in place due to insufficient flow and a time consuming effort to remove the burnt G-10 pieces was necessary before we could resume operation. There are two pressure release valves that open allow helium to exhaust in case of overpressure. These valves open between 200-250 mbar above atmospheric pressure and should remain closed during normal operation. Finally, there is a large flow rate exhaust port, generally referred to as "main exhaust"

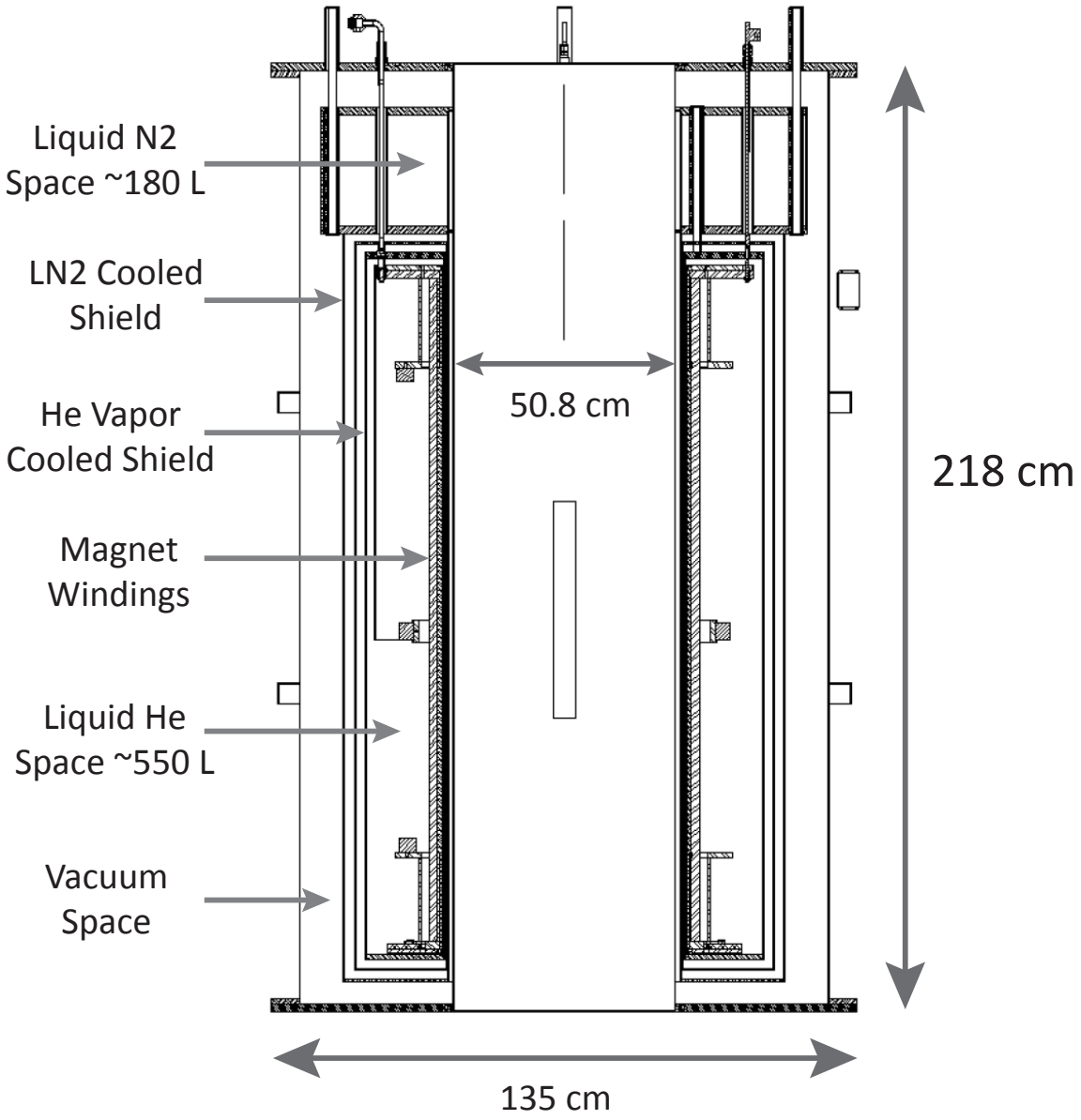

Figure 3.2: Cryogenic and Vacuum Spaces in the Three Tesla Magnet.

which is usually only opened during liquid helium fills to allow for the much larger flow of helium. There is also a single helium fill port. All of these connections on the top of the magnet are indicated in Fig. 3.3c.

The typical hold time for a nitrogen fill is about two weeks. Because the magnet windings take up the majority of the length of the helium dewar, whenever the liquid level descends, a part of the magnet is no longer covered in liquid. This makes it more likely for there to be some random heating event leading to a quench. For this reason, the helium in the magnet needs to be refilled when the total liquid level in the magnet is between $60 - 70\%$. Unlike the nitrogen boiloff time, the helium boiloff time is highly dependent on the gas flow handling conditions of the helium gas. This is true for two main reasons.

The first reason is fairly simple, the cooling of the helium space is reliant on having a sufficient amount of helium gas passing through the vapor cooled shield to provide additional cooling power. In 2006, during the course of cooling down the magnet one of the VCS exhaust lines became clogged for unknown reasons and we were not able to pass helium gas through that VCS for the remainder of the year. The difference in boiloff from 2008, when flow was going through both VCS lines, and 2006 where one was clogged are shown in Fig. 3.4. The obstruction caused a $50\,\%$ increase in the boiloff rate, decreasing the hold time from about 9 days to 6. This demonstrates the importance of passing sufficient flow through the vapor cooled shields.

The second reason for the variable boiloff has to do with the heat transfer from the warmer gas to the colder gas which is a function of the temperature and pressure gradients in the system. We are fortunate enough to work at CERN where liquid

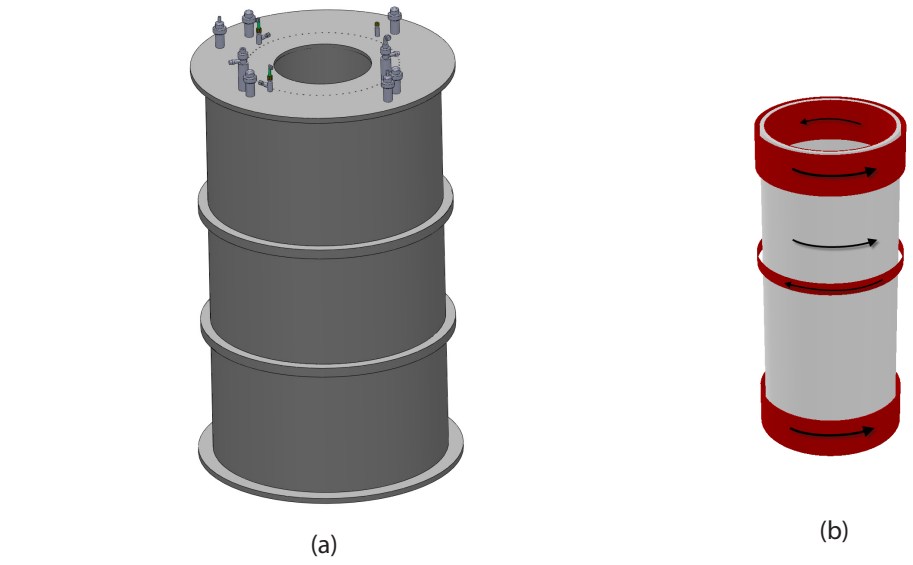

(a) (b)

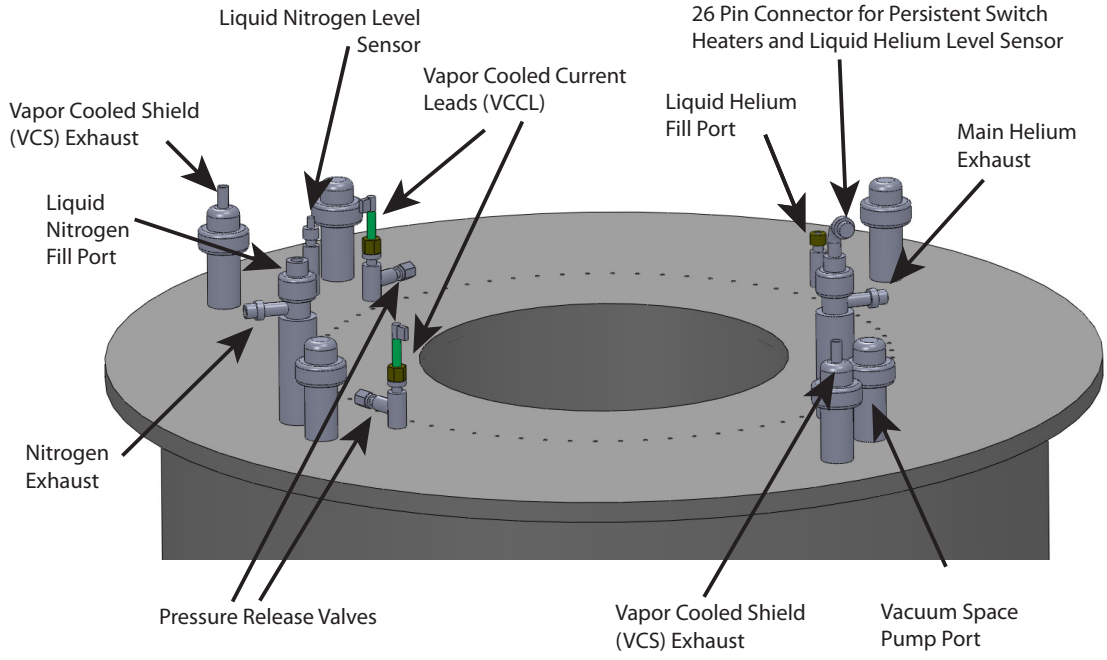

(c)

Figure 3.3: (a) Exterior profile of 3 T magnet with (b) magnet windings shown to scale. The light grey cylinder is the main winding, with the dark red cylinders being the shim coils to tailor the field, the arrows indicate the direction of current in the different coils. (c) A list of the current, vacuum, gas and cryogen connections on the top of the 3 T magnet.

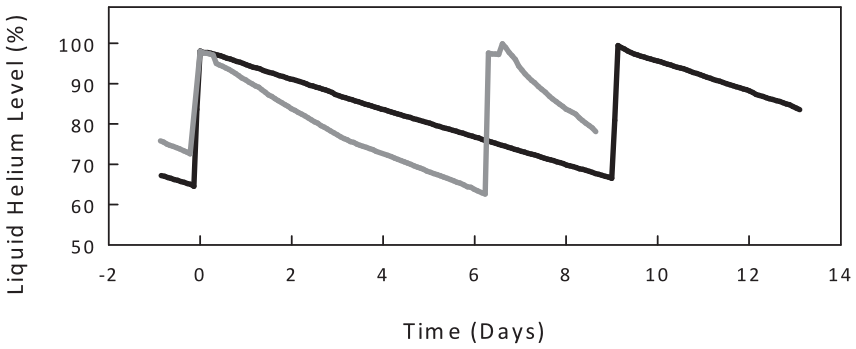

Figure 3.4: 3 T magnet boiloff and effect of blocked a blocked vapor cooled shield line. The black line is data from 2008 where there was flow through both VCS lines. The gray line is from 2006 where one of the VCS lines was blocked.

helium is provided to us free of charge, otherwise the cost of cryogens for our experiments would be prohibitive. However, to make use of this service we have to attach all of our liquid helium cryogenic spaces to a helium recuperation line. Other experiments at the antiproton decelerator and elsewhere at CERN also make use of this recovery line so there is a variability in the pressure that the magnet exhausts to. Certain conditions can lead to the onset of strong oscillations in the helium gas columns. These are known as "Taconis oscillations". These oscillations can become so strong that they can easily be felt mechanically on the latex exhaust tubes that come out of the magnet. They can also increase the heat transport between the hot and cold sections by several thousand times over that of a gas column with no oscillations [42, 43, 44]. On at least one occasion we believe that uncontrolled Taconis oscillations have lead to a quench in the magnet, although the cause could not be determined definitively.

Given the critical importance of controlling the helium gas flows exhausting from the magnet, a significant effort and investment was made to develop a robust com-

puter controlled flow system that would regulate the pressure and exhaust of the magnet both during normal operation and during critical operations such as charging the magnet. The system consists of 8 mass flow controllers with varying flow rates controlled and monitored through DC voltages, 3 normally open and 3 normally closed solenoid valves also controlled by DC voltages, 2 pressure gauges that output a DC voltage and a check valve which only allows flow in the direction away from the magnet and into the helium recuperation line. The setup and direction of the gas flow is shown in Fig. 3.5. The units of flow are in standard nitrogen liters per minute.

The mass flow controllers (MFCs), solenoid valves and pressure gauges are controlled and monitored by an opto22 controller that communicates with a computer over ethernet. It has analog output modules to control the flow output (0-5 V full scale) on each of the mass flow controllers, analog input modules to read the mass flow readings and pressure gauges (0-5 V) and digital relay modules to switch in a 24 V supply to activate the valves away from their normally open or normally closed states. The vapor cooled current leads have two sets of flow controllers due to the very large difference in flow during normal operation and during a charge. Every flow meter has a closed state leak rate proportional to its maximum flow, so during normal operation the larger mass flow controllers (called VCCL MFC 1) are closed and the valves behind them are also closed to prevent undesired flow leak, allowing the gas to go through the smaller flow controller (called VCCL MFC 2) on the same line. During magnet charging when a high flow rate is desired, the valves behind the larger flow controllers are opened and the flow is redirected through the larger controllers.

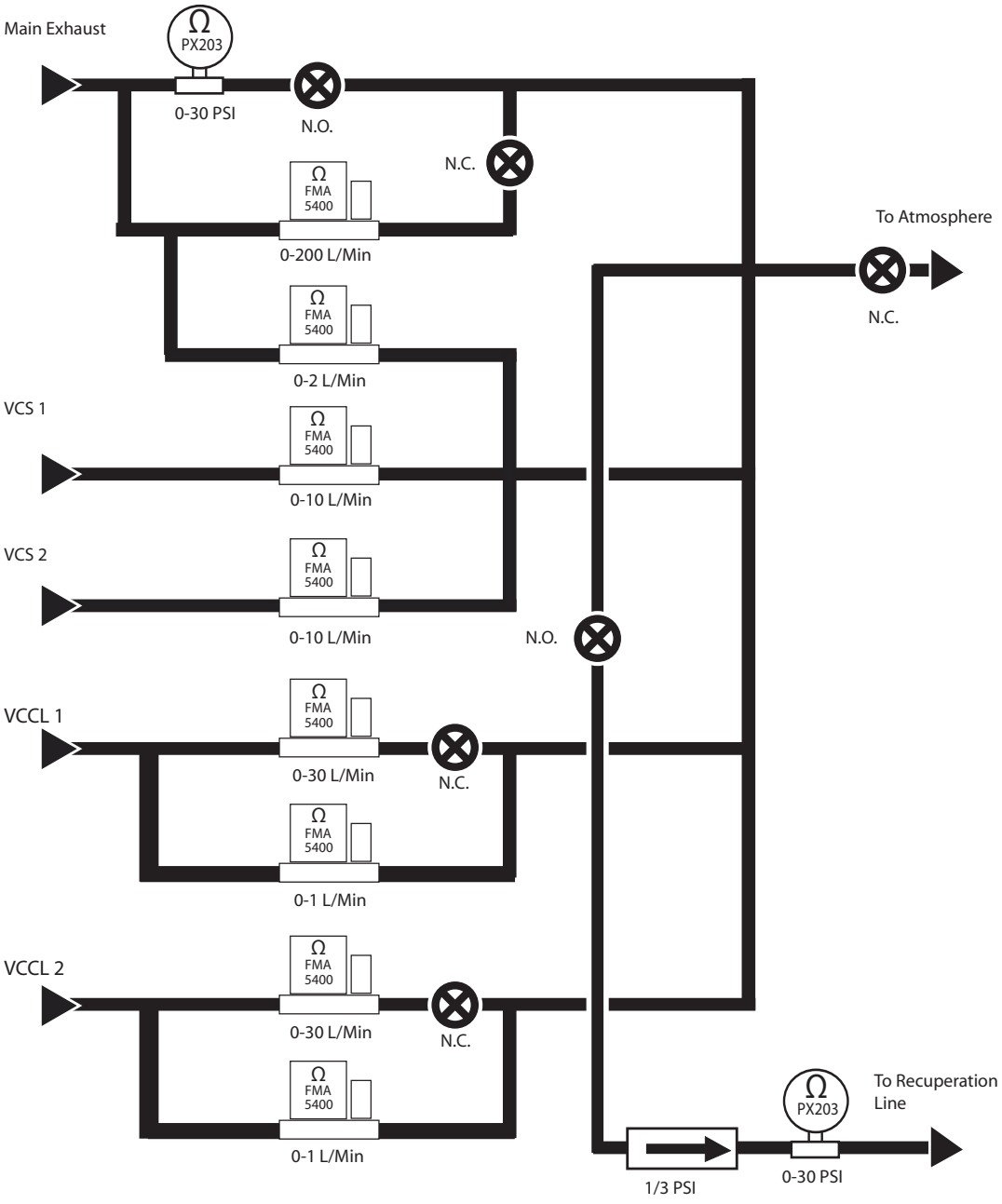

Figure 3.5: 3 T magnet flow control system. The circled X's indicate valves with N.C./N.O. = normally closed/normally open. The flow controllers (FMA 5400) and pressure gauges (PX 203) were all purchased from the Omega corporation. The check valve is manufactured by swagelock

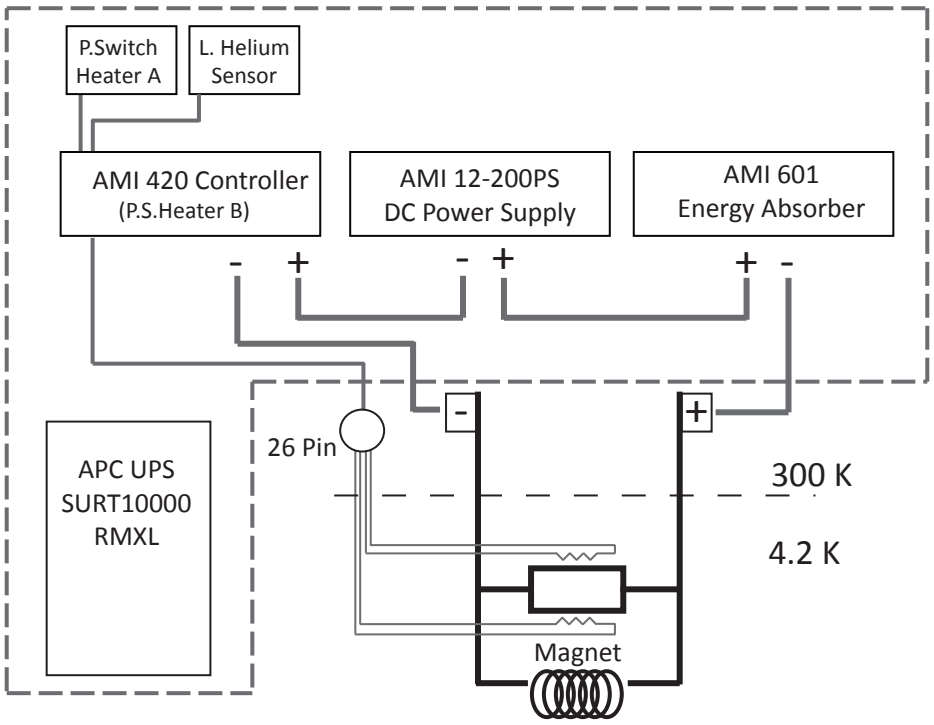

Figure 3.6: Electrical setup for charging the magnet. The dashed line surrounding the UPS indicates that get their power filtered through the UPS.

3.1.3 Electrical Setup for Charging the Magnet

This superconducting magnet, unlike the magnets in the Ioffe trap and antiproton solenoid described later in this thesis, operates in persistent mode. There are many advantages to operating in persistent mode, the most important being field stability, but there are also gains in noise reduction into the trap, a lower helium boiloff rate and a significantly lower burden for operating the magnet. In this section we describe the equipment and setup needed to charge/discharge the magnet and put it into/take it out of persistent mode.

The voltage required to charge the magnet is dominated by the inductive load of the windings, the resistance in the leads is negligible compared to it. The voltage will

oppose the change in flux and is just given by:

$$V_{charge} \simeq -L\frac{dI}{dt} \tag{3.1}$$

It is more economical to buy a single quadrant power supply, that is, a power supply that can only output a positive voltage and positive current across its terminals. However, if we were limited to only apply a voltage of one sign across the magnet, then in order to discharge the best we could do is set the power supply voltage to zero and wait for the current to dissipate through the resistance of the wires, leads and power supply. The time constant for this circuit would be:

$$\tau = \frac{L}{R} \tag{3.2}$$

Given that the inductance of this magnet is above 200 Henries, and the resistance is likely well under an ohm, we would be looking at discharge times on the range of hours, just to get to $1/e$ of the current. In order to avoid this situation, there is a more economical way of turning a single quadrant power supply effectively into a two quadrant power supply, one that can still only output one sign of current, but can effectively change the sign of the voltage across the magnet. This is accomplished through the use of the AMI 601 energy absorber. The basic purpose of the energy absorber is to ensure that there is always a five volt voltage drop between the positive terminal of the power supply and the positive current lead on the magnet. Thus if you want to charge at 2 volts, you need to output 7 volts from your power supply. However, because there is always a 5 V voltage drop (which the energy absorber needs the stored energy in circuit to generate) if you set your power supply to 3 V there will be a -2 V drop across the magnet, giving it the negative voltage it needs to discharge.

According to AMI, this is accomplished by controlling the voltage on the gates of a bank of transistors in a feedback loop to ensure that there is the required voltage drop across them. This voltage drop opposing the voltage from the power supply explains why the terminals of the energy absorbers are in the orientation shown in figure Fig. 3.6.

The setup to charge the magnet is shown in Fig. 3.6. The AMI 12-200PS (12 V, 200 Amp) DC power supply only has an input to control its voltage, not its current. Therefore, there is also an AMI 420 controller unit that has a shunt resistor in it, and sends an analog voltage control signal to the power supply to set its voltage output. Once a desired current, and current ramp rate is input into the controller, it monitors the voltage drop across its internal shunt resistor and changes the voltage in a feedback loop to ensure there desired settings are reached. As shown in Fig. 3.6 the current goes from the power supply, through the energy absorber, through the magnet and back through the controller to complete the loop.

The AMI 420 controller also contains a persistent switch heater supply. Another external persistent switch heater is also used as a backup (to ensure that one accidently turning on doesn't quench the magnet) and it along with the liquid helium level sensor supply go through the AMI controller so that all three signals go into a common bundled wire into a 26 pin connector on the top of the magnet.

An additional piece of equipment has been incorporated into the setup in order to improve the stability of the system. In 2004 several quenches occurred while charging the magnet while the antiproton decelerator was in operation. However, it was noticed that the quenches did not occur when the AD was not running, leading the group

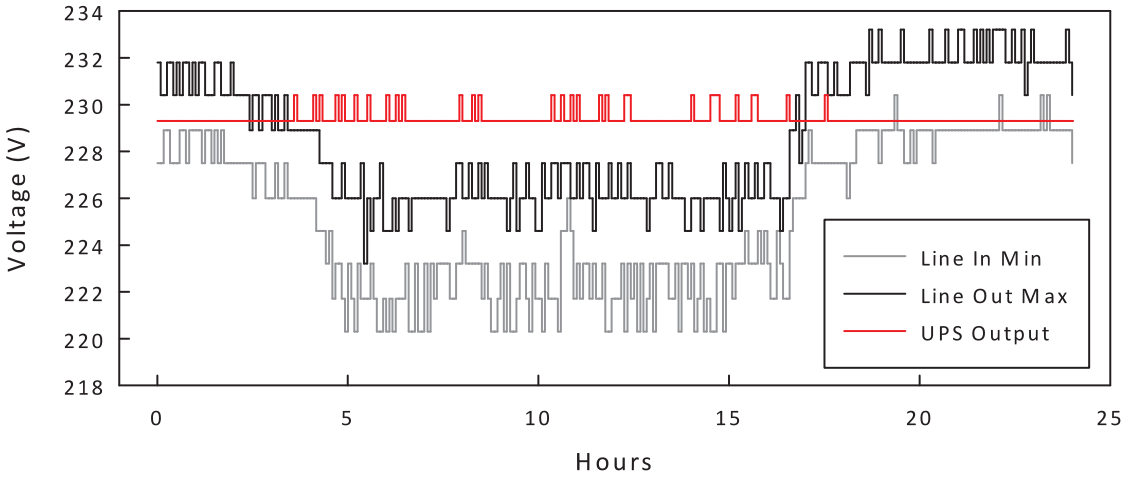

Figure 3.7: Voltage Regulation Done by 3 T Magnet UPS.

to suspect that the quenches were due to variations on the line voltage due to the heavy variable load from the AD. To try to compensate for this problem in 2006 an APC Smart uninterruptible power supply (UPS) called the SURT 10000 XL was incorporated into our setup. The 10000 standing for 10000 Volt amps of available power. The idea behind the huge energy storage capacity was so that we could finish charging/discharging the magnet even if the power went out or so we could disconnect from CERN completely to isolate ourselves from possible noise. This turned out to be unnecessary as the UPS does a substantial amount of voltage regulation even when it is in its connected to line mode. The voltage in and voltage in of the UPS can be monitored via an ethernet connection on the unit, and a plot of the max and min line voltages and UPS voltage out measured over 30 second intervals is shown in Fig. 3.7. We have not had any quenches while charging with the magnet on the UPS while the AD has been running.

3.1.4 3 T Magnet Operation

To charge the magnet, the detachable vapor cooled current leads (VCCLs) must be lowered into place and connected to the power supply as shown in Fig. 3.6. They are left pulled up and disconnected to reduce the heat load on the magnet while not charging. As we can see in Fig. 3.6 the magnet coils are shorted out by two superconducting wires running in parallel. If we try to pass any current through the magnet while these shorts are still superconducting, the inductive load of the windings will look like a much bigger impedance than the wire and all of the current will pass through the wire and not through the magnet. To change this, two small resistive heaters are placed in close proximity to sections of the two wire shorts. When this wire is heated it ceases to be superconducting, and now its impedance is significantly higher than the inductive load of the magnet, so the power supply will pass nearly all its current through the magnet. Thus the need for the persistent switch heater power supplies shown in Fig. 3.6. Once these are on, we can now start increasing the current being sourced from the power supply.

When we are done charging, we turn off the heater supplies without lowering the current and the shorts once again go superconducting. For the current being sourced from the power supply the shorts look like a smaller impedance than the magnet once we start to lower the current. Similarly, for the current in the magnet the shorts look like a much smaller impedance than the internal resistance of the power supply and intermediate equipment. Therefore the current in the magnet is preserved as it just circles in the loop bypassing the power supply. Once current being sourced from the power supply is lowered to zero, the current in the magnet will persist, and it is said

to have been put into "persistent mode".

In addition to the electrical control needed over the power supply voltage, current, and persistent switch heaters, the pressure and helium exhaust of the magnet must be closely monitored. When we begin to charge there are several new sources of heat into the trap that cause a much larger (approximately 5 times) increase in the helium boiloff. If this flow isn't carefully monitored the pressure in the magnet can quickly exceed the safety valve release pressure of 200-300 mbar above atmosphere. Resolving this situation is not as easy as just opening up a larger conductance through any port. As was previously mentioned, the vapor cooled current leads must have a sufficient flow of helium gas through them in order to make sure they do not overheat and even catch on fire. Therefore, during the charge as the pressure builds up the flow through the VCCLs must be gradually increased to at least 5 Nitrogen L/ min or higher, leaving a large safety margin for the cooling required. The VCS exhaust can also be opened more in order to try to keep the pressure around 1100 mbar absolute, a pressure high enough above the recovery line to maintain the flow through the current leads, but not so high as to risk opening the pressure release valves on the magnet. The main exhaust remains closed by activating the normally open valve on the other side of the pressure gauge (see Fig. 3.5) throughout the charge in order to maintain pressure in the magnet.

The magnet controller current, controller voltage, magnet and recovery line pressures and helium gas exhaust flow during a typical charge from 0 to 1 T in 2007 is shown in Fig. 3.8. There are a few interesting things to note about this charge. The charge rate here is $0.0085 A/s$ or approximately 80 minutes per Tesla. Nominally,

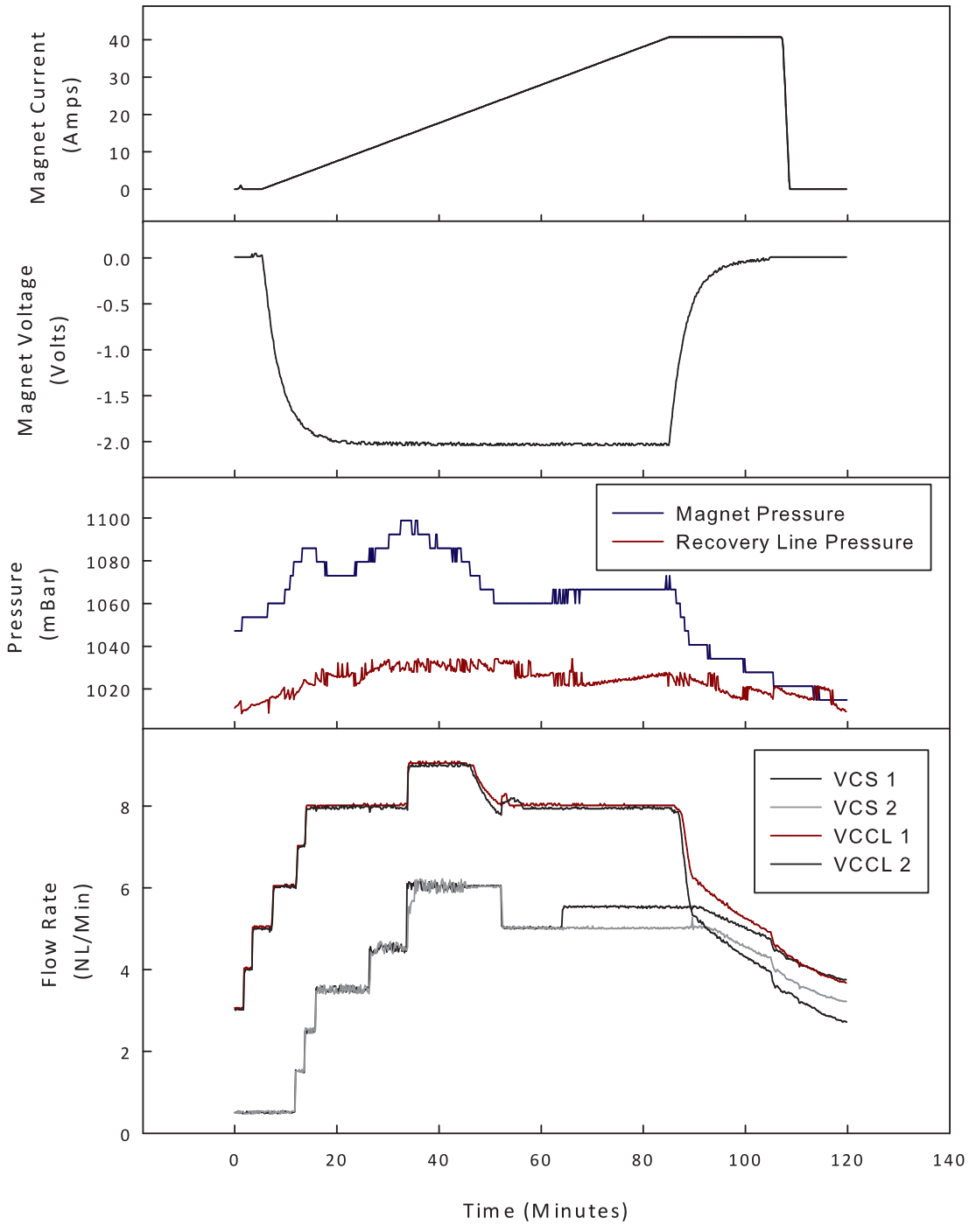

Figure 3.8: 3 T Magnet Current, Voltage, Pressure and Flow Rates During Charge from 0 to 1 T.

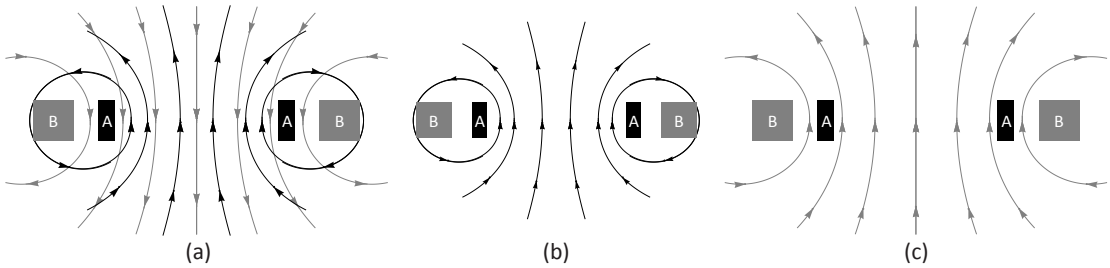

Figure 3.9: Eddy Current Model for 3 T Magnet Charge. The arrows indicate the direction of the change in flux. The three figures correspond to (a) Rising exponential (b) Flat top (c) Falling exponential voltage in Fig. 3.8.

the voltage needed to charge the magnet at this rate should just be given by equation (3.1). Because we are charging immediately from this fixed rate throughout, we would expect that the voltage profile should just be a step function, about 2 V when charging and immediately fall to zero when not. As we can see, however, there seems to be both an exponential rise and fall to the voltage profile.

Another thing we might expect would be that the boiloff would mainly be due the heat given off by the resistive heating in the vapor cooled current leads which should scale as I^2R and by the persistent switch heaters which are on throughout the charge. However, as we see in Fig. 3.8 the boiloff and pressure start to fall off dramatically as we stop the current ramp (just past 80 minutes) but while we are still running the maximum current through the VCCLs with the persistent switch heaters on. This indicates that there is some significant source of heating related to the ramping of the current.

The probable answer to both of these phenomena is the significant generation of eddy currents within the conducting, but lossy stainless steel superstructure of the magnet. The mechanism for this is illustrated in figure Fig. 3.9. The figure shows

a model where we are charging a solenoid A, whose cross section is shown, that is surrounded by a ring B of conductive but lossy ($R \neq 0$) material. During the rising exponential of the voltage curve in Fig. 3.8 the situation is depicted in Fig. 3.9a. The flux generated by A induces eddy currents in B which oppose that change in flux, thus reducing the EMF induced in A.

These eddy currents start to saturate with increasing current in B and the additional induced eddy currents are balanced out by resistive losses in B. The power being put into B by the change in flux from A is constant, but the resistive losses go as I^2R. At some point the current in B reaches a maximum and no additional change in flux due to B passes through A. This is the situation in Fig. 3.9b corresponding to the flat part of the voltage curve in Fig. 3.8 where the voltage is just what you would expect from the inductive voltage drop.

When we finish changing the current in the solenoid A, the current in B decreases now generating a flux change Fig. 3.9c in the opposite direction to the situation in Fig. 3.9a thus maintaining the EMF across A and corresponding to the falling exponential in Fig. 3.8.

The generation of these eddy currents and the resistive losses associated with them also explain the huge increase in boiloff we see when ramping compared to not ramping. This emphasizes the importance of waiting for the voltage across the magnet to reach zero prior to putting the magnet into persistent mode. On one occasion in 2008, the magnet was discharged and put into persistent mode while the current was at zero but there was still a voltage being read across the magnet. When the magnet was to be re-energized a week later, a current of greater than 0.1 amps was

read upon connected it to the power supply, corresponding to greater than 25 gauss, interfering with sensitive spectroscopy experiments that were conducted during the week. As there were still eddy currents in the surrounding material, as they died off they caused a change in flux and induced a current in the persistent superconducting coils.

In addition to closely controlling the flows during the charging of the magnet, it is also critical to have an active control of the flows and pressure even while the magnet is in persistent mode. Because the magnet is connected to CERN's helium recuperation line which has frequent changes in pressure, a uniform conductance for the helium exhaust will often lead to drastic spikes in pressure within the magnet. The onset of Taconis oscillations will also greatly increase the pressure and helium boiloff.

An additional complication is that the mass flow controllers in the helium flow control system are normally closed solenoid valves. That is, to open the valves a voltage has to be placed across the solenoid. When the flow reading is below the flow set point, the valve will open as much is necessary to try to get to the desired flow rate, up to its maximum. Therefore, whenever the flow going through the mass flow controller is less than the setpoint, the maximum current is being sent through the mass flow controllers, possibly reducing their lifetime and the lifetime of the voltage supplies. Therefore we would like a system where the mass flow controllers reduced their setpoint flow when the actual flow is below a certain amount under the setpoint.

To combat these challenges, an active computer controlled feedback system was developed. The main exhaust is closed off, as it was found that having it open very

often lead to Taconis oscillations, possibly due to its large conductance path. The VCCL lines are set to a fixed low point where the flow will seldomly go below the setpoint, and the pressure control is accomplished by varying the flow through the 2 VCS lines. If the flow in the VCSs is below the current setpoint, the setpoint is reduced until this is not the case. If the pressure is rising or above a certain threshold, the VCS setpoint is increased until either the flow is below the setpoint, or until the pressure begins to decrease.

With the improvements to the electrical charging setup of the magnet, and to the flow control system, the ATRAP collaboration now has a robust superconducting magnet system that can serve as a platform for antihydrogen experiments with minimal operator time for many years to come.

3.2 Thermal Control System

Critical to the execution of our experiment is to lower the temperature of our penning trap as much as possible. As was described in Chapter 2 the electrons and positrons have a mechanism for radiating their energy away on the order of seconds and coming into thermal equilibrium with the surrounding electrodes. The antiprotons in turn can lose some of their energy in collisions and potentially come into thermal equilibrium with the electrons and positrons. In order to magnetically trap antihydrogen, as will be discussed more in chapters **??** and **??**, the thermal energy of the particles must be less than the trapping potential, for our current Ioffe trap about 300 mK and for the best realistic Ioffe trap under 1 K.

In addition to the temperature conditions required for trapping antihydrogen,

trapping antiparticles at all requires an exceptionally good vacuum in order to minimize annihilations with gas atoms. Cryopumping onto the cold surfaces in the vacuum space is the most efficient pumping method at very low pressures and thus provides another motivation to get our trap temperature as low as possible. This section describes the thermal control systems which allowed us to get the electrode stack in our apparatus down to 1.1 K.

3.2.1 Insert Dewar, Thermal Isolation and Cryogen Spaces

The space within the penning trap where the particles are confined and manipulated is located on a vertically oriented apparatus which is lowered into the 20" bore of the 3 T magnet. While the magnet windings themselves sit in 4.2 K liquid helium, the bore is at room temperature, requiring a separate vacuum and cryogenic apparatus for the rest of the experiment. This is different than in prior antihydrogen setups, where the magnet bore was at nitrogen temperature [45]. The ATRAP and BTRAP apparatuses do not have a 77 K nitrogen shield, instead they are shielded by a series of three concentric cylinders that are held at room temperature, 60 K and 20 K respectively. The last two layers reach their temperatures by being cooled by a double stage and single stage pulse-tube cryorefrigerators. This piece of equipment is referred to as the "insert dewar", as it is inserted into the bore of the magnet, and the experiment is in in turn inserted into it. An extensive discussion of the operation of the insert dewar has been provided in a prior thesis [41] and will not be repeated here.

The experimental apparatus (either ATRAP or BTRAP) is mated with a bolt hole

pattern and a rubber o-ring to the top of the insert dewar, forming a closed vacuum space as shown in Fig. 3.10. The inside of the insert dewar is pumped out to a very low pressure, between 10^{-7} and 10^{-5} Torr. To reduce the radiation load coming from the "hat" of the experiment (where the electrical and optical vacuum access is at the top) a series of three copper radiation baffles are suspended from the top by G-10 fiberglass rods in the thermal isolation section. Using copper flexible "fingers" around their outer diameter the top radiation baffle makes good contact with the 60 K middle layer near the top, and the bottom radiation baffle makes good contact with the 20 K layer which is suspended lower down.

The only points of contact between the insert dewar and the ATRAP or BTRAP apparatus is on the o-ring seal at the hat and the two contacts at the radiation baffles. The rest of the heat load is due to mechanical and electrical connections from the hat and the 20 K radiative load from the insert dewar. Below the bottom radiation shield is a 44 L liquid helium dewar. In optimal conditions trap can have a helium hold time of about 6 days, with substantial reductions occurring if there is a thermal touch somewhere else between the insert dewar and the experiment, if there is a bad vacuum (possibly due to a leak of helium gas from the cryogenic space), or if the insert dewar hasn't reached its base temperature of 20 K.

The helium dewar is well heat sunk to the lower sections of the trap keeping everything below it between 4.2 - 9K depending on slight differences in heat sinking the electrical connections between 2006 and 2008. To minimize the heat load due to the electrical connections that run between the hat at 300 K and the vacuum feedthroughs to connect to the electrode stack at the bottom of the experiment 0.003"

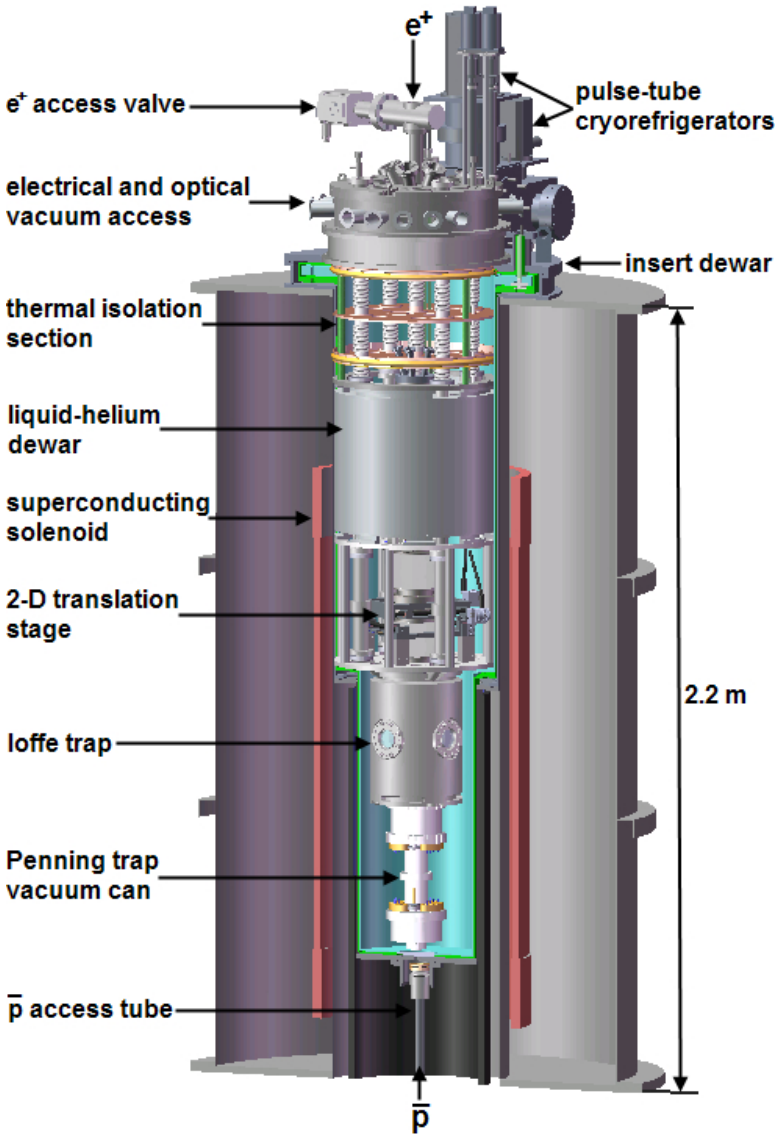

Figure 3.10: BTRAP Experimental apparatus within insert dewar and magnet, shown without the 1K pot equipment.

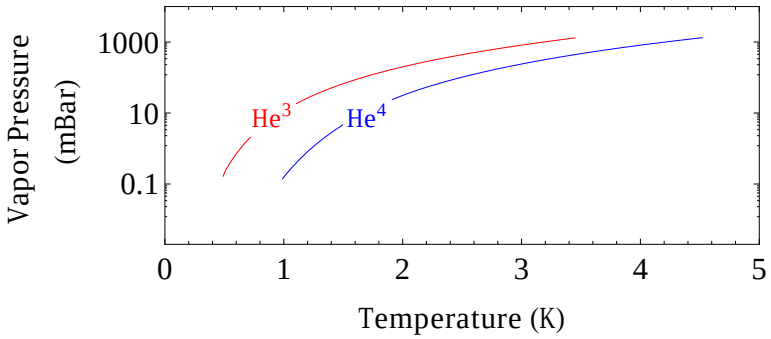

Figure 3.11: Vapor Pressure for He^3 and He^4.

thick constantan (a 55% copper and 45% nickel alloy) was used for DC lines, and microcoax was used for the RF connections. A temperature between 4.2 and 5 K at the bottom of the experiment was reached when a strong effort was made to heatsink the microcoax to both the top and bottom radiation baffles. More details on the electrical vacuum feedthroughs, thermal isolation and cryogenic systems, experiment cooldown, and helium hold time can be found in David Lesage's thesis [41].

3.2.2 1 K Pot System

Together all of the measures in Section 3.2 succeeded in reliably getting our experiment down to just over 4.2 K. Given the huge dividends for antihydrogen trapping for achieving lower temperatures, a pumped helium system was incorporated into the apparatus in 2008 in order to get the electrode stack temperature down to approximately 1 K. This subsection will describe its design and operation.

At 1 atmosphere of ambient pressure the boiling point of liquid helium is approximately 4.2 K. As the pressure decreases, it becomes easier for the more energetic atoms in the liquid to escape into a gas, and as they leave the average energy of

the liquid is decreased. They lower the energy by the latent heat of vaporization of helium, which in its natural abundance is about 83 J/mol and varies slightly between 1 and 4 K [46]. The vapor pressure of the two most common helium isotopes as a function of temperature is shown in Fig. 3.11. This is a form of evaporative cooling. In principle we could follow the vapor pressure curve of helium down further than 1 K by continually lowering the pressure to get a colder and colder liquid. However, the cooling power of the pumped helium decreases as you pump more atoms away. The more you pump out, the less atoms are left, the less can leave and the less energy can be taken out of your system. How much you can cooldown the experiment is therefore heavily reliant on the heat load that your pumped helium system is fighting against. In practice it is very difficult to make a pumped helium system (which is primarily He^4) that goes below 1 Kelvin, as the cooling power goes as [46]

$$\dot{Q} \propto \exp(-1/T) \tag{3.3}$$

Lower temperatures can be reached by using a He^3 pumped system, as its vapor pressure is higher for a given temperature as shown in Fig. 3.11 but this is both more expensive due to the cost of the isotope, and more complicated because then your 1 K pot cannot be fed from the main helium reservoir and must be a closed He^3 system. The lowest practical temperature reached with a pumped He^3 system is about 300 mK [46].

The setup for our pumped 1 K pot system is shown in Fig. 3.12. The 1 K pot is located just below the liquid helium dewar and has 4 different connections on it. First it has a larger diameter pump port which runs up through a cylindrical hole in the helium dewar, up to the hat and is connected to a scroll pump which will pump

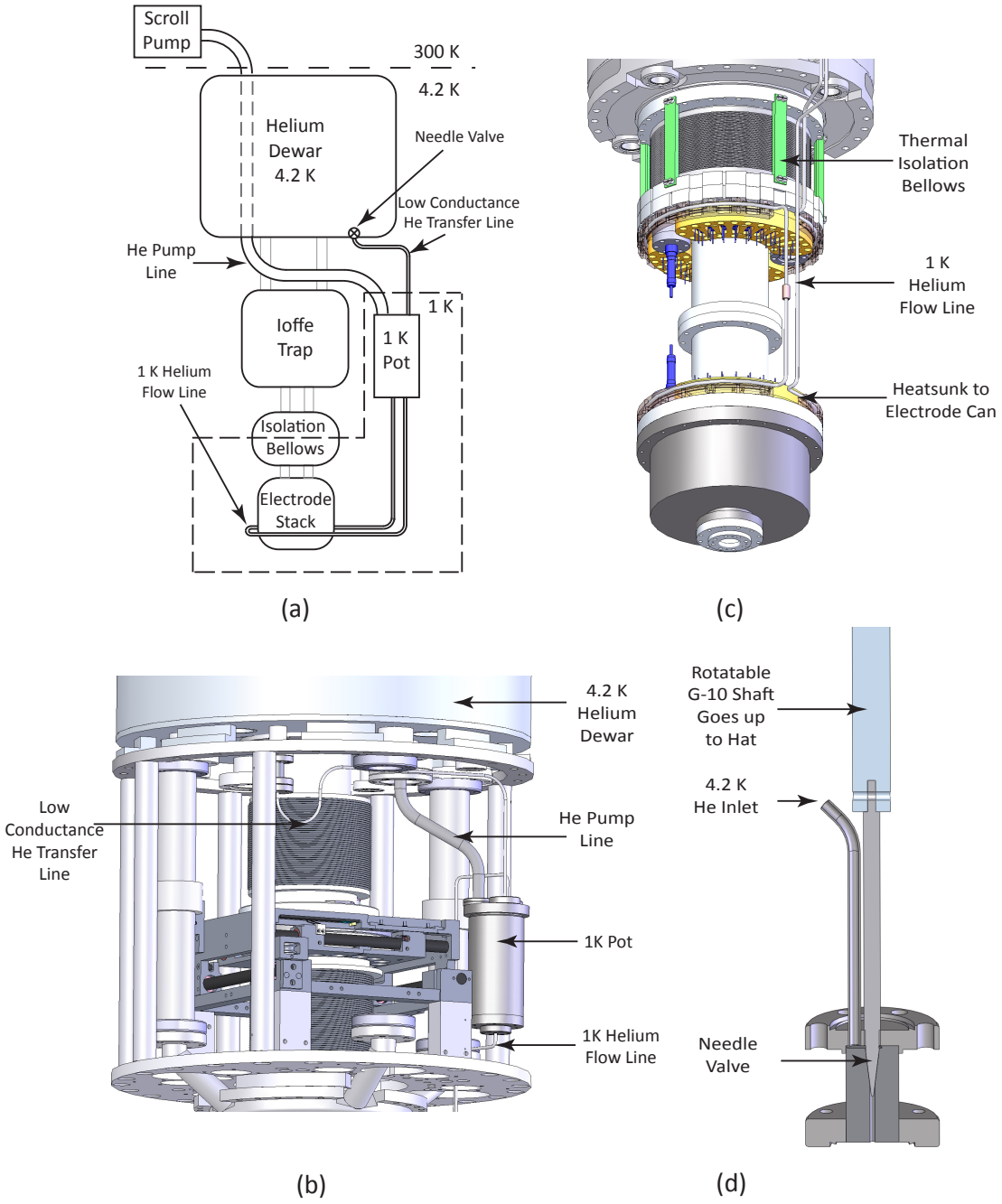

Figure 3.12: (a) 1 K Pot System Diagram. (b) The apparatus area around the 1 K pot itself. (c) The electrode trap can area and vacuum feedthrough pins. The 1 K helium flow is heat sunk to the can using clamp pieces which are shown as transparent. (d) A cross section of the needle valve at the bottom of the helium dewar.

it out to a pressure below its vapor pressure at 1 K. There are a series of half circle radiation baffles (not shown) in the pump out tube as it goes up through the helium dewar to reduce the radiative load coming down to the pot.

The second connection is a small diameter conductance line which feeds up into a needle valve at the bottom of the helium dewar and is connected to the top of the 1 K pot. This is meant to leak in liquid helium from the main dewar at a very small rate (see Fig. 3.12a, b and d). The purpose of having a very small rate is to give the helium a chance to come into thermal equilibrium with the 1 K pot before it reaches the main liquid bath in the cylinder, so as not to add more heat to the system.

The other two connections to the 1 K pot are the inlet and outlet of the 1 K helium circulation line which goes down to the bottom of the trap and makes a good thermal contact with the titanium can that surrounds the electrodes (see Fig. 3.12a and c). This is a flexible copper tube that gets clamped onto the can using copper pieces that are fixed down with a bolt hole pattern.

Because the 1 K pot has a limited cooling power, it is critical to minimize the heat load going down to the electrodes, even from the 4.2 K helium dewar. This is accomplished by inserting a titanium thermal isolation bellows just below the Ioffe trap (also at 4.2 K) which in turn is suspended below the helium dewar. Unlike the rest of the bellows in our experiment these bellows are not used to make up differences in thermal contraction, we want them to stay at a fixed length. Instead we use them because the very thin titanium walls conduct very little heat while still maintaining vacuum. To get the length to stay fixed and provide axial structural support, the bellows are supported by fiberglass G-10 support posts (see Fig. 3.12c).

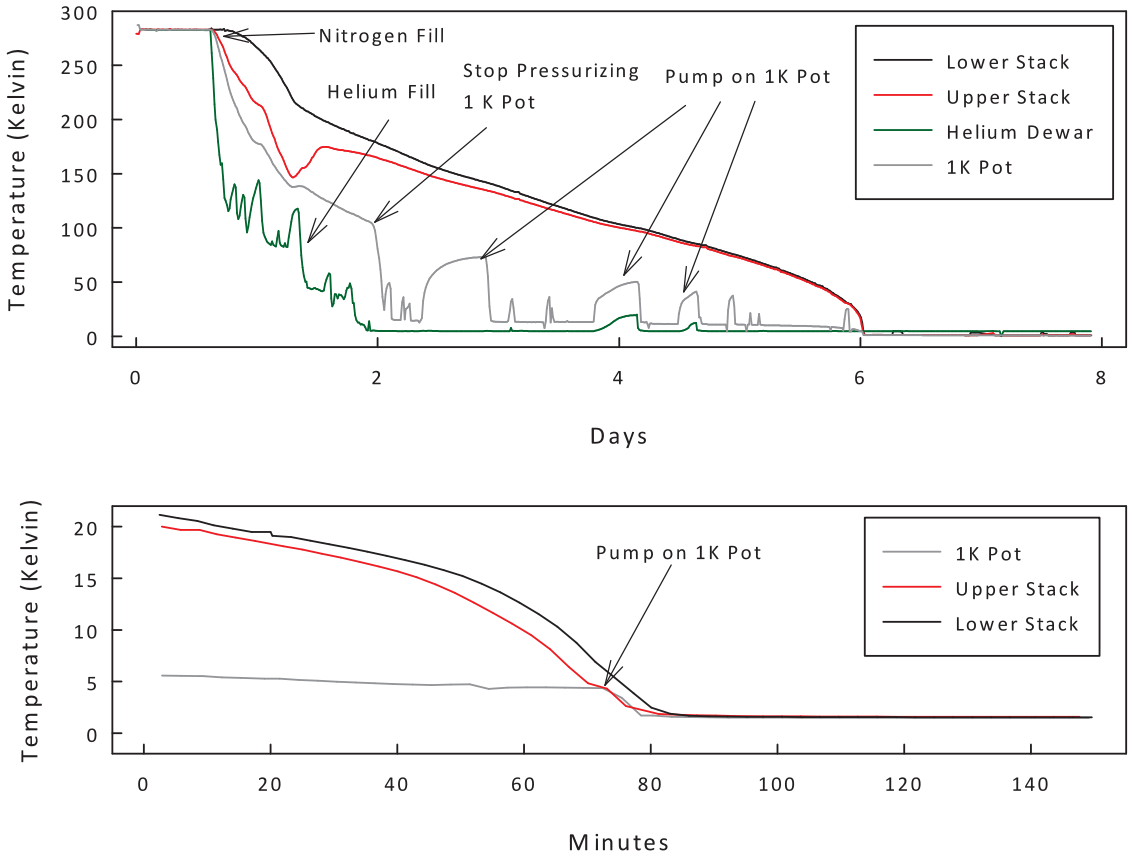

Figure 3.13: Temperature of apparatus during 1 K Pot cooldown.

The result of this system is to allow our electrode stack to be cooled down to better than 1.2 K. Unfortunately, there is a downside to the thermal decoupling of the electrode stack to the helium dewar. Whereas prior to installing the 1 K pot we were able to cooldown the electrode stack to its base temperature of around 4.2 K in about 1.5 days [41], with the 1 K pot system the initial cooldown took almost 6 days to get to the base temperature. For the future, a couple ways to speed up this process are under consideration.

The first way is to leave the experiment at nitrogen temperature for a longer time so that we can leave a small amount of nitrogen ($\sim$ 0.1 Torr) in the insert dewar

as an exchange gas that will bring the electrodes and surrounding cans in thermal equilibrium with the rest of the experiment more rapidly. However, this will not speed up the process of getting the experiment from nitrogen temperature to helium temperature, meaning it could still be on the order of 3 or more days to cooldown.

The second possibility would be to arrange a detachable heat sink system that would be controlled from the hat, much like the way that our detachable current leads work. A G-10 rod would be placed through a vacuum feedthrough on the hat. It would connect to a copper piece that had flexible copper braids heat sunk to the helium dewar. When pushed down, this copper piece would mate to a connector which a good thermal connection to the trap can. This would be left in place until the electrode stack cooled down 4.2 K. Then would be retracted in order to reduce the heatload to get to 1 K.

The cooldown procedure for the BTRAP apparatus with the 1 K pot in place is shown in Fig. 3.13. We can see that the helium dewar reaches its base temperature in two days, which could have been accelerated, but there was little point as the electrode stack was still very hot. The 1 K pot equilibrates fairly rapidly with the helium dewar as there is gas in the pump port to transfer the heat. The electrode stack takes much longer. We can see that the 1K pot warms up several times when it is pumped on before helium has accumulated in it, as the absence of a transfer gas breaks the heat transfer from the 1 K pot to the helium dewar, and the heat load from the electrode stack causes the 1 K pot to warm up. In the lower plot in Fig. 3.13, the electrodes and 1 K pot have finally cooled down enough to allow liquid helium to accumulate in the 1 K pot, at which pumping on it succeeds in bringing the

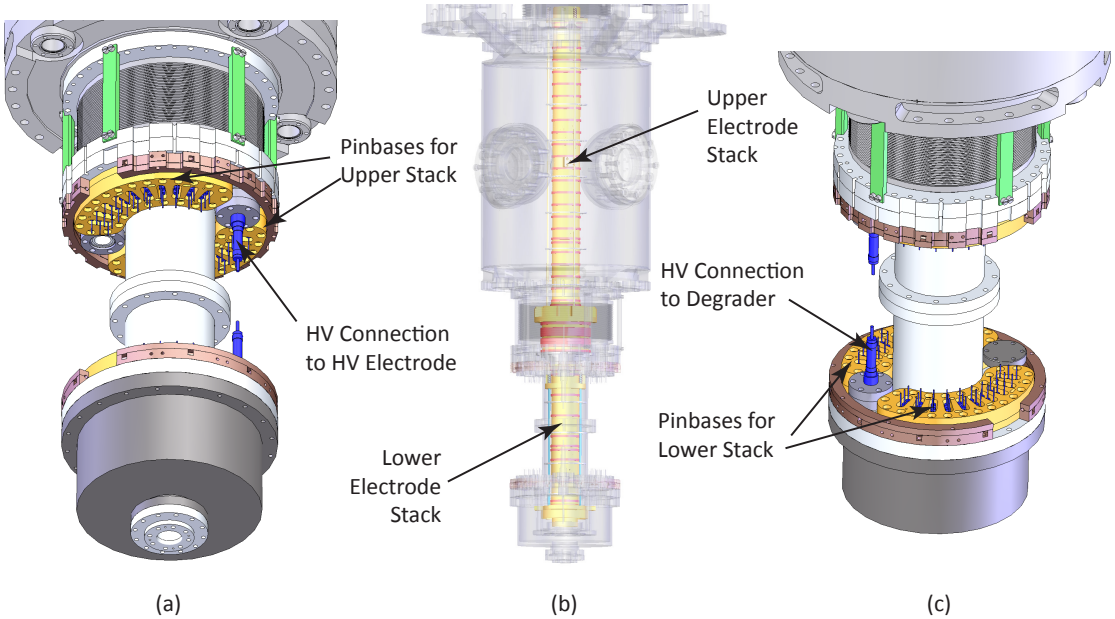

Figure 3.14: Location of electrode stack and vacuum electrical feedthrough pinbases.

temperature of both the 1 K pot and the upper and lower electrode stack to below 1.2 K.

3.3 Penning Trap Electrodes

3.3.1 Electrode Location and Sizes

The ATRAP and BTRAP apparatuses are meant to give a wide range of flexibility in conducting antiproton, positron, electron and antihydrogen experiments. In order to allow a wide range of potential structures and radio frequency signals to be sent down to the trap, as well as having sufficient room to capture positrons and antiprotons simultaneously, we built a very long (78.5 cm) stack of 36 cylindrical electrodes of uniform radial size ($\rho_0 = 18mm$) but various axial sizes. The electrodes sit in the

a separate vacuum space from the insert dewar. As shown in Fig. 3.14, they begin at the bottom of the can where antiprotons enter where there is a degrader (served to degrade the energy of the antiprotons and also to apply a high voltage to trap them). Above the degrader there is a lower stack that proceeds up about 25 cm to the bottom of the beginning of the thermal isolation bellows. Inside the thermal isolation bellows there is a high voltage electrode which goes up to 5 kV and is thus well isolated from the rest of the electrodes, that are only meant to be biased up to a kV.

Above the (5 cm) HV electrode region an upper trap proceeds approximately another 50 cm through a simple titanium can (in the case of ATRAP) or a quadrupole Ioffe trap (in the case of BTRAP). The electrode stack consists of 4 different sized axial length electrodes. The majority of electrodes in the upper stack are radius length electrodes ($z_0 = 0.5\rho_0$ in the convention from Fig. 2.2a), while the majority of the electrodes in the lower stack are endcap length ($z_0 = 0.849\rho_0$ in the convention from Fig. 2.2a). The reason for this is that the upper trap is the antihydrogen formation region, and more flexibility for varying the axial voltage is desired there. Both the upper and lower stacks also have the 5 electrode harmonic well configurations with the dimensions described in Table 2.1 consisting of a ring and two compensation electrodes, with the reference voltages being provided by either endcap or radius length electrodes.

Other than the axial variation in sizes, there is an additional difference in that some electrodes are either split azimuthally into either two or four pieces. The purpose of splitting the electrodes in two is in order to drive or detect the radial motions of the particles, there are split compensation electrodes in both the upper and lower

harmonic wells for this reason. The purpose of splitting an electrode into four is to use the rotating wall technique to spin up and change the density of charged particle plasmas [29]. There are four-split rotating wall electrodes in both the upper and lower traps. The electrodes are made of gold plated solid OFE copper and are held apart 0.18 mm apart by ceramic macor insulating rings (shown as red in the drawings in this chapter for illustration though they are actually white).

3.3.2 Trap Wiring

To get the voltages to the electrodes the signals need to pass through two different vacuum spaces. First they must pass from atmosphere into the insert dewar vacuum. This is accomplished at the hat by putting the DC lines into a standard 32 pin rubber o-ring ISO KF flanges, and the RF lines into standard SMA vacuum feedthroughs also going into pieces that mount onto ISO KF flanges. Then they must pass from the insert dewar vacuum space into the penning trap vacuum space. The DC lines are fed down to the bottom of ATRAP or BTRAP apparatuses using twisted pair constantan 0.003" thick that are individually wrapped in a teflon sheath. These are connected on intermediate terminals and passed down to connect onto a printed circuit board with filter circuits that sit on top of copper flanges fixed with indium seals that contain 30 vacuum feedthroughs. These are referred to as the “pinbases". The feedthroughs have long thick copper wires that pass through holes in the PCB filter, are soldered in place, and also give the filter boards their mechanical stability. The RF lines come down on micro co-ax lines which are attached to the same filter board via SMA connectors.

There are four spots for such flanges, but only three have been needed thus far. One lower pinbase serves the lower trap, while there are two upper pinbases which are used to pass signals to the upper trap (see Fig. 3.14). The high voltage needed on the degrader and the high voltage electrode are passed through separate high voltage vacuum feedthroughs.

Wiring diagrams for the upper and lower stacks of the ATRAP apparatus are shown in Fig. 3.15 and Fig. 3.16. The wiring diagram for BTRAP is very similar, with a slight change in location for some of the electrodes. The purpose of the circuit elements, not counting the elements needed for the particle amplifiers, are three fold. Either they are used to block DC and RF signals from interfering with each other (as is the case for the 1000 picofarad blocking capacitors in series with the RF lines, and the filters between the rotating wall electrodes), they are used to 50 Ω terminate transmission lines to block reflections [47] or they are meant to filter out electrical noise from getting down to the trap.

There are two critical reasons making large efforts to reduce the amount of electrical noise which gets down to our trap. The first is that stray noise getting down to the particles can heat them, especially if they are resonant with either their single particle motions or plasma frequencies, either adversely effecting their behavior or even causing them to leave the trap. The second reason is that such noise can very adversely effect sensitive particle detection measurements, especially if we are trying to detect small numbers of particles.

For this reason two stages of filters are placed on all of the DC lines. There is a first stage of filtering at 300 K at the hat which consists of an LC low pass filter with

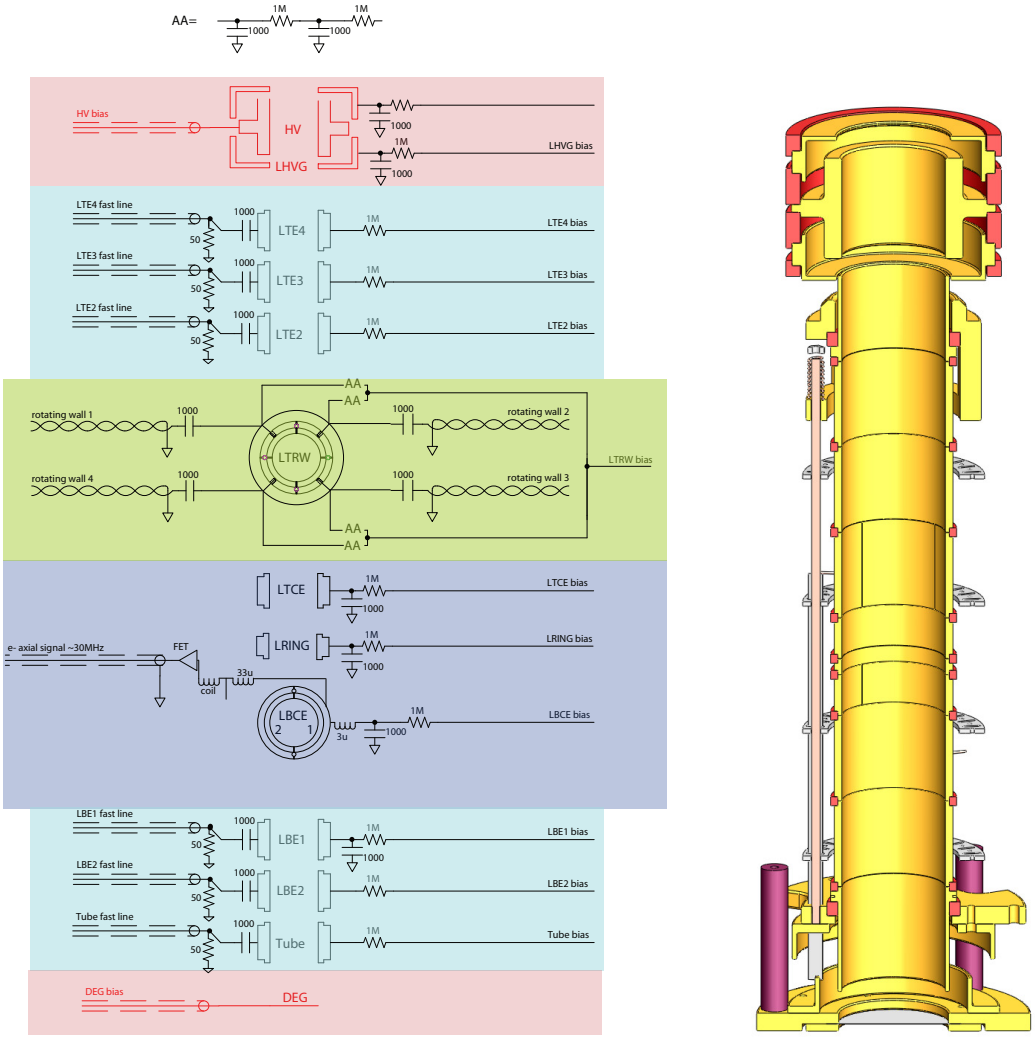

Figure 3.15: (a) Wiring diagram for ATRAP lower stack. (b) Cross section of the ATRAP lower stack electrodes. Note the duplication of the HV electrode in both upper and lower stack figures for reference. There is only HV electrode region.

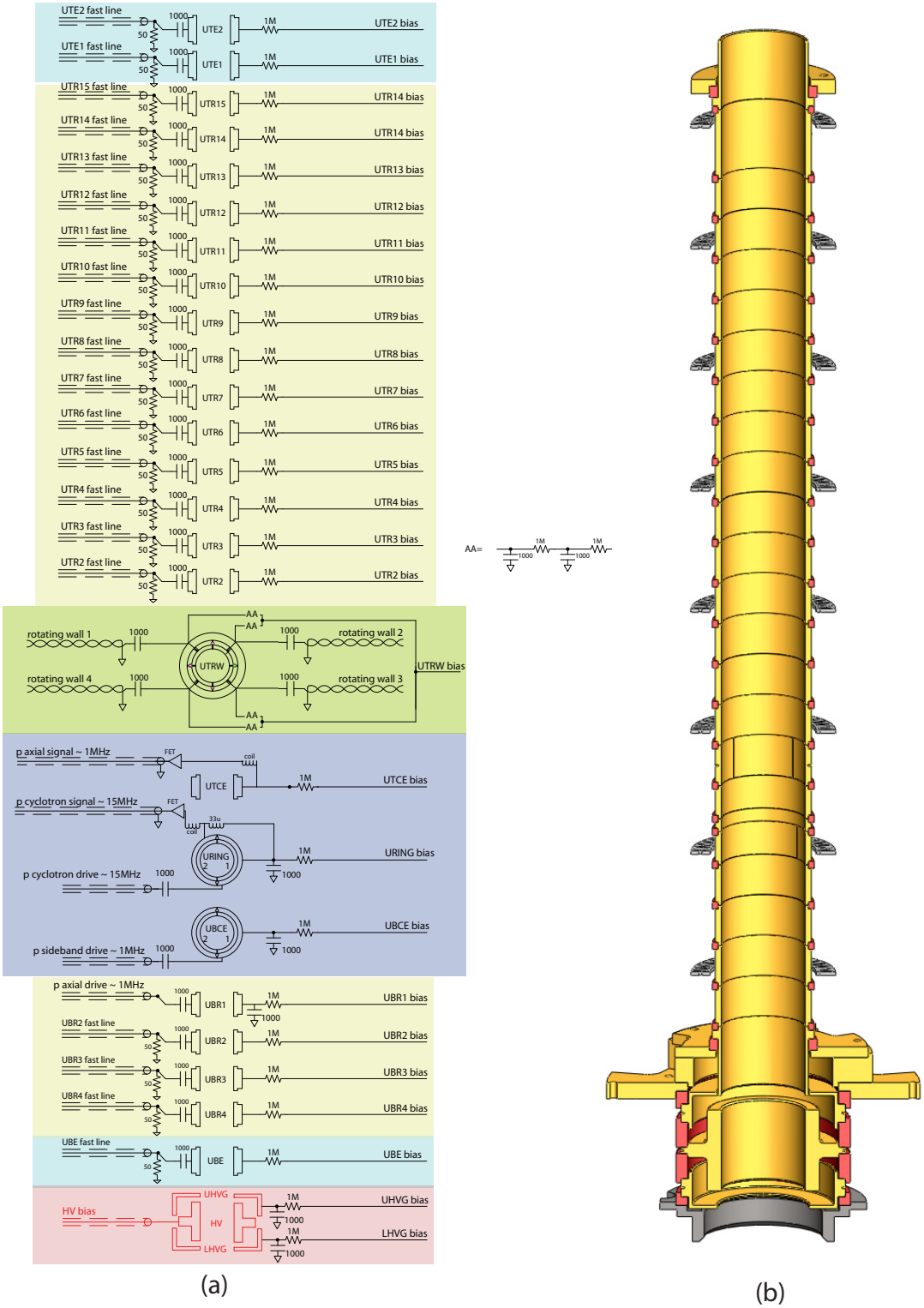

Figure 3.16: (a) Wiring diagram for ATRAP upper stack. (b) Cross section of the ATRAP upper stack electrodes.

$L = 100\mu H$ in series and $C = 0.1\mu F$ to ground, with another $R = 100M\Omega$ resistor to ground to bleed off any accumulated charge from the capacitor. This filter will cut off frequencies above $\nu = \frac{1}{2\pi\sqrt{LC}} \simeq 50kHz$. There is a second stage of filtering on most of the DC lines (shown in Fig. 3.15 and Fig. 3.16) down near the pinbase at 1.1 K. This is a low pass RC filter with a 1 $M\Omega$ resistor in series and $1nF$ capacitor to ground that will filter out frequencies above $\nu = \frac{1}{2\pi RC} \simeq 150Hz$. Our electrodes have a leakage resistance to ground of greater than 50 $G\Omega$ measured at room temperature, so the 1 $M\Omega$ resistor does not cause any appreciable voltage division. As you can notice on many electrodes Fig. 3.15 and Fig. 3.15 the RC filter shares the blocking capacitor for the DC line, and then goes 50Ω to ground, which does not change its filtering significantly, eliminating the need for a second capactitor.

3.3.3 Voltage Supplies and Support Equipment

In order to conduct all of the experiments described in later chapters we needed to have a robust setup for the rapid and precise control of many voltages and frequency sources. To accomplish this we had a number of instruments custom designed by members of the group, by the Harvard Electronics Instrument Design lab or by Win Hill, a researcher specializing in electronics at the Rowland Institute for Science in Cambridge, Massachusetts.

The voltage control setup is shown in Fig. 3.17. Each electrode voltage is individually controlled by the laboratory experiment computer. The computer sends instructions over ethernet, converted to a serial command through a fiber ring to precision digital to analog voltage supplies called biasdacs that can output between

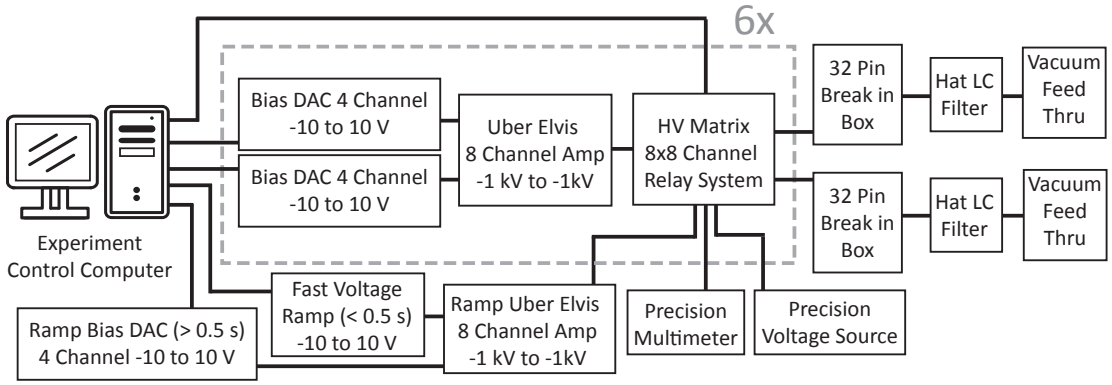

Figure 3.17: DC voltage and voltage ramp setup for biasing the penning trap electrodes.

-10 and 10 V. These were custom built for the group by the Harvard Electronics Instrument Design Lab. Each of these biasdac channels (there are 4 to a unit) get sent to precision high voltage amplifiers that have a gain of about 100 boosting the signal to between -1 kV and 1 kV. Each of these units has eight channels taking as input the signals from two biasdac units, and taking their rails from two Kepco 2 kV high voltage supplies. These amplifiers were custom built for us by Win Hill of the Rowland Institute. The name "uberelvis" follows from the names of two lower voltage predecessors, elvis and superelvis. The origin of the original name "elvis" has been lost to the ages. A new software calibration procedure using interpolation points stored in a database has been developed to account for the slight discrepancy in amplification and biasdac behavior for each of the channels, which has allowed us to achieve a precision of 50 mV, often much better, on all the channels over a range of hundreds of volts.

It is often necessary to switch in different voltage sources onto the electrodes than just the uberelvis voltages. For example, when counting out antiprotons, we

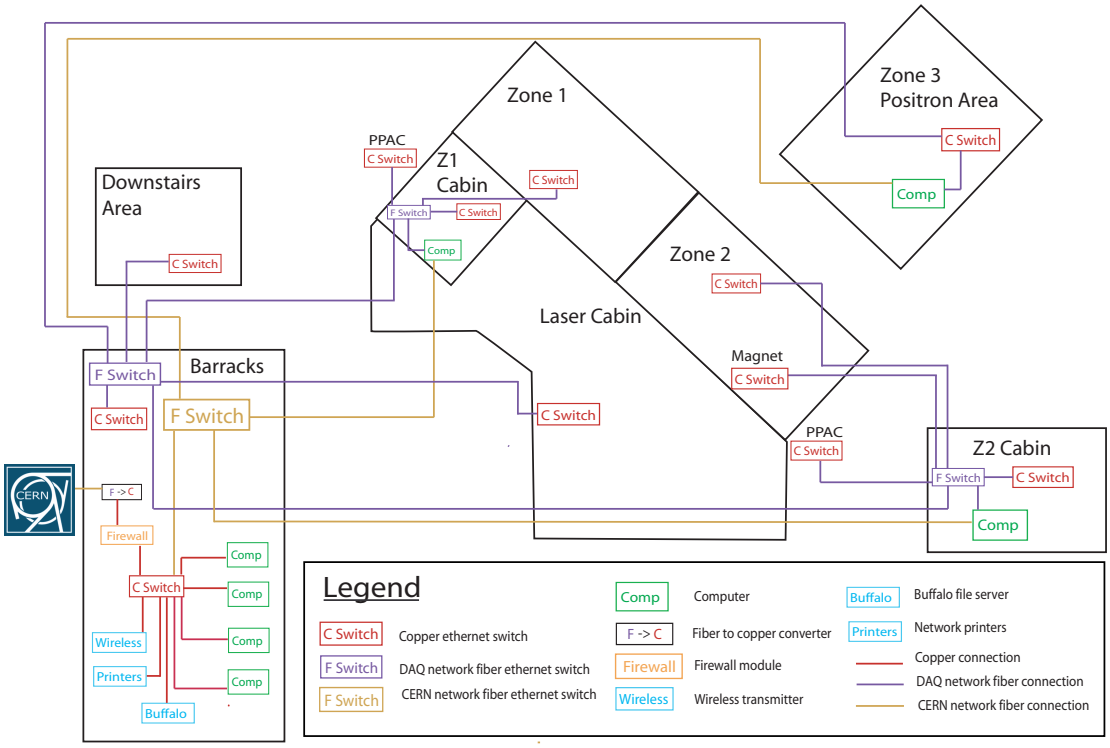

Figure 3.18: Copper and fiber ethernet configuration between experimental zones and work areas.

often want to apply a precision low voltage (0-100 V) ramp to a particular electrode. Depending on the experiment, we would like to switch which electrode the ramp is on, but we don't want to have a precision ramp supply for every electrode. We have found a way around this by using an array of 8x8 by high voltage reed relays that are computer controlled in an instrument designed and built by members of the Harvard ATRAP group which have called the "high voltage matrix". This allows us to switch in 8 different channels, one being the dedicated uber elvis and one being a 50 Ω termination to ground for each of the electrodes. In addition to different ramp sources, we also switch in precision multimeters for calibration and voltage checks, as well as precision voltage supplies that can do significantly better than 10s of mV

precision over a large range.

One additional piece of infrastructure for the support of the experiment required a significant amount of planning and work. It is critical to isolate the grounds of the different sections of the experiment, control systems, and work areas in order to minimize noise. Therefore a series of fiber and copper ethernet connections were setup throughout our experimental zone in order to provide computer control to instruments in the experimental zone, without electrically connected the areas as would have been the case with ordinary CAT5 ethernet cables. An additional challenge was to isolate the data acquisition network from the ordinary internet and CERN connected ethernet network in order to provide an additional level of security for our experiment control. The layout of the ATRAP fiber, copper ethernet system is shown in Fig. 3.18.

Chapter 4

Electrons

Critical to the loading of both antiprotons and positrons is a robust and efficient way of loading large numbers of electrons into our penning trap. Electrons are used to cool both the 5 KeV antiprotons arriving to us from the antiproton decelerator and the roughly 75 eV positrons coming to us from the positron accumulator, as will be discussed in the following chapters. In addition, electrons are a very useful tool for simulating the behavior of positrons, as well as for diagnosing many aspects of our experiment. This chapter discusses the development of an improved electron loading method, a robust method for establishing the number of electrodes loaded into our experiment, and experiments regarding the properties of electron plasmas.

4.1 Electron Production by Photoemission

Prior to 2006 the ATRAP collaboration mainly relied upon a field emission point that would send a high energy 10 nA electron beam that would release lower energy

electrons from atoms that had cryopumped onto the wall and could then be trapped. Typically this would load electrons at the rate of 0.5×10^6 per minute [23]. In our new experiments we typically need in excess of 350×10^6 antiprotons to optimally cool antiprotons, which with the old loading method would have been a nearly insurmountable bottleneck. The loading time for electrons would have been longer than our usual allotted 8 hours of beam time. The group therefore developed a new method of electron loading into high vacuum apparatus by the photoemission of electrons that could reliably produce over 10^6 trapped electrons per second [48].

4.1.1 Experimental Setup

The photoelectric effect first explained by Albert Einstein [49] gave him the nobel prize in physics and with today's commercially available high power lasers, offers us a very good method for loading electrons. Building off of work pioneered in electron lithography [50] we initially set up our electron loading apparatus using a 248 nm KrF excimer laser hitting a thin gold foil evaporated onto a saphire vacuum window. The energy of each photon is simply:

$$E = h\nu = \frac{hc}{\lambda} = 5.0\,\mathrm{eV} \tag{4.1}$$

The work function of gold is 4.2 eV [50], meaning that each of the photons is able to excite an electron out of the metal. The initial tests of this method were done with this setup in a smaller apparatus [48]. When adopting this method to the ATRAP and BTRAP apparatuses a problem was encountered because we frequently needed to load positrons on axis, making it difficult to have a photoemission gold plated window on axis at the same time. Plans were made to use a two dimensional translation stage

[41] to go back and forth between the hole needed for positron admittance and a gold plated window. Unfortunately there were some difficulties in getting the translation stage to work in a robust fashion and several redesigns were required. Furthermore, even if the stage had been working properly it would have been time consuming to continually move the stage on and off axis whenever we wanted to load positrons or electrons.

Luckily, another robust solution was found thanks to the fact that our antiproton degrader at the bottom of our electrode stack is made of beryllium which has a workfunction generally excepted to be 4.98 eV but can range between 3.6 and 5.08 in certain conditions depending on its oxidation [51], putting it below the threshold energy of our laser. Given that we could just use the degrader as our source of electrons without having additional equipment installed, this was our preferred mode of operation in the A and BTRAP apparatuses.

The path for the excimer laser light is shown in Fig. 4.1. The light is produced by a EX5/250 Excimer Laser manufactured by GAM lasers of Orlando, Florida. The laser is placed into an external trigger mode so that we can trigger it by computer control through a DG535 pulse generator with a standard 5 V TTL pulse and usually sends 10 ns $\sim$ 10 mJ pulses. The light enters into the experiment vacuum space in an area above the hat called the "cube" translation stage, whose location is shown in Fig. 4.1a and is shown in more detail in Fig. 4.1b and c. The light strikes two external mirrors that are outside of the vacuum space of the experiment that can be used to adjust the path of the light. The beam passes through a vacuum window and hits a third mirror which sits on a linear translation stage (note this is different than the

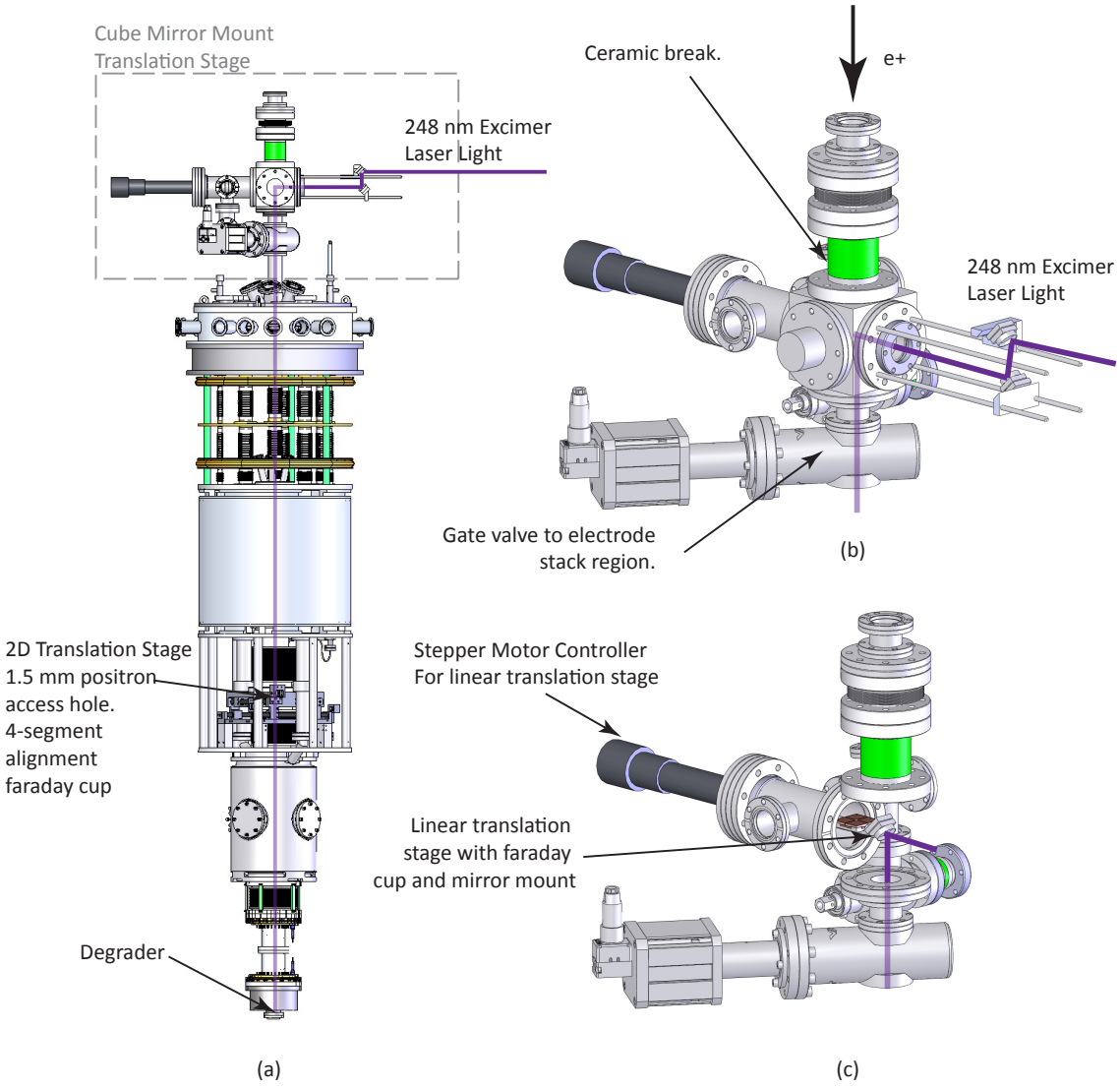

Figure 4.1: Copper and fiber ethernet configuration between experimental zones and work areas.

2-D translation stage mentioned above) that redirects it approximately 90 degrees down to the 1.5 mm hole on the 2-D translation stage where we allow the positrons to pass through.

Surrounding the 1.5 mm hole for the positrons is a set of 4 copper electrodes (faraday cups) that are 4 quadrants of a square that can be used to detect where the beam is being steered. When we have a signal on all four quadrants we can be confident the beam is passing through the 1.5 mm hole. Because the photons are also above the work energy of copper (4.70 eV) when the beam hits these faraday cups when they are biased they will release electrons which we can detect using the methods outlined in 4.3.1. From there the photons proceed down through the upper and lower electrode stacks to hit the degrader where we can apply the proper voltages to trap them. We can tell if the photons are hitting the degrader by the same method we used to detect if they were hitting the faraday cups surrounding the 1.5 mm hole.

4.1.2 Voltage Capture Profiles

Once the photons from the excimer laser are well steered onto the degrader we apply a series of voltages to trap the electrons released from the degrader as shown in 4.2. A strong potential (400 V) is applied to the electrode next to the degrader in order to accelerate the electrons liberated from the degrader away from it. If they are allowed to remain their space charge can impede the further ejection of electrons [48]. When the laser is triggered a positive voltage pulse, using an avtech DC-coupled non-linear pulse amplifier driver, is immediately sent to an electrode that usually has a negative voltage on it down a micro-coax that is 50 Ω terminated and the voltage

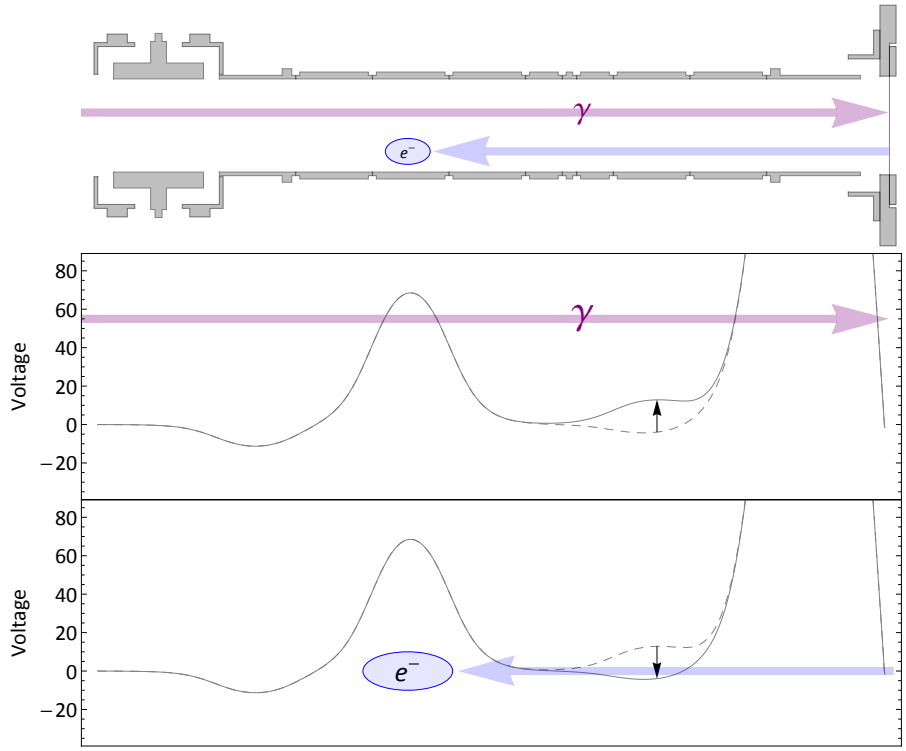

Figure 4.2: Voltage profile for electron capture. 248 nm photons from an excimer laser strike the beryllium degrader. A voltage is pulsed to a positive value allowing the electrons in, but returns to negative before the electrons can escape. The electrons subsequently cool into the deep voltage well.

drops down allowing the electrons to enter. The duration of the pulse (about 1250 ns) is such that the voltage returns to a confining (negative voltage) before the electrons have a chance to escape. The electrons will rapidly cyclotron cool into the deeper well on the central electrode and within a second this procedure can be repeated accumulating more and more electrons in the well.

In 2006 and 2007 the procedure outlined above was always done with a fixed voltage on the electrode that the electrons would be accumulated in. However, we began to see evidence relating to the behavior of our antiprotons, that were being cooled by such electrons, that the electron plasmas may have been heated more than

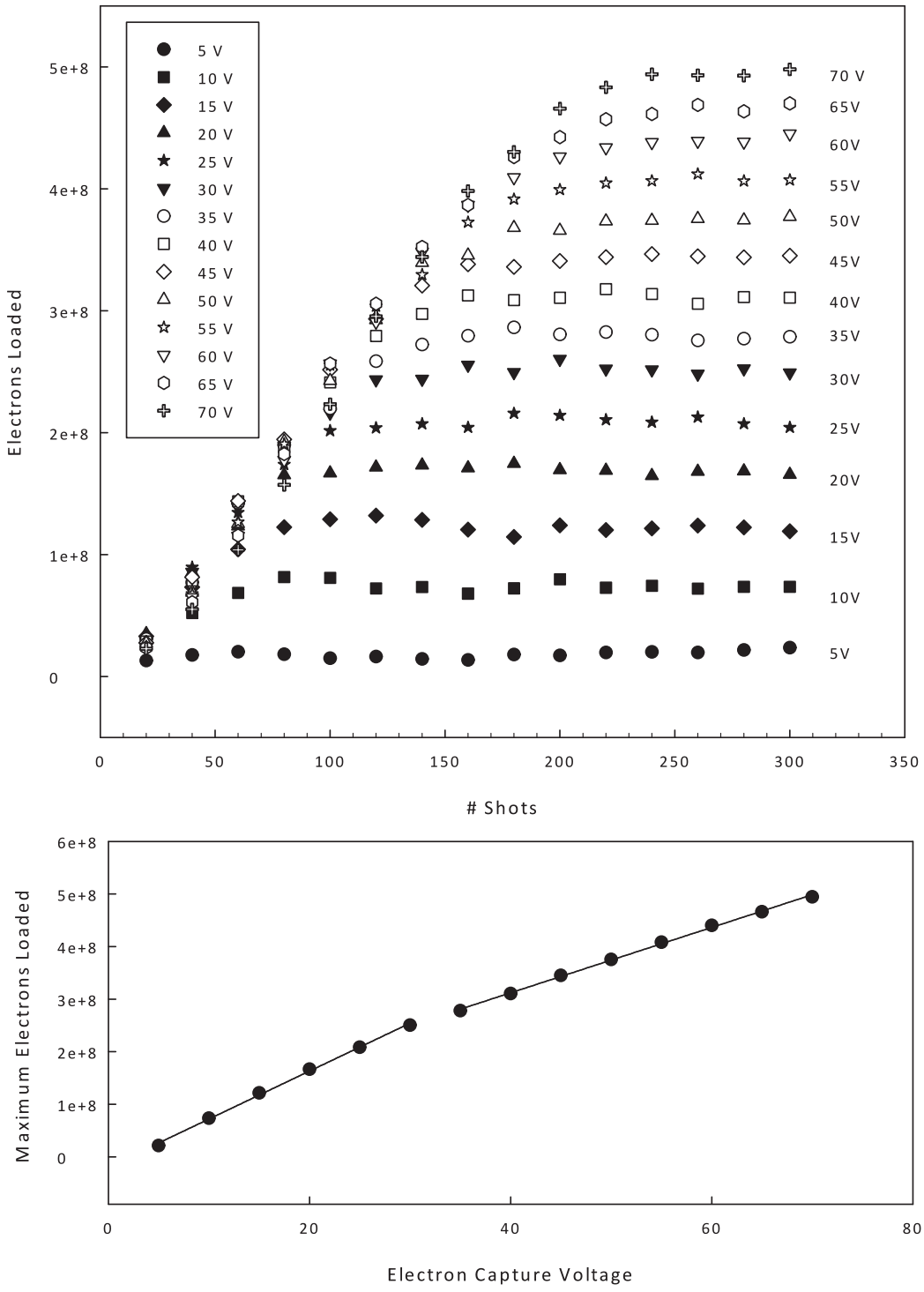

Figure 4.3: Maximum number of electrons loaded into a static well voltage. The voltage indicated is the voltage on the electron capture electrode (LTE2). Under thirty volts the loading is roughly linear at 1.8×10^6 electrons loaded per additional volt in the well. Past 35 volts it is also roughly linear, but with 1.2×10^6 loaded per additional volt in the well.

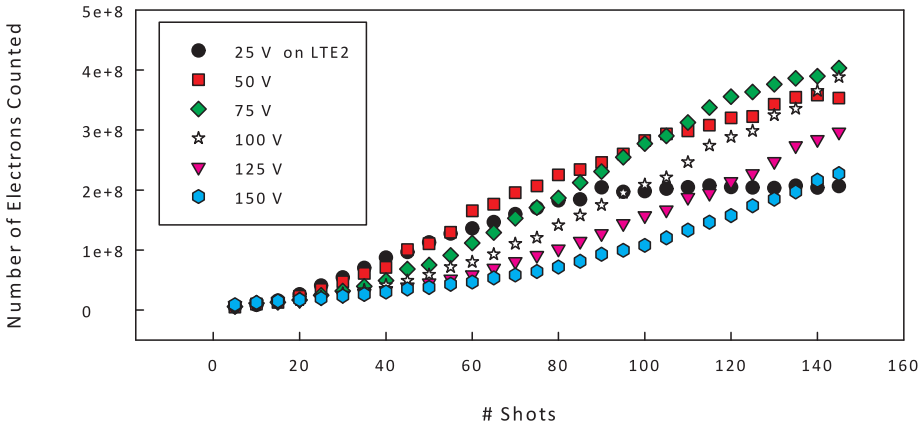

Figure 4.4: Electron load efficiency decreasing at higher voltages.

was desirable. The antiprotons would tend to leave the trap if we didn't let the electrons sit and cool for five or ten minutes in a deep ($>$ 500 V) well after loading. To try to resolve this problem, we began in 2008 loading with a variable voltage on the electron accumulation electrode. For example, the for the first shot, the accumulation electrode would have 1 volt on it, for second shot it would have 2 volts and so on until, after 50 shots it would have 50 volts on it. If we initially began with a well of 85 V, as we had before, the electrons would be going back and forth with 85 eV of kinetic energy which they would have to radiate off before sinking to the bottom of the well. With the gradual increase in voltage scheme, it is believed that the electrons can settle into bottom of the well more quickly and a less heated plasma is obtained.

Once the electrons are loaded, they can be counted out using the methods described in section 4.3. A number of experimental data points have been taken to establish the effect of the different voltage profiles on electron loading. For a static voltage on the electron load electrode (LTE2), the well fills up with a maximum number of electrons beyond which an increased number of laser shots will not lead to

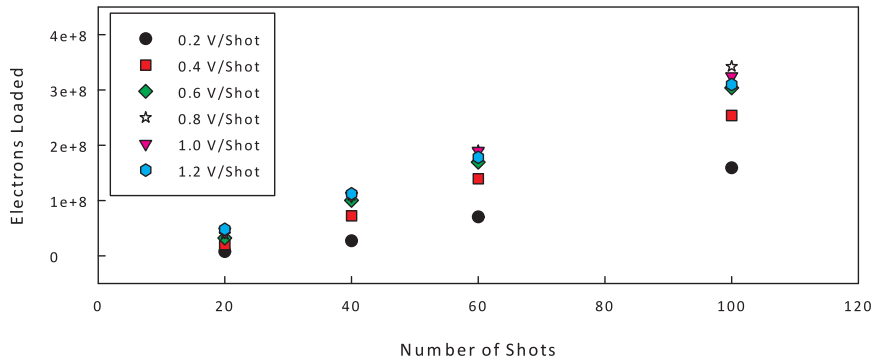

Figure 4.5: Electron loading with a sequentially raising capture potential.

more electrons being loaded. This is shown in Fig. 4.3. Beyond a certain voltage, the number loaded per shot actually begins to decrease as is shown in Fig. 4.4. The number loaded reaches its maximum between 75 and 100 volts, and begins to decrease significantly when the well is at 125 and then 150 V. This may be due to the increased kinetic energy of the electrons in the well leading to instabilities.

The efficiency of loading electrons while sequentially raising the voltage on the capture electrode (LTE2) is shown in Fig. 4.5. The voltage is increased by the same amount after every shot, beginning at the voltage increment above zero. As we can see, more electrons are loaded as we increase the increment per shot until we get to about 0.6 V per shot, at which point little gain in electron loading is seen. This is using our standard laser alignment and intensity. We can imagine that with an increased beam intensity hitting the degrader and electron yield, we could see gains with a larger increment. For most of the 2008 beam run, an increment of 1 V per shot was used. More about our electron loading method and yields has been covered in a previous thesis and paper [41, 48].

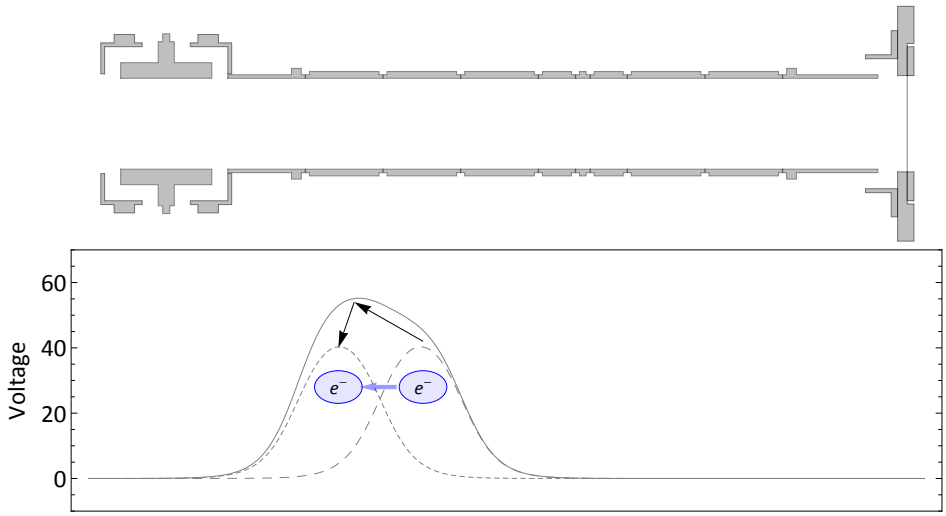

Figure 4.6: Procedure for moving particles from one electrode to another.

4.2 Adiabatic Particle Transfer Technique

Once the electrons or any other charged particle is caught in our penning trap, we can move them to any other electrode in the stack by using an “inchworm" adiabatic moving technique. When particles are located in an electrode A at a voltage $V_A = V_0$, the adjacent electrode B is placed at a voltage $V_B = V_0 + \Delta V$. The voltage in the first electrode is then set to zero $V_A = 0$ and then the voltage is set to the original voltage $V_B = V_0$. This is shown in Fig. 4.6. Typical values are $|V_0| = 50V$ and $|\Delta V| = 10V$. This is usually accomplished with little or no particle loss. Significant particle loss during this procedure is often an indication of some instability within the charged particles being moved.

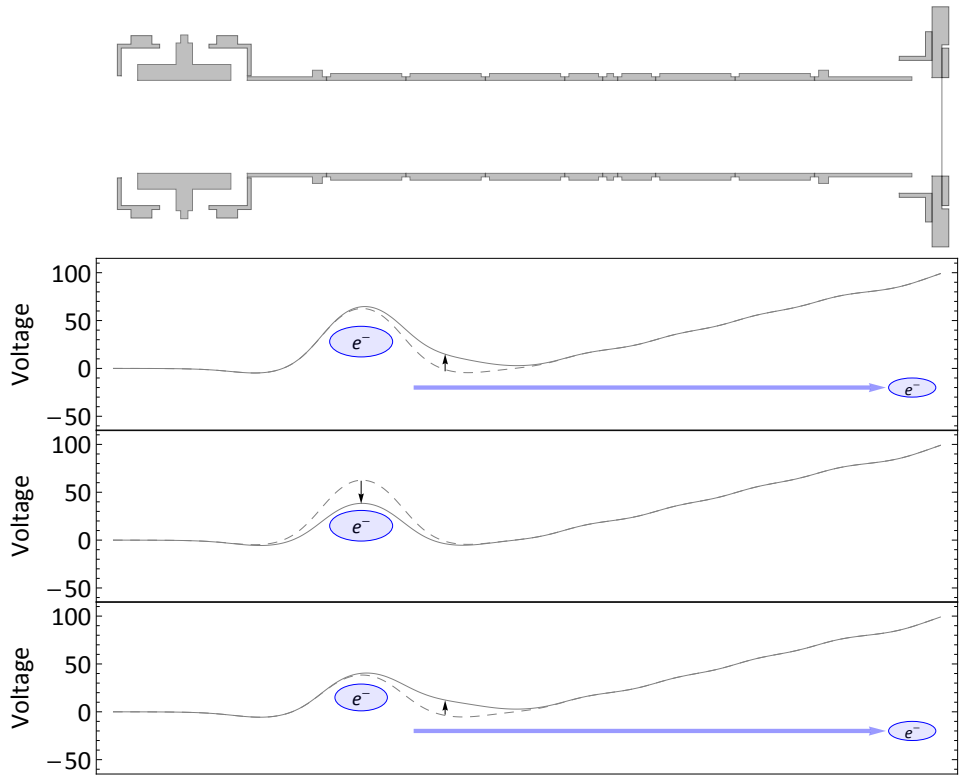

Figure 4.7: Voltages for sequentially charge counting electrons.

4.3 Electron Number Detection Methods

4.3.1 Destructive Charge Counting

A key to enabling the efficient use of the improved electron loading method is to have a reliable, reproducible and rapid method of counting the electrons. Because we are able to load electrons so quickly and reproducibly compared to previous methods, we are able to rely on destructive counting methods knowing that if we dump out and count electrons and then load in the same way we will get a similar number.

To destructively count the electrons, they are loaded into a voltage structure as shown in Fig. 4.7. At a given voltage a side wall on a neighboring electrode is pulsed

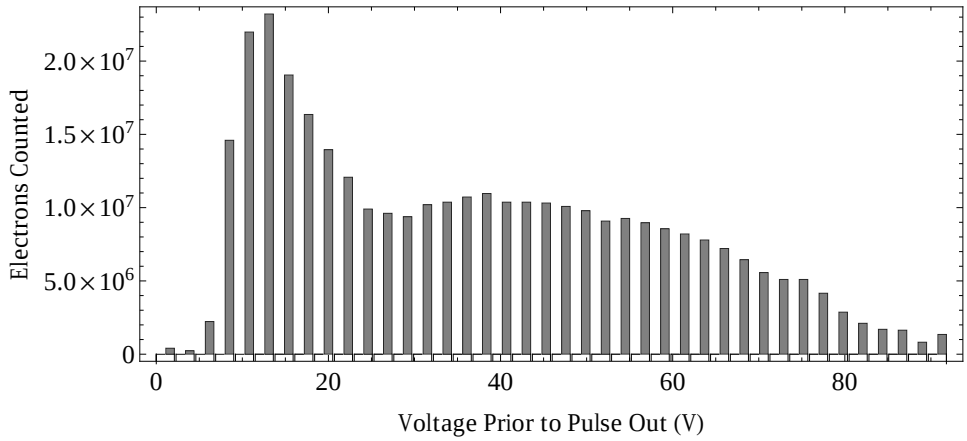

Figure 4.8: Number of electrons counted as a function of voltage, for 340 million electrons.

down typically with a 50 ns pulse, and some fraction of the total electron cloud is sent down onto the degrader where it can be counted. Our counting methods saturate at around 50 million electrons arriving on the faraday cup, therefore to count very big clouds we need to repeat this procedure by pulsing, lowering the well depth by a small amount, and then pulsing again, as shown in Fig. 4.7. The results of such a count out for a total of 340 million electrons is shown in Fig. 4.8. This sort of sequential pulse out procedure can also give us information about the energy distribution of the electrons in our plasma.

When the electrons arrive on the degrader, which in this mode we call a faraday cup, we have set up a dedicated feedback circuit to turn the deposited charge into a voltage that we can read out on an oscilloscope. The crux of the circuit is shown in Fig. 4.9a. The charge arrives into the negative terminal of an operational amplifier which draws no current, so all the charge is deposited on the feedback capacitor C_f, creating a voltage drop $V_f = \frac{q}{C_f}$. The op-amp forces its terminals to be at the

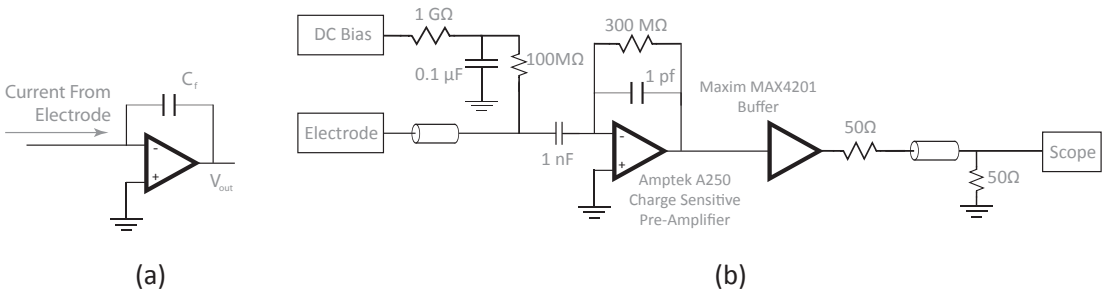

Figure 4.9: Schematic for charge counting circuit. (a) The basic feedback circuit that returns a voltage as a function of the charge. (b) The circuit as it is implemented on the faraday cup electrodes in our experiment.

same voltage, and therefore places its output at $V_{out} = V_f$ so that both of its input terminals are at ground. In this manner, an incoming charge is turned into a voltage. The voltage will be bigger depending on the size C_f which is why for small particle numbers and large amplifications we use a small value $1pF$. This value can be changed if we want to count larger numbers at a time (to raise the amount we can count before the op amp becomes saturated).

The schematic for practically implementing this on our experiment is shown in Fig. 4.9b. An amptek A250 charge sensitive pre-amplifier is used due to its noise and performance characteristics tailored specifically to this use. A Maxim MAX4201 buffer is placed after the A250 output to ensure it can drive the ensuing loads, and a blocking cap must be placed before the input of the pre-amp to ensure that it will not get damaged by the DC voltage placed on the electrode. The cylinders on the diagram indicate where there are lengths (> 1 m) of coaxial cable.

In the modified circuit we cannot ignore the added capacitance from both the coaxial line and the blocking capacitor. The coaxial line can be modeled as just having some capacitance C_{cab} to ground prior to getting to the blocking capacitor

C_{blk}. The initial charge coming into the circuit q will be divided into some q_{cab} which goes onto C_{cab}, and some charge $q_{blk} = q - q_{cab}$ which gets deposited onto the blocking capacitor. The voltage drop across the blocking capacitor will be the same as voltage drop across the cable capacitance, as they are both going to points held at ground. Therefore $\Delta V_{cab} = \Delta V_{blk}$ and therefore $\frac{q_{cab}}{C_{cab}} = \frac{q_{blk}}{C_{blk}}$. But the charge deposited onto the feedback circuit is also $q_f = q_{blk}$, so the relation between the charge read across the feedback capacitor and that actually coming off the electrode q is:

$$q_f = \frac{q}{\left(1 + \frac{C_{cab}}{C_{blk}}\right)} \tag{4.2}$$

Therefore (taking into account the 1/2 voltage divider on the output) the voltage read at the scope will be:

$$V = -\frac{Nq}{2C_{eff}} \tag{4.3}$$

Where the modified capacitance is defined as:

$$C_{eff} = C_f \left(1 + \frac{C_{cab}}{C_{blk}}\right) \tag{4.4}$$

The important conclusion here is not so much the exact reliance of C_{eff} on C_{cab} and C_{blk} as it is hard to establish those with great precision. What is important is that the entire circuit in Fig. 4.9b can be treated like the simpler circuit in Fig. 4.9a by just replacing C_f by C_{eff} and accounting for the voltage divider. C_{eff} is determined experimentally but placing several known amounts of charge into the circuit and reading the voltage off of a scope trace.

Two scope traces are shown in Fig. 4.10 utilizing this method. Fig. 4.10a shows the signal coming from the degrader for when a shot of excimer laser photons strike the degrader, causing approximately 16 million negative charges to leave the degrader.

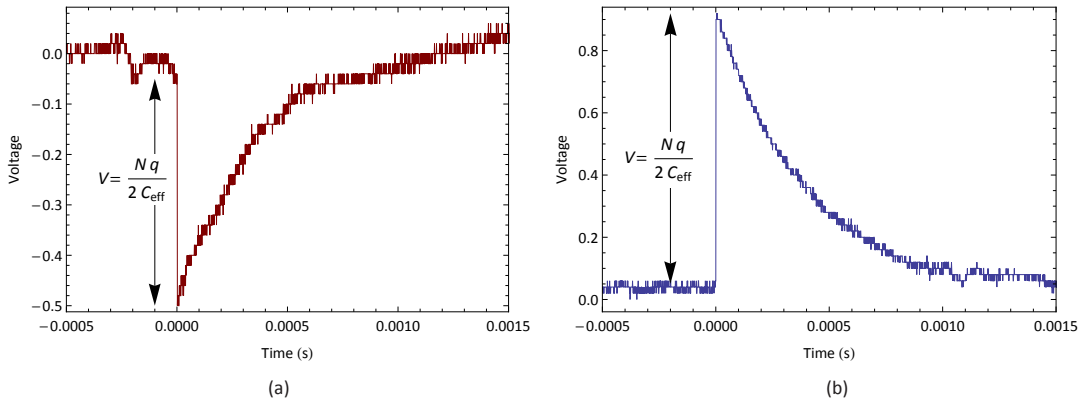

Figure 4.10: Scope traces for electrons leaving and being counted on the degrader.

Fig. 4.10b shows approximately 30 million electrons being dumped onto the degrader generating an opposite sign voltage.

4.3.2 Resonant Axial Motion Detection

In previous ATRAP antihydrogen experiments there would be far smaller electron clouds ($<$ 10 million), and a different method of nondestructive electron number detection was used, employing the interaction between the axial motion of the electron cloud and a resonant tuned circuit [23]. More about such resonant circuits and their amplifiers will be discussed in chapter 7. When no electrons are present the tuned amplifier circuit forms a response that can be seen on a spectrum analyzer that has a Lorentzian lineshape. When the axial frequency of the electrons is brought into resonance with the tuned circuit by adjusting the voltage on their confining electrode, two peaks are created rather than one. For smaller values of N (typically below 8 million in the old apparatus), the spacing between the two peaks is proportional to $\sqrt{N}$. However, for larger numbers this $\sqrt{N}$ this dependence breaks down and the

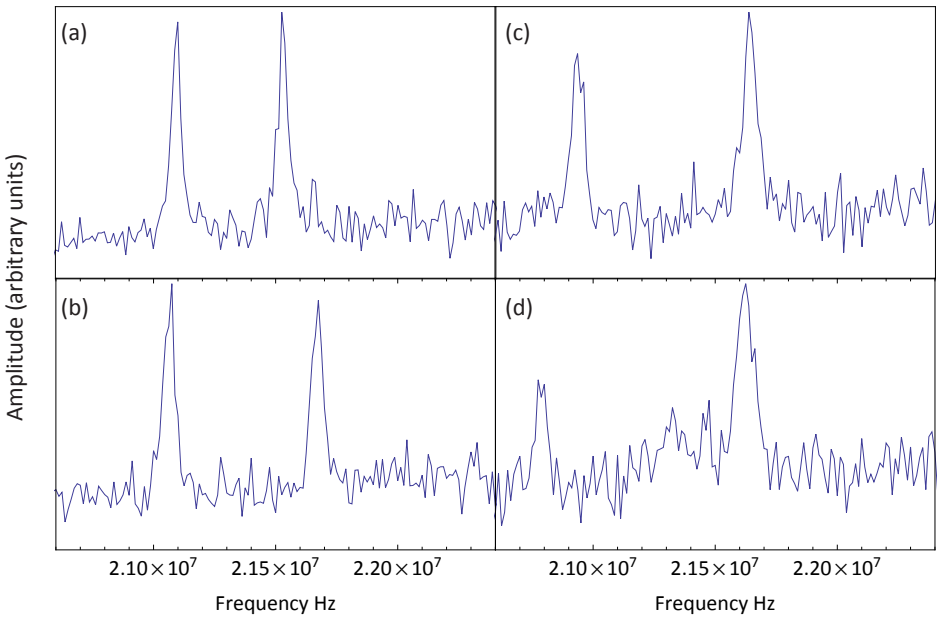

Figure 4.11: Electron axial motion response on tuned circuit amplifier. (a) 19.2 million (b) 44.4 million. (c) 79.1 million (d) 112.8 million electrons.

separation increases less and less with greater numbers, and the number can even become a double valued function of the frequency, depending on the damping rate of the axial motion [52].

Therefore, applying this non-destructive method is significantly more complicated for our large electron plasmas than it has been for the smaller numbers in the past. Having a second method of determining the number of electrons or positrons in our apparatus would be useful, however, in providing a nondestructive method of counting our positrons which take significantly longer to load. It could also provide a confirmation of our destructive positron charge counting procedure, which requires the successful suppression of secondary electrons. The procedure would be to form a number vs. frequency separation plot for both positrons and electrons, and see that they give similar results. While lengthy resonant electron studies have not been

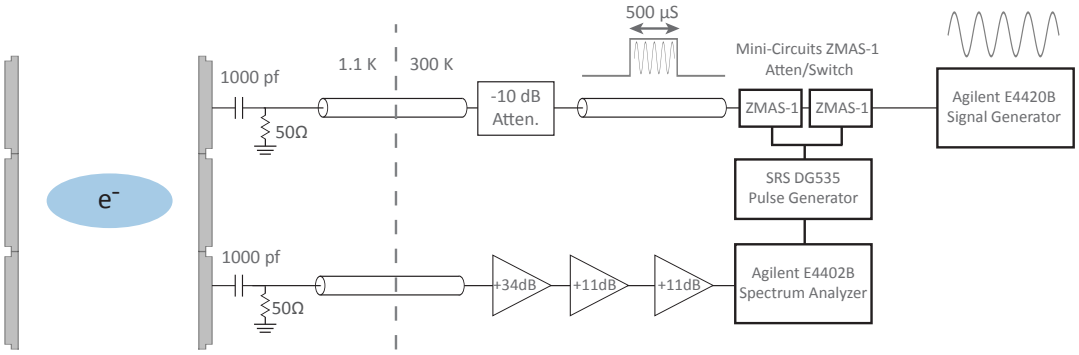

Figure 4.12: Configuration for pulsed/ free induction decay plasma mode analysis.

conducted in this apparatus, such resonant signals shown in Fig. 4.11 for different electron cloud sizes have been observed paving the way for further study.

4.4 Electron Plasma Studies

The rapid and efficient means of loading and counting a chosen number of electrons into our apparatus opens the way for us to do many plasma measurements exploring the phenomena described in section 2.4. As was described in that section, in a quadrupole potential we only need two of the parameters N, n_0, R_p, Z_p, ω or α in order to also determine the rest of them. Our electron charge counting method gives us a means of determining the total number N in our trap. To establish the second parameter we measure the frequencies of both the center of mass $l = 1$ mode and quadrupole mode $l = 2$ and use (2.78) and (2.81) (whose solutions are shown in Fig. 2.13) in order to determine the aspect ratio. The following section describes the most efficient method we have found to measure these frequencies, and presents some results.

4.4.1 Free Induction Decay Detection Method

The setup for using the free induction decay (FID) method to measure the plasma mode frequencies is shown in Fig. 4.12. The experiments have been conducted on endcap ($\rho_0 = 0.849 z_0$) length electrodes in the lower stack. The plasma modes are driven using an Agilent E4420b signal generator that outputs a continuous wave frequency. This signal is sent to an electrode above the well where we are storing the electrons. The signal from the electrode below the electrons is sent through several amplifier stages into a spectrum analyzer that is set to only measure the output of a single frequency (zero span mode). In this mode, the spectrum analyzer provides a time vs. amplitude output much like an oscilloscope but only at the frequency it is programmed to look at. In order to avoid having small signals get drowned out by the output of the function generator the signal gets truncated through the use of two rapid mini-circuits ZMAS-1 attenuator/switches that are controlled by a pulse generator. The idea is that for a brief period of time the plasma is being driven, and then after the input signal sharply drops off we will still be able to see the plasma decay from its excited oscillations, hence the name "free induction decay" measurement.

When we are looking for the different modes of the plasma our procedure is to set the signal generator to emit a particular frequency and for the spectrum analyzer to be on zero span mode at the same frequency. A pulse generator closes the two switches for a period of around 500 μs and also triggers to acquisition on the spectrum analyzer, whose output is logged on our computer. This procedure is then repeated at a higher frequency so that we can step through the region of interest looking for the modes.

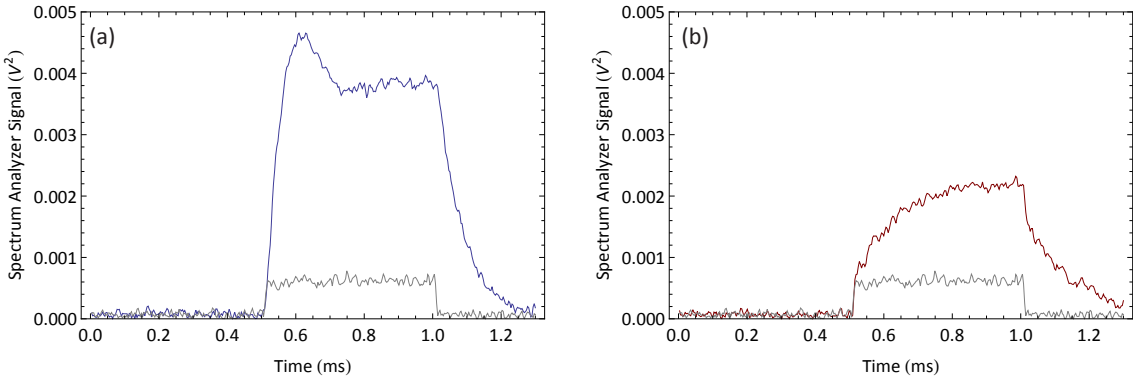

Figure 4.13: The free induction decay plasma response on a spectrum analyzer in zero span operation for (a) the center of mass $l = 1$ mode and (b) the quadrupole $l = 2$ mode. In gray on each plot is shown the no plasma response driving amplitude from the signal generator

The output of a single frequency zero span mode spectrum analyzer trace is shown in Fig. 4.13. On each of the figures the signal generated by the signal generator that is read on the spectrum analyzer when there are no electrons or we are not near a mode is shown in lighter gray. The response of the particular mode ($l = 1$ center of mass in Fig. 4.13a and $l = 2$ quadrupole is shown Fig. 4.13b). The response which occurs while the driving signal is on is called the transmission response, the tail and ring down afterwards is the free induction decay. Sample response at different frequencies for the two is shown in Fig. 4.14, the free induction decay amplitude (the amplitude at a specific time after the end of drive pulse of an exponential fit to the decay) is shown in the solid line, and the transmission response is shown in the dashed line. Lorentzians are fit to the response profiles and the frequencies of the modes are taken to be the center of the Lorentzian.

Using this technique we are able to record the quadrupole and center of mass mode frequencies for our plasmas under different parameters. This then allows us to

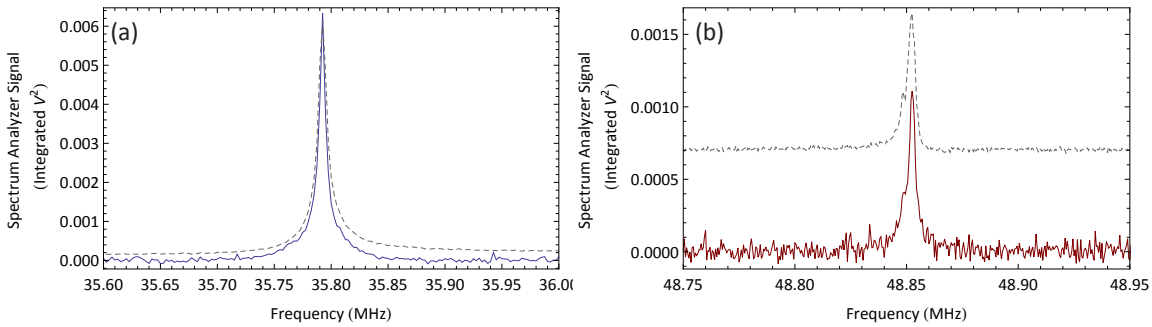

Figure 4.14: The free induction decay and transmission plasma response vs. drive frequency. The FID decay amplitude is shown in the solid line and transmission response is shown in the dashed line for typical (a) center of mass $l = 1$ mode and (b) quadrupole $l = 2$ modes.

calculate other parameters such as the density and the aspect ratio, using equations (2.78) and (2.81) that are valid for spheroidal plasmas in an ideal quadrupole potential. In reality our potential differs from the ideal quadrupole case, and the plasma mode frequencies correspond to slightly different shapes. To get more accurate results a numerical calculation using equilsor and rattle codes discussed in section 2.4 is required. The ideal quadrupole approximation gives us a good approximation to what our plasmas are doing, however, especially when they are not near the electrode boundary.

Fig. 4.15 show the results for varying the electron number, voltage and magnetic field for electrons in a 3 electrode endcap length potential in the lower stack. In each of these studies the electrons have been loaded using the variable voltage well method described in 4.1.2 with an increment of 1 volt per shot from the excimer laser. The number study was done by reloading different clouds of electrons. The voltage and magnetic field studies were performed with a single cloud each, changing the parameter and remeasuring the frequencies. It should be noted that the cloud

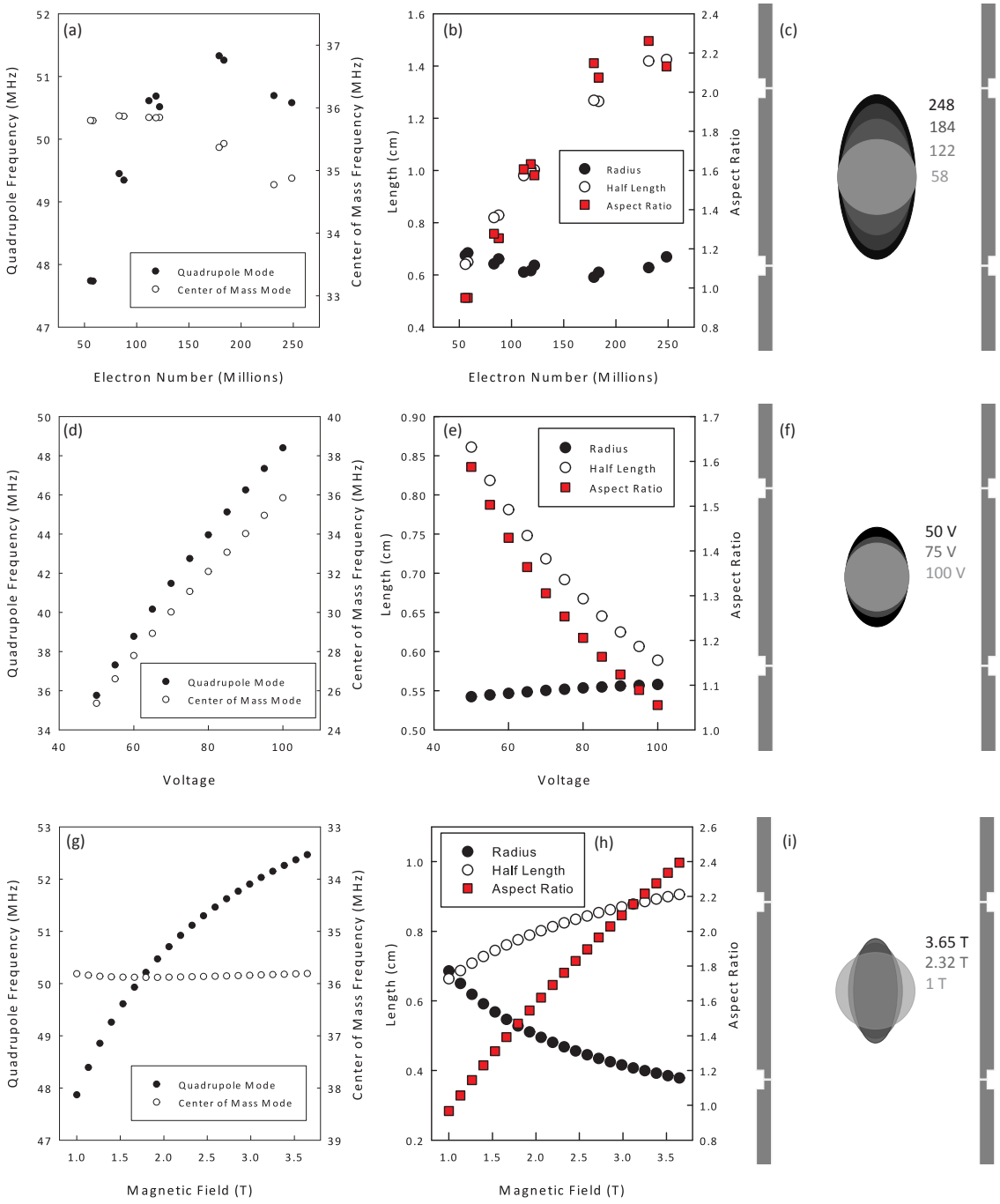

Figure 4.15: Plasma parameter measurements through mode analysis. (a) Frequencies measured for electron clouds at 1 Tesla in a 100 V well in a 3 endcap length electrode configuration. (b) calculated cloud dimensions assuming a spheroid and (c) visual representation of the shape of our clouds (millions of electrons). (d), (e) and (f) show the same for a cloud of 38.4 million electrons at 1 T while varying the voltage. (g), (h) and (i) show the same for a cloud of 60.8 million electrons in a 100 V well while varying the magnetic field.

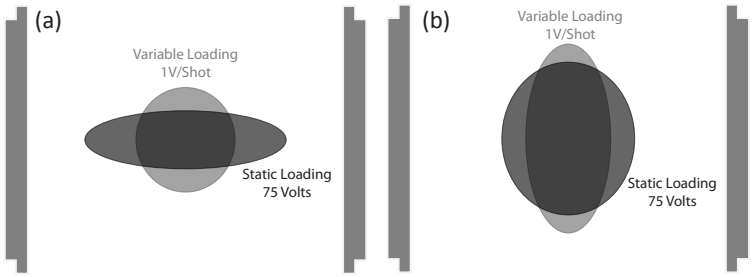

Figure 4.16: Effect of variable vs. static voltage electron loading on plasma shape.

shape does seem to depend on the alignment of the laser onto the degrader. For the same conditions but after having realigned the laser, we have had clouds with very different aspect ratios. This should not be too surprising, as electrons ejected from the degrader at different radii lead to different orbits when they are trapped.

For a given laser alignment we are able to discern some properties of our plasmas from the studies shown in Fig. 4.15. When we load larger numbers of electrons, the effect is to stretch the plasma out axially rather than radially (Fig. 4.15a-c). Increasing the voltage on confining electrode reduces the axial length of the plasma, but largely leaves the radius unchanged (Fig. 4.15d-f). Increasing the magnetic field decreases the radial extent of the plasma, and increases its axial extent moving it from a spherical to more of a cigar shape (Fig. 4.15g-i).

The shape of our electron clouds also seems to depend on the voltage profile we use to load the electrons. When using a static 75 volt well loading 40 million electrons and then lowering the well to 100 V and measuring the plasma modes, we found l=1 and l=2 frequencies corresponding to an aspect ratio of 0.29 - a disk. When loading with a variable 1 V/ excimer shot method also giving us 40 million (which took 20 shots) and lowering the well to 100 V we found frequencies corresponding to an aspect

ration or 1.06 - very close to a sphere. When this experiment was repeated for 110 million electrons, similar but less pronounced effects were seen with an aspect ratio of 1.15 compared to 2.2. These are shown in Fig. 4.16.

4.4.2 Temperature Dependent Plasma Effects

The presence of our 1 K pot system, as outlined in 3.2.2, gives us a means of varying the temperature of our electrode stack between 1.1 K and 4.2 K. The temperature of the liquid helium inside the 1K pot, and therefore the electrode stack that is thermally coupled to it, is a function of the pressure inside the pot. If we want to increase the temperature of the apparatus we just need to pressurize the 1K pot with helium gas, and if we want to decrease the temperature we simply resume pumping on it. We have temperature sensors both on the 1 K pot as well as on the upper and lower electrode stack so we are able to monitor the temperature as we apply this procedure. While doing this we can also monitor the center of mass $l = 1$ and quadrupole $l = 2$ frequencies of our plasma. Dan Dubin has worked out a theory for the temperature dependence of the quadrupole ($l = 2$) mode frequency in the case of an ideal quadrupole potential [38, 37] that was given in equation (2.83). This formula depends on the aspect ratio, which in turn can be established by also measuring the center of mass mode and using (2.78) and (2.81) to establish α.

Both the quadrupole mode and center of mass mode for our plasmas have a time dependent drift even at a fixed trap temperature, as shown in Fig. 4.17 for a plasma that is very close to spherical with an aspect ratio of 0.96. The drift is close to linear and small but significant changes can be seen in the drift of the quadrupole mode as

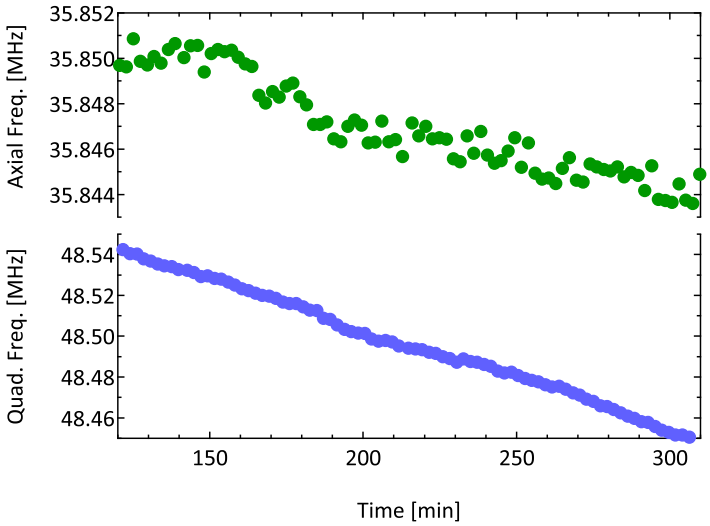

Figure 4.17: The drift of the quadrupole and center of mass modes over time for a plasma with $\alpha = 0.96$

the temperature in the electrode stack is changed. By fitting a linear curve to the data prior to and after this temperature change and subtracting it out we can obtain a drift in the quadrupole frequency associated with the temperature change.

For a perfect spheroidal plasma in an ideal quadrupole potential, this drift should be characterized by the theory referenced above in equation (2.83). However given our non-ideal quadrupole potential and the effect of the image charges on the electrodes a numerical calculation involving the rattle and equilsor code should present a more accurate result. The rattle code will take into account the effect of temperature on the plasma. As predicted in the theory, the temperature dependence should be proportional to the square of the change in quadrupole frequency. Output from rattle from temperatures ranging from 25 K to 1000 K confirm this. We extrapolated this same trend down to the 1 to 4.2 K temperatures, giving us a frequency shift vs. temperature function over that region for a given cloud shape.

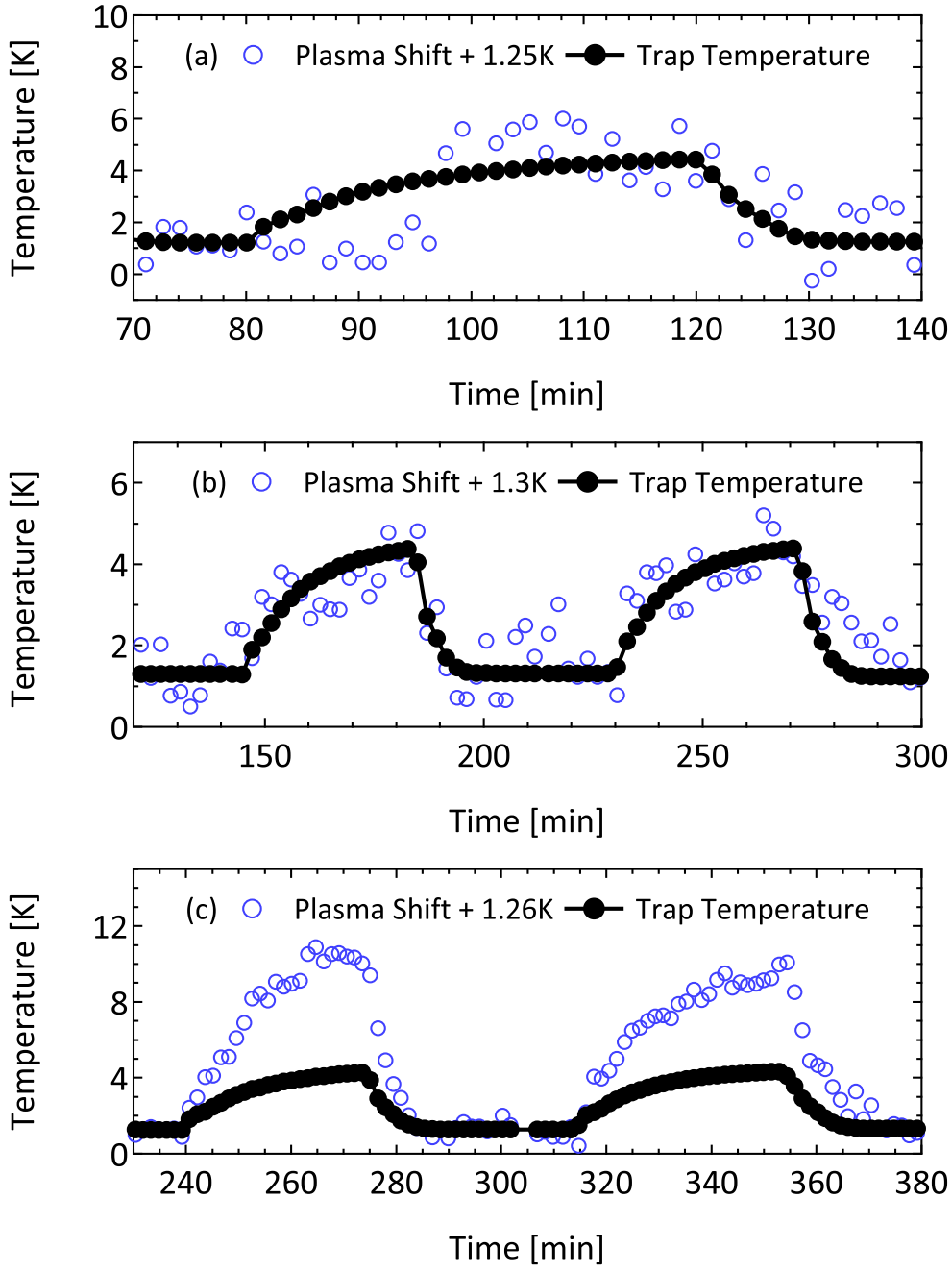

Figure 4.18: Results of temperature dependence of the quadrupole frequency shifts from 1.2-4.2 K for three plasma shapes. (a) $\alpha = 1.39$ (b) $\alpha = 0.96$ and (c) $\alpha = 0.48$.

Using this quadrupole frequency shift vs. temperature function we plotted the temperature derived from the plasma against the recorded temperature of the electrode stack for three different cloud shapes, shown in Fig. 4.18. The experiment conducted for a cigar shaped (axially extended) plasma (aspect ratio=1.39) is shown in Fig. 4.18a, for a sphere like plasma (aspect ratio=0.96) in Fig. 4.18b and for a disk like plasma (aspect ratio=0.48) in Fig. 4.18c. In all three plots we have assumed that the plasma started at the base temperature of the electrodes (indicated in each plot), but the theory and calculation only tells us about shifts and not absolute temperature. We can see the agreement is very good for the sphere case, also good for cigar case, but seems to be off by nearly a factor of three in the case of the disk like plasma. At this time, we do not understand the discrepancy on this last result.

The key finding of these experiments, however, is not so much in the scale of the temperature shift in the plasma, but in the encouraging result that the plasmas seem to equilibrate with changes in the temperature of the electrodes fairly rapidly (on the scale of minutes). This is a promising sign that we will be able to obtain electron and positron plasmas, and thus sympathetically cooled antiproton plasmas that approach the base temperature of our apparatus. This is a crucial step for trapping antihydrogen, as its temperature when formed will be bounded by the temperature of the charged particles that form it. These experiments remain preliminary, as we did not have enough time during the 2008 beam run to conduct further studies, but more information on this phenomena should be uncovered soon.

Chapter 5

Antiprotons

Antiprotons are the antimatter counterpart to protons and the two particles are predicted to have the same mass and opposite charge. The comparison of their charge to mass ratios has been confirmed down to 9 parts in 10^{-11} [53]. The existence of the antiproton was predicted by Dirac in 1931 [54] and was discovered in 1955 by Emilio Segrè and Owen Chamberlain at the University of California, Berkeley [55]. The first capture of antiprotons in a Penning trap was accomplished at the European Center for Nuclear Research by Gerald Gabrielse and collaborators in 1986 [56], and the first electron cooling of antiprotons below 0.1 eV was accomplished in 1989 [57]. Using and improving on these techniques we are able to trap, store and cool more than 10^6 antiprotons in our apparatus. This has been a challenge as we have had to operate at lower fields (1 T) then previous experiments (5-6 T). We have incorporated a field boosting solenoid in the antiproton trapping region to improve our catching efficiency. This chapter will describe the production, trapping and detection of antiprotons for our experiment.

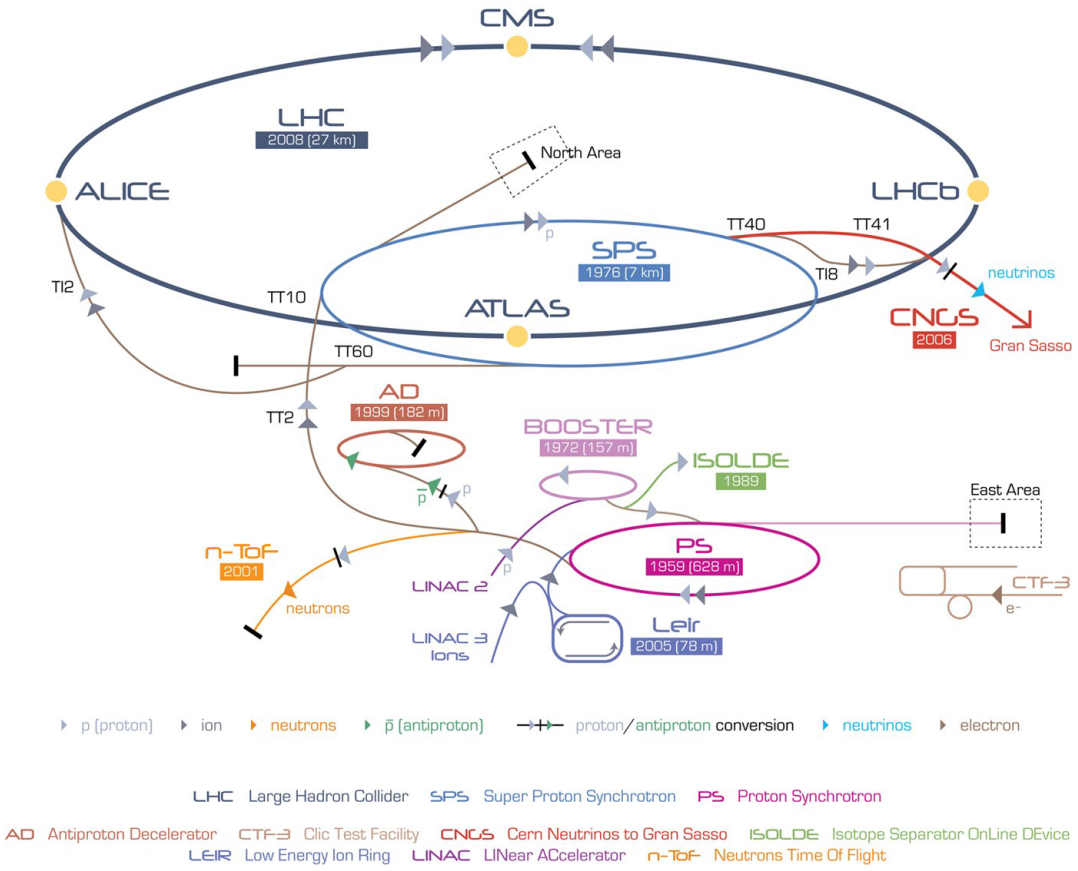

Figure 5.1: The CERN accelerator complex (copyright CERN).

5.1 Antiproton Production at CERN

5.1.1 Proton Synchotron Accelerator Complex

Antiprotons are the reason our experiment is conducted at CERN, the European Center for Nuclear Research. It is the only facility in the world that produces antiprotons at a low enough momentum (100 MeV/c) for us to trap. The full accelerator complex at CERN is shown in Fig. 5.1 but producing antiprotons does not require the energies produced by either the Super Proton Synchotron or the Large Hadron

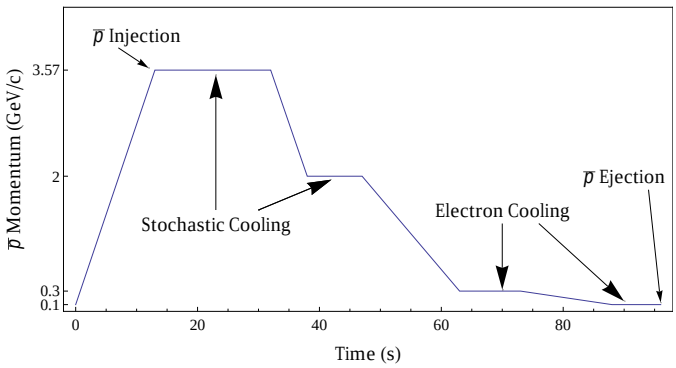

Figure 5.2: The cooling cycle for antiprotons in the antiproton decelerator.

Collider, and thus we receive the beam before it enters these larger accelerators. Protons are produced from ionizing hydrogen and sent into a linear accelerator, then into a small synchotron called the booster, before being sent to the Proton Synchotron and are then accelerated up to a momentum of 26 GeV/c. Then approximately 1.5×10^{13} protons strike an Iridium target creating 5×10^{7} antiprotons, a yield ($\bar{p}/p$) of 3.5×10^{-6}, or one $\bar{p}$ for every 285,000 protons [58]. The momentum of the antiprotons upon leaving the target is 3.5 GeV/c, at which point they are directed into the antiproton decelerator.

5.1.2 Antiproton Decelerator

The antiproton decelerator takes the antiprotons from 3.5 GeV/c down to 100 MeV/c in a series of four cooling steps over approximately 100 seconds (shown in Fig. 5.2), although this time changes slightly from year to year depending on accelerator performance. The actual deceleration of the particles is accomplished with RF cavities that apply a time changing field to slow down the antiprotons, just as they are used to increase the speed of particles in a normal accelerator. As the longitudi-

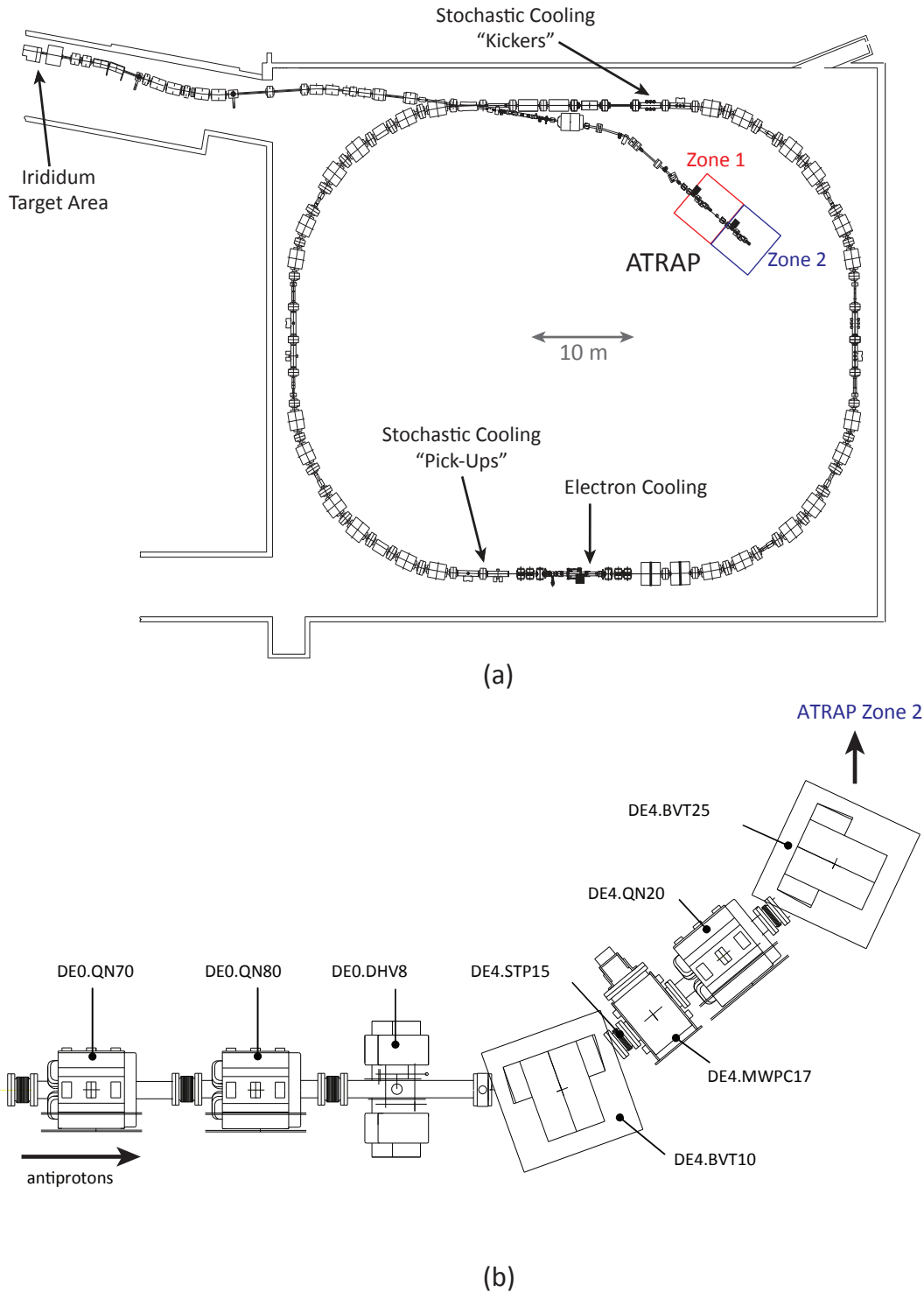

Figure 5.3: (a) The antiproton decelerator ring and (b) the ATRAP zone 2 beamline.

nal velocity is decreased, there is an accompanying increase in the transverse spread (emittance) of the antiprotons, which must be corrected at 4 times during the cooling cycle. At higher energies this is accomplished through stochastic cooling, where a series of pickups on one side of the ring detects the emittance profile of the beam and sends a correction signal to kickers on the other side of the ring prior to the beam arriving there. At lower energies, the transverse energy of the antiprotons is reduced through electron cooling where a beam of electrons proceeding longitudinally is sent along parallel to the antiproton beam. Because they have no transverse momentum, any collisions between the electrons and the antiprotons will cause the antiprotons to lose transverse momentum. After two stochastic cooling cycles and two electron cooling cycles, the antiprotons are kicked out onto a beam line that goes out to our experiment.

A diagram of the AD with the target ATRAP zones, electron and stochastic cooling locations is shown in Fig. 5.3a and the different steering magnets leading up the ATRAP zone 2 are shown in Fig. 5.3b. In order to properly steer the beam up into our apparatus, we are given remote control over the currents going through a series of horizontal and vertical bending magnets, as well as focusing quadrupoles so that we can maximize the number of antiprotons that we catch in our trap. We can also control the placement of wire chambers into the beamline in order to see how the beam is steered further up the line. The closest one to our zone (DE4.MWPC17) is shown in Fig. 5.3b. Once past the last wire chamber, we must rely on our own detection methods to guide the beam.

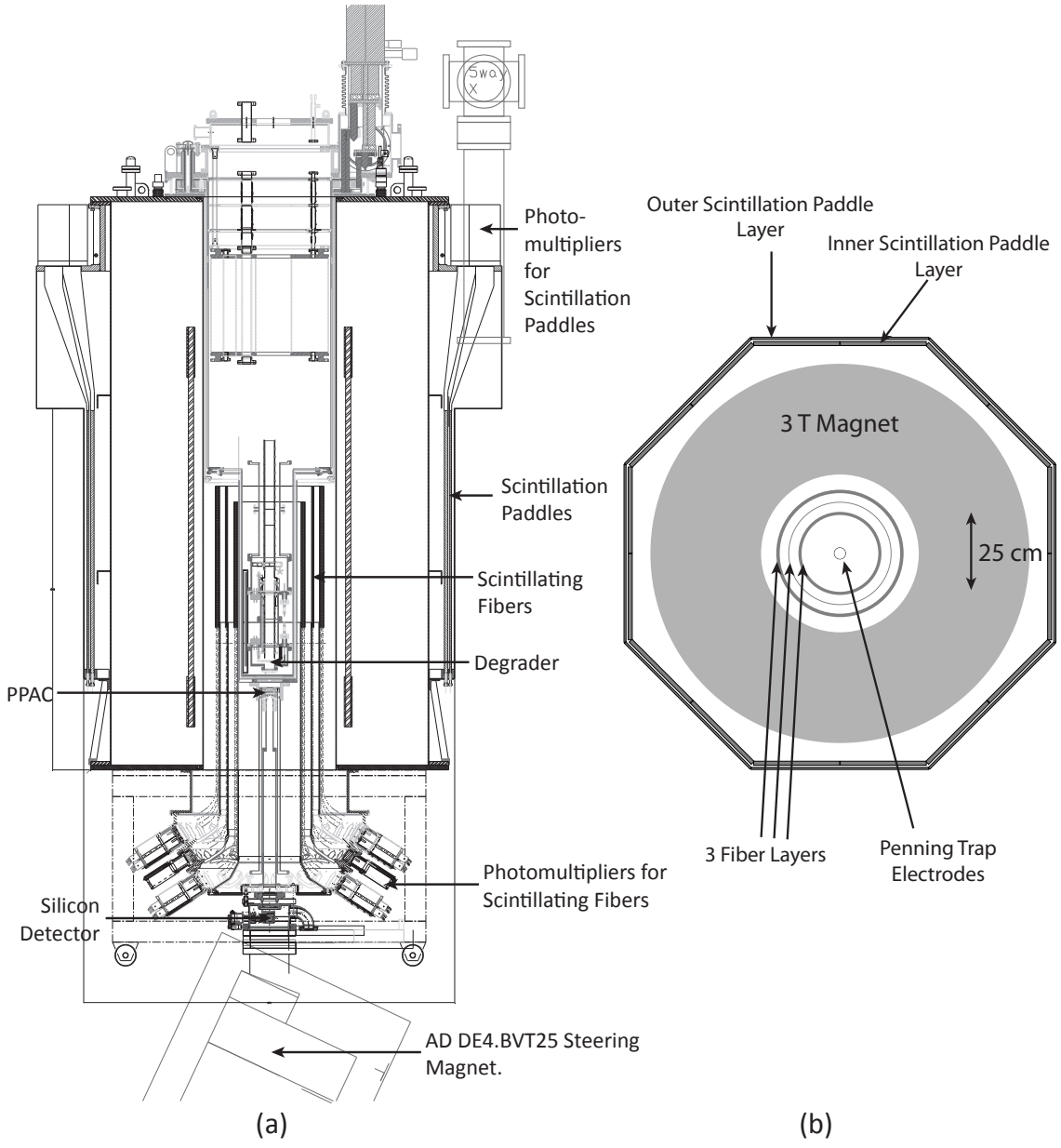

Figure 5.4: The ATRAP zone 2 antiproton annihilation and beam detector locations. (a) Side view and (b) top view.

5.2 Antiproton Beam and Annihilation Detection

The ATRAP setup for detecting the antiproton beam and annihilations is shown in Fig. 5.4. In order to steer the beam we make use of the signals coming from a silicon detector and a parallel plate avalanche counter (PPAC). In order to detect antiproton annihilations we use a series of scintillating fiber detectors and scintillation paddle detectors.

5.2.1 Silicon Detector and PPAC

Once the antiproton beam is past the last AD wire chamber, the silicon detector is our first guide to indicate where the beam is steered. It is located just above the last CERN bending magnet and about half a meter below the next detector, the PPAC, and the beginning of our electrode stack. It consists of silicon semiconductor diodes whose charge carriers will be freed when the charged particle beams passes through the material. This current is deposited across a 100 Ω resistor and the voltage is read out on an oscilloscope triggered by the beam arrival. The detector is mounted on the face of a cube. Using a motor mounted on a vacuum port controlled from outside the experiment we rotate the cube and thus move the detector in and out of place. It is a five piece 15 μm thick detector that has four quadrant pieces surrounding a central circle which blocks the path to the stack. Originally we had another four piece detector 200 μm thick which had a circular hole in the center to allow the antiprotons to go through while in use. It was found that this would clip some of the beam so it was removed and a larger hole put in its place.

The parallel plate avalanche counter is the next means we have of determining

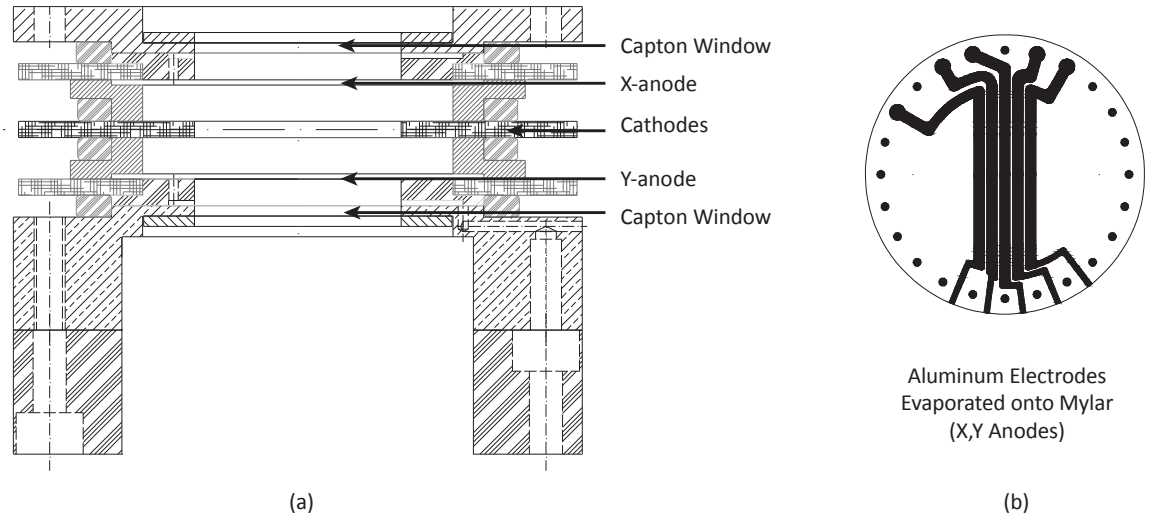

Figure 5.5: The parallel plate avalanche counter (PPAC). (a) A cross section view of the different pieces. (b) A top view of the pieces that make up the X and Y anodes, rotated 90 degrees from each other.

the path of the antiproton beam. A drawing of the cross section of the PPAC is shown in Fig. 5.5. A region is enclosed by two capton windows so that argon gas at atmospheric pressure can be flowed into it. It contains a central cathode, held at ground and two anodes above and below it that are biased to a positive voltage of 70 volts. The anodes are composed of 5 aluminium strips evaporated on a mylar foil, 2 mm wide and spaced 0.5 mm apart as shown in Fig. 5.5b. They are rotated 90 degrees from each other, so on the top anode they are oriented in the "X" direction and on the bottom anode they are in the "Y", with the path of the antiprotons and the axial magnetic field direction being labeled "Z". When the antiprotons pass through the argon gas they ionize electrons off of the atoms, and due to both the magnetic field and the electric field running vertically from the cathode to the anodes, the electrons will head nearly straight along the Z direction and get deposited on the electrode strips on the X or Y anode. This current is then passed through a resistor, whose

voltage is monitored on a scope triggered off of the antiproton pulse. By monitoring the signal on each of these strips separately we are able to tell where the antiproton beam is striking the PPAC.

Referring to our device as a PPAC is a little misleading, as we are not actually operating it in avalanche mode. If we increase the bias on the anodes sufficiently, the electrons ionized from the argon will gain enough energy to ionize other electrons before striking the electrode and an exponential (avalanche) increase in the signal is obtained [59]. We are able get a sufficient signal without turning to this avalanche mode, so we just keep the voltage low enough to keep it in a linear mode [28].

5.2.2 Scintillating Fiber and Paddle Detectors

An extensive discussion of the ATRAP detector setup of scintillating fibers and scintillation paddles for detecting antiproton annihilations has been presented in a thesis written by one of our collaborators from the Jülich research center in Germany [1] and further discussion regarding calibrations, efficiencies and uses of the detectors for our experiments has been given in a previous thesis in the Harvard group [41]. Therefore, only a brief summary of the setup and operation of this system will be given here.

The annihilation of an antiproton with a proton inside a nucleus can lead to many different combinations of particles, but on average it leads to the creation of two neutral and three charged pions [60]. When a charged particle crosses the core of the scintillating material it emits photons which follow down the length of the fiber or the paddle to a photomultiplier where the signal is amplified and read out as a voltage.

The scintillating fiber system consists of ten concentric cylinders grouped into three cylindrical frames (shown in Fig. 5.4). The fibers consist of a core material of polysterene with an acrylic cladding with a diameter of 3.6 or 3.8 mm depending on the layer. As the cross section of the fiber is round, a single layer would not have a uniform detection efficiency as there would be a variable amount of material that a particle would go through as it crossed the fiber, depending on its distance from the center. To correct for this the fibers are always placed in groups of two layers, properly offset, to guarantee a more uniform efficiency across the circumference.

There are a total of 5 sets of double fiber layers like this. The inner cylindrical form consists of two straight layers of fibers, and two helical sets which spiral around the trap axis at around 50° inclination. The coincidence between a straight fiber and helical fiber can give spatial resolution for where the particles crossed the detector, as they intersect in only one place. The middle cylindrical form consists of two straight fiber layers. The outer form, like the inner form, has two sets of straight fibers and two sets of helical fibers.

The full set of fiber detectors can be left in place when we are using the ATRAP apparatus, the version of our experiment that does not have either a Ioffe trap or a field boosting antiproton solenoid. By acquiring the spatial location of where the charged particles struck all three layers of the fibers, we are able to reconstruct the path of the particle and determine where the annihilation must have happened on the electrode stack. This is called "vertex detection". However, when we are using the BTRAP apparatus, which does have a Ioffe trap which takes up much more radial space, we can only leave the outermost fiber form in place. For most of 2006 and all

of 2007-2008 we only had the outer fiber form in place.

There are 24 scintillating paddle detectors arranged in an octagon in two layers outside of the superconducting magnet (see Fig. 5.4). The inner layer consists of two paddles per octagon side (for a total of 16) and the outside layer consists of a single paddle per octagon side.

Both the fiber and paddle detectors have their outputs binned into 40 ns increments. When a signal arrives to the photomultipliers it is put past discriminators and if it is significantly high it registers as a count for that particular channel, in that time bin. The signals are grouped in a number of different ways. For the case where only the outer fiber cylindrical form is present, the standard ones are as follows: a "fiber single" count consists of a signal registered on either of the sets of fiber layers (straight or helical). A "fiber double" count consists of a signal on both of the sets within the same 40 ns. A "paddle" count consists of a signal on both an outer paddle, and one of the inner paddles that are on the same side of the octagon as the outer paddle where the signal was registered. An additional set of signals to reduce noise are labelled as "triggers", type 1 and 2. A type 1 trigger is a coincidence between a paddle count and a fiber single. A type 2 trigger is a coincidence between a paddle count and a fiber double. For each of these groups there is a maximum of 1 count every 40 ns, so we are careful when ramping out our antiprotons not to exceed this rate.

Critical to the proper counting of the number of antiprotons for our experiments is to have a proper calibration for our different detectors. This efficiency (the number of signals per antiproton annihilation) will be influenced by the solid angle of the detec-

	Ioffe center		Degrader	
	Solid Angle	Efficiency	Solid Angle	Efficiency
Fiber doubles	0.82	0.92	0.18	0.50
Paddles	0.58	0.80	0.43	0.75
Type 2 triggers	0.58	0.77	0.03	0.40

Table 5.1: The solid angle acceptance and efficiency of the ATRAP annihilation detectors for antiproton annihilations in the center of the Ioffe trap or at the degrader [1].

tors, the generation of secondary particles, their trajectories and finally the efficiencies of a particle passing through the detectors generating a signal. Our collaborators from Jülich have done extensive Monte Carlo simulations using the GEANT4 simulation software [1] and have come up with the predicted efficiencies listed in Table 5.1.

The simulation for the paddle detector efficiency is the simplest and most easily modeled, and is thus the one we use to calibrate our antiproton numbers. The coincidence between the paddle detectors and the fiber doubles (trigger type 2) has the greatest signal to noise ratio [41] and is what we look at when we are trying to detect small numbers of antiprotons.

The results from the Monte Carlo simulations do not appear to be perfect, however. We can experimentally check to see what the relative counting rates for the different channels are by looking at a selective dumpout of antiprotons. Comparison of these numbers differ from the model listed above [41]. Because of this, we have a strong incentive to try to calibrate our detectors using a second method. Attempts to compare the annihilation signals of antiprotons to a charge counting measurement using the same methods outlined in section 4.3.1 have proven problematic because of the difficulty of modeling how many charges are liberated from the degrader when

an antiproton strikes it [41]. One promising alternative method, which will be discussed in chapter 7, is to resonantly detect the cyclotron motion of a small numbers of antiprotons (<10) using a tuned circuit and slowly dump them out to register the efficiency of the detectors. Alternatively, a larger number of particles (>100) can be counted and dumped using the axial amplifier.

5.3 Antiproton Capture

5.3.1 Further Antiproton Energy Loss

Antiprotons arrive to us from the antiproton decelerator with a momentum of 100 MeV/c corresponding to a relativistic kinetic energy of of 5.3 MeV and more than a thousand fold energy loss is necessary before we can successfully trap them using electric and magnetic fields.

The majority of the energy loss occurs as the antiprotons pass through a series of thin foils going from beam pipe leading up from the AD into our experiment (see Fig. 5.6). Most of the foils are not there for the purpose of degrading their energy and serve another purpose, thus their thickness is kept to a minimum. The energy lost in each of these materials is well understood from previous studies [61].

First, the beam goes through the PPAC going through two capton windows and three pieces of aluminized mylar where energy is also lost from collisions with the argon gas. Second, it passes through the energy tuning cell, where a gas mixture of SF6 and Helium is put through at atmospheric pressure in order to tune the energy with an energy tuning difference of about 600 keV between the cell being 100% helium

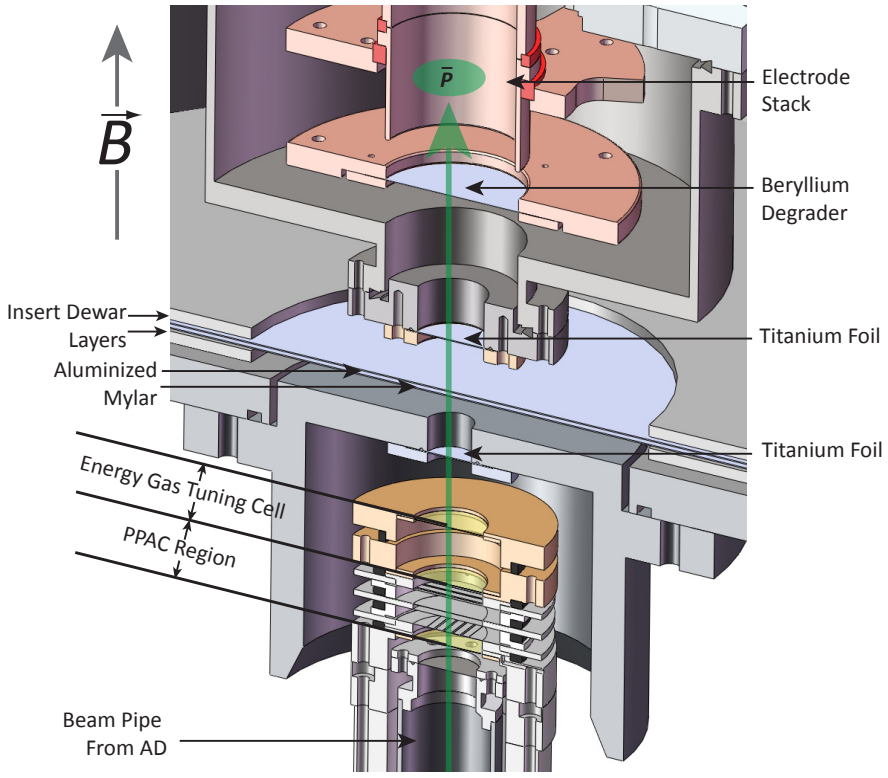

Figure 5.6: The path of antiprotons and their energy loss mechanism as they enter the electrode stack.

and it being 100% SF6. It passes through another capton window, then through a titanium foil which holds the pressure differential between the insert dewar vacuum and the magnet bore at atmosphere. There are a couple layers of aluminized mylar "superinsulation" that serve to insulate the different layers of the insert dewar from each other, whose induced energy loss cannot be ignored, and then another titanium foil holding vacuum between the insert dewar and the electrode stack space.

As a last step, the majority of the energy loss (about 3.6 MeV) occurs in the 130 μm Beryllium degrader which we also use to apply a bias voltage to the bottom of our electrode stack. The thickness of the degrader is chosen to put the antiproton energy near the center right around the 50% SF6 concentration in our gas tuning cell.

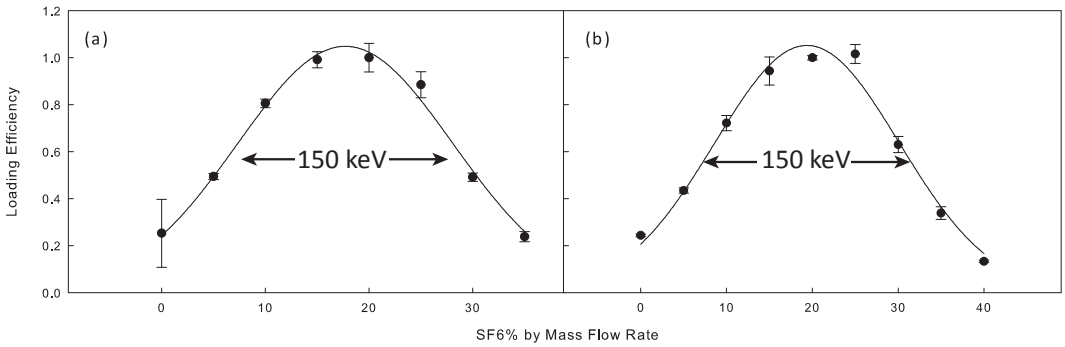

Figure 5.7: Antiproton capture efficiency as a function of the gas in the energy tuning cell. (a) Scan at 1 T (b) Scan at 2.8 T.

That way we have about 300 keV of margin for error if some of the thicknesses or calculations are a little off. By varying the SF6 % we can get an idea of the energy distribution of our antiprotons. Two such scans one at 1 T and another at 2.8 T are shown in Fig. 5.7. They are very nearly located around the same center (17% vs 19 %), showing that the tuning is mostly independent of magnetic field.

5.3.2 High Voltage Antiproton Capture

Once the energy of the antiprotons has been reduced through the steps listed above, we can trap them using our electric and magnetic fields. The radial trapping is accomplished via our axial magnetic field, and the axial trapping is accomplished by rapidly pulsing up a several kilovolt (maximum 5 kV) potential applied to the degrader, while the HV electrode is held at a fixed potential as shown in Fig. 5.8. Prior to the antiprotons arriving, the degrader is held at some positive voltage (typically 590 V) in order to suppress secondary electrons being released from the degrader, as their release can destabilize the antiprotons [23]. Applying -5 kV to the HV electrode leads to a potential of about -4.52 kV on axis. This means that we can trap antiprotons

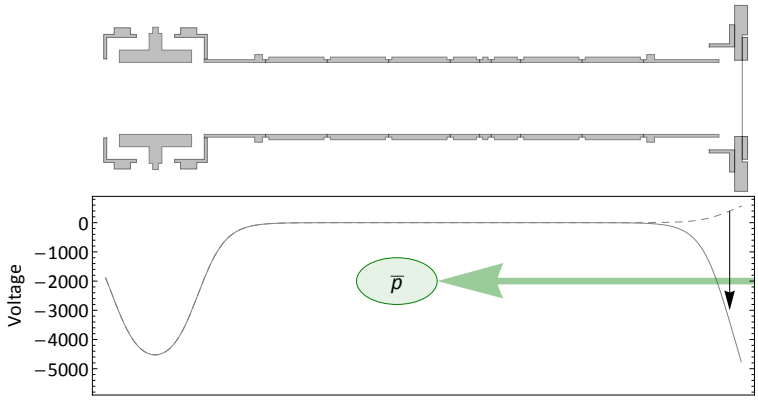

Figure 5.8: High voltage antiproton capture procedure.

coming off the degrader with greater than 590 eV of axial energy and less than 5.11 KeV.

The AD sends both a forewarning pulse (1 second prior) and warning pulse (immediately) when the antiprotons are being ejected from the ring into our beamline. We use the forewarning pulse to inhibit our fiber and paddle detectors so they are not saturated by the large signal, and we pulse up the voltage on the degrader to -5 kV in about 50 ns a set amount of time (called the HV switch delay) after the warning pulse. We vary the length of the delay to maximize our antiproton catching. We put the HV switch delay in the middle of the plateau shown in Fig. 5.9 (around 4.55 μs) as putting it too near the beginning of the plateau also risks the trapping of secondary electrons that, as mentioned above, can cause instabilities for the antiprotons [23].

The rapid pulsing of the voltage on the degrader is accomplished through the use of a HV switching circuit modified from previous designs [62] which built on work from the 1980s during the first antiproton trapping experiments [63]. At the heart of the circuit is a high voltage fast transistor switch that rapidly shorts out one of the resistors in a voltage divider between the positive and negative high voltage supplies,

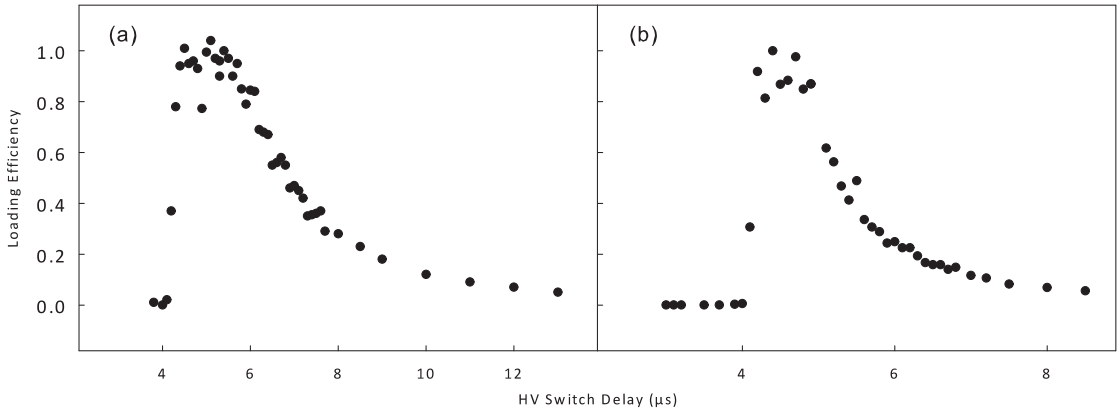

Figure 5.9: HV switch delay vs. antiproton loading efficiency at (a) 1 T and (b) 2.8 T.

thus quickly changing the voltage to the degrader. This same HV switch also provides slower ramp (50 ms) of the voltage from -5000 kV back to the positive through the use of an RC filter. The detectors can handle a count rate of one antiproton annihilation every 40 ns, meaning we can safely count up to 1 million antiprotons coming out uniformly during such a ramp. Typically we are counting tens of thousands. For larger numbers we use slower ramps.

Depending on the magnetic field, we see diminishing returns for increasing the trapping voltage for the antiprotons as shown in Fig. 5.10 where exponentials have been fit to both curves. At 1 T, the gains start to level off between 2 and 3 kV, whereas at 2.8 T we can see that we are still gaining substantial numbers of antiprotons by increasing the voltage all the way to 5 kV.

A means of analyzing this phenomena is to look at the HV ramp readout to ascertain at what voltage antiprotons are coming out at under different circumstances as is shown in Fig. 5.11. This will tell us the axial energy distribution. If we close the voltage back door on the degrader too early we will only be catching the antiprotons

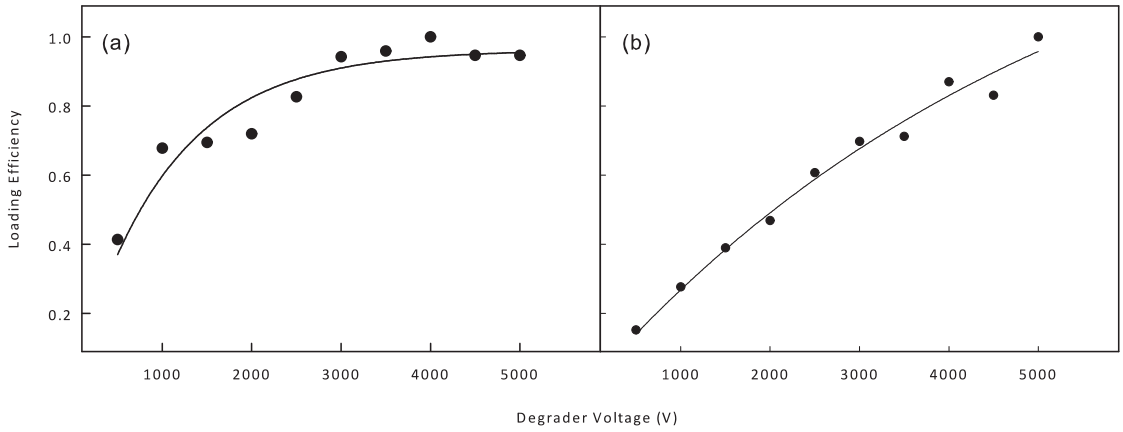

Figure 5.10: Degrader trapping voltage vs. antiproton loading efficiency at (a) 1 T and (b) 2.8 T.

with the largest axial velocity and energy. We can see that this is what is happening in the case of 2.8 T (Fig. 5.11a) for a delay of 4.1 μs. If we close the door late, all the fastest antiprotons will have bounced off of the HV electrode potential and left the trap before the door closes, and we will be left with only low energy antiprotons as is shown in Fig. 5.11a with a delay of 7.0 μs.

What is interesting in the case of 1 T, shown in Fig. 5.11a is that we never seem to trap any of the high axial energy antiprotons when our background field is at this lower value. This indicates that there is a strong correlation between the axial and radial energy of the antiprotons as they enter our trap. The maximum radial energy for particles in our trap was given in Table 2.4, which for antiprotons at 1 and 3 T are 15 and 140 keV respectively.

5.3.3 Electron Cooling of Antiprotons

Given the extremely long damping times for antiprotons (see Table 2.5) we need another mechanism in order to bring the antiprotons to a temperature low enough to

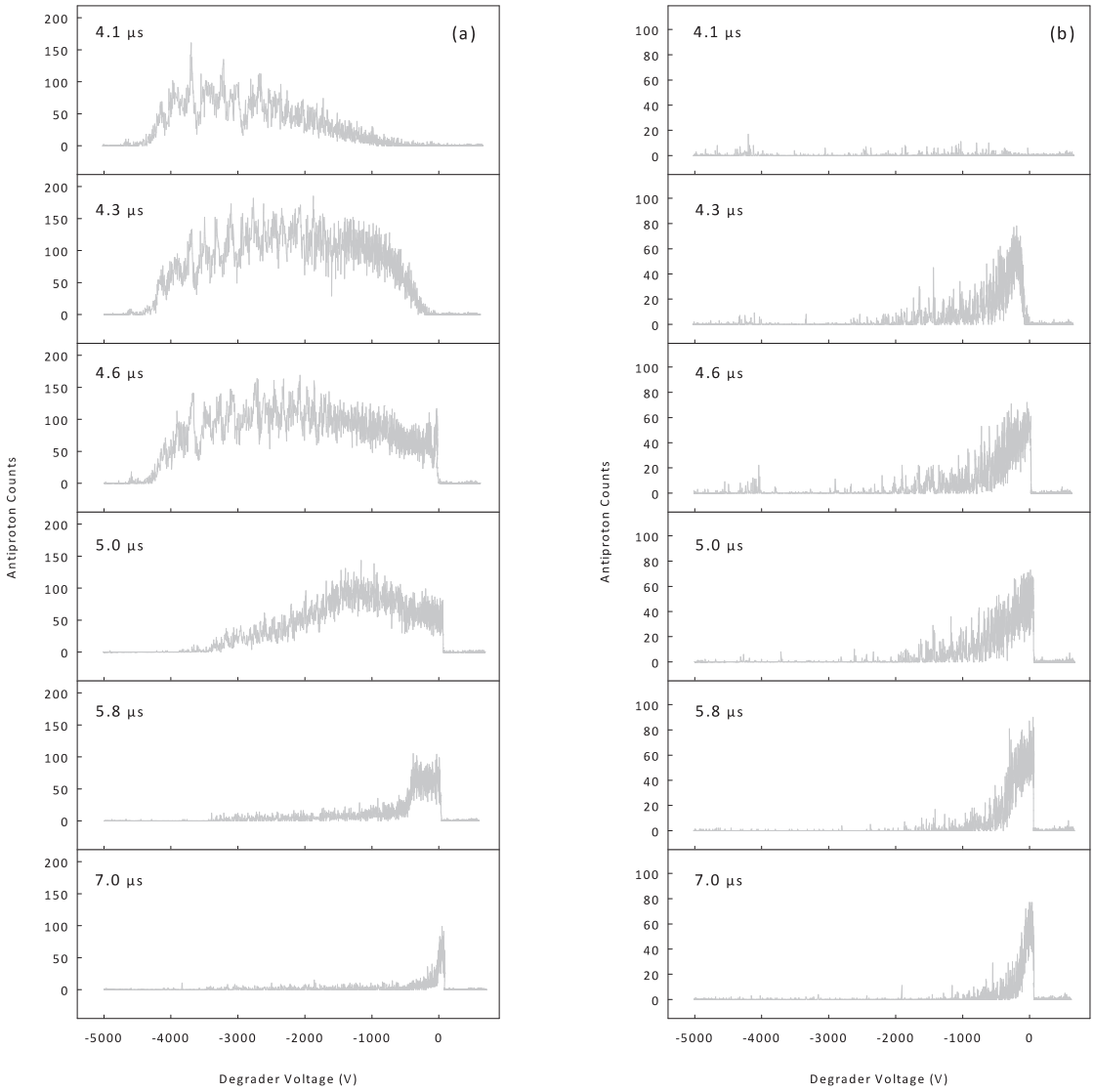

Figure 5.11: High voltage ramp profiles for antiprotons trapped using different HV switch delays at (a) 1 and (b) 2.8 T.

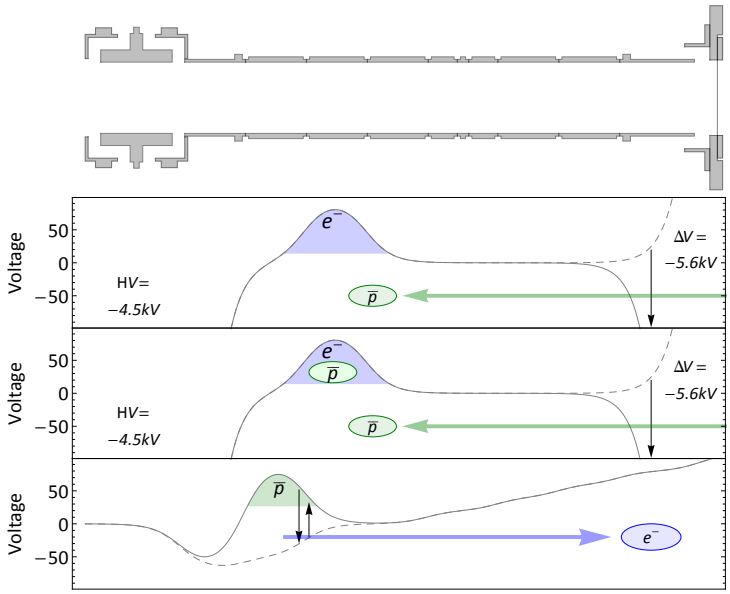

Figure 5.12: Procedure for the electron cooling of antiprotons, antiproton stacking and the pulse out of the electrons.

form antihydrogen that can be trapped in a less than 1 Kelvin deep magnetic trap. There exist a number of options for cooling antiprotons in a penning trap [24], but by far the most effective is to use electrons to sympathetically cool the antiprotons [57]. In a typical experiment, about 300 million electrons are pre-loaded on to an endcap electrode in the lower stack prior to catching antiprotons. The antiprotons are then loaded using the same methods as outlined in section 5.3.2.

Within a few seconds after entering the high voltage well the majority of the antiprotons are cooled into the smaller well with the electrons and when the voltage on the degrader is ramped from -5 kV to the positive 590 V 40 seconds later a negligible fraction of the antiprotons are lost, with almost all remaining trapped. This procedure can then be repeated with antiprotons sitting in the well along with the electrons, and taking more and more shots leads to a greater number of antiprotons accumulating in the well as depicted in Fig. 5.12. This is called "antiproton stacking". Studies have

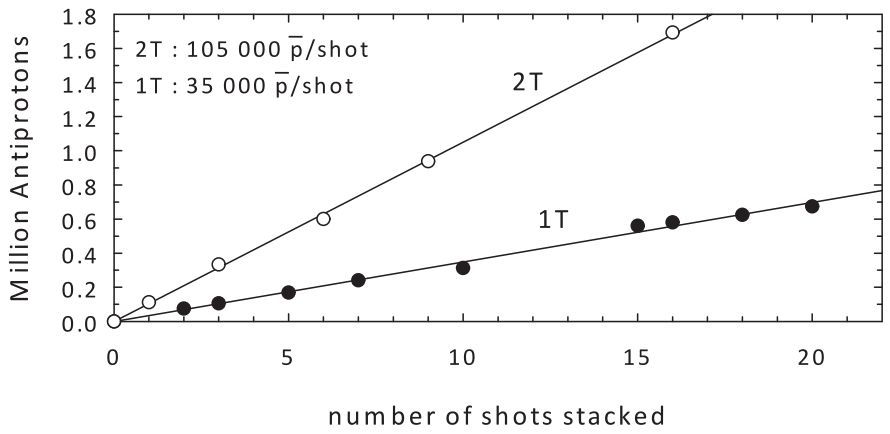

Figure 5.13: Antiproton stacking at (a) 1 and (b) 2 T in the big solenoid.

been conducted in another 18 mm radius electrode apparatus to determine the effect of voltage, electron number and cooling times on the antiproton loading [41].

Once the desired number of antiprotons have been accumulated in the well, the high voltage on the degrader and the high voltage electrode are removed and the electrons are pulsed out of the trap. This is shown in the bottom diagram in Fig. 5.12. The electrons and antiprotons are moved onto an electrode with a dedicated high voltage rapid pulse unit (DEI HV1000) tied to it via a micro coax line. A 50 ns pulse of 120 V is applied which is long enough to pulse out the electrons but not long enough to allow the antiprotons to escape, who at the same energy move at a velocity $\sqrt{m_e/m_p} = 0.02$ as quickly as electrons. The electrons are pulsed on to the degrader and we confirm their arrival using the methods described in section 4.3.1. However, since there is such a large number of electrons coming out at once it saturates our charge counting method and we can only see that greater than 50 million or so have exited. We apply a second voltage pulse on to the electrode looking for no signal on the degrader to confirm that all electrons have been pulsed out successfully.

Sample antiproton stacking in BTRAP from 2007, using these methods at two different magnetic fields in the large solenoid is shown in Fig. 5.13. There is a three fold increase in the antiproton capture rate simply by doubling the magnetic field. However, we need a lower field in order to perform our antihydrogen experiments in the Ioffe trap. Unfortunately the large inductance, and very long charging time (80 minutes/tesla) of the big magnet make changing its field constantly very unattractive. These facts have motivated us to install a smaller solenoid surrounding the antiproton trapping region.

5.3.4 Boosted Field Antiproton Capture

In 2008 an antiproton solenoid was installed in the region surrounding the lower electrode stack to add to the bias field of the big magnet. In a 1 tesla background field it is rated to go up to 4.6 tesla at 94 amps. It is rated to charge much faster than the big solenoid at a rate of 100 V across 27 henries, allowing for more than 3 amps per second (better than 7 seconds per tesla). Until now it has only been operated at a charging rate below 0.2 amps per second (about 100 seconds per tesla) as we are limited by the voltage supplies available.

The location of the antiproton solenoid with respect to the electrode stack and the other coils in the BTRAP experiment, as well as the axial field profile at a typical operating field of 2.5 T in addition to the 1 T background field and with the Ioffe trap off is shown in Fig. 5.14a. The effect on the magnetic field lines between our antiproton catching electrode and our antihydrogen formation region for such a field is shown in Fig. 5.14b. Field lines which begin at a radius of greater than 10 mm in

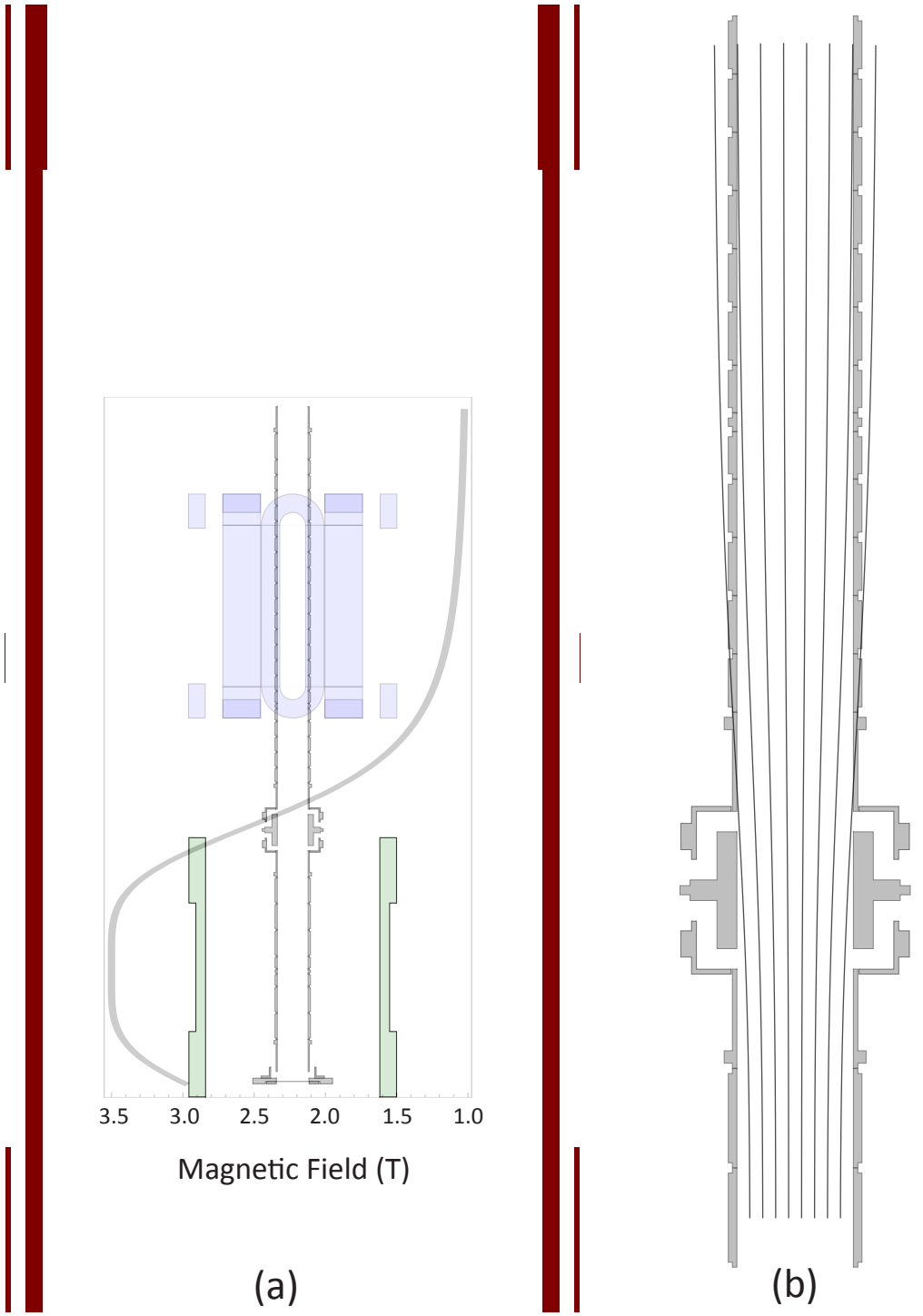

Figure 5.14: (a) Location of antiproton solenoid windings (green) with respect to electrode stack (grey), Ioffe trap coils (blue) and big solenoid coils (red). Axial field profile is with 2.5 T in antiproton solenoid, 1 T in big solenoid, and with the Ioffe trap off. (b) Field lines going from antiproton load electrode to antihydrogen experment electrode.

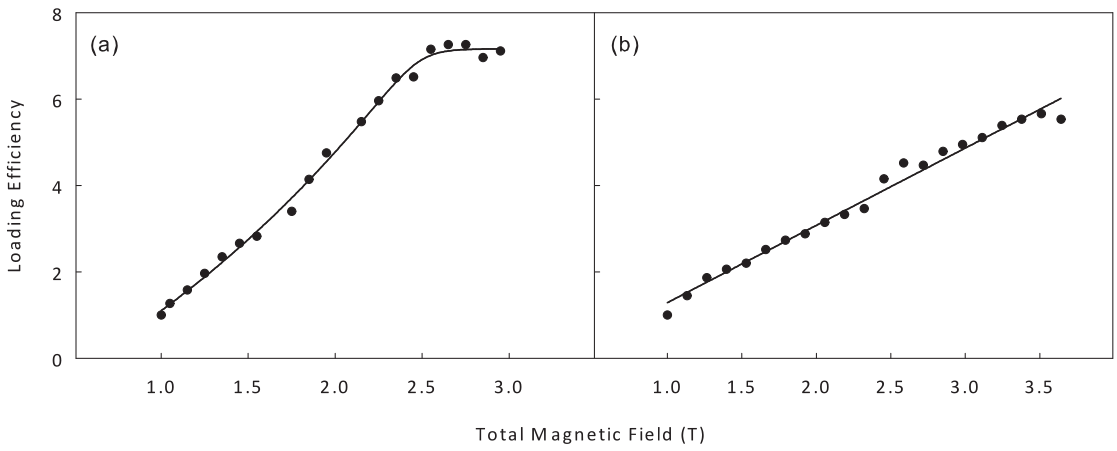

Figure 5.15: Maximum magnetic field vs. antiproton loading efficiency for (a) only the big solenoid and (b) 1 Tesla in the big solenoid and the remained in the antiproton solenoid.

the antiproton catching electrode in the lower stack will intersect the electrode wall by the time they get to their destination electrode in the upper stack.

The comparison of the improvement in HV loading efficient for the antiproton solenoid compared to ramping the field in the big solenoid is shown in Fig. 5.15 while each of the solenoids was being ramped up in field. In each case, the loading efficiency is normalized to the number loaded at 1 T. We can see that ramping the larger solenoid initially leads to a more rapid increase the catching efficiency than does ramping the smaller antiproton solenoid, but then tops out at around 2.5 T and is essentially flat afterwards. It may be that as was shown in Fig. 5.11 when we get up to high fields we begin to be limited by our axial trapping potential rather than our radial one, and this number may continue to increase if we could apply more than 5 kV in our long trapping well. The antiproton solenoid stacking is approximately linear up to 3.6 T.

The initial higher slope of the larger solenoid trapping may be due to the fact that it has a much larger fringing field than the antiproton solenoid and thus does a better

job of focusing the beam and guiding it into our apparatus. It could also be due to the more homogenous field generated by the larger solenoid than the antiproton solenoid.

Once the antiprotons are successfully stacked in the lower electrode stack we have an additional challenge in order to capitalize on the gains we get in loading efficiency. Because the antiprotons must be moved from the lower stack at a high magnetic field to the upper stack at a lower field, we risk losing a significant portion of the particles as the cloud expands. We have two basic options for transferring the antiprotons from the lower stack to the upper stack. We can either lower the field in the antiproton solenoid prior to moving the antiprotons up the stack, or we can move the particles with the field on and then lower it once they are in the upper stack so as not to interfere with further experiments.

It was difficult to categorize the loss associated with each of these techniques in the limited time the antiproton solenoid was in operation in 2008. Experiments with seemingly identical initial conditions with electrons and antiprotons would lead to very different outcomes, sometimes by more than a factor of two, for both sorts of trials. It is likely that the amount of particle loss is strongly tied to the shape of the initial plasma loaded, which was not measured prior to these experiments. The conservation condition on the angular momentum of the plasma given in equation (2.58) implies that:

$$L \simeq \sum_{j=1}^{N} \frac{eB\rho_j^2}{2} \simeq \text{Constant} \tag{5.1}$$

and that the as we change the field from B_1 to B_2, if it were to hold for each particle individually, our radius should scale as: $\rho_2 = \sqrt{\frac{B_1}{B_2}}\rho_1$. From Fig. 4.15 we see that an

electron cloud changed its radius by a factor of 1.75 as we changed the field from 3.5 to 1 T, close to the prediction above which gives $\sqrt{3.5/1} = 1.87$. The change in flux through the plasma as we change the magnetic field and change the voltages may also affect the cloud shape. We can therefore expect that the amount of loss as we use either method will be heavily reliant upon the initial cloud shape, and thus experiments measuring such loss as a function of cloud shape are planned for the future. One possibility to reduce the loss would be reduce the radial extent of the plasma prior to transferring them or lowering the field by spinning up the plasma using the rotating wall technique [64].

Chapter 6

Positrons

Positrons are the antimatter counterpart to electrons and the two particles are predicted to have the same mass and opposite charge. The comparison of their charge to mass ratios has been confirmed down to better than 2 parts in 10^{-7} [65, 66] and their g-factors have been confirmed to be equal to better than 1 part in 10^{-11}[67]. Prior to 2006, antihydrogen experiments in the ATRAP collaboration relied on a method of loading positrons using Rydberg positronium [68] that could load positrons from a radioactive ^{22}Na source at a rate of approximately 10,000 positrons/(mCi hour) into high vacuum at 5.3 tesla [23]. This rate was found to vary approximately quadratically with the axial magnetic field [69] meaning that at our operating magnetic field of 1 T we could expect a loading rate of only less than 500 positrons/(mCi hour). For the new apparatuses, ATRAP and BTRAP, commissioned after 2006 we moved to a different method of positron loading, using a buffer gas accumulator, and a new transfer method involving the electron cooling of positrons that yields a rate of up 6.5 million positrons/(mCi hour). This chapter will give a brief description of the

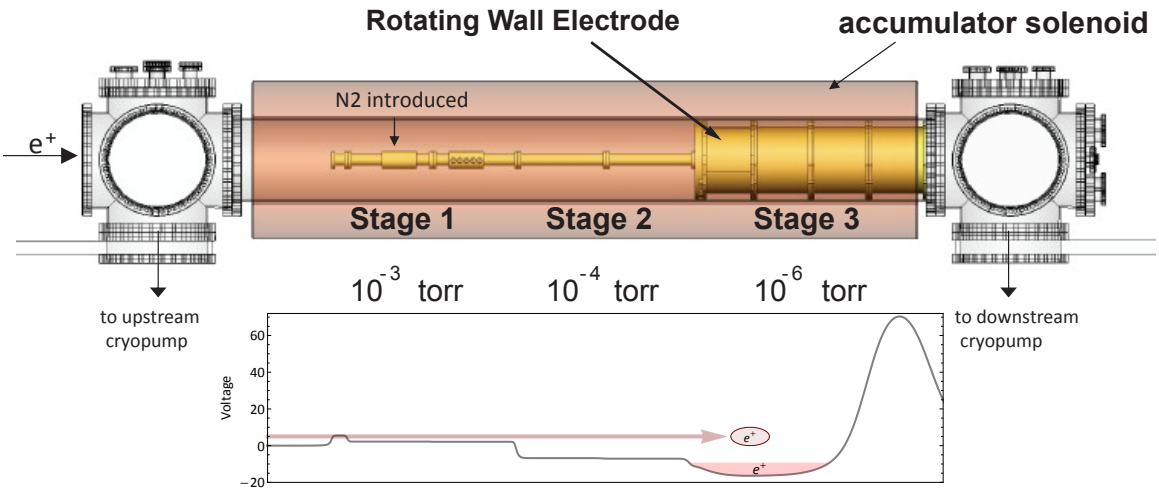

Figure 6.1: The voltages and pressures used for the buffer gas accumulation of positrons.

positron accumulation and transfer performed by our ATRAP collaborators from York University and describe the means by which we efficiently transfer the positrons a distance of nearly ten meters into our penning trap electrodes.

6.1 Positron Accumulation and Transfer

6.1.1 Buffer Gas Accumulation

The positron accumulator is set up in a separate zone in the antiproton decelerator approximately five meters away from the zone containing our 3 T magnet and penning trap apparatus, as shown in Fig. 6.2. A radioactive 50 mCi ^{22}Na source (with a half life of 2.6 years) created for us in 2006 by a South African company called iThamba undergoes β^+ decay

$$^{22}_{11}Na \rightarrow ^{22}_{10}Na + e^+ + \nu_e \tag{6.1}$$

and emits high energy positrons that pass through a neon moderator [70]. A fraction of these emerge with a low enough energy so that they can be further cooled and trapped by a three stage buffer gas accumulator modeled after those developed by Surko and collaborators [71]. This neon moderator decays over time and a corresponding decrease in the positrons loaded occurs (see Fig. 6.7a) so it must be periodically regrown. A detailed description of the positron accumulator is given in a thesis from one of our collaborators at York [72] and only a brief description will be given here.

The accumulator is very similar to the cylindrical Penning traps described earlier in this thesis, albeit with much larger electrodes (see Fig. 6.1). A large-bore, water-cooled, non-superconducting, solenoid creates a near uniform 0.15 T axial field. Inside the bore of the magnet is a set of electrodes of varying inner diameter. A small amount of nitrogen buffer gas (10^{-3} torr) is introduced into the electrodes in the end near the source and due to the pumping on both ends of the stack as it goes into the larger bore electrodes there are accompanying pressure decreases of 10^{-4} and 10^{-6} Torr as indicated in Fig. 6.1. As the positrons enter the stack they are confined radially by the magnetic field and axially by the voltages, just as in an ordinary Penning trap. They lose energy through repeated collisions with the nitrogen buffer gas and eventually cool into the deepest axial well located in the larger electrodes on the far end of the stack. To counteract the radial expansion of the plasma and compress it further [73] a rotating wall is applied on one of the larger electrodes which is split into four quadrants in the largest section of the trap. Using these methods it is possible to accumulate 26 million positrons over a 50 s accumulation cycle.

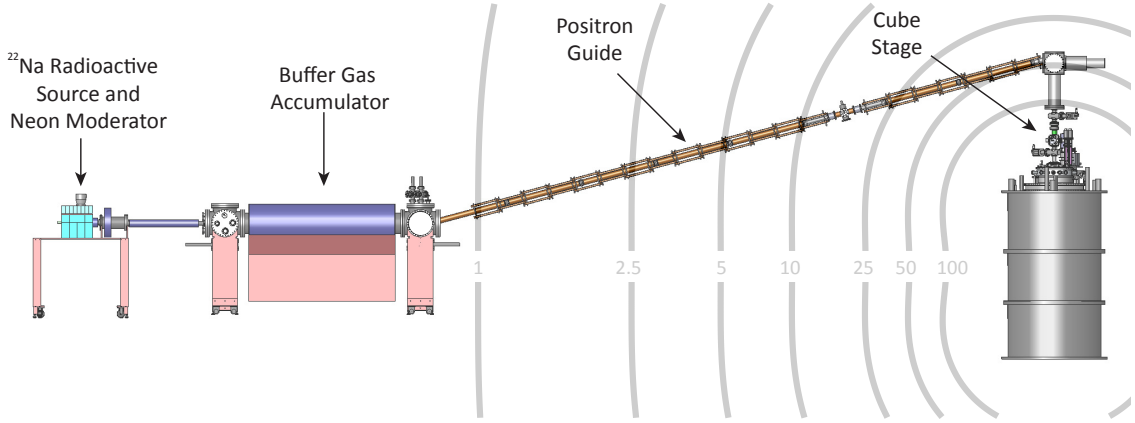

Figure 6.2: Location of positron accumulator and guide, the magnitude of the fringing field of the magnet is indicated in gauss.

6.1.2 Positron Magnet Guide

Once the positrons have gathered in the accumulator, we have the additional challenge of transferring the positrons into the Penning trap where we are accumulating antiprotons, which is 8 meters away and oriented perpendicularly to the accumulator. This transfer is accomplished through the use of a custom built positron magnet guide section built by members of York university [72]. A vacuum transfer line, surrounded by nearly 100 steering magnets, comes out of the large electrode end of the accumulator and takes a 15 degree bend proceeding upwards for about 5 meters. It then takes a 105 degree bend and proceeds about another meter where it mates with the top of the cube translation stage section shown in more detail in Fig. 4.1.

The linear translation stage in the cube can move to either put a mirror on axis for the loading of electrons, a 4 segmented faraday cup to charge count the positrons (using methods described in section 4.3.1), or can move out of the way to allow the positrons to enter into the bore of the large magnet and into our penning trap. An additional 2-D translation stage [41] is present just above the Penning trap electrodes

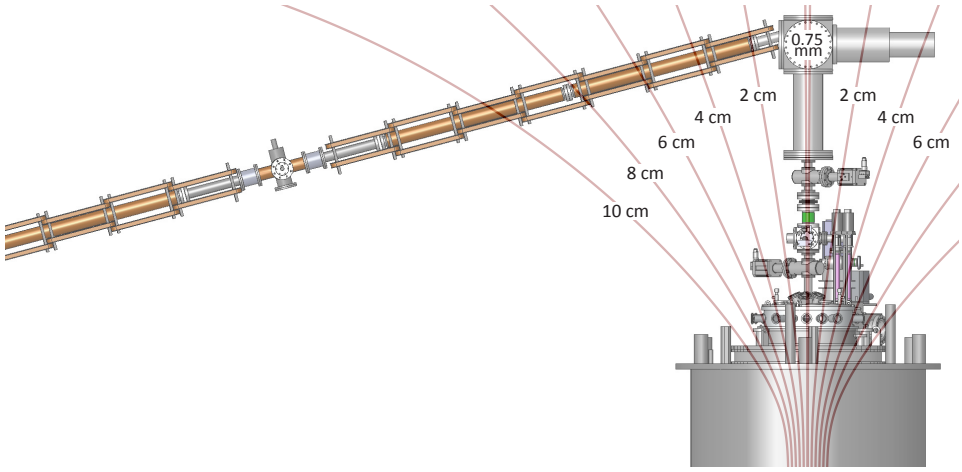

Figure 6.3: Field lines crossing the positron guide and going into the bore of the 3 T magnet. Numbers indicate the radial location of the field lines in the center of the magnet.

(location is indicated in Fig. 4.1). It has a 1.5 mm hole surrounded by a 4 segmented square faraday cup so we can do more charge counting and further analysis of the beam steering. To summarize once more: in order to transfer our positrons into the Penning trap with the antiprotons we need to hit a target 1.5 mm in diameter, from almost ten meters away. Luckily, our Canadian collaborators from York University have exceptionally good aim.

The transfer is both aided and complicated by the large fringing field of our 3 T superconducting solenoid, shown in Fig. 6.2 and Fig. 6.3. The main guiding of the positrons is accomplished through solenoidal coils surrounding the transfer line which provide an axial field of 200 gauss. The particles are pinned to the center of the guide through cyclotron motion around this field. However as they get closer to the big magnet they start to see more of a transverse component to the field due to its fringing field. To cancel this a series of horizontal and vertical rectangular shaped coils are mounted along the length of the transfer line to modify the magnetic field.

The magnetic field starts to help rather than hurt as positrons reach the 105 degree bend. Because the field lines of the magnet are converging towards its center (as shown in Fig. 6.3) if the positrons can be steered onto one of the field lines which will go into the 1.5 mm hole on the 2-D translation stage the large magnet will do most of the remaining steering for us. Field lines that begin within a radius of 0.75 mm at the 2-D translation expand to over 1 cm at 105 degree bend, making the actual target bigger. A series of solenoids in different orientations to boost the field in the bending region are present, although not shown in Fig. 6.2 and Fig. 6.3.

To initiate a transfer once the the positrons are gathered in the accumulator, they are lifted into a well which is about 10 V deep but raised about 70 V high. The voltage on the side well facing the transfer line is quickly pulsed down using an avtech DC-coupled non-linear pulse amplifier driver and the positrons are sent up the line with about 70 eV of axial energy. Because the magnets in the antiproton decelerator cycle once every 100 seconds, the changing magnetic fields can effect the steering of the positrons through the guide, and therefore the settings are chosen to steer properly only at specific times during the 100 second cycle. It was determined that the most efficient way to accumulate and transfer positrons was to accumulate for 50 seconds and transfer twice every AD cycle.

6.2 Positron Capture in Main Penning Trap

Once the positrons are well steered and on their way into the top of our electrode stack, indicated by a maximized charge counting signal on the degrader, we can trap them in a long well in the upper stack much like we can trap antiprotons in a

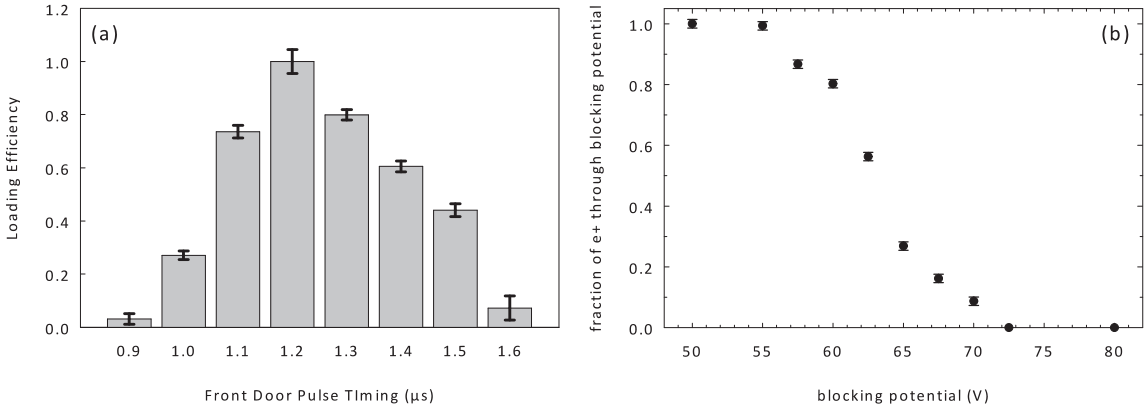

Figure 6.4: (a) Long well positron trapping efficiency vs. front door voltage delay and (b) fraction of positrons passing through a blocking potential.

long well in the lower stack. The positrons come in with a much lower energy than the antiprotons, 75 eV compared to several keV, but at a similar velocity owing to mass difference which also requires precise timing on the order of 0.1 μs for optimal trapping. A trigger signal which pulses the voltage down in the accumulator to send the positrons across the transfer line gets relayed to another pulse generator close to the antiproton Penning trap and immediately pulses down a voltage on one of the top endcap electrodes in our stack using a DEI HV1000 rapid voltage switch (as shown in Fig. 6.6 but without the electrons present). The voltage is pulsed back to its default voltage a set amount of time after this. We scan the time and the default "front door" trapping voltage on the endcap in order to maximize the number of positrons trapped into the long well, as shown in Fig. 6.4.

In order to further maximize the number of positrons caught, it is useful to slow down the positrons as they arrive in the long well, allowing the slower positrons to also enter before the fastest ones leave. To do this we raised the bottom of the long well by placing a 50 V plateau on all the electrodes between the front and back door of

the long well. The positrons in the long well can be counted out by pulsing down the voltage on the back door (the lower electrode in the stack) in the same way as the front door after they are trapped, and charge counting the positrons on the degrader using the methods discussed in section 4.3.1. Care must be taken to set up the voltages going to the degrader to suppress the emission of secondary electrons resulting from the annihilations on the degrader. Negative charges leaving the degrader would look the same as positive charges arriving on it, and could potentially inflate our counting numbers. By putting an appropriate electric field at the surface of the degrader to draw the electrons back in, we are able to suppress these electrons and properly charge count the positrons [41].

6.2.1 Electron Cooling of Positrons

Trapping positrons in a long well with energies greater than tens of electron volts (100,000+ Kelvin) is clearly not well suited for making cold antihydrogen. Furthermore, since the energy is primarily in the axial motion the cyclotron cooling mechanism will not help us unless there are enough collisions to transfer the axial energy to radial energy. With a relatively small number of positrons going back and forth in a 40 cm long well there are very few such collisions compared to our electron loading in the lower stack. Without an additional cooling mechanism the positrons can take on the order of 1000 seconds in order to cool into a well which is below the voltage of the longer trapping well (see Fig. 6.5).

Taking inspiration from our long established practice of the electron cooling of antiprotons described in chapter 5, we developed a mechanism for the electron cooling

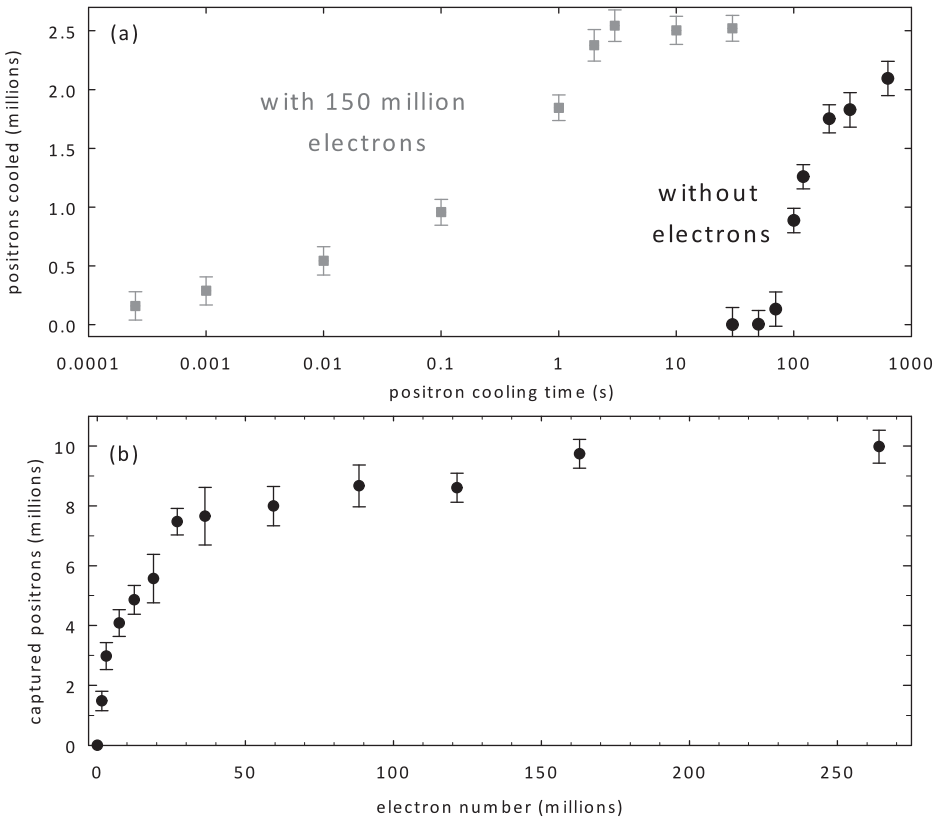

Figure 6.5: (a) Cooling time of positrons in a long well into a deeper well with and without electrons and (b) positrons loaded into the deeper well vs. number of electrons used.

of positrons. This procedure is shown in Fig. 6.6. Electrons are loaded into the lower stack as described in section 4.1 and then moved up into a nested well structure as shown in Fig. 6.6. The positrons are loaded as described above, pass through the electron cloud and the majority cool into the two sidewells in less than a second as shown in Fig. 6.5a. It has been found that approximately 150 million electrons held in one radius length electrode is the optimal number for catching and cooling positrons. Repeated positron shots can be taken in this manner until we achieve the number desired. The number of positrons stacked per bunch received is shown in Fig. 6.7b

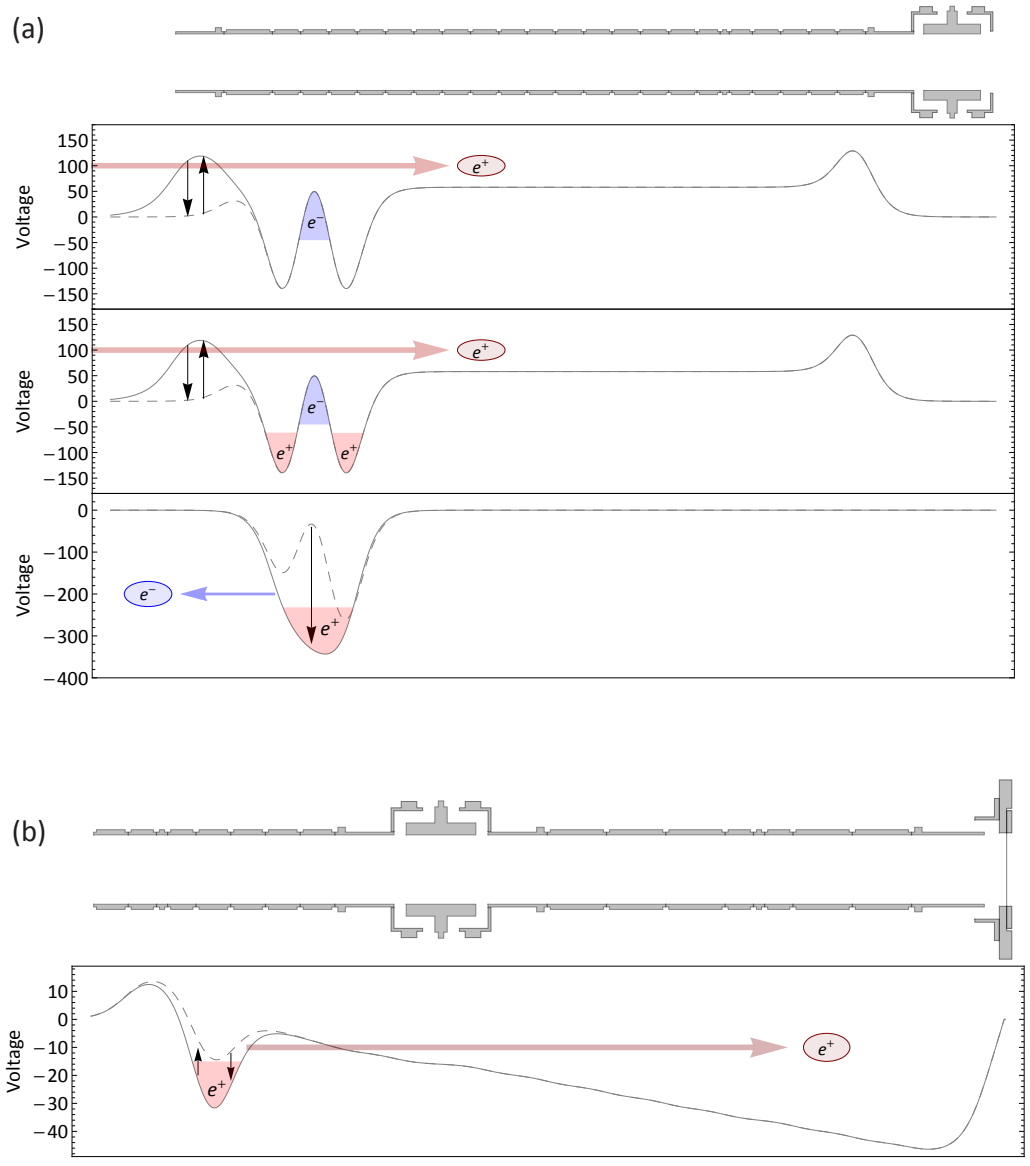

Figure 6.6: Procedure for the electron cooling and stacking of positrons. The method of removing the electrons. The method for charge counting positrons.

and is linear up until 200 million positrons. It may be that at some point we begin to fill up the wells to the point where the positrons and electrons at the bottom of their respective wells have sufficient space charge to cause an overlapping interaction region between the two charge species, which over long time scales can lead to further loss.

The cross section for both annihilation and positronium formation are low enough that we do not lose a large fraction of the positrons during this process, as shown in Fig. 6.7a, capturing approximately two thirds of the positrons which arrive to the degrader. Previous studies have established that the lifetime of positrons in a variety of metals is on the order of 10^{-10} seconds [74]. The free electron density in a typical metal is on the order of $10^{29}/\mathrm{m}^3$, whereas the electron density in our plasmas have a typical density of $10^{13}/\mathrm{m}^3$. A 1 eV positron will pass through the radius length electrode where the electrons are stored in about 10^{-8} seconds, so with our densities lower by 15 orders of magnitude it is not surprising that there are few annihilations.

Once we have gathered a sufficient number of positrons in our nested well structure, the electrons are removed through the procedure shown in the third panel of Fig. 6.6. Since the positrons and electrons have the opposite charge, we do not need to pulse out the electrons as we do in the case of protons, nor would this work as the positrons and electrons travel at the same velocity. Instead we can just slowly ramp down the well containing the electrons until they spill out the side. This is done in tens of seconds. The biases are arranged so that the electrons leave out the top of the stack and do not interfere with any antiprotons which may be located below.

When the positrons are alone in a single well they can be charge counted in

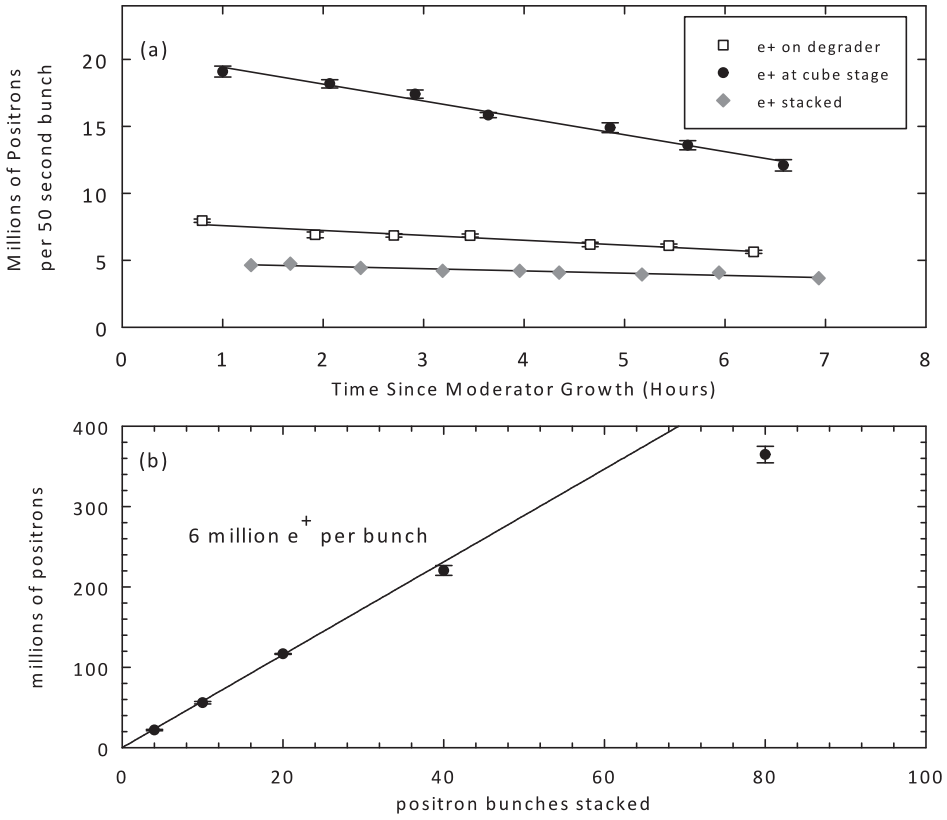

Figure 6.7: (a) Number of positrons counted on the cube stage, on the degrader and stacked in one shot as the neon moderator decays. (b) Number of positrons stacks vs. number of transfers received.

the same way as electrons using the methods described earlier in this section and section 4.3.1. After a stack the positrons are counted out from an electrode in the upper stack with a voltage structure shown in the bottom panel in Fig. 6.6. Note the voltages placed to suppress secondary electrons emerging from the degrader. As with counting electrons, we pulse on the well, raise the voltage, and pulse again until there are no positrons left.

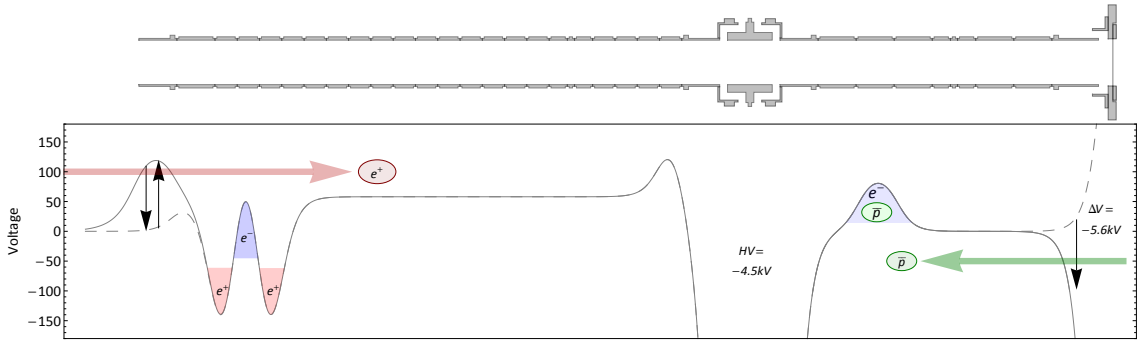

Figure 6.8: Procedure for simultaneous stacking of antiprotons and positrons. The bunches do not arrive at the same time.

6.2.2 Simultaneous Antiproton and Positron Stacking

Fortunately, the positron and antiproton stacking methods do not interfere with each other and can be performed at the same time. Prior to an antihydrogen experiment the potentials on the trap are setup as shown in Fig. 6.8. Electrons are first loaded for positrons and moved up the stack into position. A second batch of electrons for antiprotons are loaded off the degrader, with the photons from the excimer laser passing harmlessly through the existing cloud of electrons. Both load timing sequences are synchronized off of the proper signals coming from the antiproton decelerator with antiprotons arriving once every 100 second AD cycle and positrons arriving twice per cycle. When each load is done the electrons are pulsed down on to the degrader for antiprotons or ramped up and out the top of the stack for positrons. With that we have an efficient loading mechanism to accumulate large numbers of the particles we need in order to conduct antihydrogen experiments.

Chapter 7

Resonant Antiproton Detection

The axial and radial motions of the charged particles in a Penning trap as described in chapter 2 induce image charges on the electrodes that can be amplified and detected through their interactions with tuned circuits. Probing the cyclotron motion of a single antiproton and an H^- ion in the same trap [53] has yielded a precise comparison of the $p/\bar{p}$ charge to mass ratios already mentioned in chapter 5. Probing the axial motion of an electron in a Penning trap has been used to obtain a very accurate measurement of the electron magnetic moment to better than one part per trillion [75]. Efforts are currently underway at Harvard [76] and by a competing collaboration in Germany [77] to use similar techniques to do a precise measurement of the proton and antiproton magnetic moments.

We have several motivations for trying to include such resonant detection capabilities into our new antihydrogen apparatus. As was discussed in chapter 4, the axial motion of the particles can be used to count the number of electrons, positrons, protons and antiprotons [25, 45, 78] in our trap, serving as a check on the calibrations of

both our charge counting and antiproton annihilation detection methods. It is also possible to detect the cyclotron motion of single protons and antiprotons. This can potentially be used for very sensitive detector calibrations by leaking out 1 antiproton at a time from the trap and registering the count rate on the detectors as well as detecting small numbers of trapped antihydrogen ions confined in our Penning trap.

There are several circumstances that make this analysis more difficult in the ATRAP and BTRAP apparatuses than in previous experiments. For a given sized orbit, the signal generated by the cyclotron motion increases with magnetic field and both the axial and cyclotron signals decrease with the size of the cylindrical electrodes. Since we now operate at lower fields (1 T) and with larger electrodes (ρ_0 = 18 mm) than previous and ongoing experiments, our detection efficiency is significantly reduced. Furthermore, we must operate in an environment in the antiproton decelerator where there is a large amount of electrical noise with an apparatus that has hundreds of electrical connections which must be properly shielded to keep that interference out.

Despite these difficulties, several experiments have been conducted showing the feasibility of using amplifiers under these conditions to both characterize the magnetic field in our apparatus and detect the signals from single antiprotons. This chapter will summarize the design and operation of the tuned circuit amplifiers used on the ATRAP and BTRAP apparatus and present results paving the way for further study. The applications for use in antihydrogen ion experiments will be given in chapter 8.

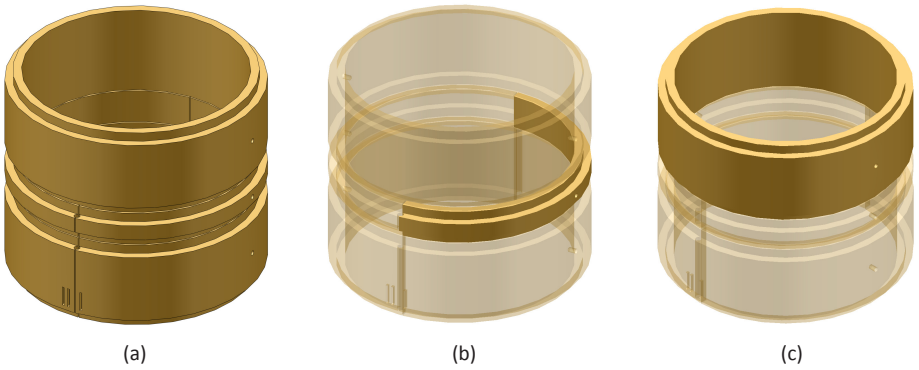

Figure 7.1: (a) The three central harmonic well electrodes, the full stack can be seen in Fig. 3.15 and Fig. 3.16. The electrodes used to detect (b) the cyclotron and (c) axial motion of the particles.

7.1 Low-Field Large-Electrode Amplifier Operation

Due to the need for well defined frequencies of the particle motions, experiments involving tuned circuit amplification in our Penning traps are exclusively conducted in a 5 electrode harmonic well configuration as described in section 2.1.2 where the center of the quadrupole potential is located in the central ring electrode. The axial motion of a charged particle in the well can be detected by monitoring the image charges created on a compensation electrode (with axial length $z_2 = 0.815\rho_0$ following the convention from Fig. 2.2), while the signal from the cyclotron motion can be monitored on an azimuthally split ring electrode (with axial length $z_1 = 0.162\rho_0$) as shown in Fig. 7.1. There is significant experience detecting the motion of charged particles in these two instances in apparatuses with $\rho_0 = 6$ mm and a magnetic field greater than 5 tesla [23, 25, 79]. Here we will discuss how our detection sensitivity in the new apparatus should compare to those measurements.

A particle moving at point $\vec{r}$ in the vicinity of electrodes labeled $i = 1, 2...n$ will

induce a current I_i on the i^{th} electrode given by:

$$I_i = -q\nabla\phi_i(\vec{r}) \cdot \dot{\vec{r}} \tag{7.1}$$

where $\phi_i(\vec{r})$ is the potential created at the location of the particle when the i^{th} electrode is held at a potential of 1 V and all other electrodes are at ground [80]. In our electrode stack, such induced currents on the electrodes can be amplified and detected. In order to achieve maximum amplification we would like to maximize the the signal $V = IR$ before it gets to the amplification stage, meaning we would like this current to be read across a very large resistance. Unfortunately, the trap electrodes have a characteristic capacitance to ground on the order of tens of picofarads. At the frequencies we are concerned with, approximately 1-50 MHz, this would lead to an impedance to ground of $Z_{eff} = \frac{1}{i\omega C}$ which is on the order of a kΩ. In other words, the image charge signal would be shorted to ground and we wouldn't see a sufficiently large signal to finely detect the particle motions. To get around this, an inductor coil to ground is added in parallel with the trap capacitance. Choosing the correct value for this tuned circuit will give a very large effective resistance on resonance, and our signal will be sufficiently large for the later amplification stages.

An LC circuit as shown in Fig. 7.2 will have a resonance (a sharp maximum in its effective impedance) at:

$$\omega_{LC} = \frac{1}{\sqrt{LC}} \tag{7.2}$$

The quality factor Q of the resonant circuit at a frequency ω is given by

$$Q = \frac{\omega_{LC}}{\Delta\omega_{-3dB}} \tag{7.3}$$

that is, the Q is the center frequency over the full width half maximum of the res-

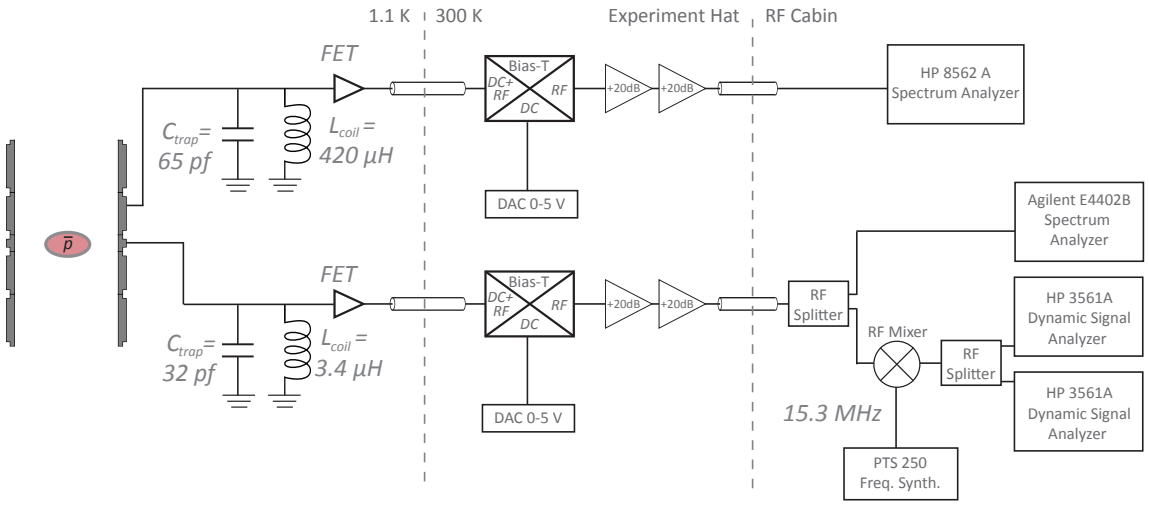

Figure 7.2: Amplification stages and signal processing for detecting the axial and cyclotron motions of protons and antiprotons.

onance. There will inevitably be some finite resistance in the line coming from the electrode and through the coil, forming some resistance in series with the inductor and limiting the size of the Q. In this setup, for the case of $Q \gg 1$ it can be shown [81] that on resonance the effective impedance of this circuit is primarily resistive with:

$$R_{eff} = Q\omega L \tag{7.4}$$

The use of this LC tuned circuit also serves another purpose by frequency filtering prior to the first amplification stage. Without this filter we would be amplifying a large amount of noise across a large bandwidth we are not interested in, saturating our FET and diminishing our signal on resonance. Given the choice, in order to get the largest possible R_{eff} we would choose a tuned circuit with a higher L and lower C, but we do our best to minimize any unnecessary capacitance and work with what we have.

Equations (7.1) and (7.4) allow us to get an idea of what sort of signal degradation

we can expect as we move to a lower field and larger electrode radius. We will start by analyzing the case of the axial motion and then move on to the cyclotron motion.

7.1.1 Axial Detection Signal Expectation

The axial motion of the particles is unaffected by the strength of the magnetic field, and the frequency is simply as was given in equation (2.36):

$$\omega_z = \sqrt{\frac{qC_2V_0}{md^2}} \tag{7.5}$$

To obtain the same axial frequency as we did in our smaller traps, we need to apply a voltage $\rho_{02}/\rho_{01} = 3$ times larger, due to the scaling factor d, but this is not a problem with voltage supplies we have available. Therefore it is possible to operate at the same frequency as before near 1 MHz. However, the larger electrodes mean that there is a larger trap capacitance than previously. Our current $\rho_0 = 18$ mm trap has a total trap capacitance of 65 pF compared to 22 pF for previous precision antiproton mass experiments [79] and 25.6 pF for the previous $\rho_0 = 6$ mm antihydrogen apparatus [23]. To operate at the same frequency we would need to decrease the inductance inversely with the increase in capacitance, meaning a decrease in our effective resistance $R_{eff} = Q\omega L$ and also in our signal $V_{eff} = IR_{eff}$.

The current induced by a particle oscillating about the center of the ring electrode on a compensation electrode follows from (7.1) and is given to first order by [23]:

$$I_z = D_1 \frac{q}{2z_0}\dot{z} \tag{7.6}$$

where $D_1 = 0.8996$ is an asymmetric expansion coefficient for a 5 electrode harmonic trap, independent of absolute electrode size, analogous to the symmetric expansion

coefficients C_j (see equation (2.17)) that were worked out in the Bessel and Legendre polynomial expansions in chapter 2. The current generated on the electrode will be reduced by a factor of $z_{02}/z_{01} = 3$. For detecting a signal from a oscillating particle, the important figure of merit is the ratio of your signal voltage to the noise background. On resonance, the noise background V_n over a frequency span $\Delta\nu$ will be given by the Johnson noise [82] of the circuit:

$$V_n = \sqrt{4k_B T R_{eff} \Delta\nu}, \tag{7.7}$$

whereas the signal voltage on resonance is given by: $V_s = I_z R_{eff}$. Past signal to noise measurements have indicated that the noise temperature in such circuits is significantly hotter than the ambient temperature of the trap (60 K vs. 4.2 K [79]) and therefore it is unclear if a lower ambient temperature reduces the noise. If we assume the same noise temperature and bandwidth sampling, than we would expect our signal to noise level to scale as

$$\frac{V_s}{V_n} = \frac{I_z R_{eff}}{\sqrt{4k_B T R_{eff} \Delta\nu}} \propto \frac{1}{z_0}\sqrt{\frac{1}{C_{trap}}}, \tag{7.8}$$

for a given particle oscillation amplitude, given that $\omega_z, T, \Delta\nu$ and Q are not expected to change. $z_{02}/z_{01} = 3$ and $C_{trap2}/C_{trap1} = 65/22$, meaning we would expect a $3\sqrt{65/22} \simeq 5$ times decrease in our signal to noise level.

This decrease in the signal strength does not mean that axial antiproton detection will not be useful. Experiments in the more optimal conditions have been able to resolve the axial motion of a single antiproton using a two drive technique [25], and it may be possible by increasing the drive strength to accomplish this in the new apparatus. A more likely use of the axial detection technique with antiprotons will

be to count a few hundred or thousand antiprotons using the same techniques for counting electrons mentioned in section 4.3.2 where the particles coupling to the LC circuit create two peaks separated by a distance $\Delta\omega$ [78]. In the regime of a few million particles it is safe to use the scaling law of $\Delta\omega \propto \sqrt{N}$ but in the limit of a few hundred particles you must use the full power spectrum prediction to get a proper count [45]:

$$P(\omega) \propto \frac{\omega_{LC}^4 \left(\omega_z^2 - \omega^2\right)}{\left[\left(\omega_z^2 - \omega^2\right)\left(\omega_{LC}^2 - \omega^2\right) - \omega^2\Gamma N\gamma_z\right]^2 + \omega^2\Gamma^2\left[\left(\omega_z^2 - \omega^2\right) + \Gamma N\gamma_z\right]^2} \tag{7.9}$$

where $\Gamma = \Delta\omega_{-3dB} = Q\omega_{LC}$, $\gamma_z = \left(\frac{d_1 e}{2z_0}\right)^2 \frac{Q^2 r}{m}$ and r is the series resistance of the LC circuit.

This technique has been used to count hundreds of protons [45]. Since this measurement only relies on the frequency separation of the peaks and not on any measure of signal strength, as long as we are able to resolve the peaks it should be possible to get an accurate count. It remains to be seen how small of a number we can count with this decreased signal strength. Critical to this method is to reduce the radius of the antiproton cloud through the use of a sideband cooling [20] technique, where a frequency $\nu_z + \nu_m$ is applied to a split compensation electrode (shown on the bottom of figure Fig. 7.1). While this has yet to be successfully accomplished in the new apparatus, there are no reasons as to why it should not work just as well as in the previous setup.

7.1.2 Cyclotron Detection Signal Expectation

Unlike the axial motion, the modified cyclotron motion of antiprotons does depend on the magnetic field and we do expect to see a decrease in our signal due to operation

at 1, rather than 5-6 tesla for a given cyclotron radius. Starting from equation (7.1) the current generated on our split ring electrode by a particle moving in the center of the quadrupole potential will be given by [25, 79]:

$$I_c = \alpha \frac{q}{2\rho_0}\dot{\rho} \tag{7.10}$$

where $\alpha = 0.356$ is a constant independent of absolute electrode size, calculated from a non-azimuthally symmetric Legendre polynomial and Bessel function expansion (where the ϕ dependence must be taken into account) similar to what we did chapter 2. In the non-relativistic limit, which we can safely use for antiprotons in small orbits, the radial velocity will be given by $\dot{\rho} = \omega_c'\rho_c'$, where ρ_c' is the size of the modified cyclotron orbit. Given the cyclotron frequency (neglecting the small voltage contribution) $\omega_c = \frac{qB}{m}$, the effective resistance of our circuit is given by:

$$R_{eff} = Q\omega_c L = \frac{Q}{\omega_c C_{trap}} = \frac{Qm}{qBC_{trap}} \tag{7.11}$$

As with the axial case the expected signal to noise ratio is given by:

$$\frac{V_s}{V_n} = \frac{I_c R_{eff}}{\sqrt{4k_B T R_{eff}\Delta\nu}} \tag{7.12}$$

As before if we keep $T, \Delta\nu$ and Q the same and put in the magnetic field dependence we would expect that our signal to noise for a given cyclotron radius goes as:

$$\frac{V_s}{V_n} \propto \frac{1}{\rho_0}\sqrt{\frac{B}{C_{trap}}}. \tag{7.13}$$

The distributed capacitance going to the split ring electrode on the new apparatus has been measured to be 32 pF, whereas in the precision proton antiproton mass measurement, the trap capacitance was 7.5 pF [79]. We are operating at a 1 tesla

field compared to their 5.85 T field [25], and as stated before the radius is larger by a factor of 3. Putting all this together we expect a $3\sqrt{5.85}\sqrt{\frac{32}{7.5}} \simeq 15$ times reduction in our signal power at 1 T, and $3\sqrt{\frac{5.85}{3}}\sqrt{\frac{32}{7.5}} \simeq 8.7$ times reduction in our signal power if we operated at 3 T for the same radius cyclotron orbit.

Even with this reduction, the detection of the cyclotron motion of single antiprotons is sensitive enough that we should still expect to see a signal. However, we would expect that we would have to put more energy into the cyclotron motion compared to previous experiments. In past experiments, the relativistic mass shift of the frequency

$$\delta\nu_c' = \nu_c'(\gamma m_0) - \nu_c'(m_0) \tag{7.14}$$

has been a reliable way to gauge the energy of the cyclotron orbit they were able to detect. As energy is put into the cyclotron motion, by sweeping a drive on the other half of the split ring electrode across the cyclotron frequency, the amplitude and velocity of the cyclotron orbit increases and the accompanying increase in mass leads to a decrease in the frequency. As the drive is turned off and the energy in the cyclotron motion is damped out through coupling to the external circuit, the orbit decreases in size, and the frequency increases. The frequency is expected to shift by [79]:

$$\nu_c' = \nu_c'(\gamma = 1) - \delta\nu_c'(t = 0)e^{-t/\tau} \tag{7.15}$$

where τ is the damping time constant set by the effective resistance of the tuned circuit on resonance. In reality this R_{eff} and thus τ vary as the frequency of the particle changes and moves across the resonance, but the variation is small enough to neglect. By fitting the decay of the frequency over time to an exponential, they were able to extrapolate out what the zero kinetic energy $\gamma = 1$ limit of the frequency should be.

ρ_0	6 mm	18 mm	
Magnetic Field	5.85 T	1	3
$\Delta\nu_c'$	0.5 Hz	3.5 Hz	31.7 Hz
E_c'	5.3 eV	34.5 eV	103.5 eV
ρ_c'	56 μm	850 μm	490 μm

Table 7.1: Minimum detectable cyclotron orbits in different electrode and magnetic field configurations. Values at $\rho_0 = 18$ mm are derived from the other measurement, assuming we can detect the same signal to noise ratio.

In the most sensitive measurements taken in 1995 and 1996, the last measured state (at which point the signal fell below the noise level where they could read it) were $\delta\nu_c' = 0.3$ Hz and $\delta\nu_c' = 0.09$ Hz respectively [79]. A more typical last measurement was around $\delta\nu_c' = 0.5$ Hz [25]. Taking this last, more conservative estimate of the detection sensitivity, we can extrapolate what is the minimum cyclotron radius we can expect to see under our conditions.

A 0.5 Hz shift in the modified cyclotron frequency in a 5.85 T field corresponds to a cyclotron energy of 5.3 eV and a radius of 56 μm, and in their setup would have generated a current amplitude of $I_{c1} = 1.06$ fA. To generate the same signal to noise, we need to generate a current on the electrodes $I_{c2} = \sqrt{\frac{B_2 C_{trap2}}{B_1 C_{trap1}}} I_{c1}$. From this, we can use (7.10) to determine the necessary velocity and thus energy, cyclotron radius and frequency shift due to the mass change to meet this minimal detection threshold. The results of these calculations are shown in Table 7.1.

The numbers given in Table 7.1 represent the best we can hope to do if we reproduce the results of the precision proton/antiproton mass measurements taken in the 1990s. They make two crucial assumptions that we must still work hard to accomplish.

The first is that we can achieve a similar quality factor Q for our tuned circuits, even though we are operating at a lower frequency. If we include the Q of the circuit as a variable, then our signal to noise power goes as

$$\frac{V_s}{V_n} \propto \frac{1}{\rho_0}\sqrt{\frac{QB}{C_{trap}}} \tag{7.16}$$

and we can expect a loss in signal proportional to the square root of Q.

The second assumption is that the Johnson noise in the circuit is the dominant source of noise that we must contend with, and not an external source of noise getting down to our electrodes and amplification stages. If the noise level goes up, we will need an even larger current induced on the electrodes in order to see the particles. The next two sections will discuss the efforts undertaken to reduce the noise getting down to our experiment, and proper circuit design to maximize the performance of our amplifier.

7.1.3 Antiproton Decelerator Noise Spectrum

The antiproton decelerator, and CERN in general, is a very electrically noisy environment and is one of the last places you would choose to to do a sensitive radio frequency measurement were it not for the need of antiprotons. The many magnets and radio frequency supplies needed to run the accelerators as well as the other experimental collaborations in the hall mean that there are many sources of noise, which change over time, that we have no control over, that can obscure the tiny signals we are trying to detect.

Fig. 7.3 shows the noise spectrum broadcast in the AD, recorded by attaching a wire loop antenna to a spectrum analyzer. We have made substantial efforts to reduce

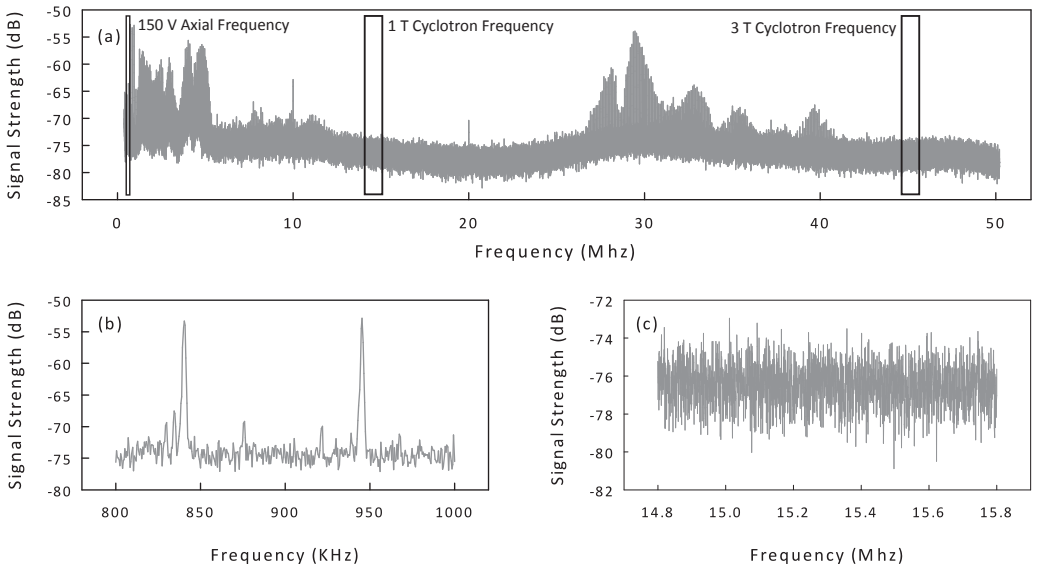

Figure 7.3: The noise spectrum in the antiproton decelerator near our experiment. (a) The spectrum from 400 kHz to 50 MHz, with the regions of the antiproton axial, 1 T and 3 T cyclotron tuned circuit resonances highlighted. (b) The 150 V axial tuned circuit resonance area. (c) The 1 T cyclotron tuned circuit resonance area.

the amount of noise that comes into our trap by ensuring that our experiment is surrounded in a faraday cage by conducting material in all directions and by eliminating ground loops, but a substantial fraction of the AD noise does manage to get down to our electrodes. As we can see there is a substantial amount of noise in the region of the axial amplifier around 1 MHz. Fortunately, we can tune the axial frequency simply by changing a voltage, so we just need to pick an inductor value for our tuned circuit that in parallel with the trap capacitance will place the resonance away from one of the large noise peaks. The two areas for doing cyclotron detection at 1 and 3 T are relatively clean, but depending on the day a substantial amount of noise shows up in that region as well. The large amount of noise around 30 MHz makes us wary of attempting cyclotron measurements around 2 T.

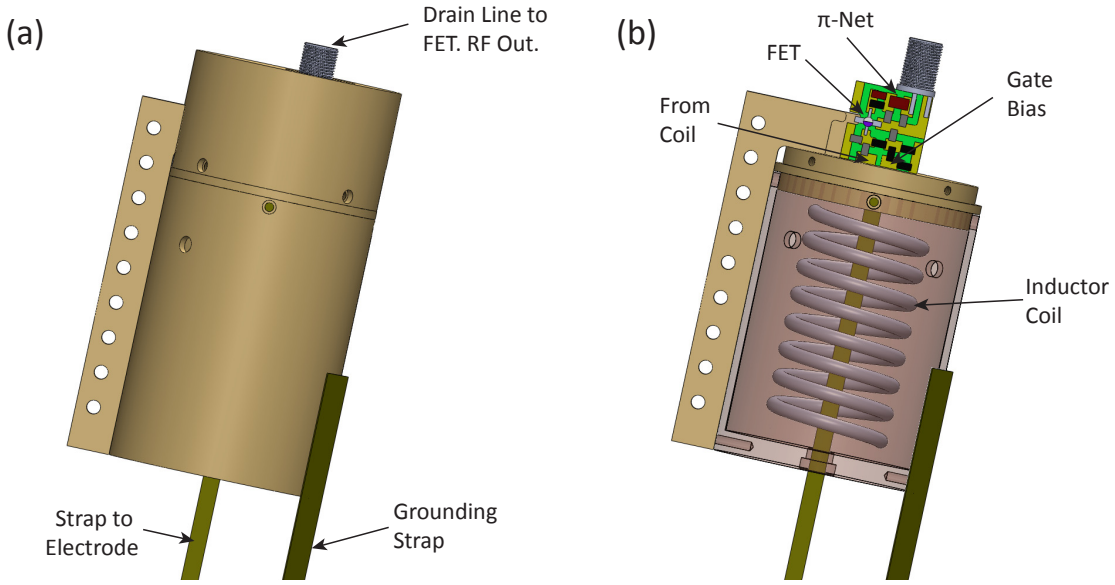

Figure 7.4: The mounting and setup of the coil and circuit board for our tuned circuit amplifiers. (a) External view of the amp can as it is mounted near the pinbase. (b) Inductor for the tuned circuit and printed circuit board with FET and other components shown.

7.1.4 Amplifier Circuit Design

The other crucial assumption underlying the calculations of signal expectation in sections 7.1.1 and 7.1.2 is that we are able to produce circuits that have a comparable quality factor Q of their resonance. Doing so is not a trivial task, and is the product of years of dedicated design work. A number of factors in the amplification chain can degrade the Q and signal of a circuit. Here a brief description of the circuit elements needed to maximize the performance of our amplifiers will be given.

Our tuned circuit amplifiers are located inside cylindrical copper or superconducting cans mounted near the pinbases surrounding our electrode stack as shown in Fig. 7.4. They are heat sunk to the pin base, and therefore reach the ambient temperature of our trap (1.2 or 4.2 K). There is a larger bottom area where the coil

is located. Because of the large inductance and precise tuning needed for these coils, they are hand wound by members of the Harvard group. For higher frequencies where a smaller inductance, and thus less turns, is needed a free standing coil is used where it can be simply supported by a copper strap connecting to the electrodes. This is the preferred method as a free standing coil will have less distributed capacitance and therefore a greater effective resistance on resonance. For lower frequencies the number of turns increases, requiring a smaller gauge wire and a teflon form to support it. Our 1 T cyclotron amplifier and electron axial amplifier were wound on teflon forms. For 3 T, it is possible to use a free standing coil for the cyclotron amplifier.

Due to the very large inductance and large number of turns needed to create a tuned circuit amplifier at the 1 MHz proton axial frequency, a superconducting coil made of NbTi also wound on a teflon form is used, to avoid the parasitic resistance which would otherwise prohibitively degrade the Q of the tuned circuit. Superconducting material cannot be used to detect the other motions, as we do not know of a material which remains superconducting at those higher frequencies.

Above the cylindrical housing which contains the inductor for the tuned circuit, a second cylindrical cavity contains a printed circuit that has a Fujitsu (or Eudyna) FHX13LG HEMT (high electron mobility transistor) FET and accompanying filtering and impedance matching circuits. The applicability of this FET to these types of experiments has been previously studied by members of the Gabrielse Harvard group conducting experiments on the electron magnetic moment [83].

The circuit elements for the three amplifiers that were used in the BTRAP apparatus in 2008 are shown in Fig. 7.5, and although they operate at different frequencies,

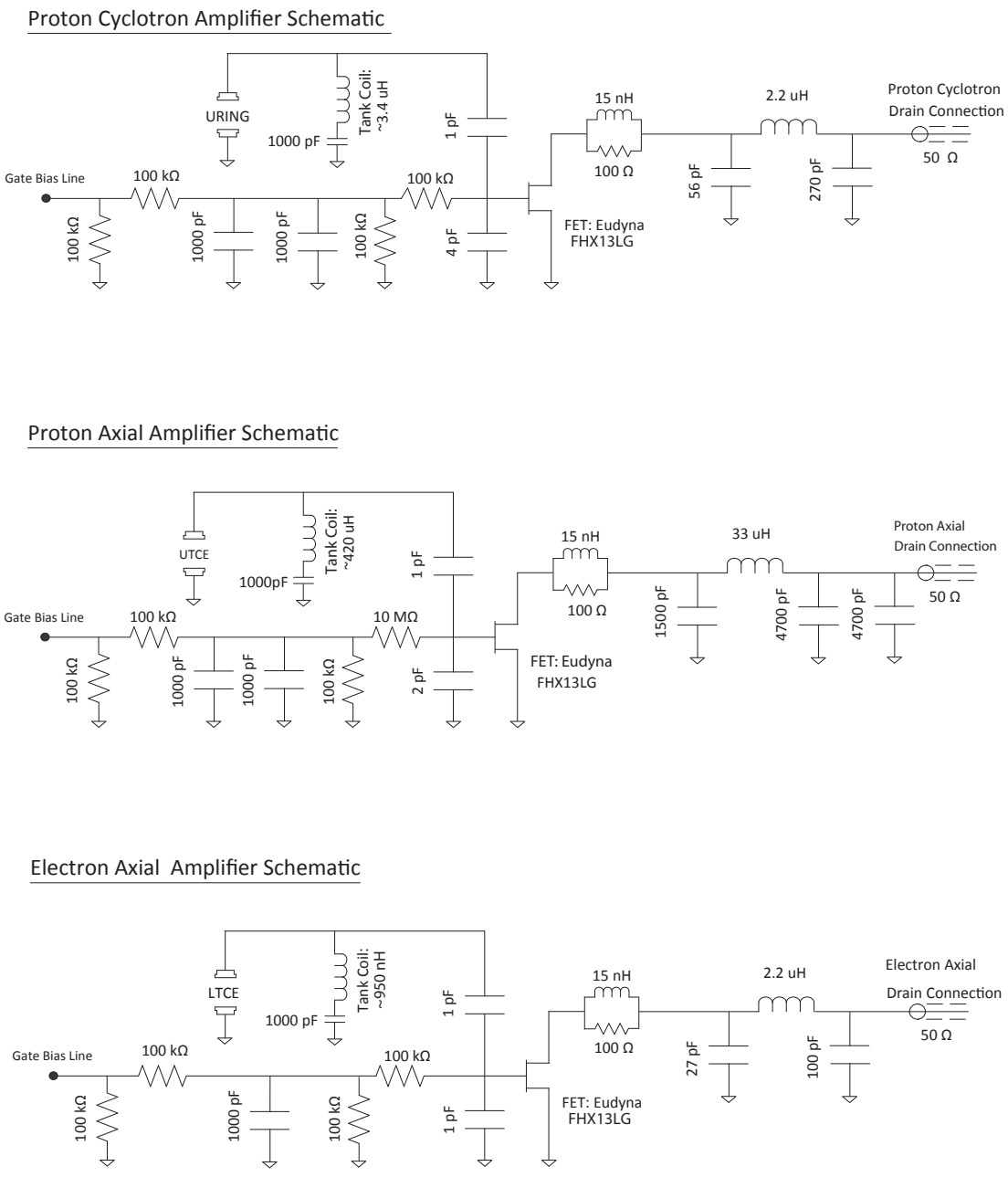

Figure 7.5: The schematics for the tuned circuit, filtering and impedance matching networks for the three particle motion amplifiers.

the components serve essentially the same purpose. Going from the gate bias line to the gate of the FET, there are a series of resistors and capacitors to ground that serve as protection for the gate of the FET and for some additional filtering. It was found that at CERN that FETs would occasionally acquire a permanent malfunction (a high drain current unresponsive to gate voltage) if we did not have a resistor to ground in order to dissipate any accumulated charge. In past experiments it was suspected that the cause of the FET malfunction was due to the presence of the radioactive positron source [23], but we experienced blown FETs even with no source present when the resistors were removed. The electron axial and proton cyclotron amplifiers have an effective resistance in the range of 100 kΩ so putting 200 kΩ to ground does not overly affect the performance of the amplifier. The proton axial amplifier has an effective resistance of several MΩ which is why a 10 MΩ resistor is placed in the protection circuit in that case. The capacitors working with the series resistor provide a low pass filter cutting off frequencies above 10 kHz.

The purpose of the capacitive divider coming in from the electrode and the coil is to increase the effective input resistance of the transistor [83]. A simple model where the FET has an input resistance R_1 between its gate and ground has the possibility of diminishing the effective resistance of the tuned circuit on resonance. The effect of the capacitive divider, with capacitors C_1 in series and C_2 to ground can be understood by rewriting that part of the circuit element as an equivalent single capacitor and single resistor in parallel to ground as shown in Fig. 7.6. By matching the real and imaginary parts of the impedance in these two circuits we find that

$$R_A = \frac{1 + \omega^2 R^2 (C_1 + C_2)^2}{\omega^2 R C_1^2}, \tag{7.17}$$

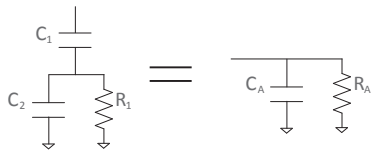

Figure 7.6: Equivalent circuit to understand the effect of the capacitive divider at the gate of the FET.

meaning the effect of the capacitive voltage divider is to increase the effective input resistance of the FET by a factor of $\frac{(C_1+C_2)^2}{C_1^2}$. The divider also reduces the overall signal to the gate and slightly detunes the resonance, so a balance in the ratio must be struck.

The small inductor and resistor in parallel at the output of the drain on the FET are a suppression circuit used to add loss at higher frequencies in order to suppress unwanted oscillations and improve stability. Past the oscillation suppression circuit is a π-network which serves to transform the 2 kΩ output impedance of the HEMT [83] to the 50 Ω impedance of the transmission line.

We have benefited tremendously from the ongoing proton experiments at Harvard. More details of the optimization and design of these amplifiers will be described in a forthcoming thesis [84].

7.2 Axial Proton Detection

Unfortunately, no axial signals from antiprotons were detected during the 2008 beam run. There are two main possibilities as to why we were unable to see a signal, even though there were definitely antiprotons in the trap and they were oscillating at the expected axial frequency (see Fig. 7.11c).

The first possibility is that the Q of our amplifier was not sufficiently high to generate a proper signal to noise ratio for the number of antiproton numbers we had, usually $10,000$ but a few attempts at detection were made with greater than $100,000$. We were able to achieve a Q of 10,000 or more when trying the amplifier out on a test jig, using a test capacitor instead of the trap capacitance, but the same amplifier placed on the experiment could not achieve a Q much above 200. As of the writing of this thesis, the cause of this degraded Q has yet to be identified.

The second possibility is that the significant amount of electrical noise present near the resonant frequency of our amplifier drowned out the relatively small signal from the antiprotons. Efforts to bring the noise getting into our trap under control and to raise the Q of the amplifier on the trap are underway, and we are confident we will able to see an antiproton axial signal soon. We were, however, able to see a proton signal on one of the axial amplifiers in our experiment as will be described in the following sections.

7.2.1 Proton Loading Method

To load protons we followed the methods used for previous antihydrogen related proton experiments conducted at Harvard [25]. This method requires a continuous beam of electrons and we used an electron gun located in the positron accumulator [72] with the beam steered through the transfer line described in chapter 6. Our collaborators from York University already had this capability set up as they were using it to aid in their steering through the transfer guide. It was found that to get a high number of electrons into the magnetic field, they had to be given close to 300

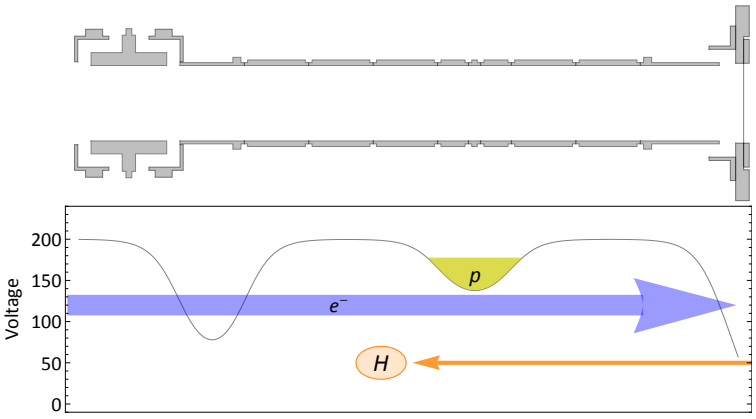

Figure 7.7: Procedure for trapping protons in the lower stack using the York electron gun.

V of axial energy. The high potential shown in Fig. 7.7 is used to slow the electron beam before it strikes the degrader to attempt to lower the energy of the electrons and entering the well.

The electron beam strikes the degrader releasing hydrogen atoms from its surface. A portion of these are ionized as they pass through the electron beam and settle into the potential well for protons. After their capture the protons are moved from the lower stack into the upper stack harmonic well where their axial signal can be detected by the amplifier on the upper compensation electrode (UTCE).

7.2.2 Axial Frequency Mass Scan Results

In addition to loading protons, the procedure outlined in the previous section also liberates other atoms and molecules off of the degrader. They too get ionized and can get confined in the same well as the protons. The species of ions located in our trap under these conditions can be probed by changing the voltage of the well and observing the response on a spectrum analyzer. The axial frequency (given in

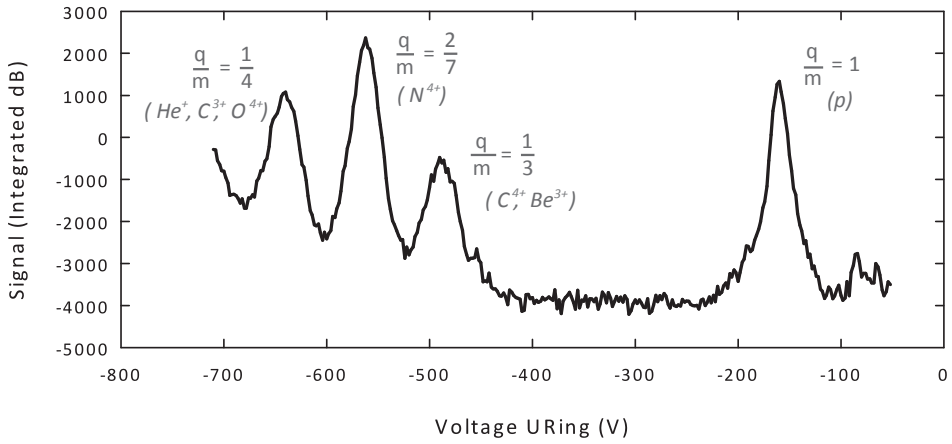

Figure 7.8: Axial resonance mass scan after loading positive ions into the trap. All of the charge to mass ratios are normalized so that the charge to mass ratio of the proton is 1. Possible ion species are indicated in the parentheses.

equation (7.5)) of the different ions is determined by their charge to mass ratio. Our tuned circuit amplifier is at a fixed frequency, 965 kHz for these experiments, but the different ions can be brought into resonance with the circuit by changing the voltage in the well.

To conduct a mass scan measurement we integrate the response of the circuit on a spectrum analyzer over a region (+/- 10 kHz) surrounding the peak of the tuned circuit resonance. We record the integral totals as we change the voltage on the electrode. As we can see in Fig. 7.8, we get a strong, but very broad, response centered around about -160 V corresponding to the oscillation of protons, and then other peaks around - 480 V, - 560 V and -640 V corresponding to ions that have charge to mass ratios 1/3, 2/7 and 1/4 that of protons respectively.

The peaks that we saw in the limited number of mass scans conducted in 2008 were very broad compared the typical mass scans conducted in past proton loading

experiments [45]. The broadness of the peaks (a full width half maximum of nearly 50 V) cannot be attributed to the range that we integrated over. A width of 20 kHz corresponds to less than 10 V. Nor can it be attributed to the ions taking some time to change their resonant frequency as scans that increased and decreased the voltage yielded the same result. As we are not sure how many particles we have loaded into the trap and at what energy, the more likely candidates for the broadness of the peaks are collisions between the ions which smear out their frequencies and particles with a high enough energy that they are not only sampling the quadratic part of the well.

In order to prevent unwanted positive ions from entering the trap as we are loading protons, a noise drive put through a low pass filter and a couple notch filters during and after the loading process has been found to successfully load only protons [45]. For a given voltage protons will oscillate at the highest axial frequency as all of the other ions have lower charge to mass ratios. Putting the filter's -3 dB point in between the closest ion species frequency and the proton frequency would clean out the unwanted ions, with the notch filters right at the proton frequency providing additional protection so as not to drive them out. This method was not successfully implemented in 2008, but the driving and filtering hardware is setup for use. You can also use a proton axial amplifier to damp the motion of the protons while heating the other ions, but our axial amplifier was in the upper stack, not the lower stack where we were loading. Loading protons into the upper stack would be difficult due to the small solid angle seen by hydrogen atoms leaving the degrader.

7.3 Cyclotron Antiproton Detection

Antiprotons that are loaded using the electron cooling methods described in chapter 5 quickly come into thermal equilibrium with the electrons, which in turn have come into thermal equilibrium with the trap. This corresponds to an energy far below an eV and, as we can see from Table 7.1, an energy too low for us to detect on our cyclotron amplifier. To see a signal from the cyclotron motion we must excite the cyclotron orbit by applying a drive on the other half of the ring electrode (see Fig. 7.1b) from where we are detecting. A drive is swept from a high to low frequency across where we believe the cyclotron resonance of the antiprotons is and we conduct measurements after the drive is turned off. The drive is swept from a high frequency to a low frequency so that we can follow the relativistic mass shift in the frequency at higher energies, and continue to drive the motion. Using this technique we are able to detect both very large numbers of antiprotons as well as the signals from single antiprotons.

7.3.1 Large Antiproton Clouds and Magnetron Sidebands

The behavior of large antiproton clouds gives a big enough signal in amplitude over a broad enough frequency range that we can observe its behavior by using an Agilent E4402B spectrum analyzer (setup shown in Fig. 7.2) without further mixing down the signal. Fig. 7.9 shows the behavior of a cloud of about 50,000 antiprotons that has been driven across its cyclotron frequency. The cloud stays excited and we can continue to detect its frequency as we change the voltage in the harmonic well. Even when there is a substantial amount of noise on the spectrum analyzer,

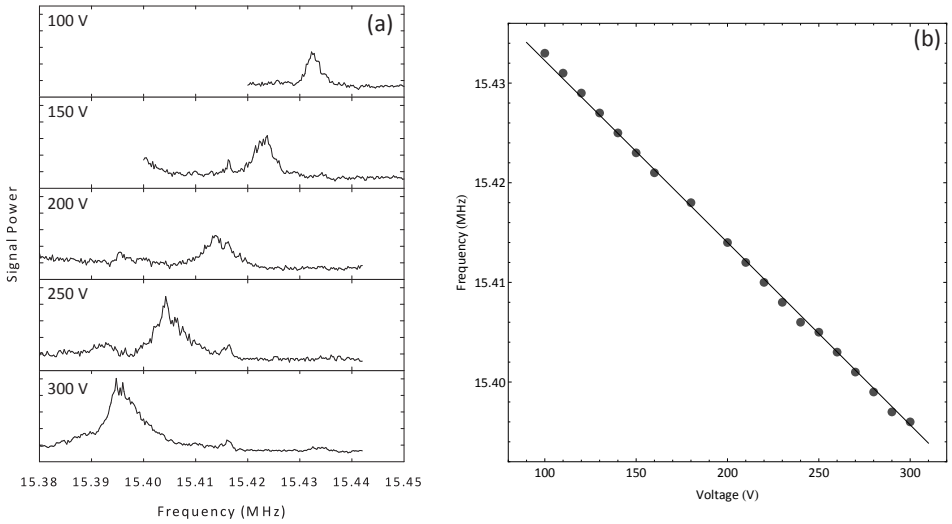

Figure 7.9: (a) The spectrum analyzer traces of the cyclotron peak as we change the voltage in the harmonic well, with the peak location shown in (b). The line represents the modified cyclotron frequency vs. voltage using the magnetic field implied by the frequency at 200 V.

the cyclotron peak of the antiprotons can be identified by looking at how the peak changes with voltage.

As described in chapter 2, the radial motion of the particles consists of both a rapid modified cyclotron velocity and a slower magnetron orbit. It is difficult to detect the magnetron orbit directly because it is at a low frequency where it is much more challenging to construct an efficient tuned circuit and there is more noise to contend with. However, the FET that we use as our initial amplification stage does some frequency mixing and makes it possible to detect the sum and difference frequencies of the modified cyclotron and magnetron motion. The drain current response of an FET in the saturation region is given by [47]:

$$I_D = k(V_{GS} - V_T)^2 \tag{7.18}$$

where V_{GS} is the gate source voltage on the FET, V_T is the characteristic turn on

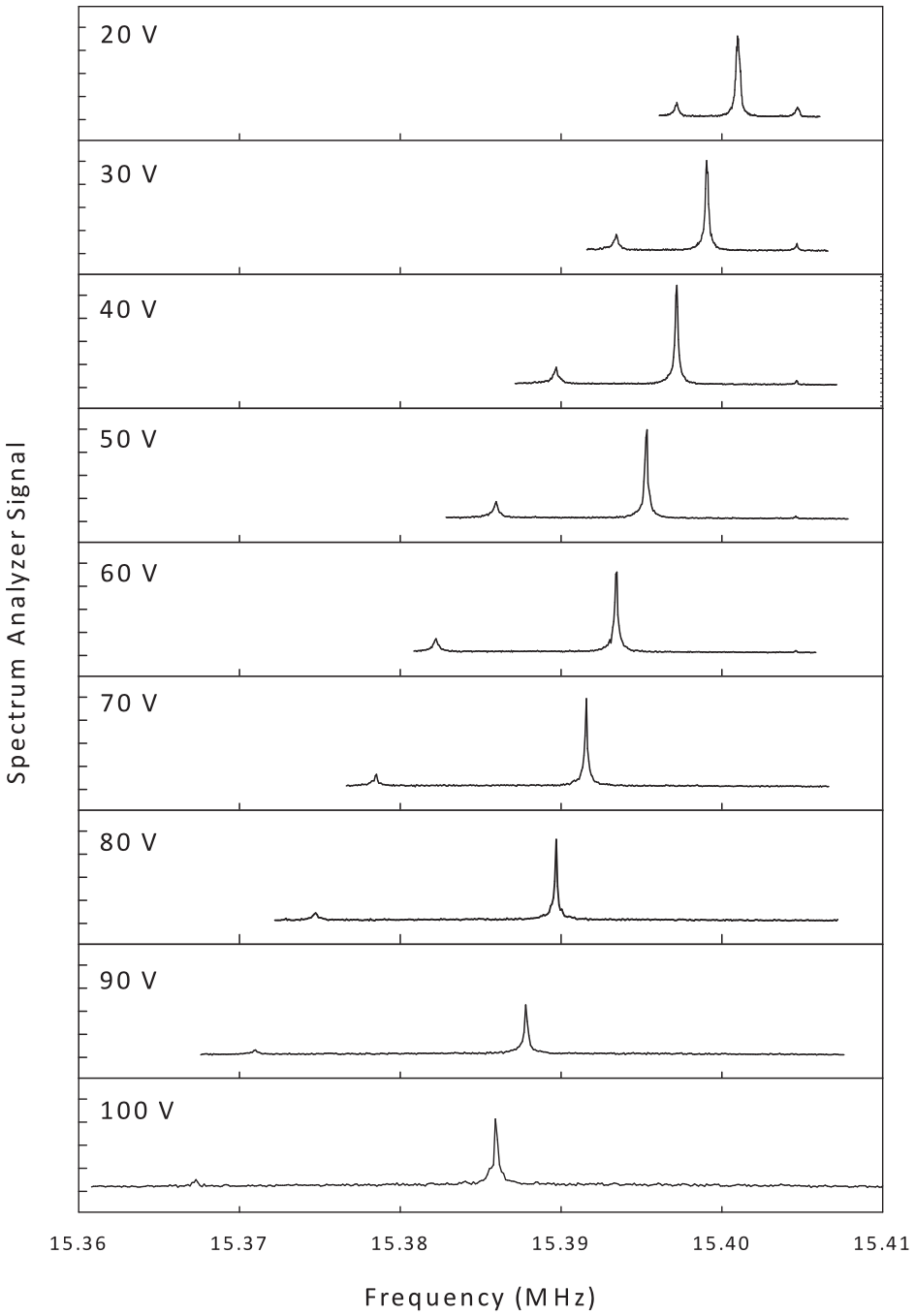

Figure 7.10: Magnetron sidebands on either side of modified cyclotron peak for about 50,000 antiprotons, changing with voltage on the harmonic well.

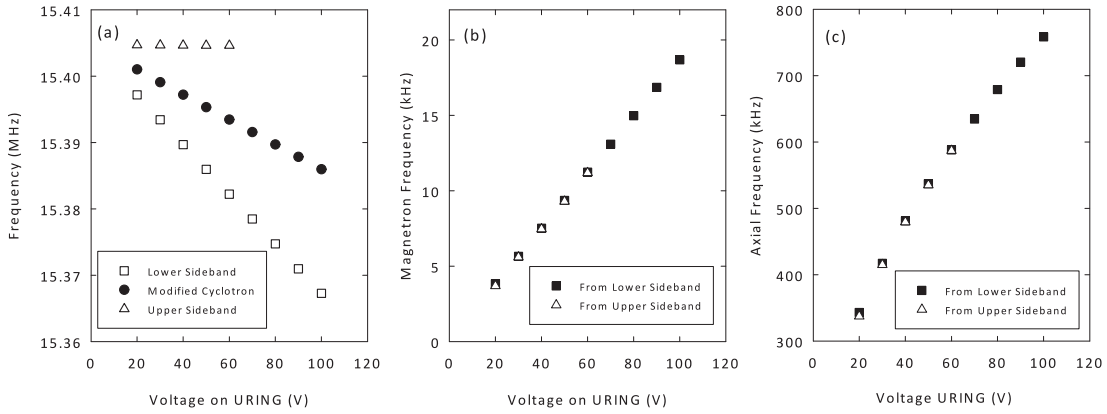

Figure 7.11: (a) Modified cyclotron frequency and sidebands vs. voltage. (b) Magnetron and (c) axial frequencies derived from them.

voltage on the gate and k is another FET dependent constant. Specific curves for our FETs confirm that we operate in a regime with a quadratic component [83]. When the two frequency components of the motion are multiplied by each other we get frequency components at $\omega_c' \pm \omega_m$ that we can see on our spectrum analyzer for large clouds of antiprotons, as shown in 7.10. The tuned circuit resonance does not completely filter out the magnetron signal before it gets to the FET due to the 1000 pF capaciator between the tuned circuit coil and ground (see Fig. 7.5) which is meant to block the DC voltage applied to the electrode, but in this case provides approximately 100 kΩ impedance at the magnetron frequency in the tens of kHz.

The observation of both the modified cyclotron and magnetron frequencies allows us to determine the magnetic field, voltage in the harmonic well, cyclotron and axial frequency of the particles without any other measurements. As was shown in chapter 2 (see equation (2.39)), the cyclotron frequency is $\omega_c = \omega_c' + \omega_m$, and the axial frequency is $\omega_z = \sqrt{2\omega_m\omega_c'}$. The magnetic field and voltage applied on the harmonic well follow

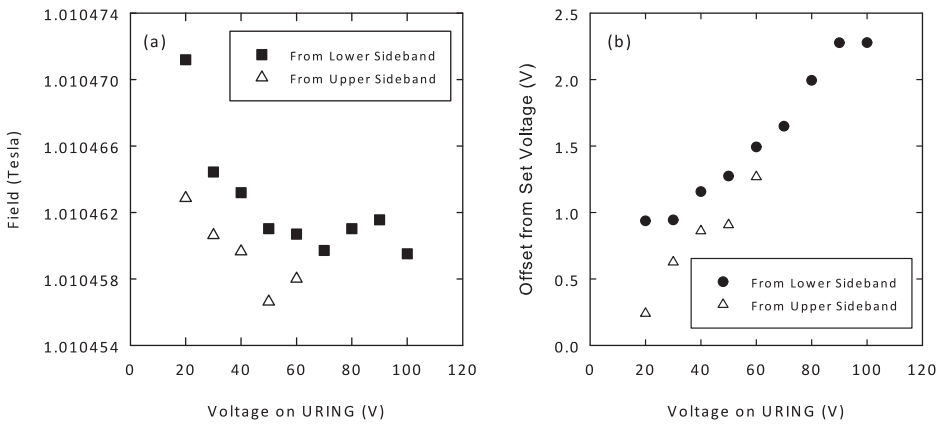

Figure 7.12: (a) Magnetic field and (b) voltage derived from the modified cyclotron and magnetron frequencies.

from these (equations (2.34) and (2.36)).

The peaks in Fig. 7.10 have been fit with Lorentzian functions, whose centers have been taken as the frequencies for calculating the magnetron and axial frequencies in Fig. 7.11 and for calculating the magnetic field and actual voltage applied to the electrodes in Fig. 7.12. The calculations assume that there is a negligible relativistic mass shift on the antiprotons, that the magnetic field is uniform and that the particles truly are moving in a quadratic potential. Given these assumptions, they allow us to identify the magnetic field to better than a Gauss, and indicate that this particular voltage source may be providing a voltage that is off by a volt or more when it gets down to the electrodes at higher voltages. In the future this could be a useful technique for characterizing the magnetic field and voltages applied in precision experiments.

7.3.2 Single Antiproton Detection

In past antiproton experiments where they have been able to detect single antiprotons, reducing the number of antiprotons was a well established procedure [25]. A drive was applied to excite the cyclotron motion of a cloud of antiprotons, and their mixed down response could be seen on an HP3561A dynamic signal analyzer. As the voltage in the well was lowered, the antiprotons with a higher axial energy would leave the trap, until single antiproton signals could be seen over a span of less than a kHz. The voltage was further reduced until the antiproton signals would disappear off the signal analyzer one at a time until a single antiproton remained. We had substantial difficulty implementing this procedure in the new apparatus due to the decreased signal and because the antiproton cyclotron response signals were not confined to a few hundred Hz but rather spread over a range of nearly 4 kHz.

There are two possible sources of large shifts in the modified cyclotron frequency, the first is due to the relativistic mass increase of the particles as they gain more energy, the second is due to magnetic field inhomogeneities in the experiment. As described in Table 2.4, the highest energy antiproton that can remain in our trap before hitting the 18 mm radius electrode at 1 T is about 15.5 keV, corresponding to a relativistic mass shift on the cyclotron frequency of at most 252 Hz. For the previous experiment conducted at 5.85 T and in 6 mm radius electrodes, the maximum radial energy of an antiproton was 59 keV, corresponding to a frequency shift of 5.6 kHz. If we see shifts larger than 252 Hz in our trap, it is an indication of a non-uniformity in our magnetic field.

The simplest term for understanding the change in the frequency due to changes

in the magnetic field is the magnetic bottle term B_2 such that the field can be written as:

$$B(\rho) = B_0 + \frac{B_2}{4}\rho^2 \tag{7.19}$$

as any linear gradient term would average out over a magnetron or cyclotron orbit.

In the precision antiproton experiments of the 1990s, this bottle term was measured to be $B_2 = 0.5$ Gauss/cm^2 [79]. This corresponds to a shift of 68 Hz for an antiproton at the maximum possible radius in the trap compared to one at the center. This large radius can be either due to a large magnetron or large cyclotron orbit. In order to get a 4 kHz shift in the frequency of our antiprotons at 1 T, we would need a magnetic bottle term of at least $B_2 = 3.24$ Gauss/cm^2. This non-uniformity will be discussed more in section 7.3.3.

In order to be able to observe the antiprotons leave the trap as they did in the previous experiments we need to set our spectrum analyzer bandwidth small enough to see the peaks disappear one by one. However, if the antiprotons are separated by a large frequency spacing compared to their bandwidth it is difficult to observe them all at the same time. This problem could be mitigated by applying a magnetron sideband drive [20] which would reduce the magnetron orbit so that as the cyclotron orbit cooled, they would all damp down to the same frequency. This was not successfully implemented in 2008, but is a means of dealing with the larger gradients in the future.

To reduce the number of antiprotons in the trap, we utilized a different technique. We applied a strong cyclotron drive at a voltage where the particles were in resonance (100+ volts) with the axial amplifier in order to damp their axial motion. We would then lower the voltage to below a volt and when we would bring the particles back

into resonance we would see that the signal had almost disappeared. We would then reapply the drive and a strong cyclotron signal would reappear. This indicated to us that we were losing the most strongly excited particles when we would dip down the voltage. The mechanism for this is not clear, as neither the magnetron or modified cyclotron orbit increase appreciably as you decrease the voltage. It could be that some of the higher energy radial energy was transferred to axial motion through collisions. It could also be that the presence of insulating patch effects on the electrodes leads to stray potentials which cause particles at large orbits to leave the trap. Whatever the mechanism, when we repeatedly use this drive dip technique, we are able to get to a very small number of antiprotons, such that we can still see signals on the spectrum analyzer even when the none are detected above the noise level on our annihilation fiber and paddle detectors.

The linewidth of the cyclotron frequency of a single antiproton has been observed to well below a Hertz [25]. From calculations done in section 7.1.2 summarized in Table 7.1 we expect that we have to give an antiproton more than 5 eV of energy before we are able to see it. Because it is hard to spot a lone antiproton signal when there is noise surrounding the tuned circuit resonance, it is necessary to give it substantially more than 5 eV of energy so that we can properly identify the peak and follow it as its frequency changes. Once we have "picked up the trail" of this antiproton, it is relatively easy to follow it as its frequency increases and energy, and thus signal, decreases.

This high energy antiproton will have a narrow linewidth and its frequency will be changing quite rapidly. In order to see it we must therefore look at it on a spectrum

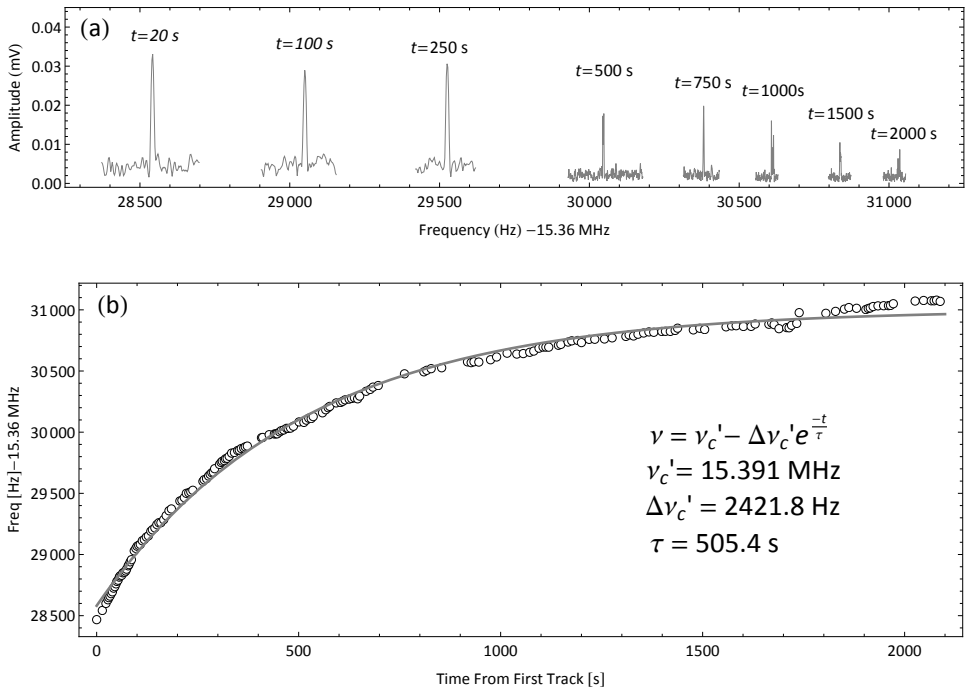

Figure 7.13: The energy decay of a single antiproton observed for 30+ minutes. (a) The signal as it appeared on the signal analyzer. (b) The frequency over time fit with an exponential.

analyzer that has a rapid sweep time so that the narrow linewidth is not averaged out amongst the noise. For this reason, we mix the signal coming from the amplifiers (see Fig. 7.2) down by 15.36 MHz and look at the remaining signal $\nu_c' - 15.36\text{MHz} < 100\text{kHz}$ on an HP3561A dynamic signal analyzer that can perform fast fourier transforms at a fast enough refresh rate for us to resolve the rapid motion of this narrow peak.

The decay of a single antiproton peak detected in this fashion over the course of more than 30 minutes is shown in Fig. 7.13. We attribute this peak as being due to a single antiproton for two reasons. First, sweeping a very narrow drive through it prior to taking this data did not cause it to split into two peaks, as usually happens in the case of two antiprotons. Second, the peak did not split into several peaks over

the course of the 30 minute scan. This scan was the result of two averages per data point in order to reduce the noise, and therefore the linewidth is slightly more broad than a similar scan with no averaging.

Although we believe this to be the signal from a single antiproton, we do not believe that this was the only antiproton in the trap during the measurement. In fact, the deviations from the exponential decay seen in Fig. 7.13b, especially near the end are likely due to interactions with other antiprotons in the trap at frequencies outside of our scanning range.

Demonstrating that we are able to detect single antiprotons in this fashion is a large step forward for our experiment on a couple of fronts. It allows us to detect and then dump out small numbers of antiprotons in order to calibrate our detectors. It also gives us the sensitivity needed for possible antihydrogen ion experiments, as will be discussed in 8.

7.3.3 Resonant Characterization of the Magnetic Field

Fig. 3.1 showed measurements with an NMR probe conducted in 2002 indicating that the uniformity of the field surrounding the electrode stack was better than 1.5 parts in 10^{-4}. This would place the maximum magnetic bottle term (see equation (7.19)) in our electrodes at $B_2 = 0.98$ Gauss/cm^2 at a central field of 1 T. As was discussed in the previous section, however, the shift in the modified cyclotron frequency that we detect indicates that we have a bottle term which is at least $B_2 = 3.24$ Gauss/cm^2.

We can see from Fig. 7.13 that a single antiproton has been obeserved to vary by

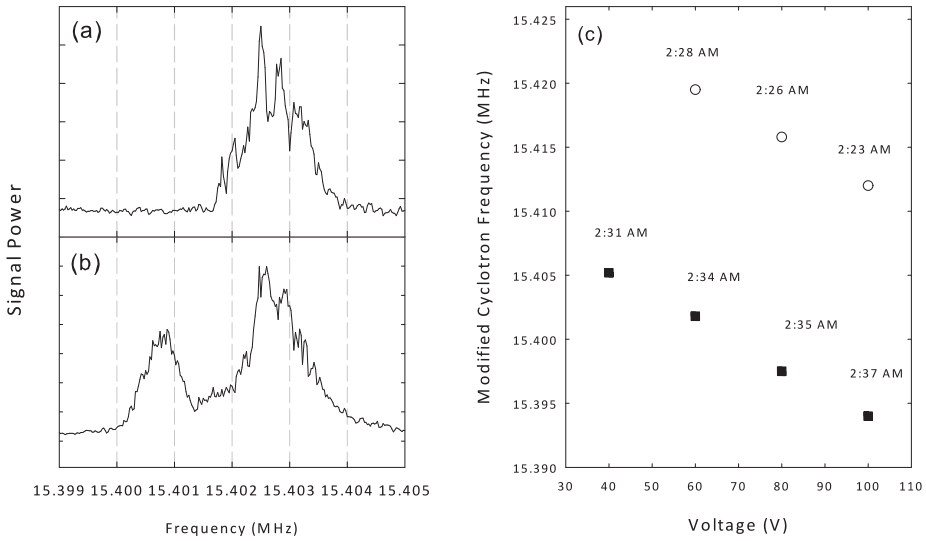

Figure 7.14: (a) Maximum observed shift in the modified cyclotron frequency indicating field inhomogeneities. (b) Unexplained modified cyclotron frequency jump after cycling the Ioffe trap.

2.5 kHz over the course of its decay. This places a lower bound on the size of the bottle. To try to get a sense of how big this bottle term was, we took a large cloud of antiprotons and tried to see how much of a change in frequency we could cause by driving them repeatedly to increase the size of their cyclotron orbits. Fig. 7.14a shows the modified cyclotron frequency response of a cloud of antiprotons with a width of 2 kHz after a drive is applied to it. By repeatedly applying more drives and sweeping down further in frequency we are able to excite some antiprotons to even lower frequencies shown in Fig. 7.14a. The largest frequency shift we could induce in an antiproton cloud was 4 kHz giving us an indication of what our minimum field inhomogeneity was.

We are unsure what is the source of this additional non-uniformity in the magnetic field. The NMR probe measurements were taken when the magnet had an empty

bore, so there must be some part of the BTRAP apparatus (where these cyclotron measurements were conducted) that is the cause. Large efforts have been made to construct BTRAP out of completely non-magnetic material, with all of the structural support being provided by titanium, aluminum or fiberglass G-10 [41]. One possible source of non-uniformity may be from the Ioffe trap which surrounds the harmonic well region in the upper electrode stack where these measurements were conducted. These measurements were always taken with no current in the Ioffe trap. However, there are two phenomena we have noticed during the operation of the Ioffe trap that make us suspect it is adding an uncontrolled element to our magnetic field even when there is no current running through it.

The first phenomena is a change in the magnetic field, observed through the cyclotron frequency, when the Ioffe trap is ramped up and then back down. When cyclotron measurements were taken before and after cycling the Ioffe trap the modified cyclotron frequency shifted by variable amounts but sometimes over 100 kHz, corresponding to a change in field of over 60 Gauss.

The second phenomena is that one occasion, shown in Fig. 7.14b, we started measuring the modified cyclotron frequencies of a cloud of antiprotons shortly (approximately 10 minutes) after ramping the Ioffe trap up and down. In the middle of the measurements there was a very sudden jump in the measured frequency of approximately 20 kHz corresponding to a field shift of more than 10 Gauss. The time indicated on the graph indicate the time the measurements were taken at, but the shift in the frequency on the spectrum analyzer in real time was observed on the order of seconds.

Chapter 8

Resonant Detection of Antihydrogen Ions

The capability of detecting single charged particles described in chapter 7 opens the possibility for sensitive detection in antihydrogen ion experiments. The most heavily pursued route, at present, for the confinement of antihydrogen atoms is through the use of a magnetic field minimum neutral atom trap as will be described in chapters 9 and 11. However, a Penning trap would confine an antihydrogen ion without the need for further apparatus. The first detection of a single antiproton in an apparatus capable of making antihydrogen is an important milestone for possible future antihydrogen ion experiments.

Antihydrogen ions could potentially be used for a precision CPT test in conjunction with their matter counterpart. It has also been proposed to use $\bar{H}^+$ (an antiproton and two positrons) as an intermediate state towards very cold neutral antihydrogen atoms for gravity experiments [85, 86]. Laser cooling of hydrogen atoms

has been demonstrated down to 8 mK [87] and the recoil limit sets the minimum achievable temperature to 1.3 mK [88] which is above the temperature needed for sensitive gravity experiments. The cooling of ions has been demonstrated down to 20 μK [89] which could in turn sympathetically cool the antihydrogen ions. One of the positrons could then be photodetached and the sub mK neutral antihydrogen atom could be used for a gravity experiment.

8.1 Expected Antihydrogen Ion Formation Rates

The expected formation rates for stable antihydrogen ions are extremely low. Recent simulations have predicted the formation of very short lived ($<$ 100 ns) antihydrogen $\bar{H}^+$ ions during the positron cooling of antiprotons [90], but no mechanism for the abundant formation of $\bar{H}^+$ that survives long enough to be detected and put to further use has been identified. The reason is that the negative hydrogen ion H^- only exists in two stable states, the $1s^2\ ^1S$ ground state and the $2p^2\ ^3P$ state [91], therefore the cross sections for producing them are exceedingly small. The known methods of producing H^- can be broken down into methods that produce H^- from H_2 molecules and those that create it from the interaction of H with electrons.

Methods of producing H^- ions from H_2 molecules include dissociative attachment:

$$H_2 + e^- \rightarrow H + H^- \tag{8.1}$$

and polar dissociation:

$$H_2 + e^- \rightarrow H^+ + H^- + e^-. \tag{8.2}$$

The combined cross section for these events for electrons in the range from 10-20 eV is

about $\sigma = 10^{-20}\,\mathrm{cm}^2$ [92]. This is an unlikely formation method in our experiment as antihydrogen have very little time to associate with each other into the molecular $\bar{H}_2$ prior to leaving our trap, and the probability of encountering another antihydrogen is very low. In addition the cross section for $H + H \rightarrow H_2$ is also very low, especially at low temperatures [93]. This also limits the production of $\bar{H}_2^+$ molecules (two antiprotons and a positron).

Creating H^- from the interaction of of H and electrons can occur through radiative attachment:

$$H + e^- \rightarrow H^- + \nu \tag{8.3}$$

and through three body collisions with electrons:

$$H + 2e^- \rightarrow H^- + e^-. \tag{8.4}$$

In order for the three body collision to have a comparable rate to radiative attachment, an electron density of $10^{20}\,\mathrm{cm}^{-3}$ is needed [92]. Our electron plasmas and positron plasmas have a typical density of $10^7\,\mathrm{cm}^{-3}$ so we are far off from this regime. The cross section for radiative attachment of electrons in the range of 1-10 eV is on the order of $\sigma = 10^{-22}\,\mathrm{cm}^2$ [92].

The interaction of positronium with antihydrogen atoms has been proposed as a mechanism for creating $\bar{H}^+$ ions [85, 86]:

$$Ps + \bar{H} \rightarrow \bar{H}^+ + e^- \tag{8.5}$$

This cross section is higher than the other processes discussed because the close proximity of the electron in the positronium gives a third body to take away excess energy in a collision. A theoretical model for the scattering of the ground states of

hydrogen and positronium:

$$H(1s) + Ps(1s) \rightarrow H^- + e^+, \tag{8.6}$$

predicts a cross section of $\sigma = 10^{-17}\text{cm}^2$ [94]. Using this model, a group has proposed a scheme to use antiprotons interacting with a positronium cloud with a density of $10^{13}\,\text{cm}^{-3}$ with an expected yield of 1 $\bar{H}^+$ ion and 10^4 $\bar{H}$ atoms per 10^7 antiprotons [95].

8.2 Mass Dependent Cyclotron Frequency Detection

The very low expected formation rate of antihydrogen ions motivates a very sensitive detection technique. While a typical antihydrogen experiment may yield more than a thousand antihydrogen atoms, antihydrogen ion experiments are unlikely to produce more than a few ions. Confirming the existence of these ions by using annihilation detection techniques will be difficult as a signal must be produced above the noise background. Furthermore, antihydrogen ions are likely to be produced in the presence of either positrons or other antiprotons yielding the possibility of false detector counts. The observation of the mass dependent modified cyclotron frequency in a Penning trap allows a single ion to be distinguished from positrons, protons and antiprotons.

The modified cyclotron frequency of the particles, as shown in chapter 2, is related to the unmodified cyclotron frequency and magnetron frequency by $\omega_c' = \omega_c - \omega_m$. The magnetron frequency is a mass independent term, therefore we expect to see a change in frequency in the modified cyclotron frequency which we observe to be equal

to the change in the unmodified cyclotron frequency. For two particles of mass m_1 and m_2 we would expect to see a cyclotron frequency difference of:

$$\Delta\nu_c' = \frac{qB}{2\pi}\left(\frac{1}{m_1} - \frac{1}{m_2}\right). \tag{8.7}$$

The tiny mass difference between an $\bar{H}^+$ (a $\bar{p}$ and two e^+) and a proton leads to a shift in frequency of $\Delta\nu_c = 8.298$ kHz/tesla. Similarly the mass difference between an $\bar{H}_2^-$ and an H_2^- (two protons and three electrons) is: $\Delta\nu_c = 4.147$ kHz/tesla. These frequency shifts are easy to distinguish, even with the field inhomogeneities described in chapter 7. The presence of other charged species is actually helpful while using this resonant detection method as it serves as a reference for comparing the frequencies.

There is a good deal of experience in simultaneously trapping H^- ions and antiprotons in the same Penning trap. In experiments involving the measurement of the H^- and $\bar{p}$ cyclotron frequencies, typically on the order of 500 H^- ions were loaded into the trap along with the antiprotons [53]. The presumed mechanism for the H^- creation was the liberation of hydrogen atoms from the degrader that would pick up an electron while passing through the cooling cloud for the antiprotons, although the exact mechanism was never investigated. No H^- ions were detected in the 2008 beam run. This may be due to our use of a much larger number of cooling electrons compared to previous experiments, 300×10^6 compared to 5×10^5 [53], that may have ionized the H^- after it was formed and before we could detect it.

Chapter 9

Ioffe Trap Design

A long term goal of antihydrogen experiments is to perform precise laser spectroscopy on antihydrogen atoms. Precision 1s-2s spectroscopy on hydrogen has been conducted both in a beam [96] and confined in a magnetic trap [16]. Due to the limited number of antihydrogen atoms that can be created, the latter option of superimposing a magnetic trap on top of the antihydrogen formation region is the path being pursued.

Trapping hydrogen in a magnetic trap for spectroscopy and Bose-Einstein condensation experiments is a well established procedure [15, 97]. In those experiments the trap walls in a hydrogen source chamber are cooled by a dilution refrigerator and are coated with superfluid helium where hydrogen is allowed to thermalize at between 200-300 mK. A rapid radio frequency discharge pulse evaporates and dissociates hydrogen whose trap-able states are loaded into a magnetic field minimum Ioffe trap. Such methods are clearly not applicable to antihydrogen as any contact with matter will result in their annihilation.

In order to trap antihydrogen we must superimpose a magnetic field minimum trap directly onto the region where the antihydrogen is formed. There are several complications to using a magnetic field minimum trap in this regime compared to the hydrogen experiments. The trap must be superimposed onto the uniform axial field of the Penning trap. The smaller number of atoms created at a temperature higher than in the hydrogen regime makes it critical to maximize the depth of the magnetic trap. Furthermore, we must be wary of the effect of such a trap on the charged particle species that combine to form the antihydrogen. This was not a concern in the hydrogen experiments where the neutral atoms were directly loaded into the trap. A considerable portion of this thesis work went towards the design, commissioning and operation of the first magnetic field minimum trap used by the ATRAP collaboration. This chapter will describe the design and considerations that went into the construction and operation of this piece of the apparatus.

9.1 Neutral Atom Magnetic Traps

The potential energy of a neutral atom with a magnetic moment $\vec{\mu}$ of a in a magnetic field $\vec{B}$ is:

$$U = -\vec{\mu} \cdot \vec{B} \tag{9.1}$$

The antihydrogen atoms formed that are detected through the field ionization method are in high Rydberg states which can have very large magnetic moments. For a hydrogen atom in high Rydberg state the magnetic moment of the atom will be a function of its orbital state. Although in the presence of strong magnetic fields, the standard n, m, l, s are no longer good quantum numbers, calculations have been

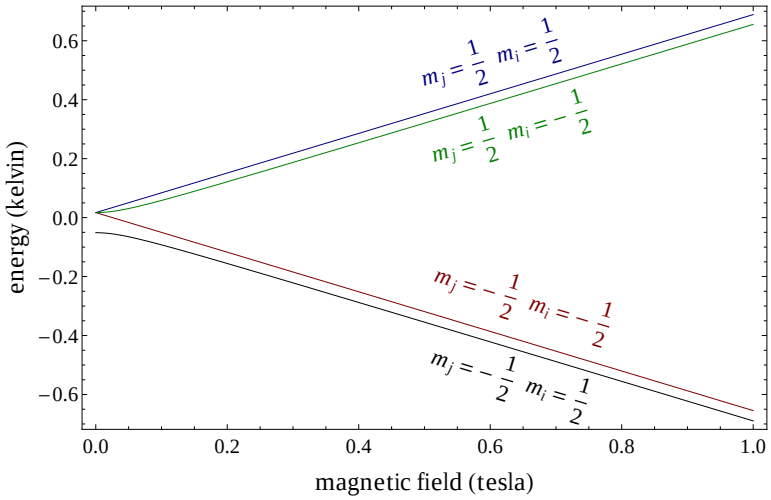

Figure 9.1: Energy of hyperfine ground states of hydrogen in a magnetic field.

done attributing the magnetic moment as a function of these quantum numbers such that the potential goes as [98]:

$$U_{n,l,m}(\vec{r}) = \mu[n, l, m, s, B(\vec{R})]B(\vec{r}) \tag{9.2}$$

In another calculation this has been further approximated for antihydrogen to $U(\vec{r}) = \mu_B m B(\vec{r})$ where m is the azimuthal quantum number and $\mu_B = \frac{e\hbar}{2M_e}$ is the Bohr magneton [99]. This gives an idea of the potential trapping enhancement that can be obtained depending on the orbital state of the positron, for a given n state you can get up to an $m \leq n - 1$ enhancement in the trap potential. The decay of a typical Rydberg atom created in antihydrogen experiments, $n = 44$ [4] down to the low n states happens on the order of 100 ms [98].

For a hydrogen atom in the ground state, where $m = 0$, the trapping is given by the energy splitting of the hyperfine states according to the different orientations of the nuclear and electron spin. The energy of these different ground states in the

field is shown in Fig. 9.1 with m_j being the projection of the total electron angular momentum in the direction of the field and m_i being the projection of the nuclear spin. Half of the ground state species are high field seekers, having a low energy configuration in the high field while the other two are low field seeking states. In a region devoid of magnetic field sources the strength of the magnetic field can have local minima but not local maxima [100]. This means it is only possible to trap the low field seeking states. When there is a high density of trapped atoms spin exchange collisions between atoms in the $m_j = 1/2$, $m_i = -1/2$ leads to a change of state to high field seeking states and those atoms are lost from the trap and only the $m_j = 1/2$, $m_i = 1/2$ remain [101, 102].

The trap depth given in units of temperature for a hydrogen atom in the ground state in a magnetic field minimum trap is $U(T) = \frac{\mu_B}{k_B} B = (0.67\text{K/T})B$ where k_B is the Boltzmann constant and μ_B is the Bohr magneton. In order to trap as many anti-hydrogen atoms as possible we would like to maximize our trap depth, the difference between the maximum and minimum magnetic field magnitude in our apparatus. The first trapping of neutral atoms in a magnetic trap occurred in two opposed, separated, coaxial current loops also known as a spherical quadrupole trap or anti-Helmholtz configuration [103] and in such a configuration it is feasible to get a trap depth of over 3 T [104]. Unfortunately this configuration requires a zero in the axial magnetic field at the center of the trap to provide the magnetic field minimum and is therefore incompatible with the uniform axial magnetic field needed in a penning trap to confine the charged particles.

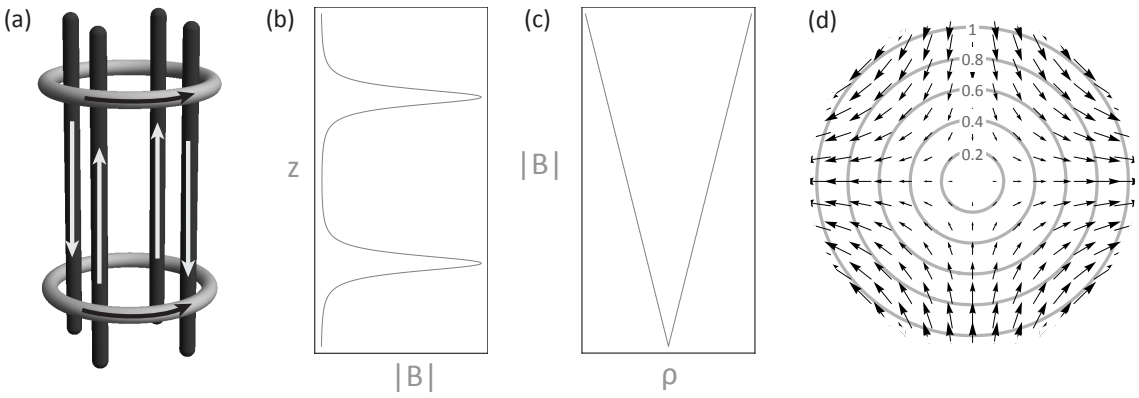

Figure 9.2: (a) Depiction of currents needed to form a pure quadrupole Ioffe trap. (b) The axial field magnitude profile at $\rho = 0$ (c) the radial field magnitude profile in the center of the trap (d) the magnetic field vectors (arrows) and magnitude (contours) in the x-y plane in the center of the trap.

9.1.1 Ioffe Traps

A Ioffe trap configuration, which consists of a radial multipole potential superimposed onto two concurrent, separated, coaxial current loops that provide trapping in the axial direction, can be superimposed onto a uniform axial field and also has advantages for the laser spectroscopy of atoms [14]. Such traps typically have a trapping potential of under 1 T. The form of the radial potential for a pure multipole field of order n is given by:

$$B(\rho, \phi) = B_w \left(\frac{\rho}{\rho_w}\right)^{n-1} \left[\cos(n\phi)\hat{\rho} - \sin(n\phi)\hat{\phi}\right] \tag{9.3}$$

where B_w is the strength of the magnetic field at the wall of the trap and ρ_w is the radius of the trap wall. In cartesian coordinates this can be written as:

$$B(x, y) = B_w \left(\frac{\rho}{\rho_w}\right)^{n-1} \{\cos[(n-1)\phi]\hat{x} - \sin[(n-1)\phi]\hat{y}\} \tag{9.4}$$

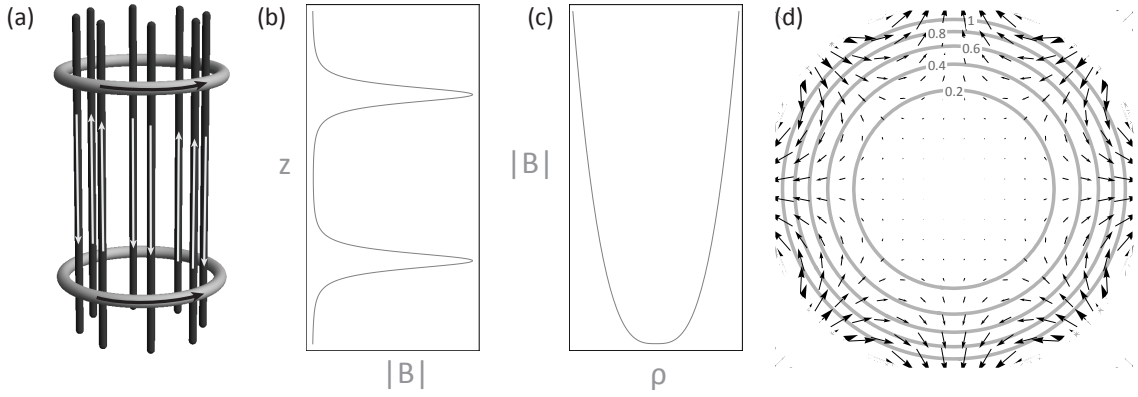

Figure 9.3: (a) Depiction of currents needed to form a pure octupole Ioffe trap. (b) The axial field magnitude profile at $\rho = 0$ (c) the radial field magnitude profile in the center of the trap (d) the magnetic field vectors (arrows) and magnitude (contours) in the x-y plane in the center of the trap.

where $\rho = \sqrt{x^2 + y^2}$. For the case of a quadrupole $n = 2$ the potential can be written as:

$$B(x, y) = \frac{B_w}{\rho_w}(x\hat{x} - y\hat{y}) \tag{9.5}$$

For an octupole $n = 4$ this can be written as:

$$B(x, y) = \frac{B_w}{\rho_w^3}\left[(x^3 - 3xy^2)\hat{x} + (y^3 - 3x^2y)\hat{y}\right] \tag{9.6}$$

The setup and fields for a pure quadrupole Ioffe trap is shown in Fig. 9.2 and a similar figure is shown for an octupole trap in Fig. 9.3. Both octupole and quadrupole Ioffe traps can be used to trap antihydrogen. The reason to favor a quadrupole trap is that it is easier to achieve a larger trap depth if your trap doesn't extend all the way to the current source (due to the more rapid drop off of the octupole field), and the trapped atoms will be confined to a smaller space for spectroscopy. The reason to favor an octupole trap is that the more uniform field region near the center leads to enhanced charged particle stability, as will be explained in chapter **??**. The Ioffe trap

that was used in the BTRAP apparatus was a quadrupole Ioffe trap and a combined octupole and quadrupole trap is currently under construction for a new apparatus.

9.2 Quadrupole Ioffe Trap Design

9.2.1 Coil Design

In order to practically realize the currents depicted in Fig. 9.2a a design using superconducting "racetrack" coils was used in the BTRAP apparatus to create the vertical current bars of the quadrupole, and two solenoids, often referred to as "pinch coils", were placed perpendicularly to the racetracks offset from each other in a Helmholtz configuration for the axial confinement. To maximize the trap depth of the Ioffe trap a variety of coil configurations were studied using Radia software [105] developed at the European Synchrotron Radiation Facility (ESRF) and using the commercial finite element method software OPERA designed by Vector Fields Ltd. First, a design was selected to maximize the number and shape of the coil windings in the space available. A critical current analysis was conducted taking into the fields created by the coils, and the maximum allowable current in the niobium titanium superconducting wire to be used. Then a structural analysis was performed to ensure that the surrounding titanium form was capable of withstanding the Lorentz forces from the coils once they were energized. An additional complication was the need for laser access ports coming in radially in between the racetrack windings.

The initial coil design work was done at Harvard. The preliminary coil shapes were then sent to our collaborators at the Jülich research center in Germany who

Figure 9.4: Coil designs considered for BTRAP Ioffe trap configuration. The yellow coils provide a field in the direction of the axial field of the penning trap, the orange coils oppose it in order to increase the trap depth.

did additional structural calculations and machined the titanium support structure. The coil windings were constructed Accel Instruments GmbH of Bergisch Gladbach, Germany, now owned by Bruker Advanced Supercon GmbH. A sample of the possible coil designs studied is shown Fig. 9.4. It is possible to construct a quadrupole using only two racetrack coils, as that does provide four vertical current bars. Similarly, it is possible to construct an octupole with four racetracks giving eight vertical current bars. In each of these cases, however, the orientation of the current on the turns of the racetracks acts to add to the axial field in one direction and subtract from the axial field in the other direction significantly diminishing the trapping potential for the atoms. For this reason, it is preferable to construct a quadrupole with four racetrack coils where the axial field from each of the turns largely cancels out near the axis ($\rho = 0$) of the trap. Due to space constraints, it is not practical to build an octupole with eight racetrack coils as racetracks must be very thin and the trap depth obtained is vanishingly small.

These studies showed that it was possible to improve the trap depth in this configuration by using different increasing sizes of racetrack going out further radially in order to maximize the amount of current surrounding the trap. It is also possible to gain in trap depth by placing additional solenoid coils, called "anti-pinch-coils" that opposed the field near the center of the trap to push down the minimum. Using these techniques it was possible to construct a coil configuration that exceeded 1 K in trap depth in a 1 T background field. Structural support for such configurations were not studied, and may have necessitated redesigns lowering the trap depth. For simplicity of design and in order to construct our apparatus in time for the 2006 beam run

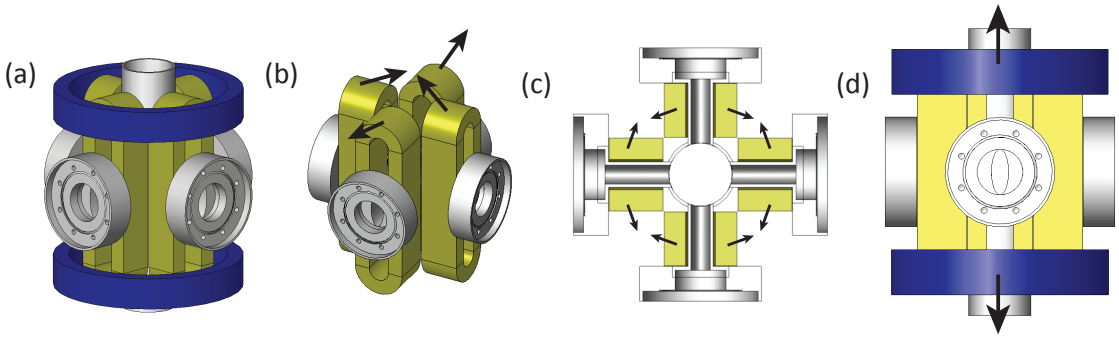

Figure 9.5: (a) The location of the racetracks (yellow) and pinch coils (blue) in relation to the laser access ports (b) the force direction on the straight segments of the racetracks (c) the force direction on the arcs of the racetracks and (d) the force direction on the pinch coils

at CERN we decided to go with a relatively simple configuration involving only one size of racetrack coil and no anti-pinch-coils with a trap depth of 375 mK in a 1 T background field.

9.2.2 Structural Design

In order to contain the substantial Lorentz forces acting on the coil windings when there is current flowing and allow for adequate liquid helium flow to keep the coils superconducting, a titanium superstructure composed of several pieces had to be machined and welded together around the coil windings. The direction of the forces on the coil windings is shown in Fig. 9.5. At full field each of the straight segments of the racetracks have more than 100,000 N of forces acting on them, the bends on the racetracks have over 50,000 N and the top and bottom pinch coils have about 20,000 and 10,000 N acting on them. An initial scheme for mounting the coil windings on a central piece of titanium that would also make up the vacuum can was devised at Harvard and the model was refined and modified by engineers at the Jülich research

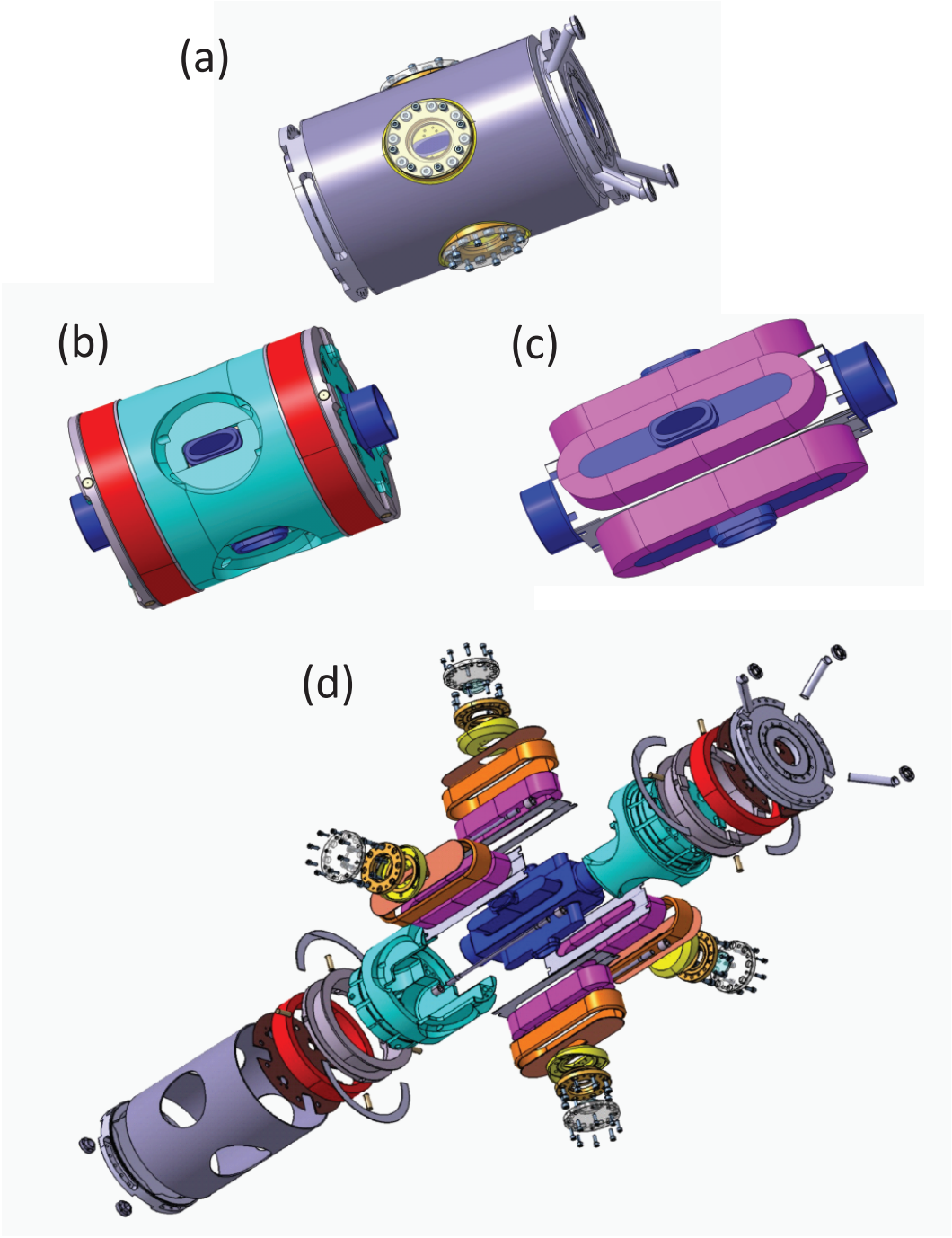

Figure 9.6: (a) The outside titanium can of the quadrupole Ioffe trap, (b) the location of the pinch coils (red) (c) the racetrack coils (purple)

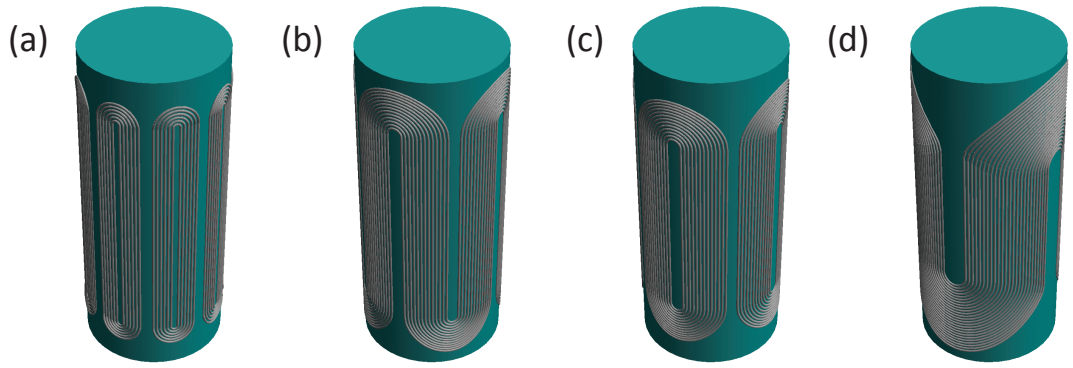

Figure 9.7: (a) The location of the racetracks (yellow) and pinch coils (blue) in relation to the laser access ports (b) the force direction on the straight segments of the racetracks (c) the force direction on the arcs of the racetracks and (d) the force direction on the pinch coils

center in Germany. The different pieces that make up the structural support of the Ioffe trap as it was ultimately built is shown in Fig. 9.6.

9.3 Octupole Ioffe Trap Design

Space constraints make it very difficult to construct an octupole trap using racetrack coil windings. In order for the axial fields created by the turns on the racetracks to cancel, eight racetrack coils are needed leaving very little room for each of the windings and a small trap depth. To achieve a higher trap depth, techniques which wind directly on to the form of a cylinder making better use of the space available are necessary.

A number of different techniques for winding the wire for a superconducting magnet onto a cylinder are shown in section Fig. 9.7. This figure shows a single layer of wire, but multiple layers are wound concentrically to achieve the desired trap depth.

Wire can be wound directly into a racetrack pattern onto the cylinder as shown for an octupole Fig. 9.7a and for a quadrupole Fig. 9.7c. As with the normal racetrack configuration, eight coils are needed for an octopole and four for a quadrupole in order to cancel the axial field from the turns. An alternative way of winding such coils is to use a “serpentine" winding pattern, where the wire is wound continuously around the whole cylinder rather than one racetrack at a time. Unlike with the racetrack configuration, each vertical segment is connected to the next with only one turn of wire. Following the direction of the current, one layer of a serpentine winding adds to the axial field in the same direction at the top and bottom of the coil. This makes it compatible with the axial background field of a Penning trap. These turns are not optimized to provide the optimal axial field profile, however, and subsequent layers are often wound in opposite directions, with the direction in the vertical segments remaining the same but the location of the crossovers being located in such a way to cancel the axial fields.

Shortly after commissioning the construction of the quadrupole racetrack shown in section 9.2, the possibility of creating an octupole trap using the serpentine winding technique was modeled and explored using the commercial OPERA software developed by Vector Fields Ltd. This initial work was passed along to another graduate student who completed the design and a combined octupole quadrupole trap is currently under construction by the Advanced Magnet Laboratory company of Palm Bay, Florida using the racetrack winding method on a cylindrical form. The new Ioffe trap is expected to have a depth of 500 mK for the octupole and 675 mK for the quadrupole and is expected to be completed and commissioned in late 2009 or early

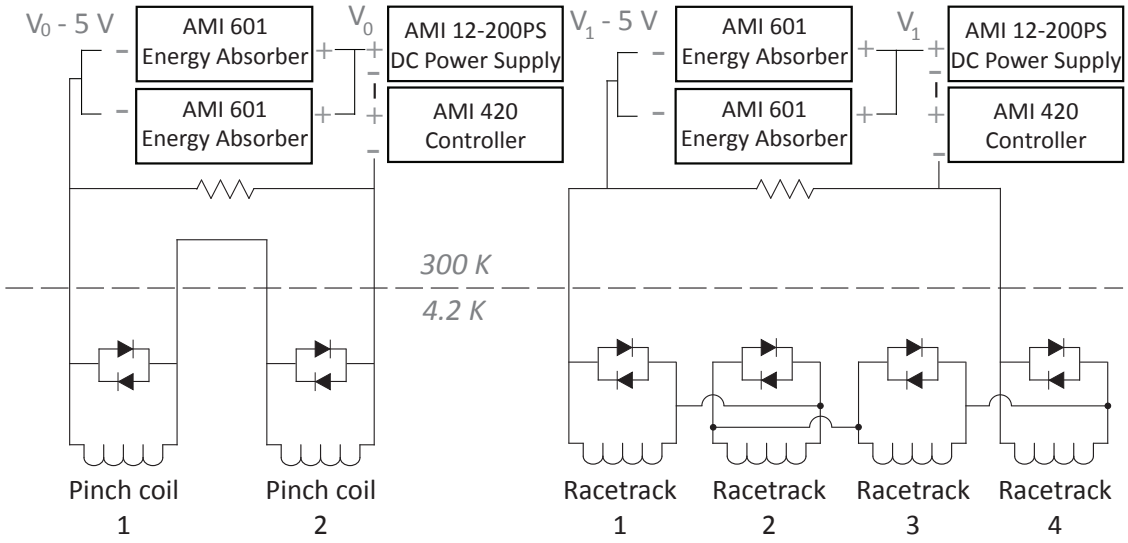

Figure 9.8: The electrical setup and protection circuits for running the quadrupole Ioffe trap.

2010.

9.4 Quadrupole Ioffe Trap Operation

9.4.1 Electrical set-up

The equipment used for charging and discharging the Ioffe trap racetrack and pinch coils is very similar to the equipment used for the large solenoid described in section 3.1.3 and more details concerning the operation of the various devices can be found there. The arrangement consists of a set of an AMI 420 current controller, a AMI 12-200 PS 12 volt 200 amp power supply and two AMI 601 energy absorbers placed in parallel as shown in Fig. 9.8. The use of two AMI 601 energy absorbers appears to have been an overdesign for the system on the part of the magnet company, as each unit can handle up to 130 amps at 25 °C and 100 amps at 40 °C whereas the

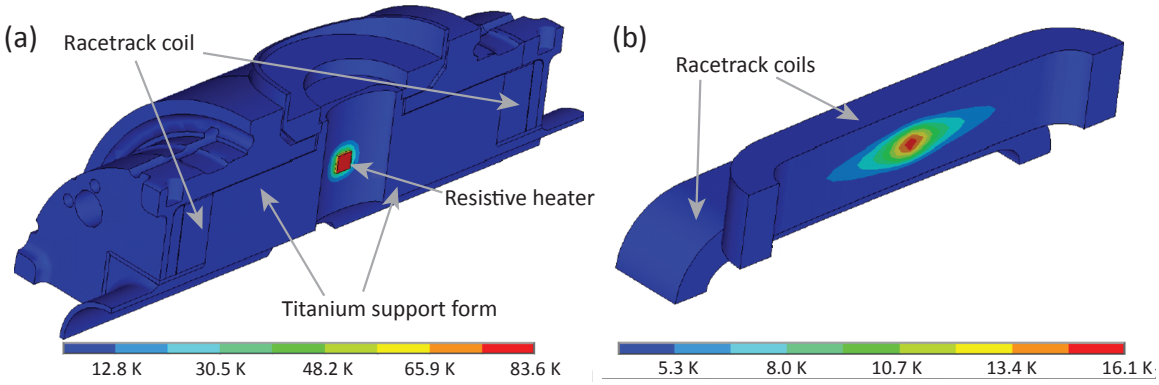

Figure 9.9: The electrical setup and protection circuits for running the quadrupole Ioffe trap.

maximum operating points for both sets of coils is under 100 amps.

The racetrack coils are all run off one power supply and the wiring across the coils is such that the current runs in the proper direction to create the quadrupole field as shown in Fig. 9.8. It was also found that the pinch coils were more stable if they were run off a common power supply, so that became the standard mode of operation. Each of the coils in the Ioffe trap came equipped with protection diodes running in both directions that would allow the flow of current for a voltage in excess of about 5 volts. In addition 8 ohm protection resistors were added across the current leads for each of the magnets in order to increase stability as recommended by the manufacturer.

9.4.2 Quench heater installation

The protection diodes limit the rate at which the magnet can be energized or de-energized. If we were to try to ramp them at faster than a voltage of 5 volts then the diodes would become activated and no more current would pass through the coils.

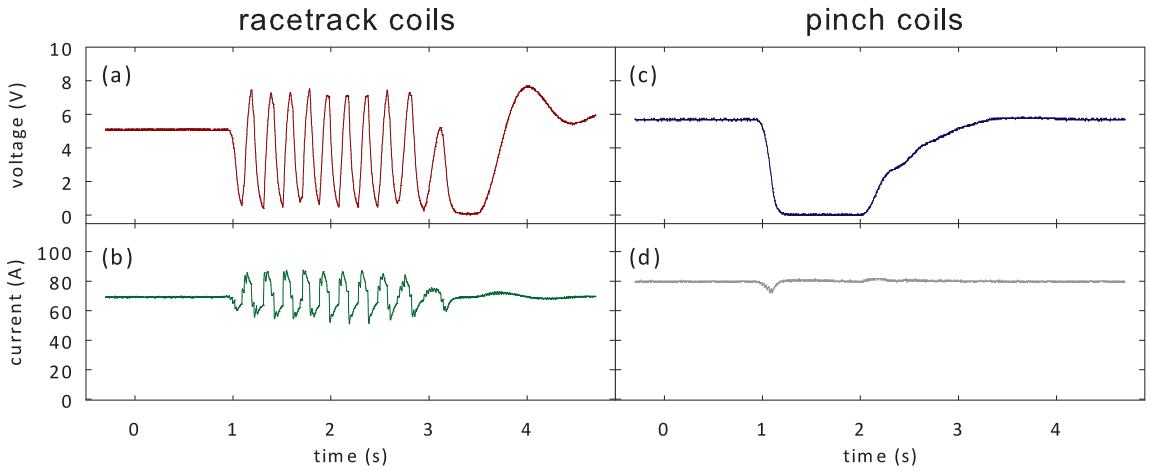

Figure 9.10: The electrical setup and protection circuits for running the quadrupole Ioffe trap.

Because we were interesting in detecting a small number of trapped antihydrogen atoms, we wanted to ramp down the magnet as fast as possible to get any subsequent antiproton annihilations to register above the background rate of our detectors. The only way to ramp the magnet down faster than what was allowed by the diodes was to induce a quench in one of the coils. The resistive heating occurring in one of the coils would ramp the coils in a few seconds rather than about a minute using the power supplies.

A resistive heater, shown in , was installed inside one of the access ports in the Ioffe trap and fastened to the titanium with epoxy. Applying ten watts of electrical power to this resistor would produce the temperatures shown in a in the titanium and in b in the racetrack itself in about one second successfully inducing a quench.

shows the signals across the coils after electrical power was run (starting at t=0) through the quench heater. The different signals require some explanation. The oscillatory behavior in the quadrupole coils is likely caused by the the diodes activating

and deactivating as the AMI 420 current controller adjusts the voltage coming from power supply to try to keep the current at a constant level. The large dip in the pinch coil voltage is likely caused by the change in flux coming from one of the racetrack coils quenching inducing an EMF in the pinchcoil that the AMI 420 current controller tries to counteract. This voltage is the clearest indicator that the quench takes all of the current out of the racetrack coil in about 3 seconds.

9.5 Summary

A first generation quadrupole Ioffe trap was designed, built and installed for use in the Penning-Ioffe trap apparatus of the ATRAP collaboration. A number of potentially higher performing but more complicated designs were explored, but ultimately a simpler more reliable design was chosen so that we could begin exploring the basic science of the new apparatus as soon as possible. A significant amount of work was done looking into possibilities for a next generation octupole and quadrupole Ioffe trap. This work was continued by another graduate student and the next generation Ioffe trap is now under construction. A quench heater system was installed to reduce the amount of time needed to bring the current out of the Ioffe trap from about 1 minute to a few seconds.

Chapter 10

Charged Particle Stability in a Ioffe-Penning Trap

The stability of charged particles in a penning trap is related to the axially symmetry of the magnetic and electric fields. The resulting conservation of angular momentum gives rise to a confinement theorem [20] ensuring the long lifetime of both individual particles and plasmas within the Penning trap. In order to magnetically trap antihydrogen using a Penning-Ioffe trap configuration, a radial multipole field must be superimposed onto the uniform axial field of the Penning trap, destroying the axial symmetry. The lifetime of charged particles in such a configuration is essential to the trapping of antihydrogen, for if a sizeable portion of the charged particles do not survive long enough to form the antihydrogen, there will be a greatly decreased chance of trapping the remaining atoms. There was some controversy over whether charged particles could remain trapped in a quadrupole Ioffe trap configuration long enough to make antihydrogen. In 2006 ATRAP demonstrated that the lifetimes of

both electrons (and thus positrons) and antiprotons was long enough to create antihydrogen [5]. This chapter will give a review of the theoretical predictions for the lifetimes of charged particles in both quadrupole and octupole configurations and then will present experimental results from the ATRAP collaboration regarding the stability of electrons and antiprotons in a quadrupole.

10.1 Theoretical Predictions

10.1.1 Field Lines in a Ioffe-Penning Trap

The uniform axial field of a Penning trap, which we label to be in the $\hat{z}$ direction, is substantially distorted by the radial multipole field of a Ioffe trap, that we label to be in the $\hat{x}$ and $\hat{y}$ or $\hat{\rho}$ direction. The field is also distorted by the radial and axial addition of the pinch coils, but since the antihydrogen is meant to be formed in the center of the Ioffe trap, where the contribution of the pinch coils is only in the axial direction, we concern ourselves with the effect of the radial field.

Magnetic field lines are a convenient way of visually understanding what is happening in a complicated configuration. They are derived by taking the magnetic field vector at each point in space, proceeding and incremental amount $\Delta\vec{r}$ in that direction, connecting the two points with a line and repeating that procedure in the limit as $\Delta\vec{r} \rightarrow 0$. Magnetic field lines obey the following differential equations:

$$x'(x,y,z) = B_x(x,y,z) \quad y'(x,y,z) = B_y(x,y,z) \quad z'(x,y,z) = B_z(x,y,z) \qquad (10.1)$$

In the absence of other forces, charged particles will be pinned to the field lines that they execute cyclotron orbits around. When we superimpose an electrostatic

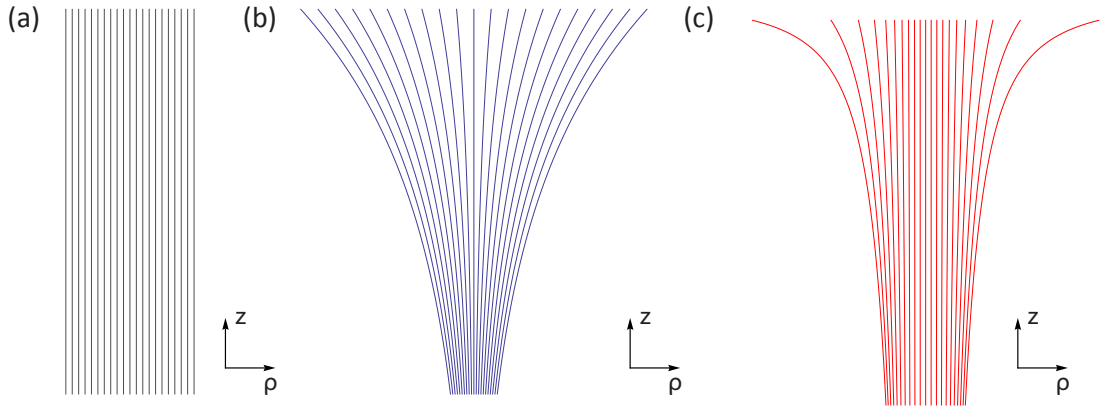

Figure 10.1: The divergence of field lines in a Penning-Ioffe trap in the 2-D planes of symmetry. (a) A Penning trap with no superimposed radial field (b) with a quadrupole field superimposed (c) with an octupole field superimposed

quadrupole field, the particles execute a slow magnetron drift which changes the field line that they are on. However, during the shorter time scales involved in axial oscillation, $\omega_z \gg \omega_m$, the particles will travel axially to a good approximation on the same field line.

In a Penning trap, the field lines proceed straight along the $\hat{z}$ direction. The superposition of radial multipole causes the field lines to move in or out radially, as well as twist in the x-y plane as they change their azimuthal angle. For a quadrupole potential of the form given in equation (9.5) the total field is given by:

$$B(x,y) = B_z\hat{z} + \frac{B_w}{\rho_w}(x\hat{x} - y\hat{y}) \tag{10.2}$$

there are two planes of symmetry where the field lines do not change their azimuthal angle: the $x-z$ plane and the $y-z$ plane. These contain the maximally radially diverging and maximally radially converging field lines. In the $x-z$ plane the field lines radially diverge with increasing z and in the $y-z$ they converge with increasing z. Similarly, for an octupole of the form given in equation (9.6) the total field is given

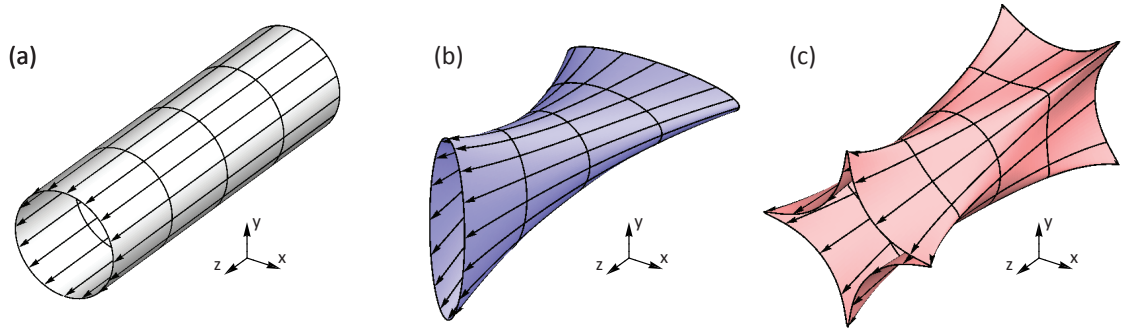

Figure 10.2: The divergence of field lines in a Penning-Ioffe trap in 3-D. (a) A Penning trap with no superimposed radial field (b) with a quadrupole field superimposed (c) with an octupole field superimposed

by:

$$B(x,y) = B_z\hat{z} + \frac{B_w}{\rho_w^3}\left[(x^3 - 3xy^2)\hat{x} + (y^3 - 3x^2y)\hat{y}\right] \tag{10.3}$$

there are four such planes of symmetry. In the $x-z$ and $y-z$ planes the field lines radially diverge with increasing z and in planes 45 degrees between in the azimuthal direction they converge with increasing z.

For the quadrupole, in the planes of symmetry, solving the differential equations in (10.1) shows that the field lines will diverge/converge as:

$$\rho(z) = \rho_{z=0}\exp(\pm\frac{B_w z}{B_z\rho_w}) \tag{10.4}$$

In the case of an octupole the field lines will diverge and converge as

$$\rho(z) = \pm\frac{\rho_{z=0}}{\sqrt{1 - 2\frac{B_w}{B_z}\left(\frac{\rho_{z=0}}{\rho_w}\right)^2\frac{z}{\rho_w}}} \tag{10.5}$$

The behavior of the field lines in the planes of symmetry where they diverge is shown in Fig. 10.1 and in three dimensions is shown in Fig. 10.2. The 3-D figure demonstrates the behavior of field lines that start in a uniform spacing on a circle

of a given radius in the middle of the z-range of the plot. We can see clearly in the 2-D picture that the field lines for the octupole diverge far less near the center of the trap then do the field lines for a quadrupole making it a better approximation to an unperturbed Penning trap configuration. This is the general reason why an octupole, or any higher order pole trap leads to longer particle lifetimes. We will now look at the particle loss mechanisms in each of the configuration.

10.1.2 Single Particle Stability

The most straightforward method of losing charged particles in a Ioffe-Penning trap is for them to just follow a field line and hit the wall of the electrodes. If a particle is to travel a certain axial distance Δz along a given field line, there is a maximum radius it can have started out at if it is to avoid hitting the wall of the trap at ρ_w. For a quadrupole this cut-off radius is given by:

$$\rho_{z=0} = \rho_w \exp\left(-\frac{B_w}{B_z \rho_w}\Delta z\right) \tag{10.6}$$

For an octupole it is given by:

$$\rho_{z=0} = \frac{\rho_w}{\sqrt{1 + 2\frac{B_w}{B_z}\frac{\Delta z}{\rho_w}}} \tag{10.7}$$

The cutoff radius for particles traveling the distance of a radius length electrode, where $\Delta z = \rho_w$, is shown in Fig. 10.3(a).

The cutoff radius is a useful criteria when it is known how far a charged particle must travel in the axial direction for a given application, such as producing antihydrogen in a nested well. However, when we are considering the stability of charged particles in a single well, we have no requirements on the axial travel of the particles

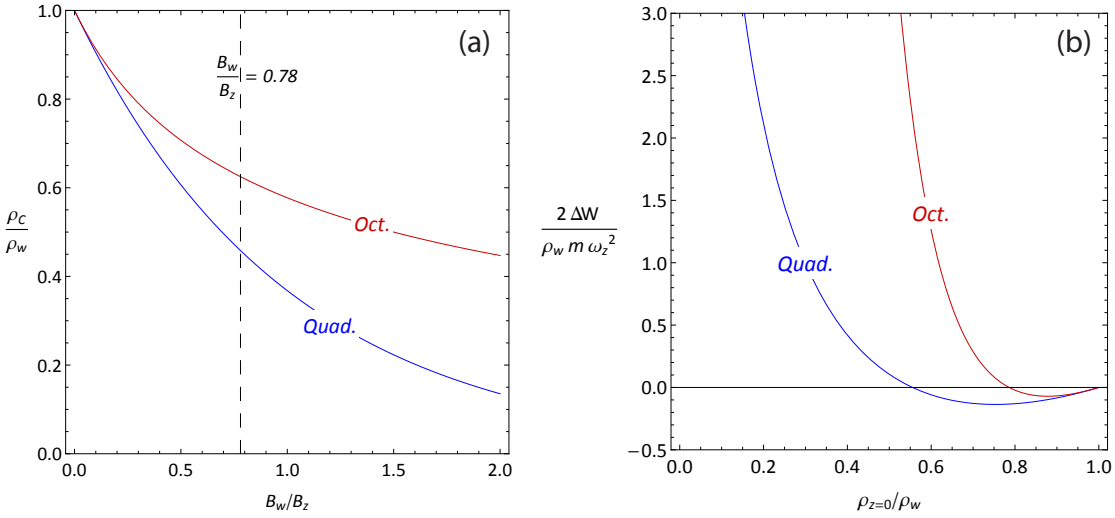

Figure 10.3: (a) The cutoff radius in ideal quadrupole and octupole Penning-Ioffe traps for travel in radius length electrodes, the BTRAP Ioffe trap had a ratio of $B_w/B_z = 0.78$ at full field.(b) the potential energy difference between the particle at a field line in the axial center of the trap $z = 0$ and where the particle would hit the wall for $B_w/B_z = 1$.

and therefore how far they do travel will be dictated by their energy and the value of the electric potential along a field line. For a low enough axial energy, the particles will only travel a short distance along the field line. We can invert equations (10.6) and (10.7) to get the axial distance traveled along a a field lone before the particle hits the wall. For a quadrupole this is:

$$\Delta z = \rho_w \frac{B_z}{B_w} \ln\left(\frac{\rho_w}{\rho_{z=0}}\right) \tag{10.8}$$

For an octupole it is:

$$\Delta z = \frac{\rho_w}{2} \frac{B_z}{B_w} \left[\left(\frac{\rho_w}{\rho_{z=0}}\right)^2 - 1\right] \tag{10.9}$$

The potential energy of a particle with charge q in an ideal quadrupole potential is:

$$W = \frac{m\omega_z^2}{2}\left(z^2 - \frac{\rho^2}{2}\right) \tag{10.10}$$

There will be a potential energy difference between the point where a charged particle starts on a field line in the axial center of the trap $z = 0$ and $\rho = \rho_{z=0}$ and where it strikes the wall, $z = \Delta z$ as given by equations (10.8) and (10.9) and $\rho = \rho_w$. If the kinetic energy of the particle at $z = 0$ is less than this potential energy difference ΔW then it will not directly exit the trap by following a field line and hitting the wall. The potential well that a particle sees may actually be larger than this as the value of the potential is not necessarily monotonically increasing or decreasing along the field line.

The potential energy difference of a particle between the axial center of the trap at $\rho_{z=0}$ and when it would hit the wall for a quadrupole is:

$$\Delta W = \frac{m\omega_z^2}{2}\left[\rho_w^2\left[\frac{B_z}{B_w}\ln\left(\frac{\rho_w}{\rho_{z=0}}\right)\right]^2 + \frac{\rho_{z=0}^2 - \rho_w^2}{2}\right] \tag{10.11}$$

For an octupole it is:

$$\Delta W = \frac{m\omega_z^2}{2}\left[\left[\frac{\rho_w}{2}\frac{B_z}{B_w}\left(\frac{\rho_w^2}{\rho_{z=0}^2} - 1\right)\right]^2 + \frac{\rho_{z=0}^2 - \rho_w^2}{2}\right] \tag{10.12}$$

In both cases if the quantity that is multiplied by $m\omega_z^2/2$ is positive, which will be a function of the relative strengths of the radial and axial fields B_z and B_w and the starting position $\rho_{z=0}$, then the kinetic energy needed to leave the trap in a single pass along a field line will increase as we increase the voltage on the electrodes and thus the axial frequency ω_z. This shows why the strength of the electrostatic well is a critical parameter in predicting the stability of charge particles in a combined Penning-Ioffe trap. If they are in a long shallow well, particles of a given energy will be able to travel further along a field line and hit an electrode, if they are in short deep well they will not.

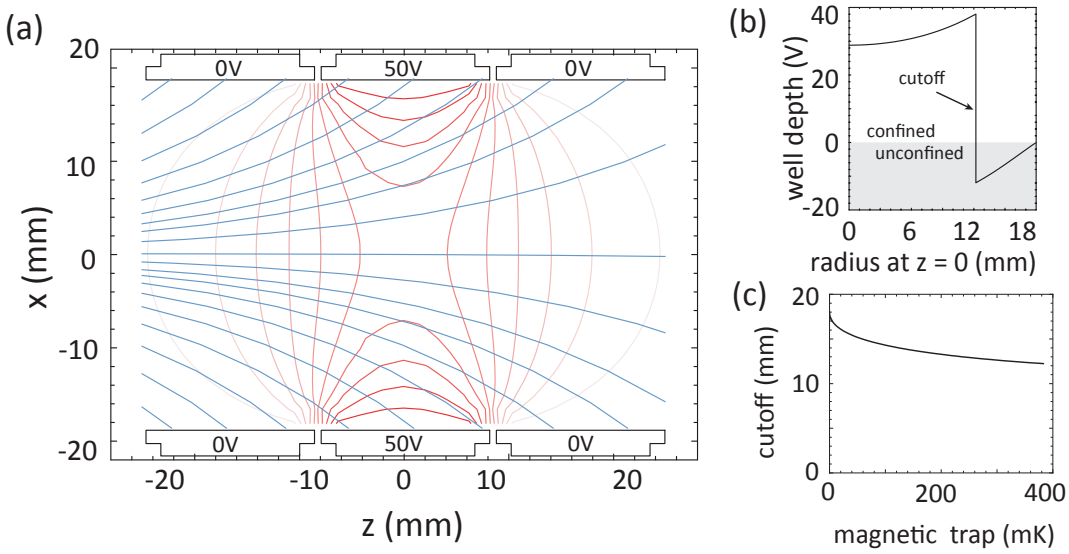

Figure 10.4: Numerical calculation of the potential well and cutoff radius seen by particles in a radius length electrode in the BTRAP Penning-Ioffe trap. (a) The magnetic field lines (blue) and electrostatic potential (red) of the Penning Ioffe trap at full field with the voltages indicated (b) the trapping potential along the field lines starting at $z = 0$ (c) the variation of the cutoff radius as a function of magnetic trap strength.

The two figures in Fig. 10.3 are approximations using the ideal forms of both the radial multipole field and the electrostatic quadrupole field. The fields in our experiment differ from this and must be calculated numerically. Fig. 10.4 shows the well depth along field lines for different starting radii in the center of a radius length electrode with 50 V applied to it, and the neighboring electrodes held at ground.

The longer term stability of charged particles in a quadrupole Penning-Ioffe trap has been discussed in a paper by Gabrielse et al. [106] as well as in several past theses [107, **?**, 41]. A brief summary of those results will be given here. Expressing the ratio of the radial and axial magnetic field strengths defined in (10.2) as:

$$R_0 = \frac{B_z}{B_w}\rho_w \tag{10.13}$$

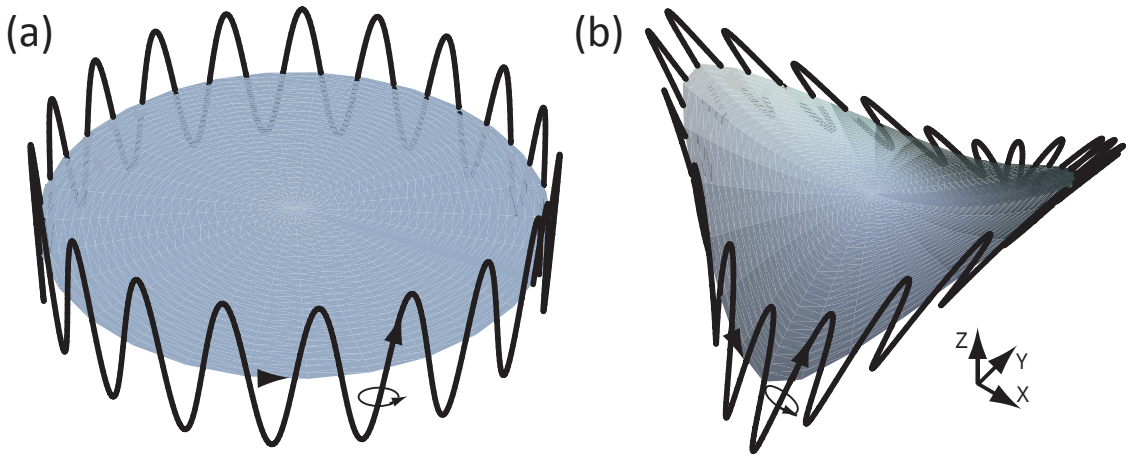

Figure 10.5: Numerical calculation of the potential well and cutoff radius seen by particles in a radius length electrode in the BTRAP Penning-Ioffe trap. (a) The magnetic field lines (blue) and electrostatic potential (red) of the Penning Ioffe trap at full field with the voltages indicated (b) the trapping potential along the field lines starting at $z = 0$ (c) the variation of the cutoff radius as a function of magnetic trap strength.

and defining $\epsilon = \omega_z/\omega_c$ the equations of motion (stated for an ideal Penning trap in equation (2.35)) become:

$$\ddot{x} = \frac{1}{2}\epsilon^2\omega_c^2 x - \omega_c\dot{y} - \frac{\omega_c}{R_0}y\dot{z} \tag{10.14a}$$

$$\ddot{y} = \frac{1}{2}\epsilon^2\omega_c^2 y + \omega_c\dot{x} - \frac{\omega_c}{R_0}x\dot{z} \tag{10.14b}$$

$$\ddot{z} = -\epsilon^2\omega_c^2 z + \frac{\omega_c}{R_0}(\dot{y}x + x\dot{y}) \tag{10.14c}$$

As in the ordinary Penning trap, this results in trajectories that can be broken down into three distinct motions $\tilde{\omega}_c, \tilde{\omega}_z$ and $\tilde{\omega}_m$ which are preserved by adiabatic invariants as shown in . Axial oscillations will occur along a field line centered around the location where there is no electrostatic force $F_{||}$ along the field line. This is given

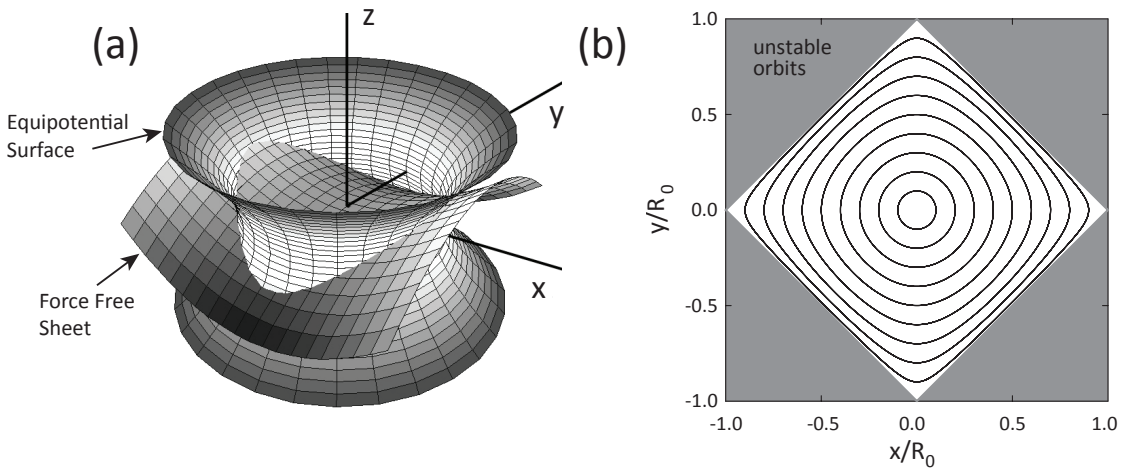

Figure 10.6: (a) The force free sheet and an equipotential of the electrostatic quadrupole. (b) Projections of of stable magnetron orbits upon the xy plane lie within a square [106]

by the condition:

$$0 = F_{||} = qE_{||} = \nabla W \cdot \hat{B} \tag{10.15a}$$

$$0 = \frac{m\omega_z^2}{2} \frac{[2zR_0 - (x^2 - y^2)]}{\sqrt{R_0^2 + x^2 + y^2}} \tag{10.15b}$$

which in turn defines a force free sheet along:

$$z = \frac{x^2 - y^2}{2R_0} \tag{10.16}$$

Magnetron oscillations will occur in the plane perpendicular to the axial oscillation. Since the magnetron kinetic energy is much smaller than the electrostatic potential energy, the orbit will be defined by the intersection of the force free sheet and an equipotential of electrostatic quadrupole field as shown in Fig. 10.6a. For an orbit to be stable there must be an intersection of the force free sheet and an equipotential throughout the full 2π rotation of the orbit through the azimuthal angle ϕ. If there is not such an intersection along the entire trajectory then there is no restoring

force for the particle along a given field line and the particle will exit the trap. This condition restricts the orbits lying within in a square bounded by:

$$x + y < R_0 \tag{10.17}$$

as shown in Fig. 10.6b. The magnetic flux enclosed by a magnetron orbit Φ_m is an adiabatic invariant and will be preserved if the magnetic field is changed slowly enough [106]. This means that a particle which starts out a certain radius with the Ioffe field off will move into a smaller orbit as the field is increased. A conservation of flux calculation shows [107] that particles starting out at a radius:

$$\rho = \sqrt{\frac{4}{3\pi}} R_0 \tag{10.18}$$

with the field off will remain in stable magnetron orbits and those starting at larger radii will not. This flux conservation condition also applies when considering the cutoff radius from equation (**??**) when we are ramping a quadrupole. Increasing the field will decrease the magnetron orbit and particles initially above the cutoff radius in (**??**) will move to a smaller radius and still remain trapped.

The lifetime of single particles in the ideal quadrupole Penning-Ioffe trap that lie on allowable magnetron orbits should be stable for exponentially long times as long as certain resonances are avoided and adiabatic invariants are not otherwise broken [106]. Resonant conditions that can cause radial particle transport occur when $\tilde{\omega}_z = 2N\tilde{\omega}_m$ where $N > 1$ is an odd integer with the N=1 being the most pronounced effect. This condition causes the transfer of magnetron energy to axial energy and since the magnetron orbit has a lower energy at larger radius, the radius increases. In the non-ideal quadrupole potential, this resonant condition can be understood as a

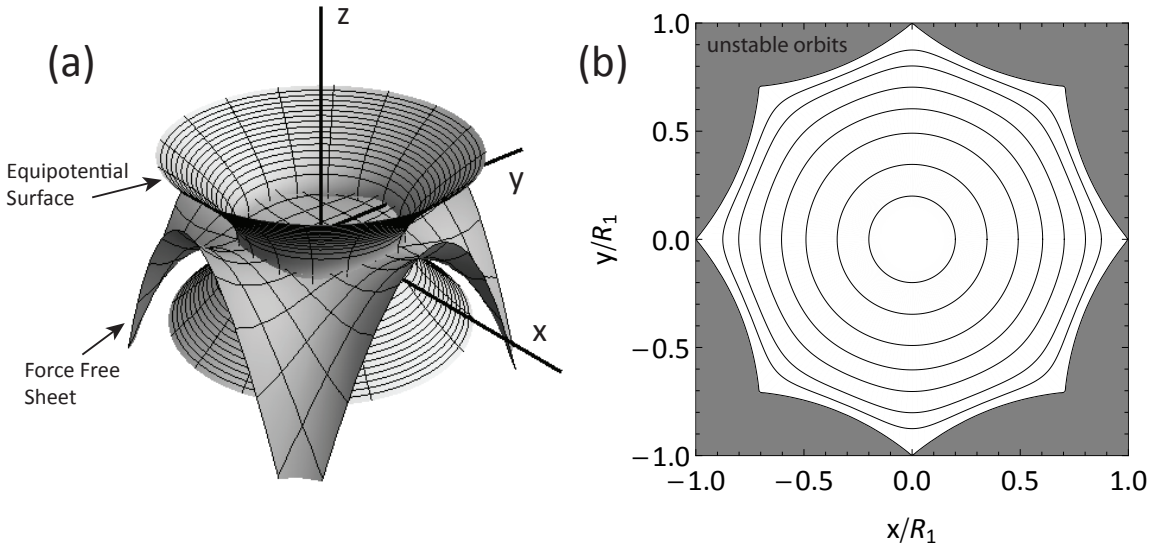

Figure 10.7: (a) The force free sheet and an equipotential of the electrostatic quadrupole. (b) Projections of of stable octupole magnetron orbits upon the xy plane

particle traveling on an outwardly propagating field line as it travels up the trap in the z direction and changing its azimuthal angle such that it is also traveling on an outwardly propagating on the way down. Off resonance these effects average out and there is no appreciable radial expansion.

Similar calculations for single particle orbits in an octupole Ioffe-Penning trap show that the force free sheet in that configuration will be given by:

$$z = \frac{B_w}{2B_z\rho_w^3}[x^2(x^2-3y^2)+y^2(y^2-3x^2)] \tag{10.19}$$

and as with the quadrupole, the allowable magnetron orbits will occur at the intersection of the force free sheet and an electrostatic equipotential. The allowable orbits are shown in Fig. 10.7 and the maximum allowable radius occurs at azimuthal angles of $\phi = 0, \frac{\pi}{4}, \frac{\pi}{2}, \frac{3\pi}{4}, \pi, \frac{5\pi}{4}, \frac{3\pi}{2}, \frac{7\pi}{4}$ and is given by:

$$R_1 = \sqrt{2}\left(2\frac{B_z}{B_w}\right)^{1/3}\rho_w \tag{10.20}$$

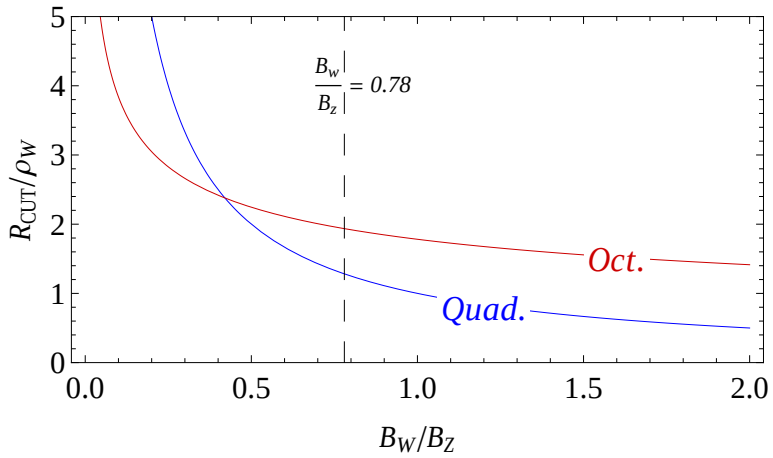

Figure 10.8: The maximum radius of an allowable magnetron orbit in quadrupole and octupole Penning-Ioffe traps as a function of radial field strength

the same adiabatic invariants will hold for the octupole as the quadrupole and the conservation of flux through the magnetron orbit should allow for stability as the octupole field is turned on slowly enough.

Figure Fig. **??** shows the maximum radii for magnetron orbits quadrupole and octupole Penning Ioffe traps as shown in equations (10.13) and (10.20). This, together with the results shown in Fig. 10.3 indicate that single particle trajectories for a particle in a Penning-Ioffe trap are stable out to a further radius in an octupole than a quarupole. A result that is not surprising given the divergence of the field lines shown in Fig. 10.1 and Fig. 10.2.

10.1.3 Plasma Stability

The collective behavior of particles in the plasma regime in a Penning trap differs from the single particle picture as described in 2. The magnetron frequency ω_m is

replaced by rigid plasma rotation frequency ω. In the presence of a radial magnetic field, the particles arrange themselves in a way to cancel the axial electric field along magnetic field lines within the plasma. Since there is no longer a quadratic electrostatic potential the axial frequency $\tilde{\omega}_z$ is now replaced by a bounce frequency related to the travel time of the particles from one end to the other $\omega_z' = 2\pi/\tau_z$. This bounce frequency will depend on both the thermal distribution and geometry of the plasma. Because there is no longer a unique axial frequency but a range of them, and because collisions between particles can knock them into a region with a different frequency, it will be more difficult to avoid the resonances described in the previous section such that $\omega_z' = 2N\omega$ where $N >= 1$ is an odd integer. The particles will radially diffuse inwards or outwards (depending on their phase) until they reach the cutoff radius ρ_{cut} at which point they will follow a field line into the wall and exit the trap.

Gilson et al. [108, 109] have proposed a model describing that the diffusion coefficient D for particles at radius ρ in a quadrupole should be:

$$D = \frac{64 z_p^3 \rho_2 \omega^2 B_w^2}{\pi^4 B_z^2} \sqrt{\frac{m}{2\pi kT}} \exp\left(\frac{-\omega^2}{2\omega_T^2}\right) \tag{10.21}$$

where z_p is the plasma half length, assumed to be uniform, although in reality it should be a function of the radius $z_p(\rho)$. ω_T is the half mean thermal axial bounce frequency in a plasma given by:

$$\omega_T = \frac{\pi}{4 z_p} \sqrt{\frac{kT}{m}} \tag{10.22}$$

A similar model has not been worked out for an octupole configuration, but Fajans et al. have made argued that, at least near the center of the trap, the transport coefficient would be significantly lower due to the smaller radial field [110].

Making the simplifying assumption that the plasma is a uniform-density cylinder, the particle loss rate can be estimated using Fick's law [**?**]:

$$\tau \simeq 0.2\frac{\rho_{cut}^2}{D} \tag{10.23}$$

Although this is a crude approximation, it demonstrates the reliance of the lifetime of the particles as reliant on both the cutoff radius and the diffusion coefficient. This indicates that the particle lifetimes in the plasma regime should be better for an octupole than a quadrupole.

10.1.4 Theoretical stability summary

Sections 10.1.2 and 10.1.3 make it clear that an octupole Penning-Ioffe trap is better when it comes to the more stable confinement of charged particles in both the single particle regime and . This was never in doubt. What has been a matter of some contention was whether the confinement within a quadrupole Penning-Ioffe trap was so degraded that no useful experiments or antihydrogen could be conducted with such a configuration. This was the concern expressed in a number of papers [108, 111, 110].

As was discussed in chapter 9 there are two reasons to prefer a quadrupole trap over an octupole trap. First, the field gradient is steeper near the center of the trap, so the trapped atoms are confined to a smaller radius and thus higher density which has advantages for spectroscopy. Even those favoring higher multipole traps have acknowledged the small trapping volume advantage of the quadrupole [110].

The second reason is that it is easier to achieve a higher trap depth in an actual quadrupole Penning-Ioffe trap than it is to achieve the same depth in an octupole

Penning-Ioffe trap. The amplitude of the current density required to generate a given field B_m at the edge of the magnet windings is the same for both configurations as the azimuthal current density required for a general multipole is [110]:

$$J = \frac{2B_M}{\mu_0} \sin n\theta \tag{10.24}$$

However, what sets the trapping field is not the magnitude of the field at the windings B_m but rather the magnitude of the field at the wall of the electrodes B_w which are necessarily at a smaller radius ρ_w than the magnet windings ρ_m. The actual magnitude of the trapping field for a quadrupole will be:

$$\Delta B = \sqrt{B_z^2 + B_m^2 \left(\frac{\rho_w}{\rho_m}\right)^2} - B_z \tag{10.25}$$

and for an octupole it will be:

$$\Delta B = \sqrt{B_z^2 + B_m^2 \left(\frac{\rho_w}{\rho_m}\right)^6} - B_z \tag{10.26}$$

The trap depth of a quadrupole falls off far less dramatically than an octupole for a given spacing between the magnet windings and the electrode walls, as is shown in Fig. 10.9. For the electrode trap design in BTRAP using an octupole trap would have led to a negligible trap depth, thus one of the driving reasons we chose a quadrupole. A new combined octupole and quadrupole Penning-Ioffe apparatus under construction accomplishes a much higher ratio of ρ_w/ρ_m by using much larger electrodes and new manufacturing techniques.

To settle the question of whether charged particles could remain trapped long enough in a quadrupole Penning-Ioffe trap configuration, we conducted experiments using both electrons and antiprotons in 2006 [5].

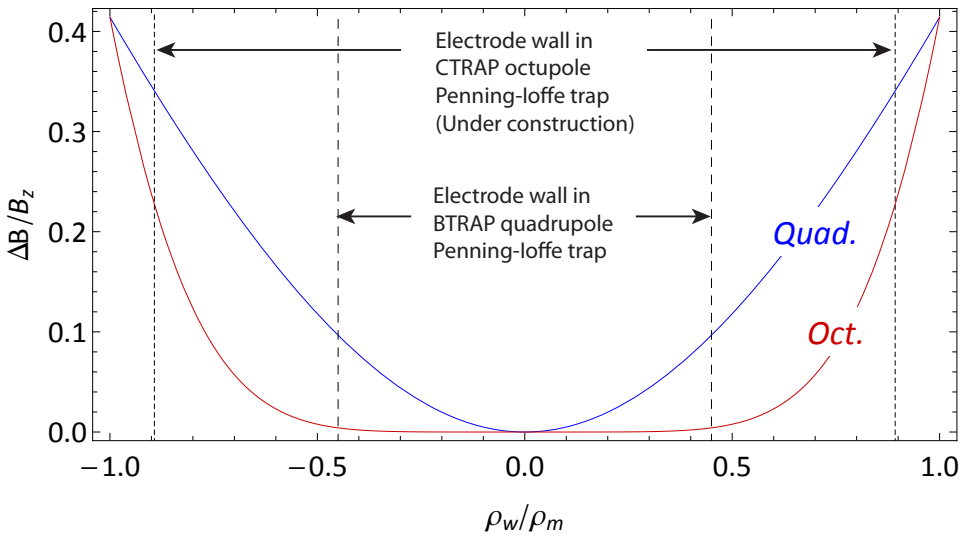

Figure 10.9: The magnetic field depth of quadrupole and octupole Penning-Ioffe trap as a function of the electrode wall radius and magnet winding radius.

10.2 Electron Stability Results

Electrons were loaded into the lower stack using the methods involving 248 nm excimer laser light described in chapter 4. They were transferred from their load electrode to the electrode in the center of the Ioffe trap as indicated in Fig. 10.10 using the transfer method described in section 4.2. The 1 K pot was not installed prior to these experiments and the trap temperature was 4.2 K. The quadrupole Ioffe trap is designed to run at full field with 69 amps in the racetrack coils producing a field at the electrode wall of $B_w = 1.67$ T at a gradient of $B = 93$ T/m.

To conduct stability tests the electrons were placed in the radius length electrode, the quadrupole racetrack coils were energized up to a given current at a rate of 0.1 amps/second, left at the full current for a certain amount of time, and then ramped back down at the same rate. Fig. 10.12(a) shows the results when 50 V is applied

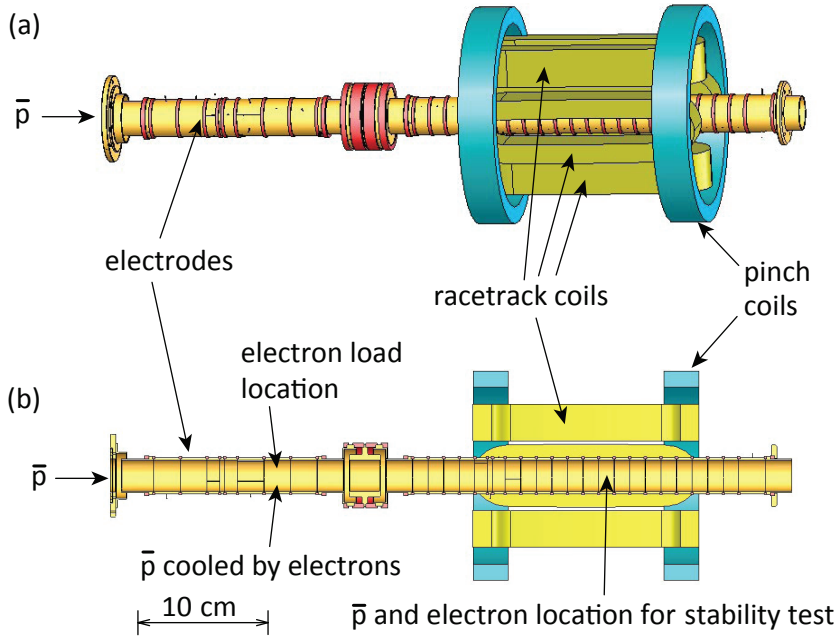

Figure 10.10: Exterior (a) and cutaway (b) view of the Penning-Ioffe apparatus used for particle stability measurements. Two pinch coils add an axially-confining gradient to the bias field. The radial quadrupole Ioffe field is produced by four racetrack coils.

to the electrode, the current in the quadrupole is ramped up, left at its maximum value for the time indicated and brought back down to zero. Fig. 10.12(b) shows the results when the current is ramped up and immediately back down for a variety of different voltages applied to the electrode and Fig. 10.12(c) shows the results when the current is ramped up, left at its maximum value for five minutes and ramped back down for a variety of voltages. Fig. 10.12(a) indicates the effects of diffusive loss over longer time periods. Fig. 10.12(b) and (c) demonstrated the very strong dependence of confinement on the voltage applied to the electrode, as was predicted in section 10.1. The dashed line in Fig. 10.12(a) and (b) indicate the radial to axial field ratio $B_w/B_z = 0.78$ that is achieved by our Ioffe trap at full field.

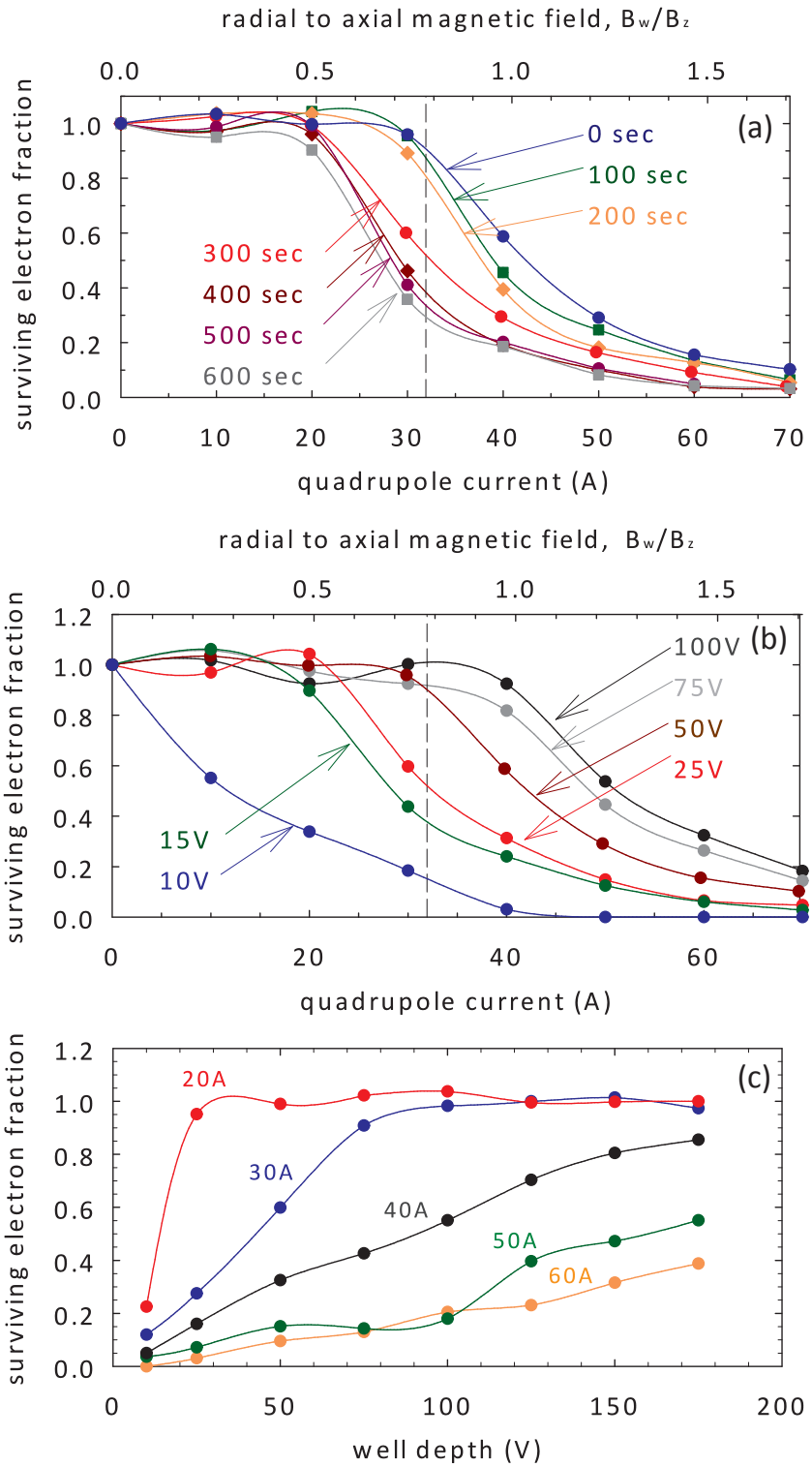

Figure 10.11: The fraction of 36 million electrons that survive a radial quadrupole field. (a) Field is ramped up to a given value, held for the time indicated, and ramped back down. The electrons were held in a 50 V potential in a radius-length electrode. (b) Current ramped up and immediately back down (c) current held for 5 minutes prior to ramping down.

Another paper [110] describes studies conducted in a quadrupole Penning-Ioffe trap under different conditions that demonstrate a higher rate of loss for electrons than what is shown here and described in Ref.[5]. There are five important differences which may explain this discrepancy. First, as we have seen the voltage applied to the electrodes on the Penning trap is an important parameter for determining stability. Ref.[110] conducted the experiments in a Malmberg-Penning trap where the confining electrode was held at ground and two electrodes on either side were given a negative potential. Ref [110] cites that the results were the same when a harmonic well was applied, but does not describe the potential used or a dependence on particle hold times, as is clearly demonstrated in Fig. 10.12(b) and (c). A stronger voltage applied should also decrease the diffusion coefficient described in equation (10.21) [41]. Second, the studies here were conducted in a radius length electrode while Ref.[110] uses two radius length electrodes, thus exponentially decreasing the cutoff radius described in equation (10.6). Third, Ref.[110] estimates their temperatures to be between 1 eV (11600 K) and 0.0004 (4.2 K), and are unable to measure temperatures below 0.05 eV (580 K) whereas we have allowed our electrons to synchrotron cool for much longer times than the synchroton cooling constant (2.6 s) and believe that our plasmas achieve a temperature close to 4.2 K. Fourth, Ref.[110] uses a background field of 0.4 T for its electron lifetime studies whereas we used a background field of 1 T. This affects both lengthens the cyclotron cooling time (16 s) and also leads to a larger radius plasma for a given angular momentum. Fifth, their method of loading electrons involved thermionic emission from a filament, whereas we used photoemission from our degrader using a 248 nm laser. This may have affected the shape of the

plasmas loaded and the temperature of the electrons.

The reliance of the hold time on plasma shape is not something that has been explored in detail but is likely an important parameter. Particle loss will increase with both increased radius and increased length, but there may be an optimal aspect ratio for maximizing particle lifetimes. Using the methods described in section 4.4 it should be possible to redo these studies with aspect ratio as a parameter. The aspect ratio can be changed through the use of a rotating wall technique [29].

Studies were conducted regarding the stability of positrons in an octupole field in 2006 by the ALPHA collaboration [112]. For a radial to axial field ratio of $B_w/B_z = 1.2$, a well depth of 49 V, an electrode radius of 22.3 mm and a trapping length of 40 mm they found that more than half of the positrons survived for a hold time of 500 s. This demonstrates the longer lifetimes of electrons and positrons for an octupole Penning-Ioffe trap than in a quadrupole Penning-Ioffe trap as was predicted in section 10.1.

10.3 Antiproton Stability Results

The same methods described in the previous section were used to test the stability of antiprotons [5]. Antiprotons were loaded into the lower stack electrode indicated in Fig. 10.10 using the electron cooling of antiproton methods described in chapter 5 and moved up to the electrode indicated in Fig. 10.10 using the techniques described in section 4.2. The current in the racetrack coils was ramped up at a rate of 0.1 amps/second, left at its maximum value for 300 seconds and then ramped down at the same rate. The antiproton loss during the ramp could be detected by looking

at the signals on the fiber and paddle detectors and at the end of the ramp, the antiprotons remaining were counted by ramping them onto the degrader.

Fig. 10.12(a) shows the resulting number of antiprotons that remained in the trap for a different maximum currents. We can see that a smaller fraction of the antiprotons remained for the case of 280,000 antiprotons than for 90,000. This is likely because a larger fraction of the antiprotons in the smaller cloud were at a smaller radius compared to the large cloud, thus decreasing the number lost due to being past the cutoff radius or increased radial transport. As we can see from Fig. 10.12(b), the vast majority of antiprotons are lost during the ramp up of the current and relatively few are lost while the current is held constant or decreased. This indicates that radial diffusion is not the dominant mechanism of particle loss and that most are probably being lost because they just travel outside of the cutoff radius which decreases as the field increases. It is likely there is significantly less loss with antiprotons than electrons because the much smaller plasmas (10^5 as opposed to 10^7) do not extend out radially or axially as far.

The ALPHA collaboration conducted tests of antiproton stability in an octupole field [112]. Their studies were conducted under the same conditions as their positron studies, described in section 10.2. They reported holding on to about 90% of their antiprotons after holding them in a 43 eV well at a field of $B_w/B_z = 1.2$ for 500 seconds. They do not specify the number of antiprotons used for their trials, making it difficult to compare directly with the results quoted above for a quadrupole. However, the results do seem to indicate an improved particle lifetime for antiprotons in an octupole Penning-Ioffe trap compared to a quadrupole.

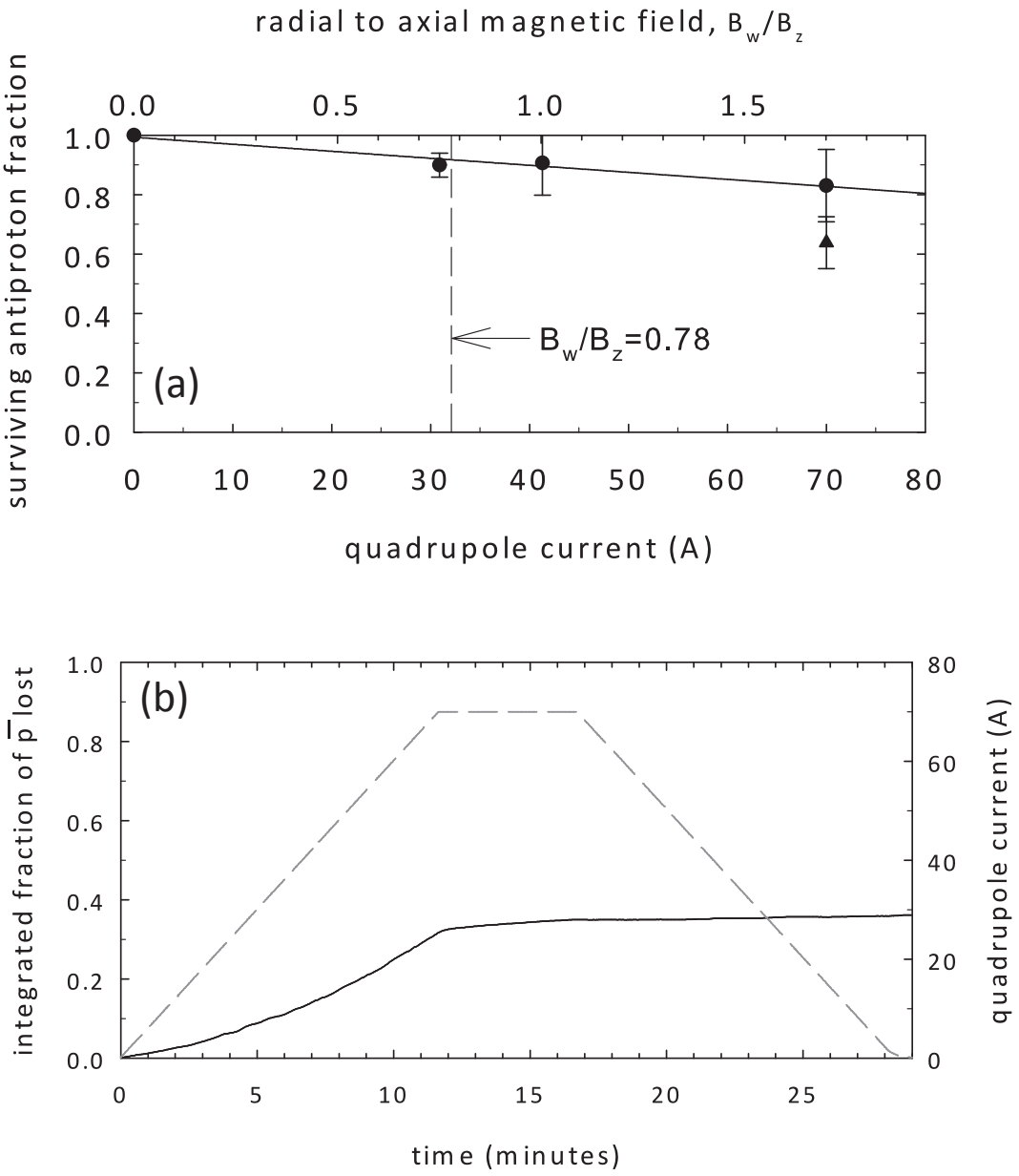

Figure 10.12: (a) Fraction of about 90 000 (circles) and 280 000 (triangle) trapped that survive a radial Ioffe quadrupole field that is ramped up to a given current, held 300 s, and ramped back down. (b) The integrated fraction of antiprotons lost (black, solid line) and the quadrupole current (gray, dashed line) as a function of time.

In summary, the lifetime of charged particles in quadrupole Penning-Ioffe trap has been shown to be long enough to perform a range of experiments in the parameters needed to achieve a trap depth of 375 mK. It is both predicted and has been shown experimentally that the lifetimes are superior in an octupole Penning-Ioffe trap, while a quadrupole offers a smaller trapping region and deeper trap depth. A next generation apparatus under construction will feature both a quadrupole and octupole Penning-Ioffe trap to more closely compare the advantages and disadvantages of both.

Chapter 11

Antihydrogen Production in a Penning-Ioffe Trap

The previous chapter described the stability of charged particles in a quadrupole Penning-Ioffe trap, here we take the next step discussing the successful formation of antihydrogen in a 375 mK deep quadrupole Penning-Ioffe trap [6]. No trapped antihydrogen atoms have yet been detected, but the demonstration of antihydrogen formation in the presence of a magnetic field minimum trap is a significant milestone of the way to trapped antihydrogen and laser spectroscopy. Prior to these experiments, two methods of cold antihydrogen formation had been demonstrated. In 2002, both the ATHENA **??** and ATRAP collaborations [4] demonstrated the formation of antihydrogen through the positron cooling of antiprotons in a nested well configuration and in 2004 ATRAP also demonstrated antihydrogen formation through the use of laser controlled positronium antiproton charge exchange process [113]. This chapter outlines the formation of antihydrogen through the positron cooling of antiprotons in

a nested well with a variety of currents flowing through the pinch coils and racetrack coils of Ioffe trap.

Even given the stability of charged particles in a Penning-Ioffe trap demonstrated in the previous chapter, there were still a number of factors that could preclude the formation of appreciable numbers of antihydrogen. First was the reduced background field compared to previous experiments, the ATHENA experiments occurred in a background field of 3 T and both sets of ATRAP measurements were conducted above 5 T. In the new experiments the background field was 1 T with the Ioffe field off and 2.15 T with the field full field for a 375 mK trap depth. Second, the presence of the radial field can cause both antiproton and positron loss, as well as change the profile of their interaction region. The antiproton loss due to following field lines out the trap will be even larger than in chapter 10 because now the antiprotons are being allowed to traverse an axial distance of 3 radius length electrodes in the nested well rather than being confined to a single radius length electrode. Despite these concerns, the generation of significant numbers of antihydrogen atoms within a Penning-Ioffe trap was demonstrated. Starting from a one tesla background field the number of antihydrogen atoms was actually found to increase as the trap depth in Ioffe trap was turned up, presumably due to the increased axial field due to the pinch coils. This chapter will describe experiments conducted leading the the publication of Ref. [6] and will also discuss some attempts with alternate antihydrogen formation schemes as well as future prospects for trapping antihydrogen.

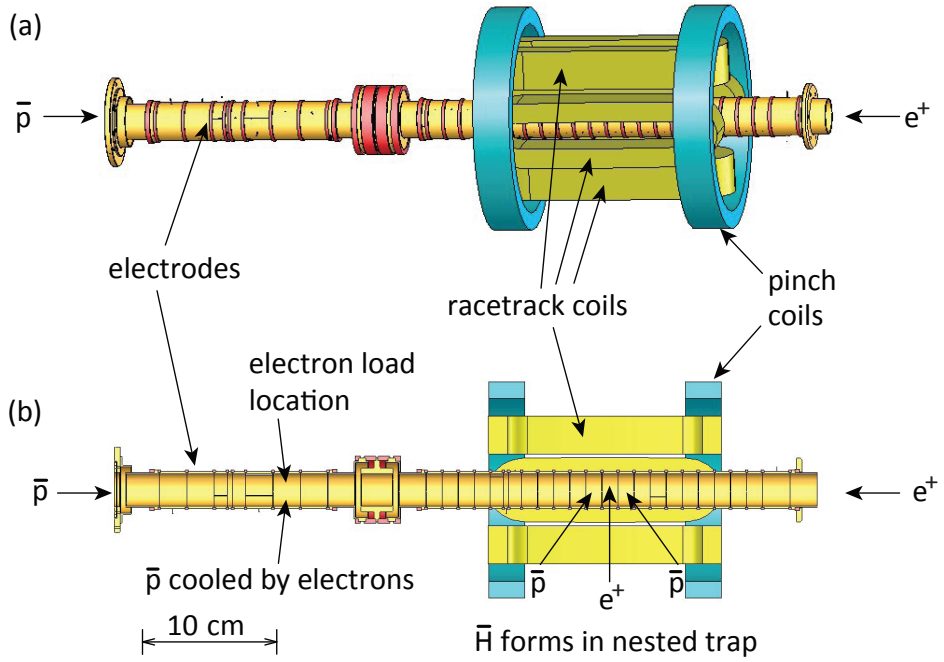

Figure 11.1: (a) Exterior and (b) cross section view of the Penning-Ioffe apparatus used to produce antihydrogen. A 1T bias field along the central axis of the electrode stack is produced by a large external solenoid (not depicted). Two pinch coils add an axially-confining gradient to the bias field. The radial quadrupole Ioffe field is produced by four racetrack coils.

11.1 Pulsed Antihydrogen Formation Method

In preparation to form antihydrogen, positrons were loaded into the upper stack using the methods described in chapter **??** and antiprotons were loaded using the methods described in chapter **??** with the Ioffe field off in a background axial field of 1 T. Both particle species were moved into the electrodes in the upper stack as indicated in Fig. 11.1 using the method described in section 4.2. Because the neon moderator for loading positrons would decay over time, as shown in Fig. 6.8a, a calibration load of positrons was taken before each trial in order to arrive at the appropriate number of positrons transfers to load the desired amount. After this calibration, 60 million

positrons and 200,000 antiprotons were loaded simultaneously using the methods described in section 6.2.2.

The method for forming antihydrogen in the Penning-Ioffe trap is shown in detail in Fig. 11.2a through Fig. 11.2f. With the Ioffe field off the positrons are placed into a nested well structure with the antiprotons loaded into a separate well structure a few electrodes further down the stack as shown in Fig. 11.2a. The antiprotons are launched into the nested well by pulsing down a voltage on one of electrodes on the side of the well for 1.75 μs as shown in Fig. 11.2b. This time was optimized to pulse in the vast majority of the antiprotons, but short enough to prevent them from reentering the initial well. This procedure was used rather than simply placing the particles next to each other in nested well in order to give the antiprotons enough axial energy so that they would interact with the positrons. During the pulse in the antiprotons cool through repeated interactions with the positrons until the settle in to the two side wells. Antihydrogen is produced during this step, but is not recorded as the Ioffe field is still off. Once the antiprotons have settled into the side wells and the antiproton annihilations have settled to the background counting rate, a voltage is changed on an electrode higher up in the stack from -150 V to 150 V in order to create an ionization detection well, that will be described below, as shown in Fig. 11.2c. The Ioffe trap is then turned on. Once the appropriate currents for the experiment are reached, the voltage on the electrode containing the positrons is slowly ramped up over 11 minutes as shown in Fig. 11.2d, initially at 0.12 eV/s,slowing to 0.04 eV/s. This brings antiprotons that previously did not have sufficient kinetic energy to interact with the positrons into contact with them, generating antihydrogen

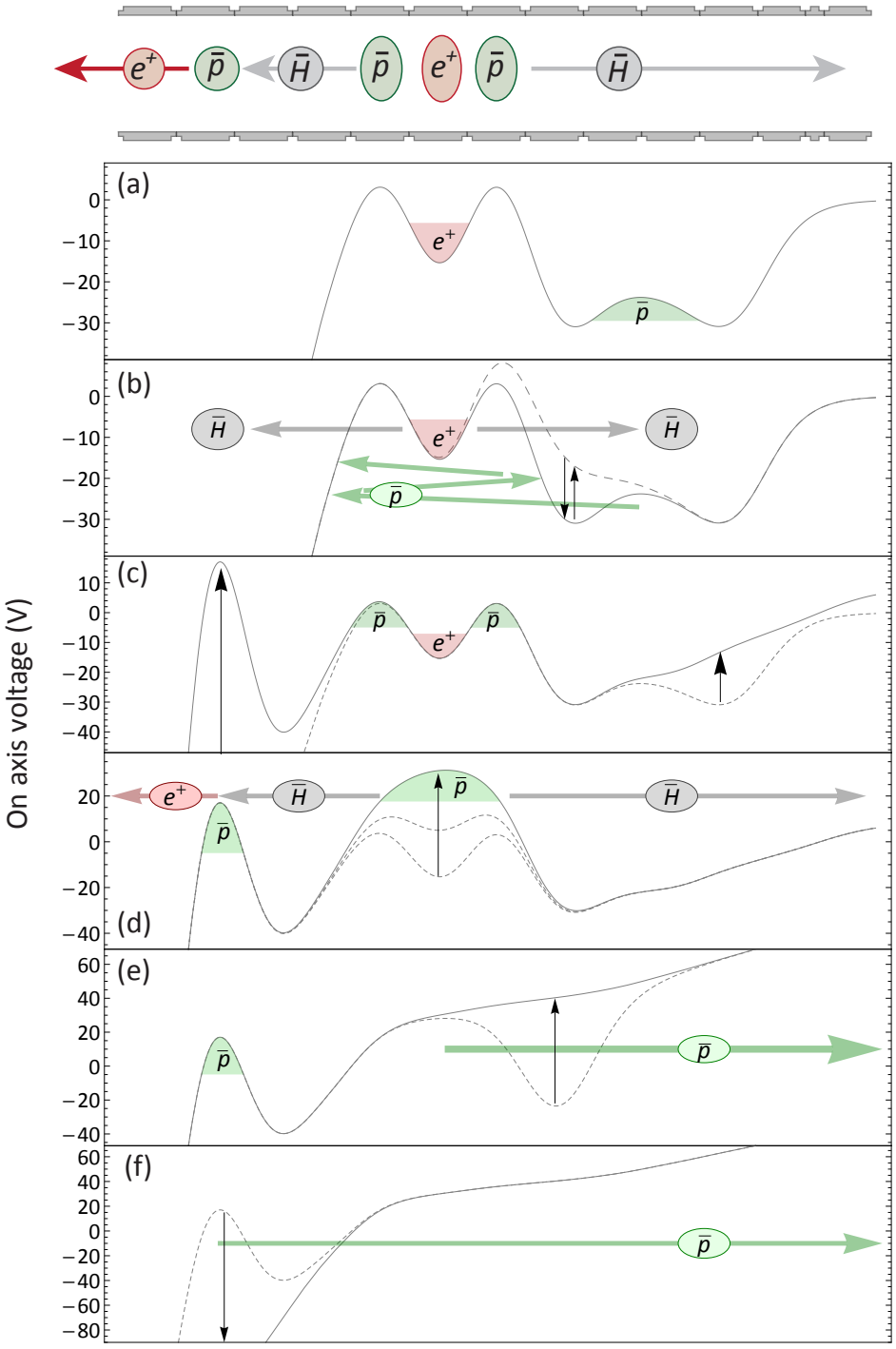

Figure 11.2: Antihydrogen formation procedure within a Penning-Ioffe trap. Details explained in text.

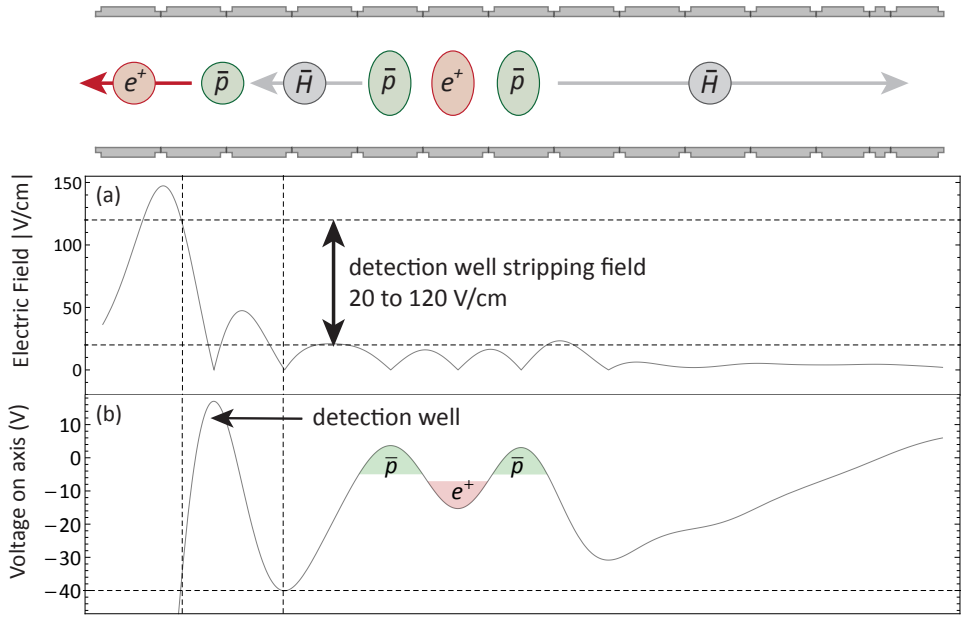

Figure 11.3: (a) The electric field used during the three body recombination procedure in Fig. 11.2d. antihydrogen atoms that are not ionized before entering the detection well shown in (b) will get ionized in the detection well.

through three body recombination with some of them depositing antiprotons in the detection well. After the ramp is complete so that the central well is inverted and of all of the antiprotons have been swept out, the Ioffe trap currents are lowered back down to zero. The antiprotons remaining in the nested well are then dumped onto the degrader using a precisely controlled voltage ramp and counted as shown in Fig. 11.2e. Finally, the detection well electrode voltage is ramped up very quickly in about 100 ms and the antiprotons in the detection well are dumped onto the degrader and counted out.

The field ionization method of detecting antihydrogen, first used by the ATRAP collaboration in 2002 [4], is depicted in Fig. 11.3. The potential depicted in Fig. 11.2c and Fig. 11.2d gives rise to the electric field profile shown in Fig. 11.3a. Any very

loosely bound antihydrogen formed which is heading towards the detection well will get stripped prior to reaching the detection well by the electric field which has a maximum of 20 V/cm. Antihydrogen which are more tightly bound than this and reach the detection well will see ionization fields up to 120 V/cm and if they are ionized, the antiproton will be deposited in the detection well while the positron will be repelled away. No antiprotons are able to reach the detection well unless they had formed antihydrogen, a fact that is verified by running through a null experiment with no positrons. When pulsing out the detection well to count the antiprotons, they can be counted in a rate which is significantly higher than the background rate of our antiproton annihilation detectors. Due to these fact, this is a background free method of detecting antihydrogen.

The relation between ionization field and the size of an antihydrogen atom radius has been calculated as approximately [114]:

$$\mathcal{E}_z > 3.60\,\mathrm{V/cm}\left(\frac{\mu\mathrm{m}}{\rho}\right)^2 \tag{11.1}$$

which means that for detection well fields between 20 V/cm and 120 V/cm we are able to detect antihydrogen atoms with radii between 0.17 µm and 0.42 µm.

Fig. 11.4 shows the superposition of magnetic and electric fields that are present during the ramp up of the quadrupole Penning-Ioffe trap. The effect of the Ioffe field on the antiprotons as they are mixing with the positrons at the beginning of the positron electrode voltage ramp is depicted in Fig. 11.5. Antiprotons which are confined within the side wells at a given energy (depicted in Fig. 11.5 for 18 eV) will follow field lines until they reach an equipotential that surpasses their kinetic energy, and then will proceed back. As we can see Fig. 11.5b antiprotons that start out at

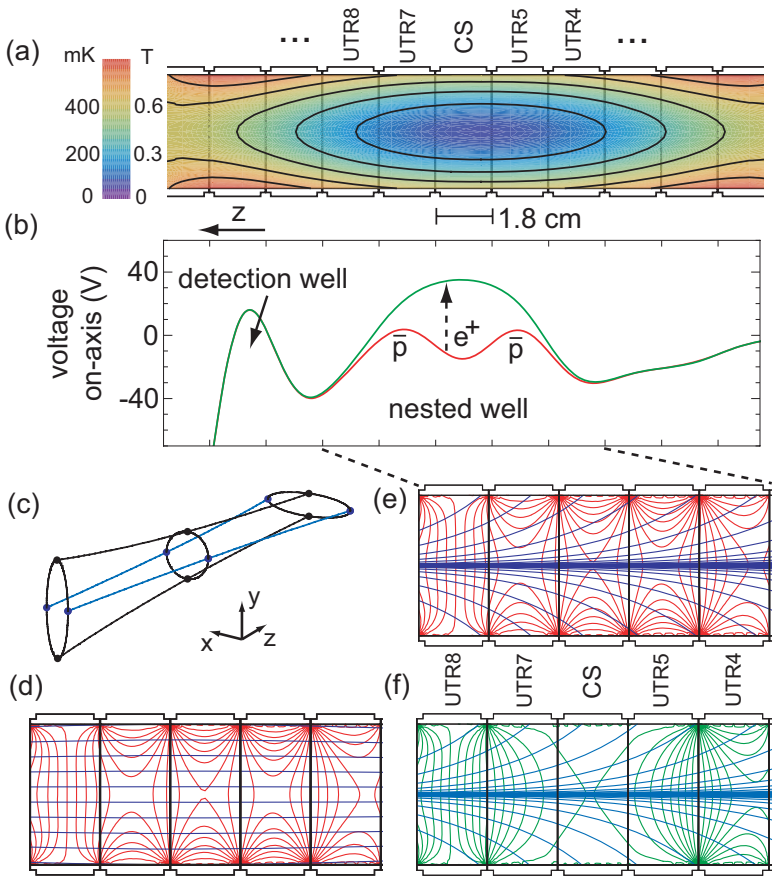

Figure 11.4: (a). Potential wells seen by charges on-axis (b) during (red) and after (green) $\bar{H}$ production, with corresponding equipotentials for these two cases (d) to (f).

certain radius will follow a field line into an electrode and annihilate.

11.2 Experimental Results

Repeated trials of the procedure described in the previous section at different Ioffe trap depths yielded the results shown in Fig. 11.6a. The trap depth is given for antihydrogen atoms in the low field seeking ground state in temperature units where $T = 0.67|\Delta B|$. The number of antihydrogen atoms formed, which was normalized

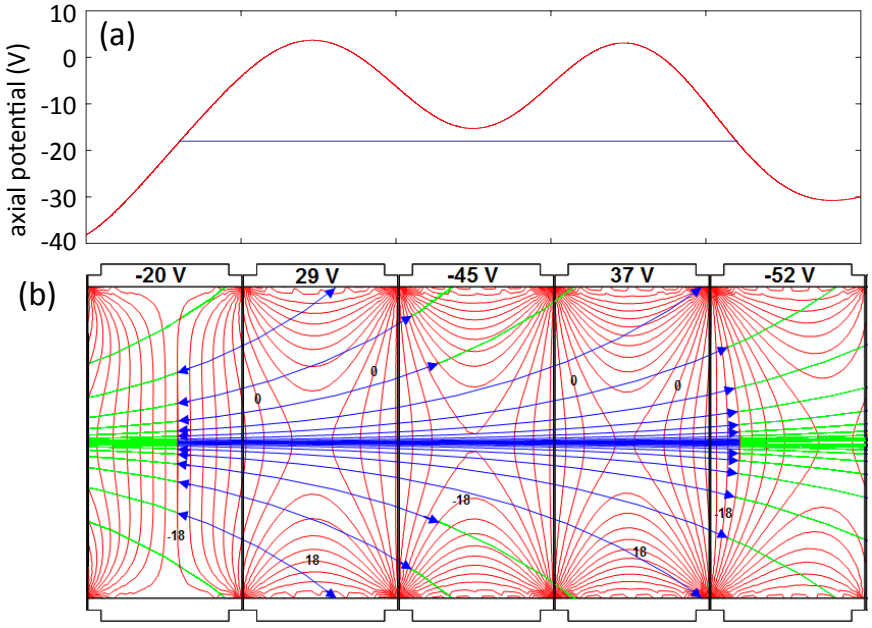

Figure 11.5: (a). Potential wells seen by charges on-axis (b) during (red) and after (green) $\bar{H}$ production, with corresponding equipotentials for these two cases (d) to (f).

to the number of antiprotons used, initially decreases with the addition of the Ioffe trap field, but then begins to increase around 300 mK. It was suspected that the mechanism for this increase was the increased axial field provided by the pinch coils. To investigate this, the trials were repeated with only running the current in the pinch coils. As can be seen in Fig. 11.6b, there is an appreciable increase in the antihydrogen production due to the presence of the pinch coil fields. The anomalous looking data just below 200 mK and 400 mK were reproducible, but remain unexplained. The increased yield at the higher field is likely due to an increase in the positron plasma density which would increase the three body recombination rate. The yield with the radial field is less than with only the pinch coils running, but the net effect is indeed an increase in the amount of antihydrogen produced.

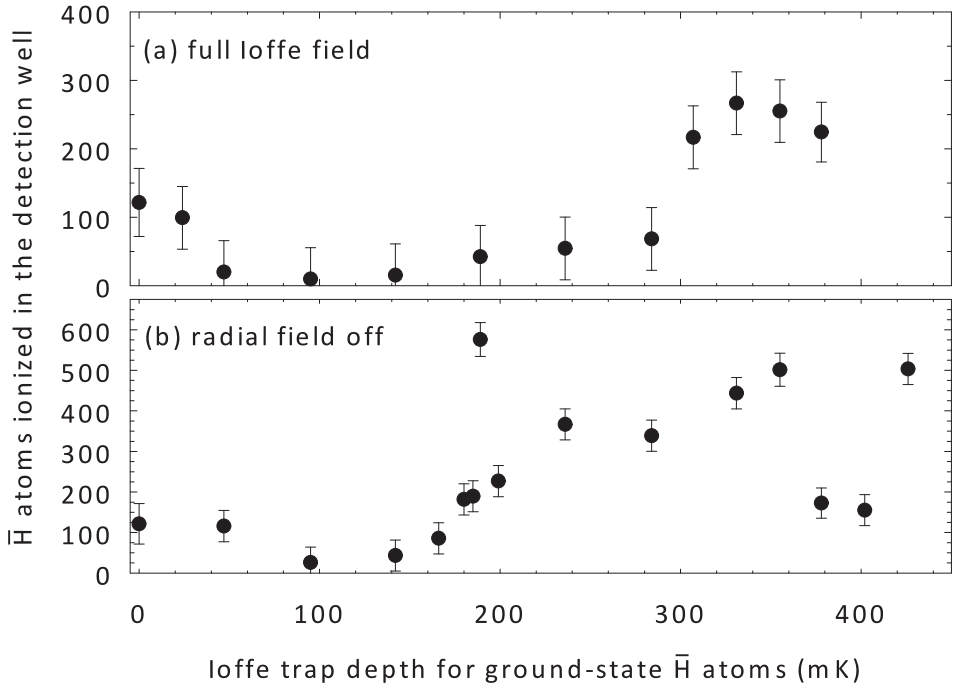

Figure 11.6: Number of $\bar{H}$ ionized in the detection well per trial within the Ioffe trap (a) and within only the axial field of the Ioffe trap (b), as a function of the trap depth. $\bar{H}$ numbers are normalized to an average of 0.1 million $\bar{p}$ per $\bar{H}$ production and detection trial, with reproducibility error bars.

Further information about the dynamics of the antihydrogen formation can be understood by examining the energy distribution of antiprotons remaining in the nested well. Fig. 11.7 shows the results of a series of trials with the Ioffe trap off; instead of ramping the positron electrode in the nested well at a rate of 0.12 eV/s, slowing to 0.04 eV/s as for the experiments depicted in Fig. 11.6 the ramp rate was varied and the effect on the axial distribution of the antiprotons left in the nested well was recorded. Fig. 11.7 demonstrates that the longer the interaction time with the positrons, the lower the axial energy of the antiprotons as we would expect.

Another set of data was recorded by noting the axial energy of the antiprotons left in the nested well for different Ioffe trap depths. This is shown in Fig. 11.8. As

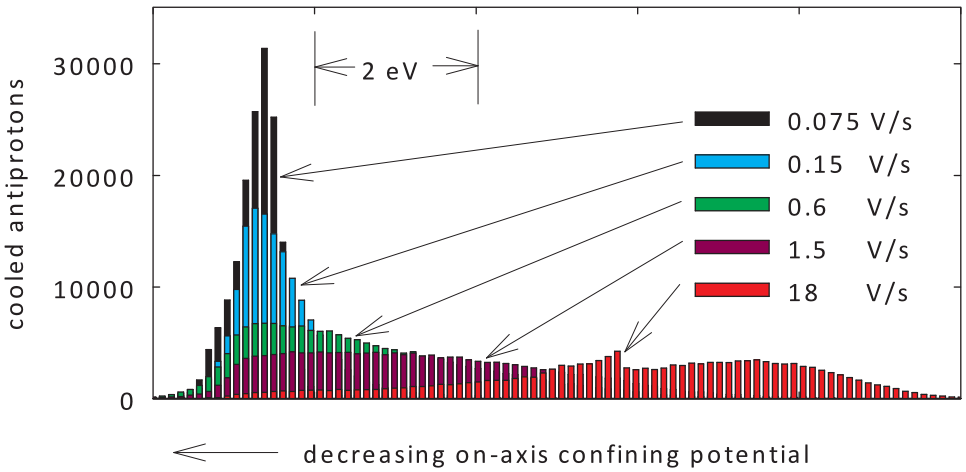

Figure 11.7: The energy distribution of antiprotons remaining in the nested well after antihydrogen formation as a function of nested well ramp rate. We can see that the longer the antiprotons are allowed to interact with the positrons the lower their axial energy is and the more efficiently they cool to the bottom of the well.

the strength of the Ioffe trap increases, fewer high energy antiprotons are left in the nested well, indicating that the higher energy ones have left the trap by following field lines and hitting the electrode. This is a demonstration of the cutoff radius effect described in chapter 10.

Several attempts were made to detect any trapped antihydrogen that might have been formed through this procedure. Instead of ramping the Ioffe trap down after the step depicted in Fig. 11.2d, the electric potentials were swept out to get rid of any remaining charged particles, and then the Ioffe trap was ramped down as quickly as possible in order to try to produce an annihilation signal above the background rate of our detectors; to get above this background we would need a single of twenty antihydrogen annihilations per second. In 2007 we were limited to a ramp down rate of about a minute due to the limit set by the protection diodes across the racetracks. If we put a voltage across the current leads greater than the 5 V diode drop then the

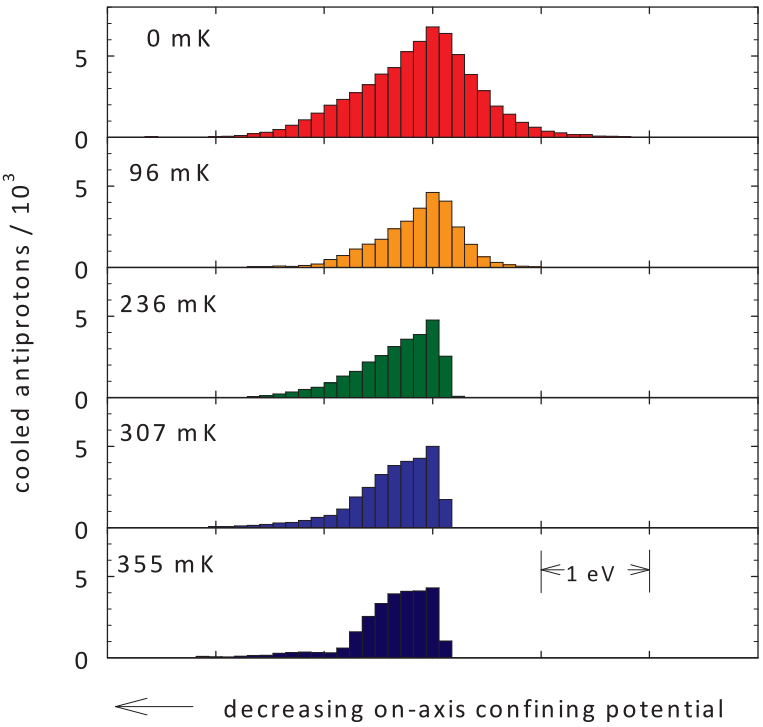

Figure 11.8: The energy distribution of antiprotons remaining in the nested well after antihydrogen formation as a function of trap depth in the Ioffe trap. We can see that as the radial field increases we cease to see high energy axial antiprotons, an indication that antiprotons are being lost due to radial excursions past a cutoff radius.

current would just dissipate through the diodes and we would not achieve a faster ramp rate. In 2008, with the quench heater installed, one of the racetracks could be caused to quench as described in section and the current leaves the trap on the order of a few seconds. Using both methods no antihydrogen atoms were detected above background. The new apparatus under construction will not have these protection diodes and will feature a fast dump resistor switch to take all of the current out of the Ioffe trap in less than second.

11.3 Alternate Methods and Prospects for Trapping Antihydrogen

The method outlined in section Section 11.1 is a procedure that yields a certain amount of antihydrogen with a certain energy distribution. In order to try to maximize the chances for trapping antihydrogen we can try to improve two parameters, first we can try to increase the number of antihydrogen atoms produced and second we can try lower the energy of the antihydrogen atoms produced. Unfortunately, a method which improves both parameters has not been identified: methods that produce large numbers of antihydrogen also produce them at high energies, while the methods that are believed to produce them at a lower axial energy also yield a much smaller number of antihydrogen atoms.

In 2004 [115] and in subsequent experiments [?] the velocity of antihydrogen produced in a nested well using both a pulsed in method, similar to the one described above, and a driven method, described below was measured and indicated an antihydrogen axial energy around 0.2 eV (2400 K). A subsequent theoretical paper was published interpreting these results, and determined that this high velocity may be the result of a slower antihydrogen atom undergoing a charge exchange with a faster antiproton moving in the sidewell [116], meaning that there maybe significantly slower antihydrogen being produced that we have so far been unable to detect. Regardless of the actual temperature of the antihydrogen formed, there are some basic guidelines that should be followed to decrease the axial energy of the antihydrogen. Due to the nearly 2000 fold mass difference between antiprotons and positrons, the energy of the

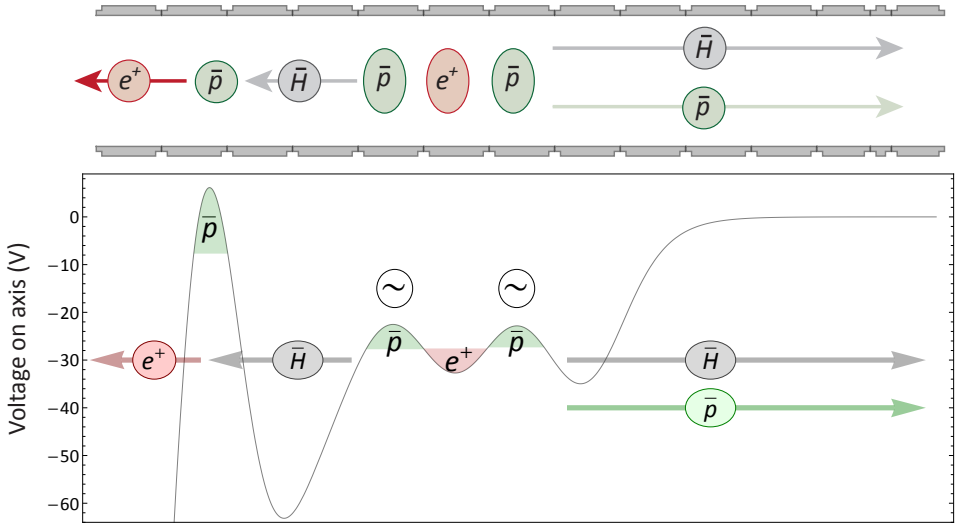

Figure 11.9: Typical potential structure used for noise driven antihydrogen production.

antihydrogen atom will be dominated by the velocity of the antiproton at the time of formation. Therefore the natural way to try to form cold antihydrogen is to diminish the velocity of the antiprotons, and ideally have them at rest in thermal equilibrium with the trap. This section will describe three alternative methods of producing antihydrogen and discuss their likely effects on the antihydrogen temperature.

11.3.1 Noise drive antihydrogen formation

The most effective method of producing large numbers of antihydrogen atoms has been to a apply a radiofrequency drive to the antiprotons sidewells of a nested well in order to drive them through the positron plasma. This method was usually practiced throughout 2002 to 2004 by applying a single drive near the resonant frequency of the antiprotons at the bottom of the sidewells [117]. This would excite the antiprotons at the bottom of the well which would subsequently collide with higher energy antipro-

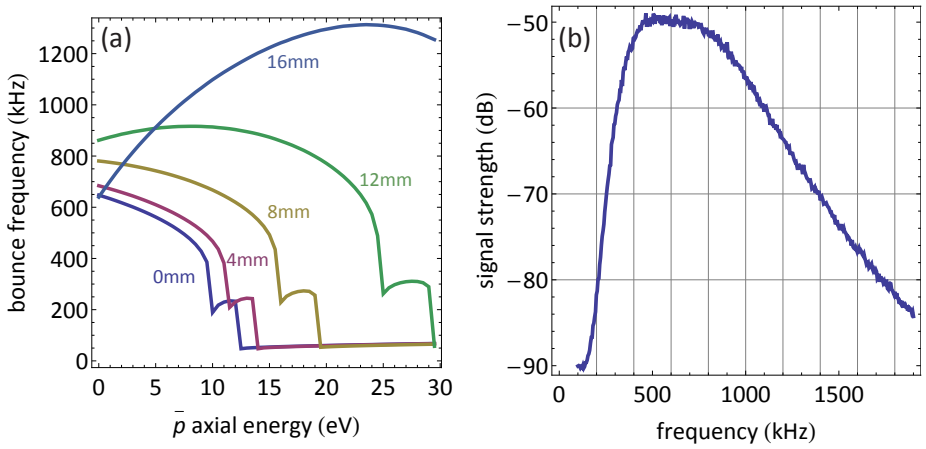

Figure 11.10: (a) The bounce frequencies of antiprotons in the nested well structure in Fig. 11.9 at different radii, the sharp drop in frequency is due to antiprotons moving from a sidewell into the entire nested well. (b) the spectrum of the noise drive applied.

tons increasing the energy of the entire distribution. In 2007 and 2008 we chose to do a slight variation on this technique by applying a broadband noise drive to both wells rather than a single frequency drive.

A typical potential structure for a noise drive antihydrogen experiment is shown in Fig. 11.9. The drives are applied on the two sidewells and the potential is arranged so that any antiprotons which are driven above the top of the nested well structure exit down the electrode stack and away from the detection well. For a driven antiproton to enter into detection well it would have to increase by more than 10 eV in a single pass and then also collide with another antiproton to lose enough energy to settle into the well. It has been confirmed that this does not happen by running the same experiment without positrons.

Fig. 11.10a shows the bounce frequencies in the nested well structure in Fig. 11.9for antiprotons with a given energy above the bottom of the sidewell for different radii.

This chart is for the lower (left) sidewell but the other sidewell is nearly identical. The sharp drop in frequency occurs as the antiprotons move from one of the sidewells to the overall nested well. In order to optimally drive the antiprotons we would like to apply a broadband frequency drive which only drives the motion in the sidewell but not in the nested well as this would cause unnecessary antiproton loss. To accomplish this, the noise drive function from an SRS DS345 was fed into two bandpass Chebyshev filters producing the spectrum in Fig. 11.10b so that there was a significantly reduced drive for frequencies in the full nested well. The amplitude of the drive was varied from experiment to experiment, and it was found that as many as 1700 antihydrogen atoms could be created and detected in the nested well using this method, a significant increase compared to the pulse launched method described. The quench detection method described in section Section 11.2 was attempted for the noise drive trials as well, and no signals were detected above background.

11.3.2 Radiative recombination trials

Rather than try to increase the number of antihydrogen produced, a few trials were attempted to try to create very cold antihydrogen by inverting the nested well and having antiprotons on the central electrode and slowly ramping the central antiproton well down and through the positrons. Because in this case antiprotons would not be moving through a dense positron plasma and instead positrons moving through antiprotons, the dominant reaction mechanism would not be three body recombination, but rather radiative recombination. The rate for this reaction is about 6 orders of magnitude lower than three body recombination [118] but has a better chance of

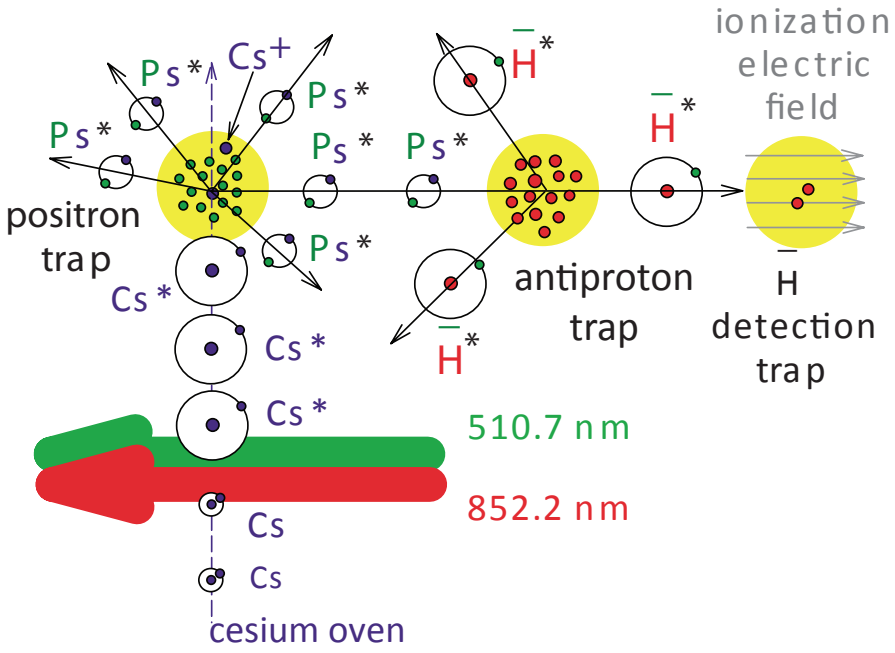

Figure 11.11: Schematic of laser-controlled antihydrogen production.

producing cold antihydrogen as the antiprotons are not traveling axially. In a limited number of trials, no antihydrogen atoms were detected above background using the Ioffe trap quench detection method.

11.3.3 Laser controlled antihydrogen production

The most promising method for producing antihydrogen with very low axial energy is the Rydberg positronium charge exchange method pioneered by ATRAP in 2004 [113]. This method uses cesium atoms excited in a two stage laser process to $\simeq n_{Cs} = 37$. The cesium travels through a positron cloud and gives off its outer electron to form positronium, which then charge exchanges with antiprotons to form antihydrogen as shown in Fig. 11.11. Once again, because the antiprotons are held in a single electrode

presumably in thermal equilibrium with their surroundings, this should produce very low axial energy antihydrogen atoms. In those trials, $14 \pm 4\,\bar{H}$ were produced over the course of 6 trials. With the increased number of positrons and antiprotons now available to ATRAP, it should be possible to increase these numbers in the new apparatus. It may however be a challenge to to promote the same laser excitations in the presence of the Ioffe trap field. Preliminary work for installing a cesium charge exchange apparatus was done in 2007 and 2008. In 2007 an electrode with an access hole for allowing a cesium beam to enter was installed, and in 2008 a mechanical structure with a cesium getter oven and fibers for laser access was installed into one of the access ports in the Ioffe trap. No cesium laser cesium excitations were observed within the apparatus in 2008 but work is ongoing in 2009.

11.4 Summary

The formation of antihydrogen in a 375 mK deep quadrupole Penning-Ioffe trap was demonstrated through a pulsed nested well three body recombination method. This has definitively put to rest fears that it would not be possible to form antihydrogen in such a trap [111, 112, 119]. The number of antihydrogen produced compared to 1 T is actually increased when turning on the Ioffe trap, likely due to the presence of the increased axial field from the pinch coils. No trapped antihydrogen atoms were observed above background, but these experiments have proven that antihydrogen formation in a magnetic trap is feasible and have paved the way for future experiments. A new apparatus with a deeper electric trap is being built and may yield very exciting results.

Chapter 12

Conclusion and Future Directions

The work described in this thesis represents several significant advances towards magnetically trapped antihydrogen atoms bringing closer the long term goal of laser spectroscopy. The research conducted from 2002 to 2004 in the previous generation of apparatuses demonstrated that cold antihydrogen could be formed by two methods [4, 113] and provided valuable insight into the properties of the atoms formed [117, 115] but the experiments had to be substantively rethought to make them compatible with a magnetic field minimum Ioffe trap to confine the antihydrogen. To maximize the chances for trapping antihydrogen, operation in a lower magnetic field had to be demonstrated and optimized, the number of positrons and antiprotons loaded had to be significantly increased and the temperature of the apparatus had to be lowered. It was also necessary to show that charged particles could be stored in a Penning-Ioffe trap for a sufficiently long time to form antihydrogen. Furthermore, adapting sensitive detection techniques to the new apparatus had to be undertaken to proceed with possible antihydrogen ion experiments and precise detector calibrations. All of these

goals were accomplished and some of the largest hurdles to trapping antihydrogen have now been overcome. However, magnetically trapped antihydrogen has yet to be detected and significant challenges remain.

The amount of new equipment installed at CERN between 2006 and 2008 enabling the results in this thesis and which will serve as a robust platform for future experiments is impressive. Two new experimental zones were setup, one housing a 247 Henry 20 inch bore 3 T superconducting magnet attached to the CERN antiproton decelerator beamline and another containing a new buffer gas positron accumulator. The two zones were successfully interfaced to allow for the efficient transfer of over 10 million positrons every 100 seconds. Two new Penning-Ioffe trap apparatuses were constructed each featuring 36 cylindrical electrodes 36 mm in diameter with precise voltage control going from -1000 V to 1000 V on each electrode and 5 kV going to two designated HV electrodes. Each electrode is also equipped with the capability of receiving fast pulse signals, RF drives and monitoring of electrical pickup allowing for a very wide range of experiments in the future. Both apparatuses were capable of reaching a base temperature between 4 °K 5 °K, and the BTRAP apparatus was equipped with a pumped helium system allowing the electrode stack to reach a temperature an even lower temperature of 1.2 °K. The apparatuses are capable of storing antiprotons for 15 hours with no detectable loss of due to annihilations with a background gas, corresponding to a background pressure of less than 3×10^{-16} Torr. This is especially impressive considering that the apparatus is attached to the positron buffer gas accumulator approximately 10 meters away.

Significantly larger numbers of antiprotons, electrons and positrons were loaded

than previous experiments. At a background field of 1 T, up to 35,000 antiprotons were typically loaded per 100 second AD cycle compared to about 15,000 per AD cycle at 5 T in the new apparatus. With the installation of the antiproton solenoid which temporarily boosts the field in the lower electrode stack, the antiproton capture rate was boosted by a factor of 5 by bringing the axial field up to 3.6 T. However, a means of transferring all of those antiprotons back into a low field region without significant loss has not been mastered. A new electron loading method was developed reliably allowing for the accumulation of over 10^6 electrons per second compared to the previous methods allowing for only about 8500 electrons per second [48]. A new positron accumulation and transfer method was developed allowing for the accumulation of 6.5 million e^+/(mCi hour) at a field of 1 T compared to the previous rate of 10,000 e^+/(mCi hour) at 5 T.

Tuned circuit amplifiers were installed onto the electrodes in the Penning trap to monitor the cyclotron signals coming from antiprotons and the axial oscillation signals coming from both antiprotons and electrons. The antiproton cyclotron signals were measured for large antiproton clouds, and in combination with magnetron sidebands allowed for a characterization of the homogeneity and profile of the magnetic field. The axial frequency of antiprotons was measured indirectly through a combination of the cyclotron frequency and magnetron sidebands, and the axial frequency of protons was measured directly. The cyclotron signal from a single antiproton was detected and followed as it decayed for greater than half an hour, demonstrating the sensitivity needed for antihydrogen ion experiments and precise detector calibrations at a lower magnetic field and in larger electrodes than had been accomplished before.

A 375 mK deep (for ground state $\overline{\mathrm{H}}$ atoms) quadrupole Ioffe trap with four laser access ports was designed, built, and commissioned for use in ATRAP experiments. The combined Penning-Ioffe trap was used to demonstrate the stability of both electrons and antiprotons in a quadrupole Penning Ioffe trap configuration [5]. The formation of antihydrogen using three body recombination was demonstrated at a lower field, 1 T, than had been accomplished before. The same trap was used to demonstrate the formation of antihydrogen in the presence of a 375 mK Penning-Ioffe trap [6]. These experiments resolved a controversy as to whether the long term stability of charged particles in such a configuration to form antihydrogen was possible [108, 111, 110]. A quench inducing heater system was installed in order to take the current out of the Ioffe trap in a few seconds, rather than approximately a minute as limited by the protection diodes.

These results have paved the way for the trapping of antihydrogen and have informed the construction and design of the next generation of apparatus. Now that it has been proved that antihydrogen can be formed in the presence of Ioffe trap, progress towards detecting trapped antihydrogen must proceed by improving a series of parameters:

1. **The temperature of antihydrogen when it is formed should be lowered**. The temperature of the apparatus has been lowered to $1.2\,^{K}$, but the measurements taken of the antihydrogen velocity in the past suggest the antiprotons are created at temperatures much higher (2000 °K) than the temperature of the electrodes [115]. More recent theoretical interpretations have concluded that this velocity measurement may be the result of a charge exchange between

much slower moving antihydrogen and faster moving antiprotons [116]. Regardless, methods that are likely to produce slower antihydrogen such as positronium charge exchange [113] must be pursued and optimized in the new experiment. More sensitive detections of the temperature of the positron and antiproton plasmas in different experiments should also be undertaken.

2. **Larger numbers of antihydrogen atoms should be produced**. Different formation methods lead to a different yield and temperature of antihydrogen atoms. It may be that a high yield method which produces slightly hotter antihydrogen will be more successful than the low temperature lower yield methods. Driven antihydrogen experiments have produced very high numbers of atoms and may prove to be the most promising method for trapping through sheer force of numbers. The yield of the low temperature experiments, such as the positronium charge exchange, can be improved by increasing the density and size of antiproton and positron plasmas. The antihydrogen formation rate can also be improved by limiting the loss of charged particles due to the radial field from the Ioffe trap. The second generation ATRAP Penning-Ioffe trap will have an octupole field that will have a smaller amount of loss and thus is likely to produce more antihydrogen. It will also have a quadrupole field.

3. **The trap depth of the Ioffe trap should be increased.** The first generation Ioffe trap had a depth of 375 °mK. For a Maxwell Boltzmann distribution around 1.2 °K this would trap about 11% of ground state antihydrogen atoms. The second generation Ioffe trap will have a trap depth of approximately 600 °mK which would trap about 20%, while a trap solely optimized for depth could

likely give a 1 °K depth trapping about 35%. The second generation trap under construction should improve the prospects for trapping by about a factor of two, and can be considered a significant advance.

4. **The current ramp down rate of the Ioffe trap should be improved to increase trapped antihydrogen detection sensitivity**. The present Ioffe trap, with the quench heater system, can remove the current within a few seconds, but to reliably detect antihydrogen above the background rate of our annihilation detectors would require twenty antihydrogen annihilations per second. The second generation Ioffe trap will incorporate a high power insulated gate bipolar transistor (IGBT) switch along with an external dump resistor allowing for current to be removed in 100 ms or less significantly improving detection sensitivity.

5. **A better understanding and control of internal antihydrogen states should be pursued**. Antihydrogen produced thus far is believed to be created in high Rydberg states [117] and if it were to be trapped it would eventually cascade down to to the lower n-states [99]. The dynamics of this and the subsequent behavior in a Ioffe trap are not yet fully understood and may present hurdles to both trapping and spectroscopy. Different antihydrogen formation methods such as three body recombination, positronium charge exchange and radiative recombination all produce antihydrogen in different states. Methods are also being pursued to control the state distribution of antihydrogen through the use of half cycle pulses.

Progress on all of these fronts is currently underway at CERN, and the new apparatus,

CTRAP, to be commissioned in late 2009 or 2010 incorporates all of the experience that has been learned from ATRAP and BTRAP. With continued hard work, and if nature decides to be kind, the trapping and laser spectroscopy should follow yielding exciting scientific results.

Bibliography

[1] Zhongdong Zhang, Ph.D. thesis, Ruhr-Universität Bochum, 2007.

[2] G. Baur, G. Boero, S. Brauksiepe, A. Buzzo, W. Eyrich, R. Geyer, D. Grzonka, J. Hauffe, K. Kilian, M. Lo Vetere, M. Macri, M. Moosburger, R. Nellen, W. Oelert, S. Passaggio, A. Pozzo, K. Rohrich, K. Sachs, G. Schepers, T. Sefzick, R.S. Simon, R. Stratmann, F. Stinzing, and M. Wolke, Phys. Lett. B **368**, 251 (1996).

[3] M. Amoretti, C. Amsler, G. Bonomi, A. Bouchta, P. Bowe, C. Carraro, C. L. Cesar, M. Charlton, M. J. T. Collier, M. Doser, V. Filippini, K. S. Fine, A. Fontana, M. C. Fujiwara, R. Funakoshi, P. Genova, J. S. Hangst, R. S. Hayano, M. H. Holzscheiter, L. V. Jorgensen, V. Lagomarsino, R. Landua, D. Lindelof, E. L. Rizzini, M. Macri, N. Madsen, G. Manuzio, M. Marchesotti, P. Montagna, H. Pruys, C. Regenfus, P. Riedler, J. Rochet, A. Rotondi, G. Rouleau, G. Testera, A. Variola, T. L. Watson, and D. P. van der Werf, Nature **419**, 456 (2002).

[4] G. Gabrielse, N. S. Bowden, P. Oxley, A. Speck, C. H. Storry, J. N. Tan, M. Wessels, D. Grzonka, W. Oelert, G. Schepers, T. Sefzick, J. Walz, H. Pittner, T. W. Hänsch, and E. A. Hessels, Phys. Rev. Lett. **89**, 213401 (2002).

[5] G. Gabrielse, P. Larochelle, D. Le Sage, B. Levitt, W.S. Kolthammer, I. Kuljanishvili, R. McConnell, J. Wrubel, F.M. Esser, H. Glueckler, D. Grzonka, G. Hansen, S. Martin, W. Oelert, J. Schillings, M. Schmitt, T. Sefzick, H. Soltner, Z. Zhang, D. Comeau, M.C. George, E.A. Hessels, C.H. Storry, M. Weel, A. Speck, F. Nillius, J. Walz, and T.W. Haensch, Phys. Rev. Lett. **98**, 113002 (2007).

[6] G. Gabrielse, P. Larochelle, D. Le Sage, B. Levitt, W. S. Kolthammer, R. McConnell, P. Richerme, J. Wrubel, A. Speck, M. C. George, D. Grzonka, W. Oelert, T. Sefzick, Z. Zhang, A. Carew, D. Comeau, E. A. Hessels, C. H. Storry, M. Weel, J. Walz, and A. T. R. A. P. Collaboration, Phys Rev Lett **100**, 113001 (2008).

[7] M. Niering, R. Holzwarth, J. Reichert, P. Pokasov, Th. Udem, M. Weitz, T. W. Hänsch, P. Lemonde, G. Santarelli, M. Abgrall, P. Laurent, C. Salomon, and A. Clairon, Phys. Rev. Lett. **84**, 5496 (2000).

[8] S. Eidelman *et al.*, Physics Letters B **592**, 1 (2004).

[9] G. Lüders, Ann. Phys. **2**, 1 (1957).

[10] C. S. Wu, E. Ambler, R. W. Hayward, D. D. Hoppes, and R. P. Hudson, Phys. Rev. **105**, 1413 (1957).

[11] J. H. Christenson, J. W. Cronin, V. L. Fitch, and R. Turlay, Phys. Rev. Lett. **13**, 138 (1964).

[12] D. Colladay and V. A. Kostelecký, Phys. Rev. D **55**, 6760 (1997).

[13] R. Bluhm, V. A. Kostelecký, and N. Russell, Phys. Rev. Lett. **82**, 2254 (1999).

[14] D. E. Pritchard, Phys. Rev. Lett. **51**, 1336 (1983).

[15] H. F. Hess, G. P. Kochanski, J. M. Doyle, N. Masuhara, D. Kleppner, and T. J. Greytak, Phys. Rev. Lett. **59**, 672 (1987).

[16] C. L. Cesar, D. G. Fried, T. C. Killian, A. D. Polcyn, J. C. Sandberg, I. A. Yu, T. J. Greytak, D. Kleppner, and J. M. Doyle, Phys. Rev. Lett. **77**, 255 (1996).

[17] M. Corradini A. Dax H. Dølrath Y. Enomoto S. Federmann S. Friedreich R.S. Hayano H. Higaki M. Hori; D. Horvťath C.A. Hunniford H. Imao S. Itoh B. Juhťasz Y. Kanai K. Kira H. Knudsen H-P E. Kristiansen N. Kuroda M. Leali E. Lodi-Rizzini M. Lund V. Mascagna O. Massiczek Y. Matsuda R.W. McCullough K. Michishio S.P. Møller A. Mohri Y. Nagata T. Pask W. Pirkl H Saitoh P. Somkuti A. Sťotťer K. T?okťesi H.A. Torii U. Uggerhøj K. Umlaub V.L. Varentsov L. Venturelli E. Widmann Y. Yamazaki Z. Yoshida P. Zalťan N. Zurlo D. Barna;, M. Charlton, ASACUSA STATUS REPORT: ASACUSA progress during 2008 and plans for 2009 (*CERN-SPSC-2009-005 / SPSC-SR-040*).

[18] Hans G. Dehmelt, "Autobiography for 1989 Nobel Prize in Physics", Published in "Les Priz Nobel", 1990.

[19] J. D. Jackson, *Classical Electrodynamics, 3rd Edition* (John Wiley and Sons, Inc., New York, 1975).

[20] L. S. Brown and G. Gabrielse, Rev. Mod. Phys. **58**, 233 (1986).

[21] Erik. A. Westwig Burce R. Kusse, *Mathematical Physics: Applied Mathematics for Scientists and Engineers, 2nd Edition* (Wiley-VCH, New York, 2006).

[22] G. Gabrielse, L. Haarsma, and S. L. Rolston, Intl. J. Mass Spec. Ion Proc. **88**, 319 (1989), ibid. 93, 121 (1989).

[23] A. Speck, Ph.D. thesis, Harvard University, 2005.

[24] S. L. Rolston and G. Gabrielse, Hyperfine Interact. **44**, 233 (1988).

[25] David Phillips, Ph.D. thesis, Harvard University, 1996.

[26] Francis F. Chen, *Introduction to Plasma Physics* (Plenum, New York, 1974).

[27] R. J. Goldston and P. H. Rutherford, *Introduction to Plasma Physics* (Inst. of Phys., London, 1995).

[28] P. Oxley, Ph.D. thesis, Harvard University, 2003.

[29] D. H. E. Dubin and T. M. O'Neil, Rev. Mod. Phys. **71**, 87 (1999).

[30] L. D. Landau and E. M. Lifshitz, *Mechanics (Third Edition)* (Pergamon Press, New York, 1976).

[31] Ronald C. Davidson and Nicholas A. Krall, Phys. Fluids **13**, 1543 (1970).

[32] S.A. Prasad and T.M. O'Neil, Phys. Fluids **22**, 278 (1979).

[33] R.C. Davidson, *Physics of Nonneutral Plasmas* (Addison-Wesley, Redwood City, CA, 1990).

[34] S. Ichimaru, *Statistical Plasma Physics Vol. 1: Basic Principles* (Addison-Wesley, Redwood City, CA, 1992).

[35] L. D. Landau and E. M. Lifshitz, *Electrodynamics of Continuous Media* (Pergamon Press, Oxford, 1960).

[36] D. H. E. Dubin, Phys. Rev. Lett. **66**, 2076 (1991).

[37] M. D. Tinkle, R. G. Greaves, C. M. Surko, R. L. Spencer, and G. W. Mason, Phys. Rev. Lett. **40**, 352 (1994).

[38] D. H. E. Dubin, Phys. Fluids B **5**, 295 (1993).

[39] R. L. Spencer, S. N. Rasband, and R. R. Vanfleet, Phys. Fluids B **5**, 4267 (1993).

[40] Johnny K. Jennings, Ross L. Spencer, and K.C. Hansen, Phys. Plas. **2**, 2630 (1995).

[41] D. Lesage, Ph.D. thesis, Harvard University, 2008.

[42] T. Yazaki, Phys. Rev. E **48**, 1806 (1993).

[43] A.; Narahara Y. Yazaki, T.; Tominaga, J. Heat Transfer. **105(4)**, 889 (1983).

[44] U. H. Kurzweg and Ling de Zhao, Physics of Fluids **27**, 2624 (1984).

[45] D. S. Hall, Ph.D. thesis, Harvard University, 1997.

[46] Frank Pobell, *Matter and Methods at Low Temperatures* (Springer Verlag, Berlin, 1992).

[47] P. Horowitz and W. Hill, *The Art of Electronics, Second Edition* (Cambridge University, Cambridge, 1989).

[48] B. Levitt, G. Gabrielse, P. Larochelle, D. Le Sage, W.S. Kolthammer, R. McConnell, J. Wrubel, A. Speck, D. Grzonka, W. Oelert, T. Sefzick, Z. Zhang, D. Comeau, M.C. George, E.A. Hessels, C.H. Storry, M. Weel, and J. Walz, Physics Letters B **656**, 25 (2007).

[49] A. Einstein, Ann. Phys. **17**, 132 (1905).

[50] Xinrong Jiang, C. N. Berglund, Anthony E. Bell, and William A. Mackie, J. Vac. Sci. Technol. B **16**, 3374 (1998).

[51] R. D. Dixon and L. A. Lott, Journal of Applied Physics **40**, 4938 (1969).

[52] X. Feng, M. Charlton, M. Holzscheiter, R. A. Lewis, and Y. Yamazaki, J. Appl. Phys. **79**, 8 (1996).

[53] G. Gabrielse, A. Khabbaz, D. S. Hall, C. Heimann, H. Kalinowsky, and W. Jhe, Phys. Rev. Lett. **82**, 3198 (1999).

[54] P.A.M. Dirac, Proc. Roy. Soc. **A133**, 62 (1931).

[55] O. Chamberlain, E. Segrè, C. Wiegand, and T. Ypsilantis, Phys. Rev. **100**, 947 (1955).

[56] G. Gabrielse, X. Fei, K. Helmerson, S. L. Rolston, R. L. Tjoelker, T. A. Trainor, H. Kalinowsky, J. Haas, and W. Kells, Phys. Rev. Lett. **57**, 2504 (1986).

[57] G. Gabrielse, X. Fei, L. A. Orozco, R. L. Tjoelker, J. Haas, H. Kalinowsky, T. A. Trainor, and W. Kells, Phys. Rev. Lett. **63**, 1360 (1989).

[58] D. Möhl, Hyperfine Int. **109**, 33 (1997).

[59] Herbert Stelzer, Nuc. Inst. Meth. **133**, 409 (1976).

[60] Claude Amsler, Rev. Mod. Phys. **70**, 1293 (1998).

[61] G. Gabrielse, X. Fei, L. A. Orozco, S. L. Rolston, R. L. Tjoelker, T. A. Trainor, J. Haas, H. Kalinowsky, and W. Kells, Phys. Rev. A **40**, 481 (1989).

[62] J. Estrada, Ph.D. thesis, Harvard University, 2002.

[63] X. Fei, R. Davisson, and G. Gabrielse, Rev. Sci. Instrum. **58**, 2197 (1987).

[64] F. Anderegg, E. M. Hollmann, and C. F. Driscoll, Phys. Rev. Lett. **81**, 4875 (1998).

[65] P.B. Schwinberg, R.S. VanDyck, and H.G. Dehmelt, Phys. Lett. A **81**, 119 (1981).

[66] R. J. Hughes and B. I. Deutch, Phys. Rev. Lett. **69**, 578 (1992).

[67] R. S. VanDyck, P. B. Schwinberg, and H. G. Dehmelt, Phys. Rev. Lett. **59**, 26 (1987).

[68] J. Estrada, T. Roach, J. N. Tan, P. Yesley, and G. Gabrielse, Phys. Rev. Lett. **84**, 859 (2000).

[69] N. Bowden, Ph.D. thesis, Harvard University, 2003.

[70] R. G. Greaves and C. M. Surko, Canad. J. Phys. **74**, 445 (1996).

[71] C. M. Surko, M. Leventhal, and A. Passner, Phys. Rev. Lett. **62**, 901 (1989).

[72] D. Comeau, Ph.D. thesis, York University, 2009.

[73] E. M. Hollmann, F. Anderegg, and C. F. Driscoll, Physics of Plasmas **7**, 2776 (2000).

[74] Stephan Berko and Frank L. Hereford, Rev. Mod. Phys. **28**, 299 (1956).

[75] D. Hanneke, S. Fogwell, and G. Gabrielse, Physical Review Letters **100**, 120801 (2008).

[76] D. Hanneke, S. Fogwell, N. Guise, J. Dorr, and Gabrielse. G., in *Proceedings of ICAP XXI* (World Scientific, New Jersey, 2008).

[77] José Verdú, Susanne Kreim, Joseba Alonso, Klaus Blaum, Slobodan Djekic, Wolfgang Quint, Stefan Stahl, Stefan Ulmer, Manuel Vogel, Jochen Walz, and Günter Werth, in *Penning Trap Measurement of the Magnetic Moment of the Antiproton*, edited by Dieter Grzonka, RafałCzyżykiewicz, Walter Oelert, Tomasz Rożek, and Peter Winter (AIP, Bonn (Germany), 2005), No. 1, pp. 260–265.

[78] D. J. Wineland and H. G. Dehmelt, J. Appl. Phys. **46**, 919 (1975).

[79] A. Khabbaz, Ph.D. thesis, Harvard University, 1998.

[80] W. Shockley, J. Appl. Phys. **9**, 635 (1938).

[81] D. DeMaw, *The Radio Amateur's Handbook* (The American Radio Relay League, Newington, CT., 1971).

[82] H. Nyquist, Phys. Rev. **32**, 110 (1928).

[83] B. D'Urso, Ph.D. thesis, Harvard Univ., 2003.

[84] N. Guise, Ph.D. thesis, Harvard University, 2009.

[85] J. Walz and T. Hänsch, General Relativity and Gravitation **36**, 561 (2004).

[86] J.Walz, H.Pittner, M.Hermann, P.Fendel, B.Henrich, and T. W. Hänsch, Appl. Phys.B **77**, 713 (2003).

[87] I. D. Setija, H. G. C. Werij, O. J. Luiten, M. W. Reynolds, T. W. Hijmans, and J. T. M. Walraven, Phys. Rev. Lett. **70**, 2257 (1993).

[88] W.D. Phillips, S.L. Rolston, P.D. Lett, T. McIlrath, and N.Vansteenkiste, Hyperfine Interact. **76**, 265 (1993).

[89] E. Peik, G. Hollemann, and H. Walther, Phys. Rev. A **49**, 402 (1994).

[90] D. Vrinceanu, S. X. Hu, S. Mazevet, and L. A. Collins, Phys. Rev. A **72**, 042503 (2005).

[91] G. W. F. Drake, Phys. Rev. Lett. **24**, 126 (1970).

[92] H. Massie, *Negative Ions, Third Edition* (Cambridge University Press, Cambridge, 1976).

[93] R.J. Gould and E.E. Salpeter, Astrophys. J. **138**, 393 (1963).

[94] P K Biswas, Journal of Physics B: Atomic, Molecular and Optical Physics **34**, 4831 (2001).

[95] P. Perez and A. Rosowsky, Nuc. Inst. Meth. A **545**, 20 (2005).

[96] M. Fischer, N. Kolachevsky, M. Zimmermann, R. Holzwarth, Th. Udem, T. W. Hänsch, M. Abgrall, J. Grünert, I. Maksimovic, S. Bize, H. Marion, F. Pereira Dos Santos, P. Lemonde, G. Santarelli, P. Laurent, A. Clairon, C. Salomon, M. Haas, U. D. Jentschura, and C. H. Keitel, Phys. Rev. Lett. **92**, 230802 (2004).

[97] Dale G. Fried, Thomas C. Killian, Lorenz Willmann, David Landhuis, Stephen C. Moss, Daniel Kleppner, and Thomas J. Greytak, Phys. Rev. Lett. **81**, 3811 (1998).

[98] T. Pohl, H. R. Sadeghpour, Y. Nagata, and Y. Yamazaki, Phys. Rev. Lett. **97**, 213001 (2006).

[99] C L Taylor, Jingjing Zhang, and F Robicheaux, J. Phys. B **39**, 4945 (2006).

[100] W.H. Wing, Progr. Quant. Electr. **8**, 181 (1984).

[101] Harald F. Hess, Phys. Rev. B **34**, 3476 (1986).

[102] Harald F. Hess, Greg P. Kochanski, John M. Doyle, Naoto Masuhara, Daniel Kleppner, and Thomas J. Greytak, Phys. Rev. Lett. **59**, 672 (1987).

[103] Alan L. Migdall, John V. Prodan, William D. Phillips, Thomas H. Bergeman, and Harold J. Metcalf, Phys. Rev. Lett. **54**, 2596 (1985).

[104] C.I. Hancox, S.C. Doret, M.T. Hummon, L Luo, and J.M. Doyle, Nature **431**, 281 (2004).

[105] P. Elleaume, O. Chubar, and J. Chavanne, in *Proceedings of the 1997 Particle Accelerator Conference* (PUBLISHER, ADDRESS, YEAR).

[106] T. M. Squires, P. Yesley, and G. Gabrielse, Phys. Rev. Lett. **86**, 5266 (2001).

[107] P. Yesley, Ph.D. thesis, Harvard University, 2001.

[108] E. Gilson and J. Fajans, in *Non-neutral Plasma Physics IV*, edited by F. Anderegg, L. Schweikhard, and C. F. Driscoll (AIP, New York, 2002), Vol. 606, p. 378.

[109] E. Gilson, Ph.D. thesis, University of California at Berkeley, 2001.

[110] J. Fajans and A. Schmidt, Nuc. Inst. Meth. A **521**, 318 (2004).

[111] J. Fajans, W. Bertsche, K. Burke, S. F. Chapman, and D.P van der Werf, Phys. Rev. Lett. **95**, 155001 (2005).

[112] G. Andresen, W. Bertsche, A. Boston, P. D. Bowe, C. L. Cesar, S. Chapman, M. Charlton, M. Chartier, A. Deutsch, J. Fajans, M. C. Fujiwara, R. Funakoshi, D. R. Gill, K. Gomberoff, J. S. Hangst, R. S. Hayano, R. Hydomako, M. J. Jenkins, L. V. Jørgensen, L. Kurchaninov, N. Madsen, P. Nolan, K. Olchanski, A. Olin, A. Povilus, F. Robicheaux, E. Sarid, D. M. Silveira, J. W. Storey, H. H. Telle, R. I. Thompson, D. P. van der Werf, J. S. Wurtele, and Y. Yamazaki, Phys. Rev. Lett. **98**, 023402 (2007).

[113] C. H. Storry, A. Speck, D. Le Sage, N. Guise, G. Gabrielse, D. Grozonka, W. Oelert, G. Scheppers, T. Sefzick, J. Walz, H. Pittner, M. Herrmann, T. W. Hänsch, D. Comeau, and E. A. Hessels, Phys. Rev. Lett. **93**, 263401 (2004).

[114] D. Vrinceanu, B. E. Granger, R. Parrott, H. R. Sadeghpour, L. Cederbaum, A. Mody, J. Tan, and G. Gabrielse, Phys. Rev. Lett. **92**, 133402 (2004).

[115] G. Gabrielse, A. Speck, C. H. Storry, D. Le Sage, N. Guise, D. Grzonka, W. Oelert, G. Schepers, T. Sefzick, H. Pittner, J. Walz, T. W. Hänsch, D. Comeau, and E. A. Hessels, Phys. Rev. Lett. **93**, 073401 (2004).

[116] T. Pohl, H. R. Sadeghpour, and G. Gabrielse, Physical Review Letters **97**, 143401 (2006).

[117] G. Gabrielse, N. S. Bowden, P. Oxley, A. Speck, C. H. Storry, J. N. Tan, M. Wessels, D. Grzonka, W. Oelert, G. Schepers, T. Sefzick, J. Walz, H. Pittner, T. W. Hänsch, and E. A. Hessels, Phys. Rev. Lett. **89**, 233401 (2002).

[118] G. Gabrielse, S. L. Rolston, L. Haarsma, and W. Kells, Hyperfine Interact. **44**, 287 (1988).

[119] W. Bertsche, A. Boston, P.D. Bowe, C.L. Cesar, S. Chapman, M. Charlton, M. Chartier, A. Deutsch, J. Fajans, M.C. Fujiwara, R. Funakoshi, Gomberoff, J.S. Hangst, R.S. Hayano, M.J. Jenkins, L.V. Jørgensen, P. Ko, N. Madsen, P. Nolan, R.D. Page, L.G.C. Posada, A. Povilus, E. Sarid, D.M. Silveira, D.P. van der Werf, Y. Yamazaki (ALPHA Collaboration), B.Parker, J.Escallier, and A.Ghosh, Nuclear Instruments and Methods in Physics Research A **566**, 746 (2006).